A prototype Cylindrical And Tiny Spectrometer for the rapid energy analysis of space plasmas

Robert Bedington

Mullard Space Science Laboratory

Submitted to UCL for the degree of Doctor of Philosophy

2012

I, Robert Bedington, confirm that the work presented in this thesis is my own. Where information has been derived from other sources, I confirm that this has been indicated in the thesis.

Abstract

Miniaturised space plasma analysers allow for lower cost plasma measurements for space science and for space weather monitoring applications; further miniaturisation will make possible nanosat-scale plasma instruments. Small instruments produced in large numbers are ideal for very-large-scale swarm and constellation missions. The field of MEMS (micro-electro-mechanical systems) potentially enables all these possibilities.

This thesis introduces these themes and describes the conception and development of CATS (Cylindrical And Tiny Spectrometer), an instrument designed with MEMS in mind. CATS uses an innovative, highly-miniaturised, concentric cylindrical geometry that is able to measure simultaneously, multiple energies of both electrons and ions in space plasmas.

A prototype of a CATS analyser head has been fabricated – the critical electrodes by electron discharge machining – and has been demonstrated with 30 eV to 8 keV electrons in a laboratory environment. A CEM (channel electron multiplier) and a CCD (charge coupled device) have been adapted for use with the prototype. The CCD is a back-illuminated, ion-implanted device that has been used to detect electrons directly—the first known use of such a device in an analyser instrument.

The prototype design has also been extensively modelled using SIMION charged particle ray-tracing simulations, run within a tool-kit of specially created and highly sophisticated IDL automation and analysis routines. This has revealed the focussing properties of the design and options for improvements.

The experimental results were compared with the simulation results and discrepancies were revealed that suggested deviations from the design specification. These deviations were confirmed, in part, by a visual inspection.

Recommendations for future work and possible applications of the instrument are discussed, including the destination of the current CATS prototype and CCD detector: PoleCATS, a student-led, educational project to develop a low-altitude sounding rocket instrument.

Contents

List of Figures

List of Tables

List of Equations

List of symbols

K	K factor
$E_{selected}$	Peak energy selected by a CPA (eV)
$V_{applied}$	Voltage applied between CPA electrodes (V)
G	Geometric factor (cm^2 sr eV/eV)
$N_{detected}$	Number particles of detected by detector at exit of CPA electrodes
N_{in}	Number of particles entering CPA instrument aperture
A	Area of instrument aperture (cm^2)
Ω	Solid angle of range of input angles incident on instrument entrance aperture (sr)
ΔE	FWHM of CPA energy response, at a fixed electrode potential (eV)
E_{peak}	Peak energy of CPA energy response, at a fixed electrode potential (eV)
R_0	Mean radius of curvature of a CATS channel [cylindrical CPA] (mm)
ΔR	CATS channel width (CPA electrode separation distance) (mm)
R_{outer}	Radius of the outer (larger) CATS CPA channel wall (mm)
R_{inner}	Radius of the inner (smaller) CATS CPA channel wall (mm)
ΔR_{exit}	Width of CATS exit apertures in dimension parallel to CPA plates (mm)
E_{max}	Maximum energy detectable by CATS (eV)

V	Electric potential (V)
E	Electric field
$\Delta\theta$	Range of elevation angles entering CATS (°)
$\Delta\phi$	Range of azimuth angles entering CATS (°)
x	co-ordinate axis
y	co-ordinate axis
z	co-ordinate axis
S	Charge measured on strip of wedge and strip anode (C)
W	Charge measured on wedge of wedge and strip anode (C)
Z	Charge measured on background anode of wedge and strip anode (C)
$\eta(x)$	CCE as a function of distance away from the back surface
η_0	CCE at back surface of CCD
L	Length of region of reduced CCE in CCD (µm)

Glossary of Acronyms

ADU	Analogue-digital unit
AMMICE	Advanced Mass and Ionic Charge Composition Experiment
AMPS	Advanced Miniature Plasma Spectrometer
AMPTE	Active Magnetospheric Particle Tracer Explorers
ASPERA	Analyzer of Space Plasma and Energetic Atoms
ASPOC	Active Spacecraft Potential Control
AutoGEM	Automated geometry simulations
CAD	Computer Aided Design
CAPS ELS	CAssini Plasma Spectrometer ELectron Spectrometer
CATS	Cylindrical And Tiny Spectrometer
CATS+CCD	CATS analyser with CCD detector setup
CATS+CEM	CATS analyser with CEM detector setup
CATSscan	Flatbed scanner image of the CATS misalignments
CCD	Charge-coupled device
CCE	Charge collection efficiency
CEM	Channel Electron Multiplier
CEM	Channel electron multiplier

CMOS	Complementary metal-oxide-semiconductor
COR2	Second Coronagraph instrument on STEREO
CPA	Curved plate analyser
CPO	Charged Particle Optics
DLP	Digital light processing
DRIE	Deep Reactive Ion Etching
EDM	Electron discharge machining
EMCCD	Electron Multiplying CCD
ESA	European Space Agency / Electro-static analyser
FlaPS	Flat Plasma Spectrometer
FONEMA	Fast Omni-directional Non-scanning Energy Mass Analyser
FOV	Field of view
FWHM	Full width at half maximum
GEANT4	GEometry ANd Tracking v.4
GOES	Geostationary Operational Environmental Satellite
gu	Grid unit
HARP	Hyperbolic electrostatic Analyzer working in a Retarding Potential mode
HEEA	High Energy Electron Analyser
HV	High voltage
IC	Integrated circuit
ICL	Imperial College London
IDL	Interactive Data Language

IES	Ion and Electron Sensor
IMP	Interplanetary Monitoring Platform
IMS	Ion Mass Spectrometer
INTEGRAL	INTErnational Gamma-Ray Astrophysics Laboratory
IRM	Ion Release Module
KOH	Potassium Hydroxide
LabVIEW	Laboratory Virtual Instrumentation Engineering Workbench
LEEA	Low Energy Electron Analyser
LEPIC	Low Energy Plasma and Ion Calibration
LIGA	Lithographie, galvanoformung, abformung
LN2	Liquid nitrogen
LV	Low voltage
MCP	Microchannel plate
MEDUSA	Miniaturized Electrostatic DUal tophat Spherical Analyser
MEMS	Microelectromechanical systems
MESA	Miniaturized ElectroStatic Analyzer
MIPA	Miniature Ion Precipitation Analyser
MMS	Magnetospheric Multi Scale / Miniaturised Mass Spectrometer
MSSL	Mullard Space Science Laboratory
NASA	National Aeronautics and Space Administration
OMC	Optical Monitoring Camera
PA	Potential array

PACIDERM	Plasma Automated Chamber Integrated Data Extraction Routine Miscellany
PCB	Printed circuit board
PEACE	Plasma Electron And Current Experiment
PID	Payload interface document
PoleCATS	Polar test of the Cylindrical And Tiny Spectrometer
PXI	PCI eXtensions for Instrumentation
RAPID	Research with Adaptive Particle Imaging Detectors
REXUS	Rocket EXperiments for University Students
RF	Radio frequency
RPA	Retarding potential analyser
RTG	Radioisotope thermoelectric generator
SCA	Single channel analyser
SEM	Scanning Electron Microscope
SiO_2	Silicon Dioxide
SNR	Signal to noise ratio
SOHO	Solar and Heliospheric Observatory
SOI	Silicon on insulator
SPENVIS	Space Environment Information System
SSD	Solid state detector
STEREO	Solar TErrestrial RElations Observatory
SUMER	Solar Ultraviolet Measurement of Emitted Radiation
SWICS	Solar Wind Ion Composition Explorer

SWIM	Solar WInd Monitor
SXI	Solar X-Ray Imager
TBC	To be confirmed
TDM	Technical Data Management
THEMIS	Time History of Events and Macroscale Interactions during Substorms
TID	Total Ionising Dose
TIMAS	Toroidal Imaging Mass-Angle Spectrograph
TOF	Time of flight
TQ	Trajectory quality
UCL	University College London
UKUBE	United Kingdom Universal Bus Experiment
UV	Ultraviolet
UVCS	Ultraviolet Coronagraph Spectrometer
WISPER	Wafer Integrated SPectrometER

Chapter 1

Space Plasma Analysers

This chapter describes the background and context into which this work fits. It starts with a few words on space plasma and why one would want to analyse it, before imparting on a brief overview of plasma instrumentation, starting very broadly but quickly focussing on the area of interest. It will introduce the instrument concepts and techniques that have been used in the past and some of the miniaturised instruments that have been developed from these.

1.1 Space plasma

Plasma is a state of matter in which the constituent particles are so energetic that some of them, or all of them, are able to overcome the attractive potentials of opposing charges and instead of remaining as atoms they exist as independent ions and electrons. This results in a state that cannot be entirely described by the physics of solids, liquids or gases alone.

Plasmas are not particularly common on Earth. Outside of laboratories, fluorescent lights and plasma TVs they are only usually found in flames and lightning. For the Universe as a whole however this is unusual, since more than 99 per cent of known matter is in the plasma state: most obviously in stars, being big balls of plasma, but surprisingly, and even more abundantly, in the tenuous interstellar medium. In fact, you only need to leave the Earth by about 100 km before all the matter around you, all that within and above the ionosphere, has to be modelled using plasmaphysical

methods [8].

The Sun's corona continuously emits streams of charged particles. These particles are mostly electrons and protons and they form a highly energetic, highly conductive plasma that has sufficient kinetic energy to escape the Sun's gravity and propagate through the solar system. This plasma is referred to as the solar wind and when it reaches objects in the solar system it interacts with them in different ways, depending chiefly on their magnetic properties.

Mars for example, has no substantial magnetic field so has little to deflect or moderate the incoming solar wind, which scavenges the upper atmosphere and gradually sweeps it away into space. Four billion years ago, Mars is believed to have had a planetary dynamo, creating an enveloping magnetosphere protecting a much denser Martian atmosphere. It is theorised that there were once large oceans, but when the magnetic dynamo ceased the atmosphere was gradually lost and Mars became the barren and desolate world we find today [5, 29].

Earth on the other hand retains a planetary magnetic dynamo and a magnetosphere that extends for many thousands of kilometres into space. Since plasma is formed of charged particles, it interacts with Earth's magnetic field causing interesting phenomena. Some particles are accelerated to MeV energies, and constrained by electromagnetic forces hurtle along closed paths around the Earth in the radiation (Van Allen) belts.

The particles can also find themselves directed into the Earth's magnetotail, where they can become involved in magnetic reconnection events. In these events, vast amounts of energy are released by processes which fundamentally challenge our understanding of the physics of magnetic fields. The resultant effect is that the plasma particles that have collected in the tail are sent streaming back towards Earth, following the magnetic field lines down towards the Earth's poles and then, when they encounter the atmosphere, interact in such a way to produce what we see as the aurorae, like those shown in figure 1.1.

Solar wind–magnetosphere interactions have other, less desirable effects. During particularly violent 'geomagnetic storms', satellite electronics can suffer radiation damage or be short-circuited by penetrating energetic charged particles, power distribution grids

Figure 1.1: Aurorae above Esrange rocket base in Swedish Lapland.

on Earth can be damaged by induced currents and the occupants of aeroplanes flying in polar regions can receive high radiation doses. There are thus several reasons – scientific, commercial and technical – why the monitoring, measuring and studying of space plasma and the resultant space weather is not just desirable, but necessary.

1.2 Space plasma environments

The Earth's magnetosphere creates regions which contain plasmas with different energies and fluxes—at low Earth orbits the plasma is typically cold and dense, further out at geostationary orbit the plasma is hotter and less benign. The topography of the plasma structures can be seen in figure 1.2. The Earth is the circle at the centre of the figure; the Sun is someway beyond the left hand border, the Earth's magnetotail stretches off the right side of the page.

Characteristic average omni-directional differential ion and energy fluxes (differential particle flux times particle energy) for some of these regions are shown in figure 1.3. It can be seen here that measured maximum fluxes of ions vary within approximately six orders of magnitude and measured maximum fluxes of electrons within approximately three orders of magnitude.

Elsewhere in our solar system a myriad of plasma environments can be found (fig-

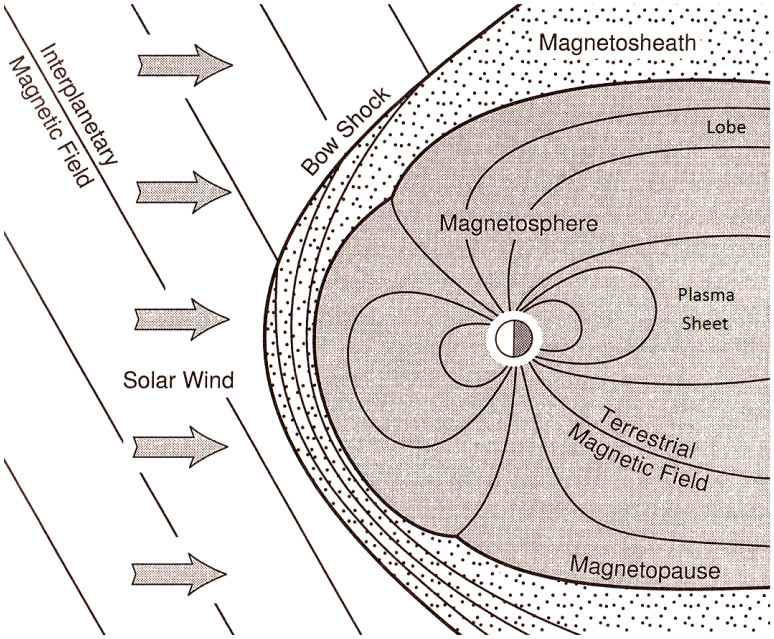

Figure 1.2: Plasma structure of Earth's magnetosphere [8].

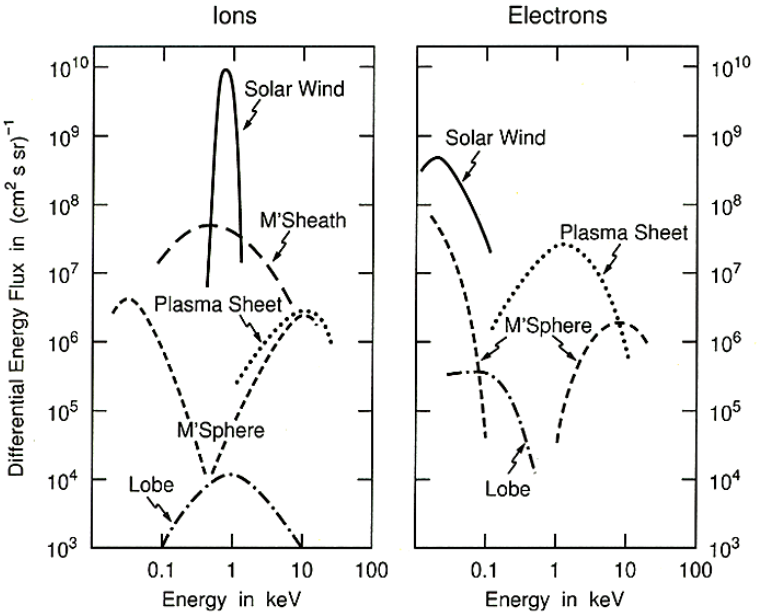

Figure 1.3: Typical differential energy fluxes measured around Earth's magnetosphere [8].

ure 1.4). These can be comet-like for the unmagnetised bodies and massively varying

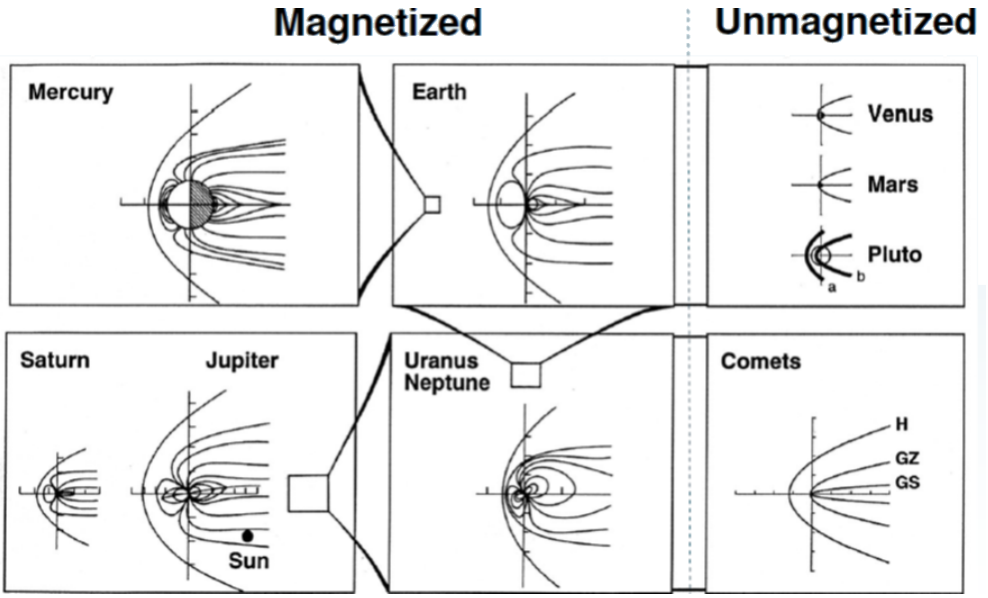

Figure 1.4: Comparison of the plasma environments – scale of bow shocks and magnetic field lines – of magnetised and unmagnetised solar system bodies. Circle at Pluto indicates the orbit of Charon with a) aphelion and b) perihelion predicted bow shocks. H: Halley, GZ: Giacobini–Zinner and GS: Grigg–Skjellerup [25, 75].

for the magnetised planets—depending on the different magnetic dipole strengths and orientations, spin rates, particle sources (such as moons and ionospheres) and particle sinks (such as rings) [25].

1.3 Studying plasma in the solar system

Plasma in the solar system is studied using a variety of remote sensing and in-situ methods. Coronagraphs on satellites like STEREO and SOHO are used for the remote sensing of dynamic plasma in the corona. Figure 1.5 shows a CME (Coronal Mass Ejection), a large cloud of high energy plasma and magnetic field ejected from the Sun. The plasma is visible through the Thomson scattering of solar photons. Earth-based remote plasma sensing techniques include all-sky auroral imagers and radar experiments like ionosondes.

This thesis is concerned however with in-situ instrumentation: instruments on rockets,

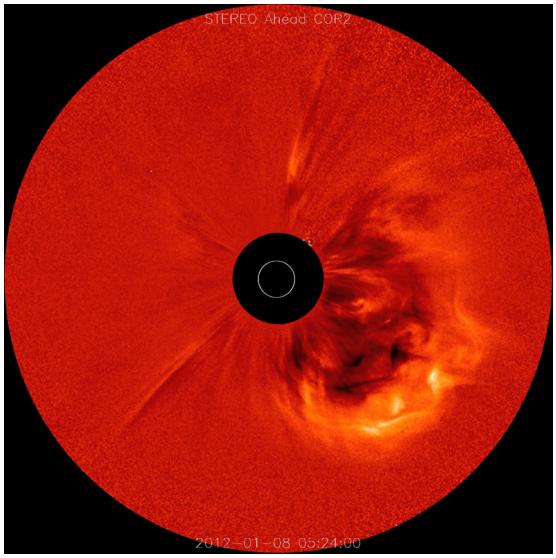

Figure 1.5: A coronal mass ejection as viewed by STEREO Ahead COR2 instrument. Source: http://stereo.gsfc.nasa.gov/img/stereoimages/preview/Diff_COR2_JanA.jpg

.

satellites and interplanetary probes that venture into the solar system plasmas to study directly their fields and particles. While this has the advantages of direct rather than inferred measurements, it is subject to some fundamental complications. Naturally there are the usual technical constraints associated with space based instrumentation: power and communications limitations, ionising radiation and the high monetary cost of lifting something into space, but there are also at least two plasma-specific issues.

Firstly, the in-situ measurements record the plasma parameters and how they vary with time at the location of the instrument on the spacecraft. Since the plasma is varying temporally and spatially, and the spacecraft is moving also, there is an ambiguity as to whether a variation in the measured plasma is due to a time variation or a position variation. The desire to deconvolve these variations has resulted in multi-point measurement plasma missions such as ESA's Cluster [37] and NASA's MMS (Magnetospheric Multi Scale) [112] multi-satellite missions.

Secondly, many plasma measurements require an electric potential to be measured compared to ground (zero volts). By definition space has no ground, so the internal spacecraft ground has to be used instead. Unfortunately the spacecraft itself can become charged by spacecraft resources (like RTGs, radioisotope thermoelectric gen-

erators) as well as by photoelectrons, which are produced on its surface when sunlit. Additionally to changing the ground potential for measurements, this spacecraft charging also has the effect of creating a (Debye) sheath of plasma around the craft which can confuse measurements and repel similarly charged low energy particles. This sheath will be smaller in denser plasmas where the characteristic interaction (Debye) lengths are shorter.

The spacecraft potential can usually be deduced with instruments such as Langmuir probes (which will be described later) and with specialised devices, like ASPOC on Cluster, it can be actively controlled. Instruments can also be mounted on booms that extend beyond the Debye sheath.

1.3.1 Electromagnetic fields

Solar system plasmas often contain electromagnetic fields, whose field-line topologies should be mapped to be understood. Waves, rapidly changing fields, can be superimposed on top of these fields. Electric and magnetic field and wave instruments are briefly introduced in the following subsections and further details can be found in [125].

Electric

Electric fields are measured by taking a voltmeter reading across two points in the plasma. The simplest option is using a single antenna for one point and the spacecraft body as the second. This arrangement, somewhat misleadingly referred to as a monopole antenna, is not usually ideal as it is susceptible to spacecraft generated interference. To avoid this a dipole arrangement can be used with two antennae protruding from opposite sides of the spacecraft, extending beyond the Debye sheath and photoelectron cloud so that the electric field can be inferred by measuring the potential difference between them.

Examples include cylindrical dipoles – consisting of two conducting cylinders – or spherical double probes, spheres on the end of long booms or wires. While these too will suffer from charging, a bias current can be drawn from the probes to mitigate it [103]. The ESA Cluster satellites each use four such $\sim$10 cm diameter spherical probes on $\sim$40 m wires held taut by the spin of the spacecraft. Using opposite pairs, a 2D mea-

surement of the field can be made. In some missions, including THEMIS [4], the third (orthogonal) dimension is also measured, albeit with less accuracy, by a short stiff boom deployed along the spacecraft spin axis [52].

Magnetic

A loop antennae can be used to detect the magnetic component in plasma waves while static magnetic fields can be measured using magnetometers [118]. The most widely used form of magnetometer in space plasma missions is the fluxgate magnetometer [105] which is shown schematically in figure 1.6.

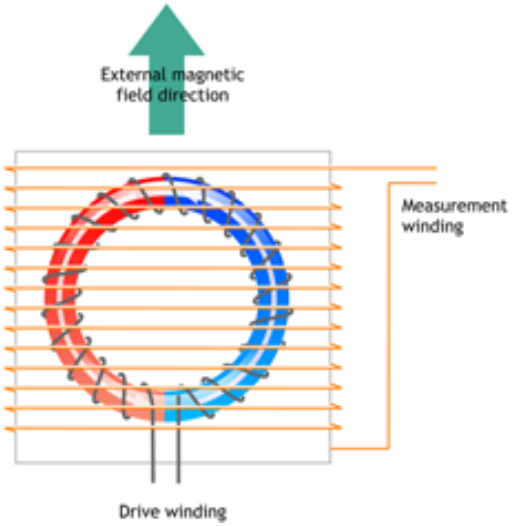

Figure 1.6: Schematic of a fluxgate magnetometer.
Source: http://bluebird.physics.ualberta.ca/carismaweb/content/view/72/1/

The circular magnetic core has a toroidal drive winding around it which is supplied with an alternating current. The voltage driving this current is shown in figure 1.7a and the magnetic field induced in the core is shown in figure 1.7b. It can be seen from figure 1.7b that the magnetic core is driven to saturation point with one polarity, then to saturation point with the other polarity with each voltage alternation, shown here in colour coordination with figure 1.6.

Figure 1.7c shows that in the absence of an external field (i.e. a field to be measured) that there is no net field from the core, but when there is an external field present the magnetic hysteresis process is asymmetrical and this can be detected as an induced

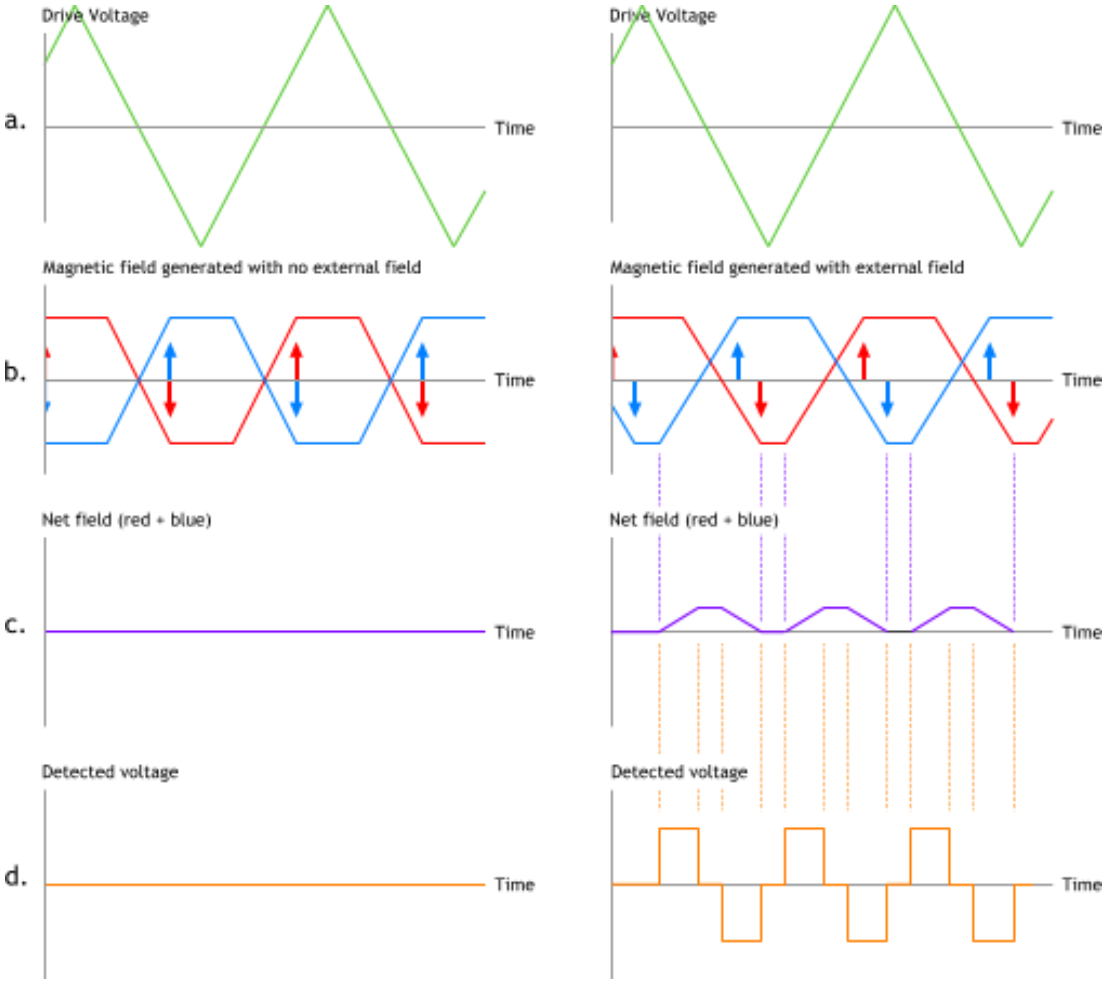

Figure 1.7: Graphs describing the operation of the magnetometer in figure 1.6. Source: http://bluebird.physics.ualberta.ca/carismaweb/content/view/72/1/

voltage in the sense windings (figure 1.7d).

1.3.2 Particles

Particle instruments are used to obtain the velocity, number density and mass of plasma particles, which are then used to infer many further bulk properties of the plasma. They may detect electrons, ions, neutrals or a combination. A suite of particle instrumentation is usually required to measure all the parameters for all species of particles over a wide range of energies. It is on particle instrumentation that this project is based and so it is particle instruments that shall be focussed on from now onwards.

One of the simplest forms of plasma particle instrument is the Langmuir probe. Such instruments have been used extensively since the earliest space plasma missions, e.g. the cylindrical probe flown in 1958 during the first geophysical year [16]. A Langmuir probe is a bare metal charge collector that is mounted on a boom projecting from the spacecraft. The current flowing from the probe is measured as the voltage applied to it is varied. The resulting curve allows for the deduction of the plasma electron temperature and electron and ion densities as well as the spacecraft potential (due to spacecraft charging as discussed in section 1.3).

More sophisticated particle instruments can measure the velocity distribution function of plasma particles, taking into account both their energy and direction of travel. Bulk parameters like density, velocity and pressure can then be derived from the moments of this distribution function. They usually have an analysing and/or collimating component or components that direct particles onto different detectors or different regions of a position sensitive detector. The analysing and collimating sections filter out, focus or sort the plasma particles into bandpasses (or sometimes high or low passes) according to a particle's velocity, charge, mass or a combination of those parameters. The detector converts the arrival of the particles into currents or charge pulses which can be amplified, quantified and recorded. These recorded data can be in the form of the number of particles, deposited charge, deposited energy or a combination.

Ion mass can be obtained by solid state detectors and time of flight techniques. Energy/charge and mass/charge ratios are usually obtained using electric and magnetic field based techniques. Appropriate techniques and detectors are combined to produce

an instrument with the desired measurement capabilities. These three methods, solid state, time of flight and electromagnetic field shall now be outlined.

Solid State

Solid state instruments work on the principle of measuring the energy deposited in a p-n junction of semi-conductor material (usually silicon) and are generally the preferred method for the detection of most kinds of particles with energies of several keV or more. They often have an angle filtering (collimating) feature mounted in front of them so the particle's direction can be determined.

As the incident plasma particles penetrate into the silicon, they impart energy to it in the form of electron-hole pairs, with an average energy of process of 3.64 eV [42]. It is the electrons from these pairs that are collected and counted to measure the particle's energy. For energetic ions this is quite effective as they will transfer most of their energy to the silicon, for energetic electrons it can be more complex as they have a greater tendency to scatter back out the material and deposit only a fraction of their total energy [126].

Time of Flight

Time of flight (TOF) analysers are used to measure the time it takes for an ion to move along a certain trajectory. A start signal is created as the ions enter the instrument, often through the production of secondary electrons as the ions pass through a thin foil. A stop signal is created usually when the ion hits a detector e.g. a solid state detector. The length of the path and the time taken allow the velocity of the particle to be determined. If the ion's energy is known, from the solid state detector or a separate energy analysing section, then the ion's mass can be determined [132].

The Ion Mass Spectrometer (IMS) instrument on Cassini, shown in figure 1.8 has a sophisticated example of this, using a varying strength, reflecting electric field for improved measurement resolution [92].

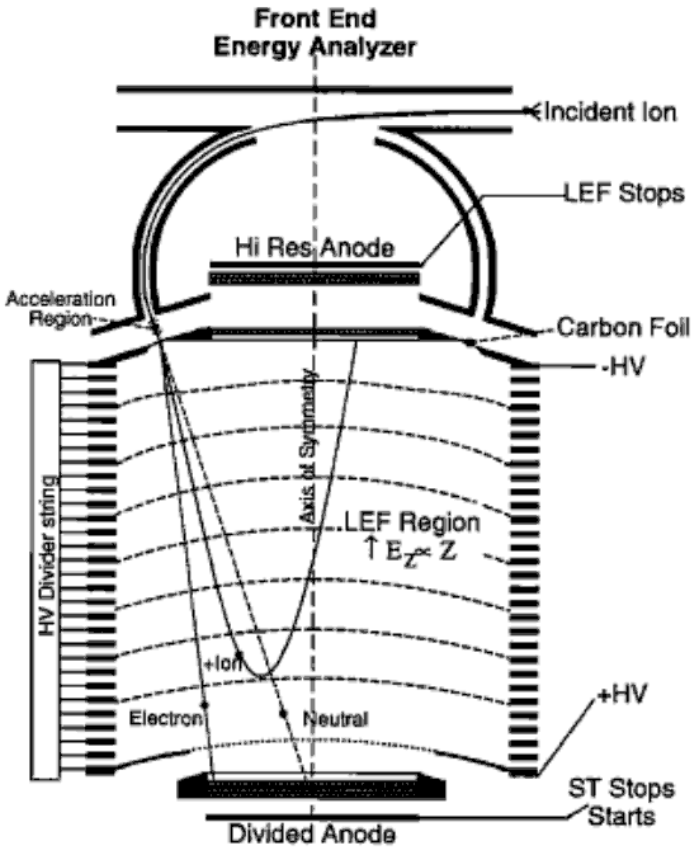

Figure 1.8: IMS instrument on Cassini. It is approximately cylindrically symmetric about the central axis [92].

Electric field and magnetic field based analysers

Electric and magnetic fields can be used to deflect charged particles to determine their properties (the previous section has shown an example of the former). For the energy analysis of particles it is more common to use electric fields, since the energy dynamic range is larger (10^3:1 for magnetic compared to 10^5:1 for electric) the required mass of magnetic material is large and the shielding of the magnetic field can be problematic [135]. Magnetic fields therefore tend to be reserved for mass analysers. The TIMAS instrument[1] for example, has first an energy analysing electrostatic analyser section which then passes the selected ions into a mass analysing magnetic analyser section [113]. The FONEMA[2] instrument on the ill-fated Mars 96 mission used quite different analysers and in the opposite order, the magnetic field based mass analysis preceding the electrostatic based energy analysis [63]. This instrument will be discussed further in section 1.4.2.

Mass analysis can be achieved with electric fields also. Quadrupole analysers have four conducting rods parallel to the ions trajectory. An oscillating RF electric field is created between opposing pairs of rods and only ions with a certain mass/charge ratio resonant with that field will be able to pass through. The Galileo probe sent to Jupiter had a sophisticated example of such an instrument [95] .

This project however is concerned with electrostatic energy analysers and these will be the subject of this introduction from here. Electrostatic energy analysers are well suited to detecting the very lowest energies of charged particles (a few keV and below) and are introduced in the following section.

1.4 Electrostatic energy analysers

Electrostatic energy analysers (ESAs) use a static electric field to alter the trajectories of charged particles. The deflection of the trajectory is proportional to the energy/charge ratio. Only certain trajectories can be transmitted through the analyser to a detector. By stepping through different electric field strengths, by using a sweepable high voltage

[1] Flown on the Polar mission.

[2] Fast Omni-directional Non-scanning Energy Mass Analyser

power supply, different energy/charge ratios can be sampled. This section covers the main categories of ESA: retarding potential analysers (RPAs), spectrographs, curved plate analysers (CPAs) and top hat analysers (as a special kind of CPA).

1.4.1 Retarding potential

Retarding potential analysers in their simplest forms are just a grid in front of a detector. A potential applied to the grid repels away particles below the corresponding energy/charge ratio, and lets pass those with a greater ratio. More sophisticated RPA instruments use modulated voltages on the grid to allow photoelectrons formed on the detector to be subtracted. Instruments like HARP (flown on the Phobos mission) are essentially gridless RPAs through the use of specially arranged hyperbolic electrodes [124].

While an RPA applies a parallel electric field to repulse the lower-energy charged-particles, the other electrostatic energy analysers in this section are dispersive field analysers. These dispersive field analysers apply an electric field that is perpendicular to the charged particles' trajectories to deflect particles onto detectors. This therefore allows much lower voltages than those required to fully repulse a particle and allows an energy bandpass filter rather than simply a high pass filter and thus facilitates more sophisticated measurements.

1.4.2 Spectrograph

Charged particles traversing a perpendicular electric field will experience a deflection proportional to their energy/charge ratio. A suitably placed position-sensitive detector (or multiple detectors) can therefore be used to deduce the energy/charge ratio of a particle by the location in which it is detected.

This approach was used in the FONEMA instrument. In this instrument there was additionally a magnetic field parallel to the electric field, shown in figure 1.9. At the detector the ions are thus displaced by mass/charge over one direction axis and by energy/charge in the perpendicular direction axis and arranged in curves (Thomson parabolas) according to their species.

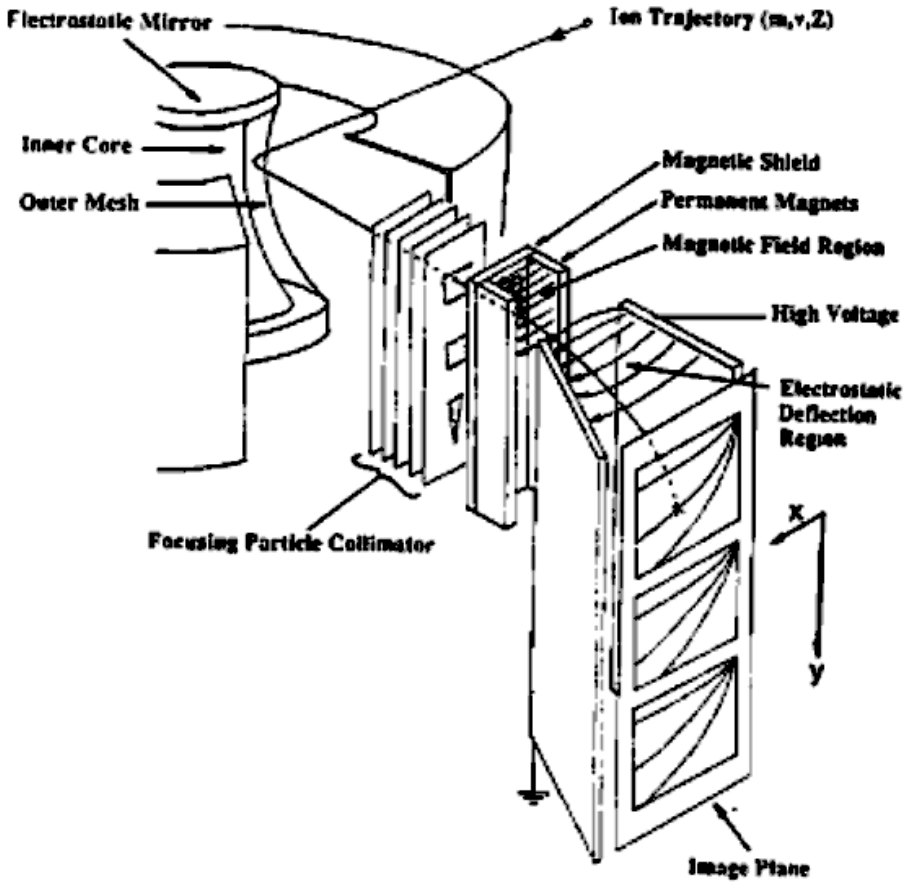

Figure 1.9: Exploded view of FONEMA Thomson parabola spectrograph [63]

1.4.3 Curved plate

Curved plate analysers use two closely spaced curved electrodes that provide a centripetal force such that only particles with a narrow range of velocities are deflected the right amount to pass through the narrow gap between them to a detector. While the spectrograph method above can measure different energy/charge ratio particles simultaneously, curved plate analysers are spectrometers which only instantaneously measure a narrow bandpass of energies. The bias on the plates is rapidly varied with time to sample the desired energy range. Despite this limitation they are very commonly used because they can make measurements with great accuracy and can be designed to resolve particles from multiple directions simultaneously thus 'imaging' the plasma. A myriad of different geometries of curved plates have been flown on space analysers, but the most regularly used are those shown in figure 1.10.

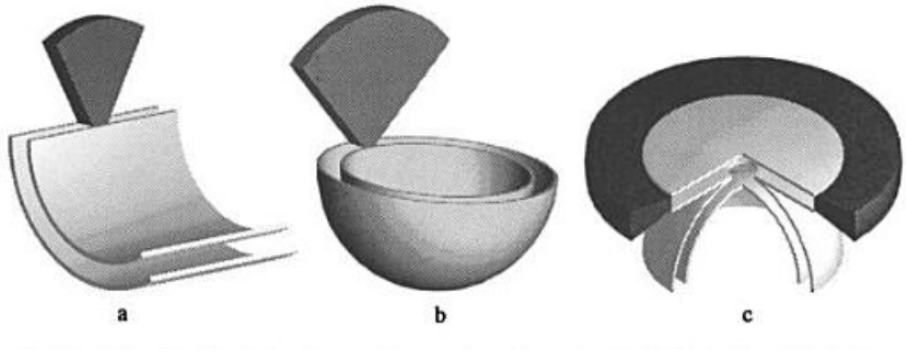

Figure 1.10: Common CPA geometries: a. Cylindrical, b. Spherical, c. Top Hat, with shading indicating fields of view [46].

Perhaps the simplest arrangement for CPAs is of sections of two concentric cylinders, as in figure 1.10a. This was used in early instruments such as the ion spectrometer on Mariner 2 [94].

Concentric spherical plates, shown in figure 1.10 b, are a progression of the curved plate design and allow a range of input angles to be sampled simultaneously. These have been used on instruments such as the Giotto three-dimensional positive ion analyser (with a 270° truncation angle) [67] and the IMP plasma probe [135].

Toroidal geometries, such as that used in the previously mentioned TIMAS instrument [113] (but not shown in figure 1.10) provide a logical progression from the spherical

plates and having two radii of curvature allow for another degree of freedom in the electrostatic optics design. The most widely used variant of a spherical geometry however, was the symmetric quadrisphere or 'top hat' geometry. This allows for a flattened 360° field of view which is shown in figure 1.10c and discussed in the following section.

1.4.4 Top hat analysers

Figure 1.11 shows a cross section through a top hat electrostatic analyser with elevation selecting deflector plates. The instrument is cylindrically symmetric about an axis that passes from top to bottom through the centre of the figure, creating two concentric hemispheres at the heart of the instrument.

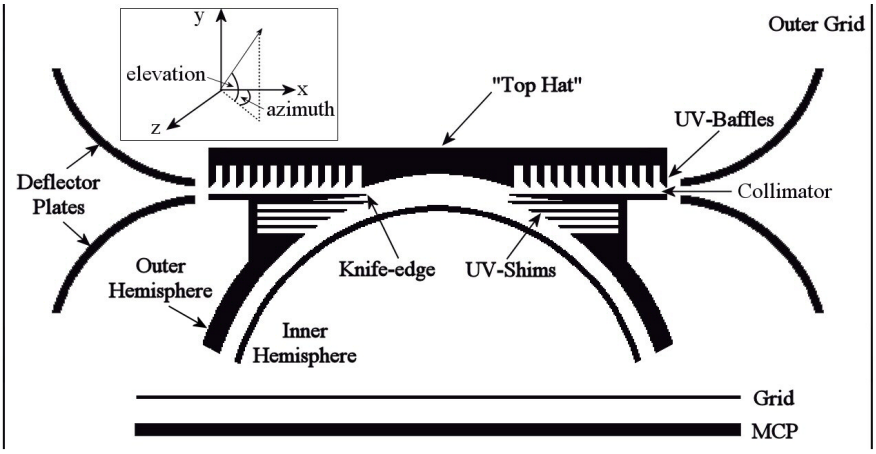

Figure 1.11: Top hat electrostatic analyser, with elevation selecting deflector plates [27].

Particles enter through the outer grid and are deflected by voltages on the deflector plates into the collimator section. Only particles within a narrow bandpass of elevations will be able to pass through the collimator into the top hat. The outer hemisphere and collimator are electrically grounded and a voltage is applied to the inner hemisphere, creating an electric field between them. This field is used to attract the desired particles into the gap between the hemispheres. By the nature of the forces experienced by the particles in this gap, only particles with a narrow band of energy/charge ratios will continue to pass along between the hemispheres without hitting the sides and being conducted away. These 'successful' particles that do not hit the sides can then be detected by a detector at the bottom, e.g. an MCP (microchannel plate) behind a grid. By changing the voltages applied to the deflector plates, different elevations

can be detected. By changing the voltage applied to the inner hemisphere, particles of different energy/charge ratios can be selected and detected. The hemispheres also provide a useful focusing property. All particles with the same azimuth are focussed onto the same part of the detector, regardless of which part of the aperture they entered.

The first satellite with a top hat instrument was AMPTE IRM [102]. The top hat design has become very commonly used for the most demanding scientific missions and is a design with which MSSL now has a particularly proud heritage.

1.5 Particle detectors

Detectors, as section 1.4 has mentioned, are the final destination of the particles selected by the analysers discussed in that section. Since these detectors are behind analyser heads, the energy/charge ratio of the particle is already known and in most implementations it is the detector's primary function to measure only the flux of particles. The most common forms of particle detector in space plasma analysers past and present are discussed in the subsections below, namely Faraday cups, channel electron multipliers, micro-channel plates and solid state detectors.

1.5.1 Faraday cup

A Faraday cup is simply a collector plate electrode that the charged particle falls onto and charges up [19]. Detection can be by a sensitive ammeter to ground or as the voltage across a resistor to ground. The concept is thus not entirely dissimilar to the Langmuir probe mentioned in section 1.3.2 and in the same way as is done with Langmuir probes, voltages can be applied to the cup to repel unwanted particles. Such detectors were used on early RPA instruments, like that described in [18], for the investigation of interplanetary plasma.

1.5.2 Channel electron multiplier

The introduction of channel electron multipliers (CEMs) in the 1960s brought single-particle counting to space plasma physics [38]. As figure 1.12 shows, CEMs are in essence, glass cylinders that have been coated with a semiconducting layer.

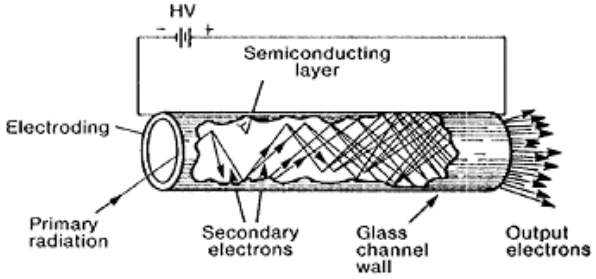

Figure 1.12: A straight CEM [79]

A high voltage (2 kV to 3 kV) is applied between the ends of the channel. When a plasma particle (or photon) is incident on the more negative end (e.g. the left side in figure 1.12), it enters the channel and hits a side-wall. If this side-wall collision is sufficiently energetic, secondary electrons are released. These secondary electrons are mostly ejected normal to the side-wall and are immediately accelerated by the electric field towards the opposite, more positive, end of the channel (e.g. the right side in figure 1.12). Consequently they hit another side-wall with enough energy to release more secondary electrons and so an avalanche process ensues.

For every electron or ion that enters a straight CEM, 10^3 to 10^5 electrons can exit the other end, gains $> 10^8$ are possible with curved CEMs [79]. A short distance from this other end is placed an anode, which is biassed even more positively than the end of the CEM. To this the exiting cloud of electrons is attracted. The electron cloud produces a charge pulse which is sensed and counted electronically.

The probabilities of different energies of different plasma particles and photons starting an electron avalanche (detection efficiencies) are outlined in table 1.1.

To improve the detection efficiency, lower energy impacting plasma particles can be pre-accelerated into the CEM with the application of a suitable potential to the front of the CEM. This front potential can also be used to repel away undesired low energy particles of one polarity.

Figure 1.13 shows a modern CEM as sold by Dr Sjuts Optotechnik GmbH. The associated electronics are not shown.

Table 1.1: Detection efficiencies of channel multipliers based on results from CEMs and MCPs [110].

Type of radiation	range	detection efficiency (%)
Electrons	0.2 - 2 keV	50-85
	2 - 50 keV	10-60
Positive ions	0.5 - 2 keV	5-85
(H+, He+, A+)	2 - 50 keV	60-85
	50 -200 keV	4-60
U.V. radiation	300 - 1100 Å	5-15
	1100-1500 Å	1-5
Soft X-rays	2 -0.5 Å	5-15
Diagnostic X-rays	0.12 - 0.2 Å	∼1

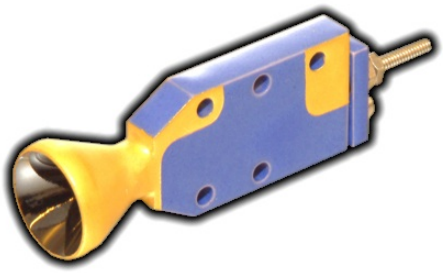

Figure 1.13: Dr Sjuts CEM type KBL10RS. It is a few cm long, the funnel on the left is in the sensing end, the protrusion on the right is the anode.
Source: http://www.sjuts.com

1.5.3 Microchannel plate

MCPs are essentially arrays of many tiny CEMs, as shown in figure 1.14.

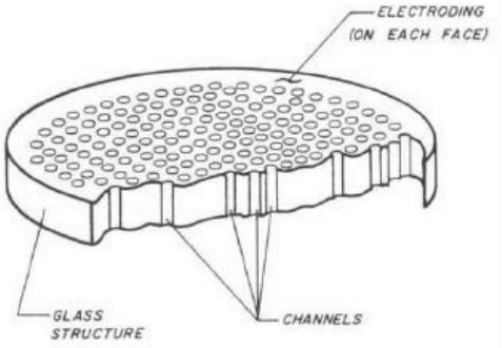

Figure 1.14: Microchannel plate (cutaway view) [79].

They can be made from glass fibres with lead glass claddings formed into arrays and then drawn and sliced at a slight angle. Consequently they are operated very much like CEMs. A high voltage is applied between the faces of the MCP and an anode underneath collects the electron clouds. The anode is most often segmented to allow the position of the charge cloud to be determined. Such details will be discussed later in chapter 5. Like for the CEM, the front surface is often biassed to pre-accelerate the desired particle and/or to repel unwanted particles. The detection efficiencies are similar to CEMs, as described in table 1.1.

MCPs are commonly used detectors for the most sophisticated instruments as their position sensitivity allows multiple particle properties to be measured simultaneously on the same detector, e.g. particle trajectories on 'imaging' spectrometers such as top hats and mass/charge and energy/charge on FONEMA.

Operating MCPs in pairs with their channels angled in opposing directions is referred to as a 'chevron pair' arrangement and is shown in figure 1.15.

This improves the total gain and reduces the likelihood of ion feedback. Ion feedback is the effect whereby stray ions above the anode (produced by ionisation of gas by the exiting electron cloud) are accelerated up the MCP pore, where they can cause an unwanted electron avalanche. With the chevron pair arrangement the rogue ions typically impact the channel walls within a shorter distance, before they have gained

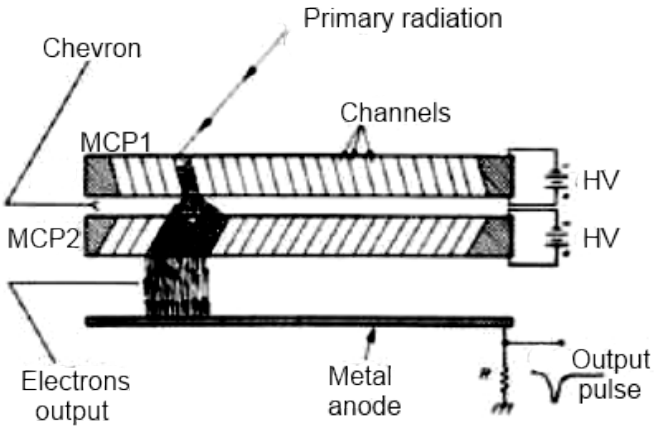

Figure 1.15: Side view of MCPs in chevron pair configuration [79].

sufficient kinetic energy to initiate a large secondary electron shower [76].

1.5.4 Solid state detectors

Solid state detectors (SSDs) have been introduced already in section 1.3.2 as they can also be used as instruments by themselves, without an energy filtering head. Although they cannot usually detect the lowest energies of particles that the CEMs and MCPs are sensitive to, they are sometimes used behind analyser heads; in SWICS[3] for example, the particle energy measurement is made with increased accuracy by combining the ESA and SSD data [50]. AMPS is another ESA and SSD combination and will be discussed later in section 1.7.2.

Unlike CEMs and MCPs, SSDs are not inherently high voltage devices so if a pre-accelerating voltage is to be applied, it is done with external grids and electrodes. Combined with the fact that SSDs are typically only sensitive to particle energies of tens of keV upwards, this means they are more frequently used for higher energies of particles only. The RAPID[4] experiment on Cluster, for example, uses SSDs to study electrons from 20 keV to 400 keV and even higher energies of ion [131]. Special treatment procedures however allow silicon-based detectors to be made sensitive to much lower energies of particle: ion-implanting enabling sensitivity to particles with hundreds of eV [121] and delta-doping making detectable particles with energies with low tens of

[3]Solar Wind Ion Composition Spectrometer

[4]Research with Adaptive Particle Imaging Detectors

eV [96].

While CCDs (charge-coupled devices) are more conventionally used to detect photons, they are very similar to SSDs and their electron detecting capabilities have been well documented [30, 120]. They will play a significant role later in this project as a novel electron detector for a miniaturised low-energy (0.5 keV to 8 keV) electron analyser, their first known application to such an instrument. Since they are not a conventional detector for electrostatic analysers, their full introduction shall be postponed until chapter 5.

1.6 Plasma energy spectrometer instrument parameters

The performance of electrostatic analyser instruments can be assessed by various parameters and accordingly these terms will arise throughout this thesis.

1.6.1 Energy parameters

For simplicity this section will assume electrons or protons, otherwise for 'energy' read 'energy/charge ratio'.

Energy Resolution: quantifies how accurately the instrument is able to correctly resolve the energy of a particle and is defined as the full width at half maximum of the successfully transmitted particle energy distribution (assuming it is approximately Gaussian) divided by the peak energy of the transmitted particles. It is thus a percentage of the peak energy and it is in the nature of electrostatic analysers that this number is a constant for a given analyser, regardless of the voltage applied to it (and thus the field strength within the instrument).

Energy Acceptance: describes the range of energies that can be transmitted to the detector.

K-factor (or plate factor): describes the ratio of the peak energy of the particles selected by the analyser, to the voltage applied across its electrodes (equation 1.1).

$$K = \frac{E_{selected}}{V_{applied}} \tag{1.1}$$

1.6.2 Angular parameters

Angular Resolutions: elevation (polar) resolution and azimuthal resolution, the full width at half maximum of the successfully transmitted particles' elevation and azimuthal distributions respectively (again, assuming they are approximately Gaussian).

Angular Acceptances: describe the total elevation and azimuthal ranges of energies that can be transmitted to the detector.

1.6.3 Other parameters

Geometric factor: The geometric factor is required to be able to make accurate quantitative measurements with the instrument as it defines the relationship between count rate and phase space density. It is the ratio of the number of particles that enter the aperture of the instrument, to the number that are transmitted to the detector, as a function of the particles' entry position and velocity and is calculated by equation 1.2 [28].

$$G = \left(\frac{N_{detected}}{N_{in}}\right) A\Omega \left(\frac{\Delta E}{E_{peak}}\right) \tag{1.2}$$

Here G is the Geometric factor, $N_{detected}$ is the number of particles detected at the detector, N_{in} is the number of particles that enter the aperture, A is the area of the aperture, Ω is the solid angle of the range of trajectories of the entering particles, ΔE is the energy range of the entering particles and E_{peak} is the peak energy of the particles selected for the voltage that the analyser is set to ($\frac{\Delta E}{E_{peak}}$ being the energy resolution as described previously). For an accurate geometric factor measurement it is necessary that the particles entering are uniformly distributed in angle, position and energy and that the instrument angular, energy and position acceptance ranges are covered or exceeded. Geometric factors are usually quoted in units of cm^2 sr eV/eV.

While in its strictest sense it is dependent only on the geometry of the charged particle optics, the detector efficiency is sometimes included within it, for the convenience of having one number to describe the sensitivity of the entire instrument.

Duty cycle: refers to the length of time required to get a full set of measurements. This is usually achieved by cycling (sweeping) through different voltages on analyser electrodes to sample different energy ranges.

Instruments with deflector plate electrodes would also cycle through voltages on these extra electrodes to sample different angular directions.

This parameter is essentially limited by the electronics and sometimes by spacecraft spin rates.

1.7 Miniaturised plasma spectrometers

From the first space missions through to the early 1990s, the improving performance of one generation of plasma instrumentation to the next would typically be accompanied by an equivalent increase in instrument mass and power consumption. This was driven by a 'design to performance' philosophy and consequently lead to an increase in mission costs and a reduction in flight opportunities. Combined with decreasing budgets this brought about a new mission philosophy 'faster, cheaper, better', where instrument designers were required to make increasingly capable instruments but with reduced resources [135].

Although it was not an entirely successful paradigm [87], access to space did improve and an appetite for ever smaller satellites came about that continues today. While initially the emphasis was on miniaturising electronics and satellite subsystems, as sizes continued to reduce, so then the instrument scientists began to reduce the size of their instruments. This has resulted in many successful small instruments for microsatellites, smallsats and regular spacecraft alike. Three kinds of miniaturised CPA instruments are discussed below as examples in the following sections. Back-to-back top hats, nested spherical analysers, and a cylindrical CPA with a TOF cell.

1.7.1 MEDUSA - Miniaturized Electrostatic DUal tophat Spherical Analyser

MEDUSA (figure 1.16) is a miniaturised dual top-hat instrument design that has flown on the Astrid-2 and Munin microsatellites in 1998 and 2000 respectively.

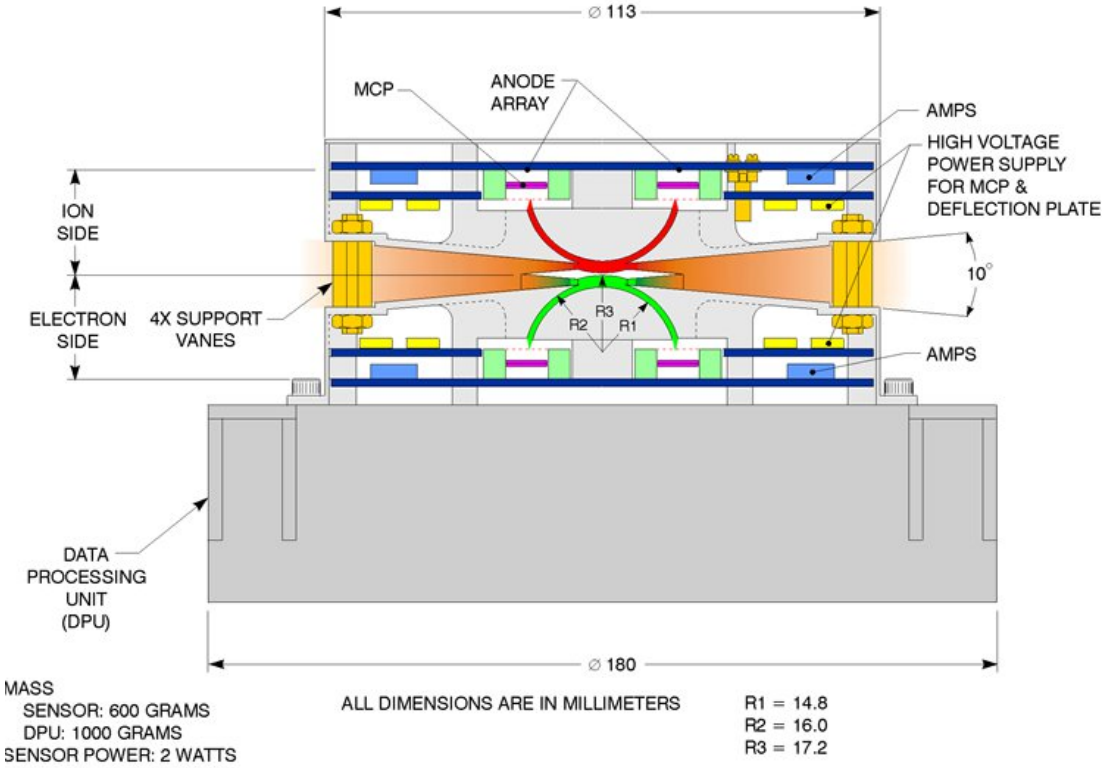

Figure 1.16: MEDUSA on Astrid-2 and Munin microsatellites [73]

Miniaturisation is achieved by scaling down the size of the top hat ESAs to ∼3 cm across and by combining what would otherwise be two separate instruments into one, with a shared aperture. The same design of ultra compact top hat has been used on the ASPERA-3 instrument on Mars express [6] and the ASPERA-4 instrument on Venus express [7], although in both cases just a single analyser, for electrons only, was used.

The back-to-back, two-in-one, design has also been used on instruments such as the Ion and Electron Sensor (IES) on the Rosetta mission. This instrument, shown in figure 1.17, fits into an even smaller package.

It uses toroidal top hats without a separating top-cap and has added angular deflection electrodes at the input aperture so that a wider field of view can be scanned.

1.7.2 AMPS - Advanced Miniature Plasma Spectrometer

This is another instrument for simultaneously measuring both ions and electrons, but with only one high voltage electrode, and the possibility of using only one detector. As

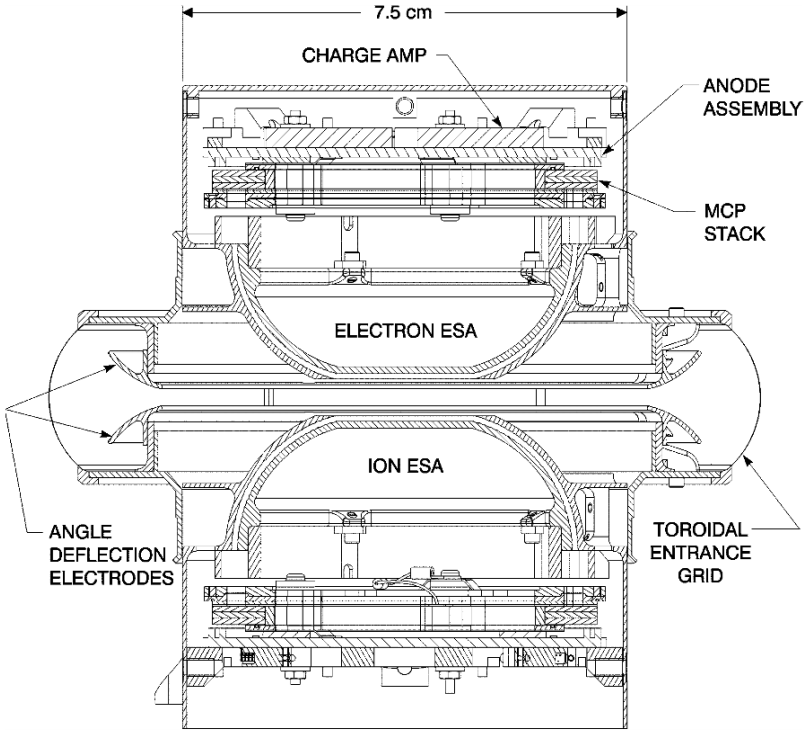

Figure 1.17: The Ion-Electron Spectrometer on Rosetta [21]

can been seen in figure 1.18, this is achieved with a nested spherical geometry.

When different voltages are applied to the central electrode, different energies of electron are transmitted through the outer channel and different energies of ion are transmitted through the inner channel. The analyser hemispheres are made from electroplated nickel which allows them to be 95±5 µm in wall thickness. The outer shell radius is 4.5 cm.

Figure 1.19 shows a novel MCP detector developed for this instrument.

Through the selective deposition of electroding material on the MCP surfaces, different voltages can be applied simultaneously to different parts of the MCP to allow the concurrent detection of electrons and positive ions through the two separate channels. This potentially allows for additional resource savings by using only one set of readout electronics with a position sensitive anode.

It happened however, that the flight version of the AMPS (a space weather monitor on a nuclear event detecting payload) used a different detector configuration: 5 CEMs

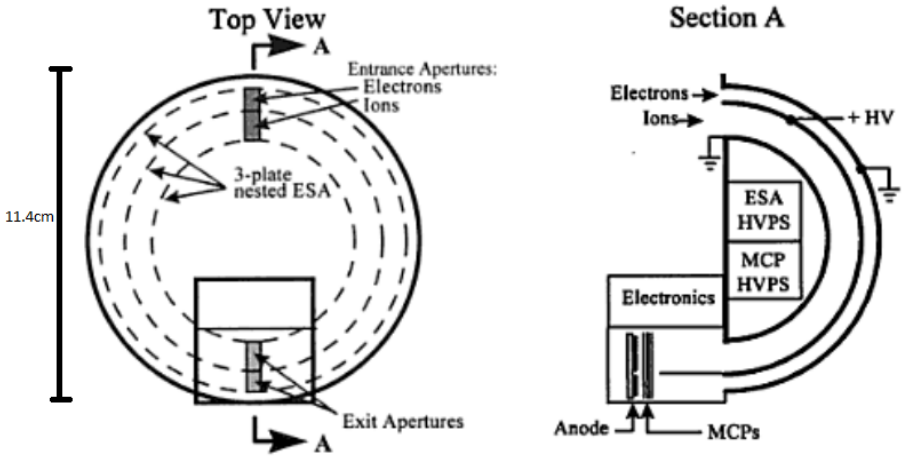

Figure 1.18: AMPS schematic (MCP detector configuration) [46].

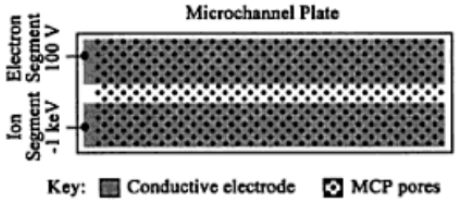

Figure 1.19: Custom MCP detectors for AMPS [46].

and an SSD (figure 1.20).

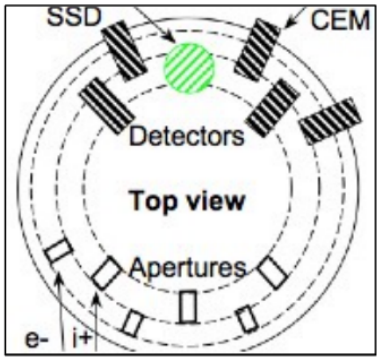

Figure 1.20: Detector configuration used on the flight model AMPS instrument [47].

Although there was no mass analysis component, the combination of ESA filtering and careful analysis of the SSD measurements, allowed for the differentiation of some critical ion species [55].

1.7.3 MIPA - Miniature Ion Precipitation Analyser

This instrument, for the BepiColumbo mission to Mercury and the Chandrayaan 1 lunar mission (where it is known as SWIM - Solar Wind Monitor), is unlike the instruments discussed above as it detects only ions, not electrons, and it has a mass discriminating TOF section [91]. As can be seen in figure 1.21, it uses a cylindrical geometry ESA with a truncation of 127°.

This is a commonly used truncation angle for its inherent focussing properties (discussed in [61]). The electronics are not shown in the figure but consist of two 12x6 cm PCBs.

1.7.4 Discussion

While the instruments discussed above were selected to be a range of different approaches to miniaturised CPAs and are not directly comparable in the roles they perform, it is nevertheless interesting to see their numbers together in table 1.2, which will be a point of reference for future discussions.

These examples have shown some approaches to miniaturisation that have inspired, or that will be seen to resonate with my work. These include:

Table 1.2: Comparing parameters of miniaturised instruments

Sensor	MEDUSA (e-)	MEDUSA (i+)	IES (both)	AMPS (e-)	AMPS (i+)	MIPA (i+)
Geometry	Dual spherical top-hat		Dual toroidal top-hat	Nested spherical		Cylin + TOF
Year first launched	1998		2004	2004 (planned)		2008
Power	2.9 W		1.85 W	1 W		1.5 W
Energy range	4 eV to 22 keV	2 eV to 12 keV	1 eV to 22 keV	2 eV to 40 keV	1 eV to 30 keV	10 eV to 15 keV
Energy resolution ($\frac{\Delta E}{E}$)	15%	25%	4%	25%	20%	7%
Field of view	$10^\circ \times 360^\circ$		$90^\circ \times 360^\circ$ (2.8π sr)	nearly 2π sr		$9^\circ \times 180^\circ$
Total geometric factor ($cm^2 sr \frac{eV}{eV}$)	1.9×10^{-4}	4.2×10^{-4}	$(2\times)\ 5 \times 10^{-4}$	3×10^{-4}	4×10^{-4}	1.8×10^{-3}
Mass	1.5 kg		1.04 kg	1 kg		0.45 kg

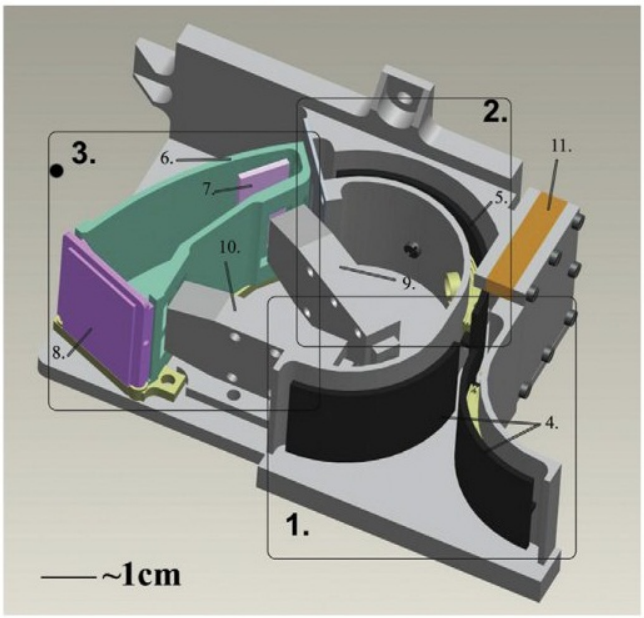

Figure 1.21: MIPA - Miniature Ion Precipitation Analyser. 1. Angle selecting section, 2. Energy selecting section, 3. Mass determining section, 4. HV deflection plates, 5. HV CPA plates, 6. TOF cell, 7. 'start' conversion plate, 8. 'stop' plate, 9,10. 'start' and 'stop' ceramic CEMs, 11. UV attenuating baffles block [91].

- Combining functions, e.g. electron and ion detection.
- Nesting electrodes to provide multiple channels.
- Consideration of novel detectors for electrons and ions.
- Use of simpler CPA geometries used on earlier instruments.
- The option of adding deflector plates to extend angular range.[5]

1.8 Summary

From a starting point of introducing plasma as a common yet interesting phenomenon in the solar system, methods for studying it have been discussed, focusing on the space-farer's privilege of in-situ measurements. After covering briefly the possibility of studying the electric and magnetic fields in the plasma, particular attention was paid

[5]Although this is not an aspect that has been studied in any detail

to particle instrumentation and more specifically to electrostatic analysers, in which MSSL has a rich and successful history.

The analyser geometries, particle detectors and instrument parameters that will be discussed throughout this thesis have now all been met and it has been seen how they have been implemented in some of the miniaturised instruments of the past. The energy and flux ranges of significance to the terrestrial magnetosphere have been highlighted and some approaches to miniaturisation have been identified.

From here, the focus is on even greater miniaturisation.

Chapter 2

Highly Miniaturised Analysers

In chapter 1 we have seen that there has been a trend towards increasingly miniaturised plasma analysers and evidence for this continued trend will be seen in this chapter.

Here is discussed the further miniaturisation that is within reach through MEMS (Micro Electro Mechanical Systems) techniques and the motivations for highly miniaturised analysers. It will look at some of the steps that have already been taken in this direction in this field which will be seen to inspire my contribution, CATS - the Cylindrical And Tiny Spectrometer, in the next chapter.

2.1 MEMS - a path to unprecedented miniaturisation

In December 1959 Richard Feynman gave a landmark lecture titled "There's plenty of room at the bottom" to the American Physical Institute. In this talk he discussed and popularised the intellectual underpinnings of the fields that would later become MEMS and nanotechnology. His message was that there are no physical laws preventing us from making things really, really small. At the end of the talk he set two challenges with cash prizes. The first, to build a working electric motor no larger than a 400 µm cube. The second, to print text at scale such that the entire Encyclopaedia Britannica could fit on head of a pin. The first challenge was accomplished in less that a year by William McLellan, who made a 250 µm, 2000 rpm motor. The second was achieved in 1985 when T Newman and RFW Pease successfully printed the first page of "A Tale of Two Cities" in a 5.9 µm square using electron beam lithography [41]. The field of

MEMS is a rapidly developing one and covers many areas and products. Accelerometers for airbags were an early MEMS device and these have since been advanced to produce the sorts of accelerometers now found in smartphones and Nintendo Wiis for motion controlled video games. Microfluidic devices are paving the way for portable and automated devices for medicine applications, and microoptics devices are found in modern DLP projectors and advanced new astronomical instrumentation [93]. Just as the microelectronics revolution saw rapid miniaturisation and mass production of electronics starting in the 1970s, the MEMS revolution is now well under way and is shrinking just about everything else [23].

Two of the striking attractions of MEMS are their massively reduced resource footprints (lower mass, power requirements, smaller size) and their suitability for mass and batch production. Figure 2.1 shows some of the motivations for plasma analysers with lower resource requirements and for plasma analysers that can be produced easily in large numbers, and highlights some of the applications applicable to both lists.

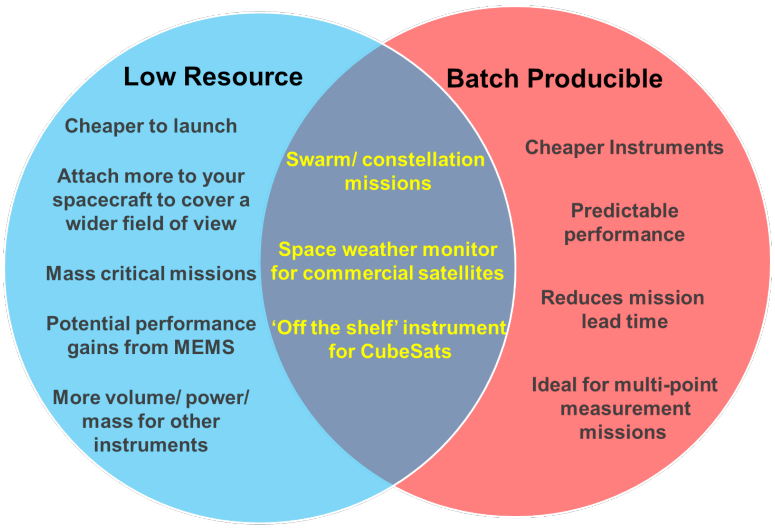

Figure 2.1: Motivations for a low resource plasma analysers (blue), motivations for a batch producible design (red), and applications which draw on both of these (purple).

These applications are discussed in the following subsections, followed by a discussion of production and performance considerations of miniaturised instruments.

2.1.1 An off-the-shelf CubeSat instrument

CubeSats are semi-standardised platforms to enable low-cost access to space primarily for education and technology demonstration purposes [58].

A large, and growing, number of off-the-shelf components exist for them already from companies such as Clyde Space[1]. With the advantages shown in figure 2.1, small, batch produced plasma analysers could be added to this inventory. Since plasma instrumentation is most useful in suites, such an analyser could be packaged with a magnetometer and high energy particle sensor using shared electronics as an off-the-shelf 'space-weather package'. Such a concept has been discussed at [72].

2.1.2 Instruments for commercial/government satellites

Small batch-produced plasma sensors might also find applications in more conventional aerospace markets. Instruments could be designed to:

- Trigger the satellite into a low-power safe mode to protect it during harsh geomagnetic storms.
- Allow nuclear events to be differentiated from background space weather [55].
- Detect ion thrusts of nearby spacecraft [123].
- Function as a ram direction sensor when in solar eclipse by using the spacecraft velocity to detect stationary ions [26].

2.1.3 Swarm / constellation missions

Section 1.3 has mentioned already the ambiguity of in-situ measurements from single sensors alone and the consequent desire for multi-point measurements. This desire has existed for some time. The renowned space scientist Jim Dungey said of space plasma physics in 1966 "Looking to the future I believe that progress requires bunches of satellites, though these are as yet in no published programme. One is continually

[1] http://www.clyde-space.com

conscious of this need for reasons which have a direct analogue on the ground... Since satellites are being launched singly, the scientific returns are less than they could be" [3].

Although there have since been constellations of 5-6 such satellites with the THEMIS [4] and Cluster/Double Star missions [37, 86], larger numbers are still desired by space plasma scientists. Cross-scale, a constellation of 12 satellites, was proposed and studied for an ESA Cosmic Vision medium sized mission [111], but was ultimately rejected.

The NASA Magnetospheric Constellation mission proposal was even larger, having three dispenser ships each deploying 30 spacecraft equipped with a full suite of instrumentation [40]. This mission has also been indefinitely shelved however. The instruments proposed for it were very similar to those discussed in section 1.7. Had it used MEMS-based instrumentation it could be made much smaller.

QB50 is a much lower-budget multi-satellite mission and is scheduled to launch in the first half of 2015 [116]. It will make multipoint measurements in the lower thermosphere (90-320 km), with a swarm of 50 CubeSats. These altitudes are not a well studied region since orbital lifetimes there are short, causing regular satellites to not be cost effective. CubeSats containing highly miniaturised instruments are sufficiently cheap to make the venture justifiable.

2.1.4 Miniaturisation considerations

As plasma analyser designs have shrunk, so the engineering required has become more challenging. Manufacturing and alignment tolerances become increasingly strict and assembly is complicated as screws and fittings become large compared to the size of the pieces, and ever finer grids become ever more fragile. With MEMS however, the crystal structures of the materials from which the components are made can become the guidelines along which a piece is shaped, allowing for extreme accuracy in manufacturing. Additionally, reduced numbers of separate parts in batch fabrication and assembly allows higher reliability compared to macro-scale integration [65]. Furthermore, the small gaps between these miniaturised electrodes require correspondingly smaller voltages since the K-factors are higher and so the power supplies required are simpler and less resource-hungry.

A negative consequence of miniaturisation however, is the loss of geometric factor that

occurs as the device shrinks. Funsten and McComas describe in [46] how the geometric factor of a spherical geometry analyser is shown to decrease in proportion to the square of the mean radius of curvature of the two spherical plates.

High geometric factors can still be accomplished however by:

1. More efficient design of the charged particle optics,
2. Relaxed measurement resolution requirements,
3. Multiple instances of miniaturised instruments.

An example of increased design efficiency would be the arrival of the top hat instrument, whose cylindrical aperture removed the cosine term in the polar angular response that is otherwise present for flat aperture CPAs. This enhances the geometric factor without reducing the measurement capabilities. If the science requirements of the instrument allow for it however, then the geometric factor can be increased at the expense of measurement resolutions by, for example, increasing the gap between the electrode plates.

The third option, multiple instances of miniaturised instruments, can allow for preservation of a larger instrument's geometric factor and measurement performance and yet still make large savings in spacecraft resources as is illustrated conceptually in figure 2.2.

Large numbers of small instruments add further benefits, they add redundancy and can be placed around the spacecraft pointing in different directions to give a very wide field of view, compared to a large single sensor. Taking this approach to an extreme, an instrument could be built into the entire skin of the spacecraft itself.

2.2 Microfabrication

Microfabricated and MEMS devices are made from a variety of materials using a variety of processes that have largely been developed from those used in the semiconductor electronics industry. The most common methods – LIGA, bulk micromachining and surface micromachining – as well as the more conventional method of electron discharge machining (EDM) are introduced in the following subsections.

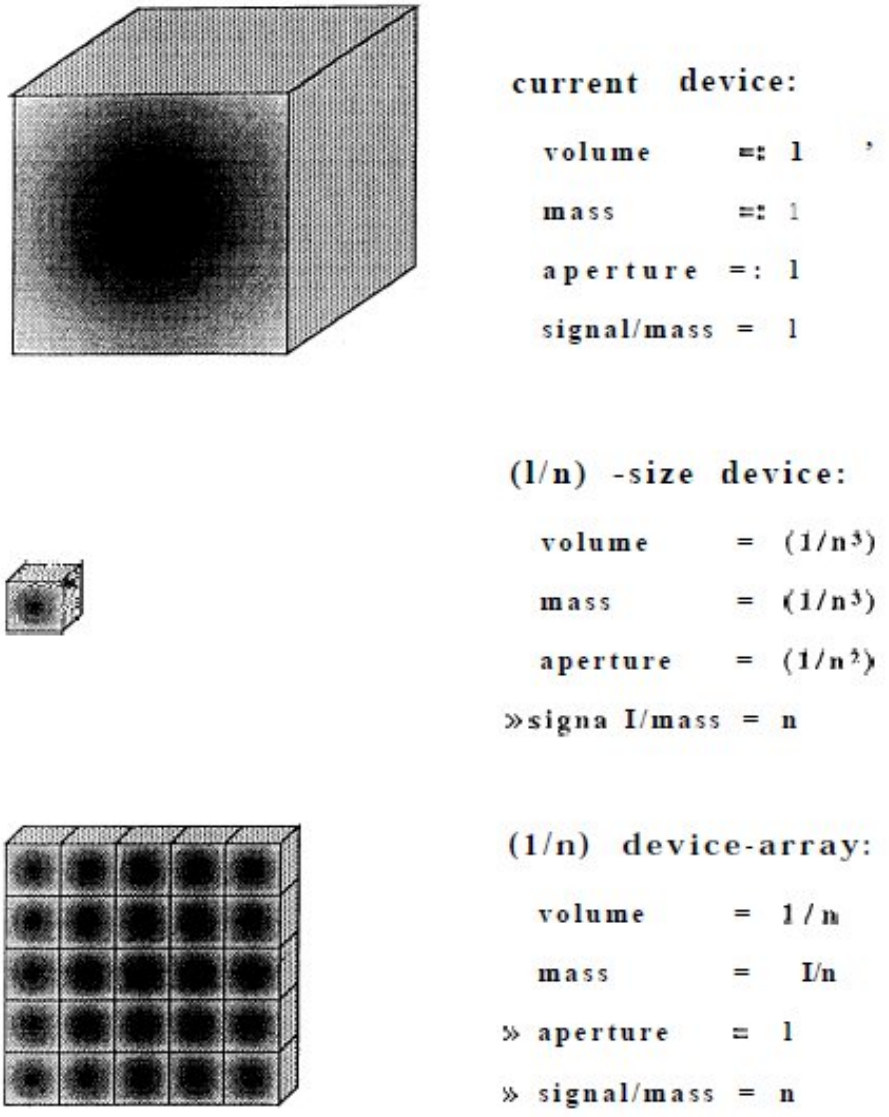

Figure 2.2: Reducing mass and volume while maintaining sensitivity and resolution, by shrinking and replicating a design [119].

2.2.1 Conventional machining

Conventional machining methods, like cutting, milling and turning on a lathe can produce complex 3D shapes in a wide variety of materials down to a feature size of 10 µm to 25 µm and are used for making larger packaging components for MEMS devices.

EDM or spark erosion as it is also known, is perhaps at the borderline of conventional and MEMS methods. It can be used to create small complicated designs in hard materials, with tight tolerances, sometimes close to 1 µm. It uses two electrodes: the piece to be shaped and a 'tool' piece. The electrodes are closely spaced with a dielectric liquid between them. A voltage is applied between the electrodes and the distance between them is reduced so the electric field increases to the point where the (liquid) dielectric breaks down. As current flows, small amounts of material are eroded from the electrodes and carried away by the liquid.

2.2.2 LIGA

LIGA (Lithographie Galvanoformung Abformung) allows for on-demand manufacturing of high aspect ratio structures with lateral precision below 1 µm and thicknesses of several hundred microns. A mould is made in PMMA using x-ray lithography. The mould is then filled with electroplated metal to create a microfabricated metal object. This metal object can be the finished component or it can be a mould itself for mass producing plastic MEMS components [101]. Figure 2.3 shows a cartoon of the LIGA process.

2.2.3 Bulk micromachining

Bulk micromachining is able to make use of the entire thickness of a silicon wafer and thus, like LIGA, is also able to make high aspect ratio components. The bulk micromachined components can then be combined using wafer bonding methods to create more complex structures. Wet etching methods can be used to make both isotropic and anisotropic etches. Isotropic etches create spherical and curved cuts in the silicon; anisotropic etches occur when etchants erode differently orientated planes of the crystal lattice at different rates and can be used to create very accurately angled

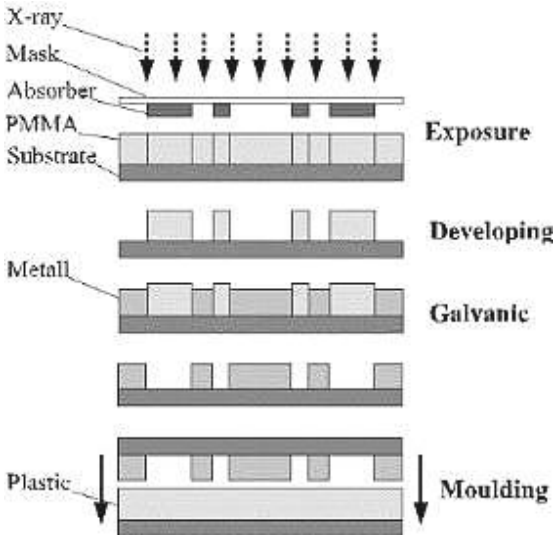

Figure 2.3: LIGA fabrication process [101]

cuts in the silicon (e.g. v-grooves). Dry (plasma) etching, such as deep reactive ion etching (DRIE) can create straight walled cuts with great depths compared to their widths (high aspect ratios) [23]. The profiles of these different kinds of etches are shown in figure 2.4

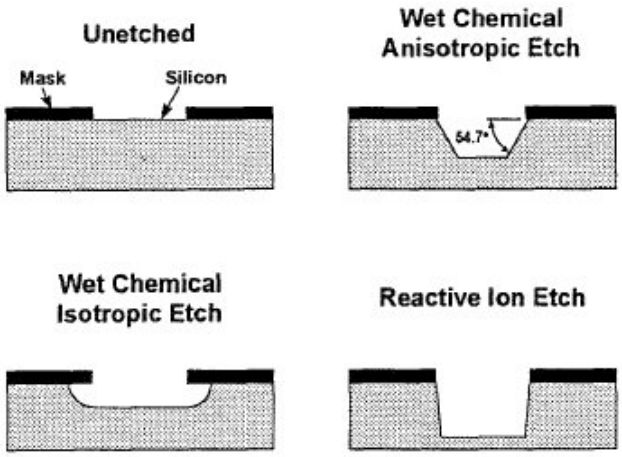

Figure 2.4: Etch profiles in <100> oriented silicon substrate [65]

2.2.4 Surface micromachining

Surface micromachining involves the deposition of structural and sacrificial layers upon a substrate. By carefully patterning and etching layers and depositing new ones, the sacrificial layers can be cut away to produce very complex and elaborate shapes and mechanical systems, see figure 2.5.

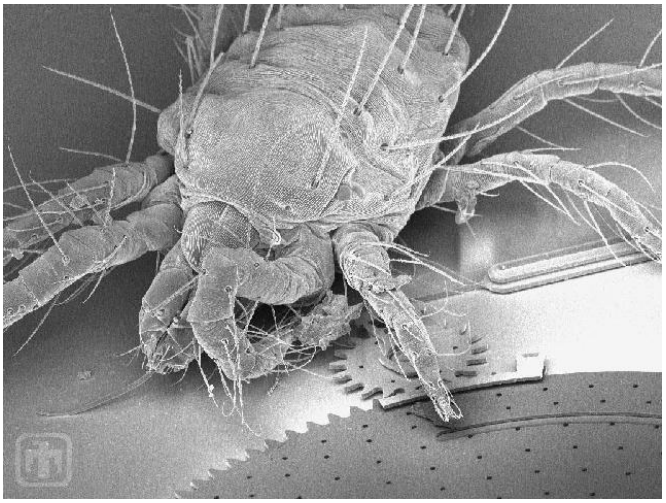

Figure 2.5: An early micromotor built in the SUMMiT surface micromachining technology. For size comparison a microscopic dust mite is shown on top. Source: http://www.memx.com/images/spider-mite.jpg

2.2.5 Comparison

The capabilities of the MEMS methods discussed in the previous sub-sections are summarised in table 2.1.

With the currently available MEMS processes, the more complex, elegant focussing CPA geometries like toroids and the top hat are very difficult, if not impossible, to reproduce, and simpler ones like planar and cylindrical plates must be used instead. Sophisticated geometries however, are of less importance when the brute force of large numbers of micro-sized analysers are used, as discussed in section 2.1.4. In this scenario each analyser element can be configured to cover different angular regions, energies and particle species.

Surface micromachining offers limited aspect ratio compared to other methods so it

Table 2.1: Comparing MEMS fabrication methods (not including EDM) [101]

Capability	LIGA	Bulk Micromachining	Surface Micromachining	Conventional Machining
Feature size	$\sim 3\,\mu m$ to $5\,\mu m$	$\sim 3\,\mu m$ to $5\,\mu m$	$1\,\mu m$	$\sim 10\,\mu m$ to $25\,\mu m$
Device thickness	> 1 mm	> 1 mm	$13\,\mu m$	Very large
Lateral dimension	> 2 mm	> 2 mm	2 mm	> 10 m
Relative tolerance	$\sim 10^{-2}$	$\sim 10^{-2}$	$\sim 10^{-1}$	$> 10^{-3}$
Materials	Electroplated metals or injection moulded plastics	Very limited material suite	Very limited material suite	Extremely large material suite
Assembly requirements	Assembly required	Assembly required	Assembled as fabricated	Assembly required
Scalability	Limited	Limited	Yes	Yes
MicroElectronic integratability	No	Yes for SOI bulk processes	Yes	No
Device Geometry	Two-dimensional, High aspect ratio	Two-dimensional, High aspect ratio	Multi-layer, Two-dimensional	Very Flexible, Three-dimensional
Processing	Parallel processing at the wafer level	Parallel processing at the wafer level	Parallel processing at the wafer level	Serial processing

is unlikely to be usable alone since electrostatic optics generally require similar length scales in three dimensions. LIGA and bulk micromachining offer possibilities for high aspect ratio structures and although these require more assembly than surface micromachined devices, they can still be produced in batches at a wafer level.

A typical approach taken by the pioneers in MEMS-based charged particle optics are a combination of bulk micromachined and conventionally machined parts and some examples are discussed in the next section.

2.3 MEMS plasma spectrometers

MEMS have already been used for charged particle optics and for some space plasma analysers. In the following subsections are described:

- The first openly discussed MEMS plasma analyser for space; an array of micromachined Bessel boxes.
- A ground-based microfabricated mass spectrometer with a cylindrical electrostatic analyser.
- MEMS based plasma analysers used primarily on the US Air force FalconSat programme.

2.3.1 Micromachined Bessel boxes

One of the first microfabricated space plasma analysers was a prototype developed at NASA JPL in the 1990s [119]. It uses a Bessel box design; a cylinder with apertures at either end and a central beam stop. Electric fields are applied within the cylinder to deflect particles of certain energies around the beamstop and out of the aperture onto a detector [1].

In the micromachined instrument a simplified form of Bessel box is replicated four times in an array. It is made by isotropic wet etching of <110> silicon wafers, assembled together as shown in figure 2.6. Of the wafer layers, five are 0.2 mm thick and two are 0.8 mm thick. The outermost layers are grids with 0.1 mm holes at 0.8 mm spacings, bulk etched with potassium hydroxide (KOH) using thermally grown silicon dioxide

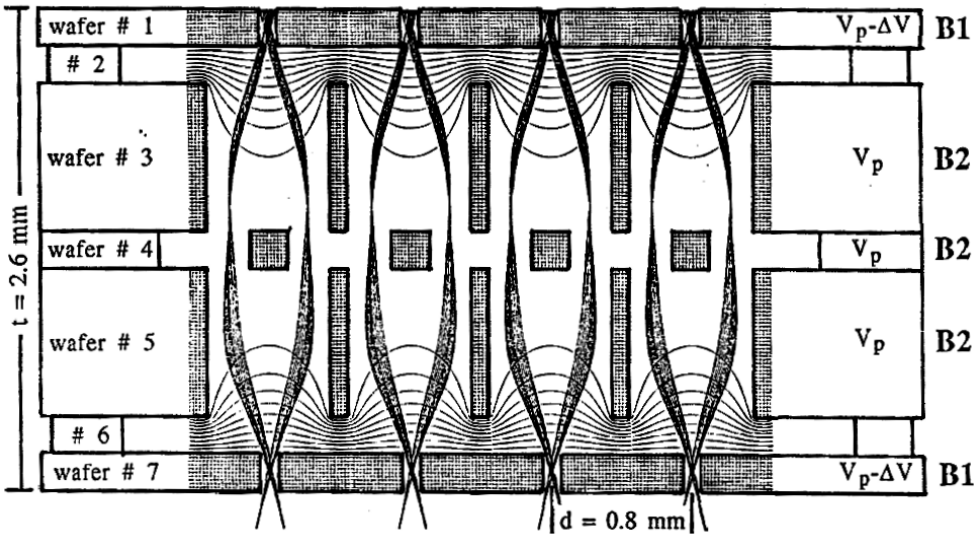

Figure 2.6: An array of micromachined Bessel boxes made with 7 wafers [119].

(SiO_2) as an etching mask. The electrode areas have thin layers of titanium, platinum and gold deposited on the SiO_2 by electron beam evaporation, to provide a homogeneous surface function.

Figure 2.7 shows a simulated ray tracing of the energy dependant nature of the particle trajectories that allows the design to function. The central beam stop prevents high energy particles from passing straight through and only very specific energies can be deflected around it and out the exit aperture. This gives the instrument a very accurate energy resolution of about 1%.

Although there appear to be no reports of a flight version of this design, it does seem to have been the intellectual predecessor to the series of instruments flown on FalconSats that will be discussed in section 2.3.3.

2.3.2 Micro mass spectrometer

Ground-based mass spectrometry is a big industry and microfabricated devices offer several advantages. As well as portability these advantages include:

- Low vacuum requirements – because of shortened mass separator length.
- Small sample and carrier gas consumption – since the internal chambers are small.

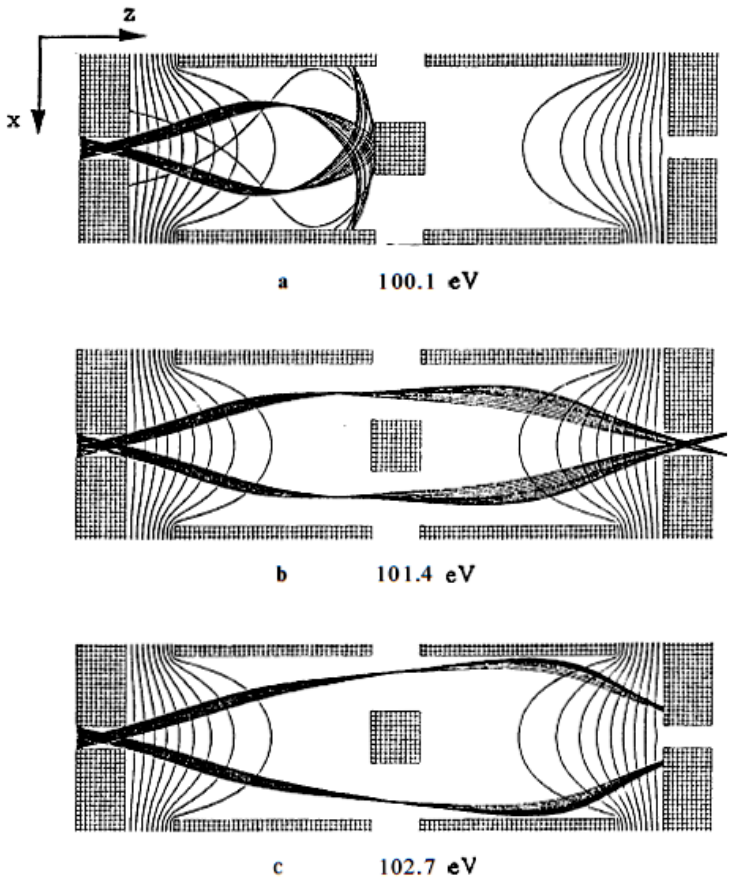

Figure 2.7: Simulation of micromachined Bessel box with different energy particles at constant electrode voltages, demonstrating the origin of the 1% energy resolution [119].

- Low voltage and thus low power consumption – since the gaps between electrodes are small. This therefore allows the use of standard integrated circuits.

Several such instruments use the quadrupole design [43, 48] (outlined in section 1.3.2) but the Micro Mass Spectrometer (MMS) discussed here is of particular relevance to this project as it uses a CPA. Figure 2.8 shows a schematic overview of the instrument. Ionised samples from the ionisation chamber first pass through a gated time of flight

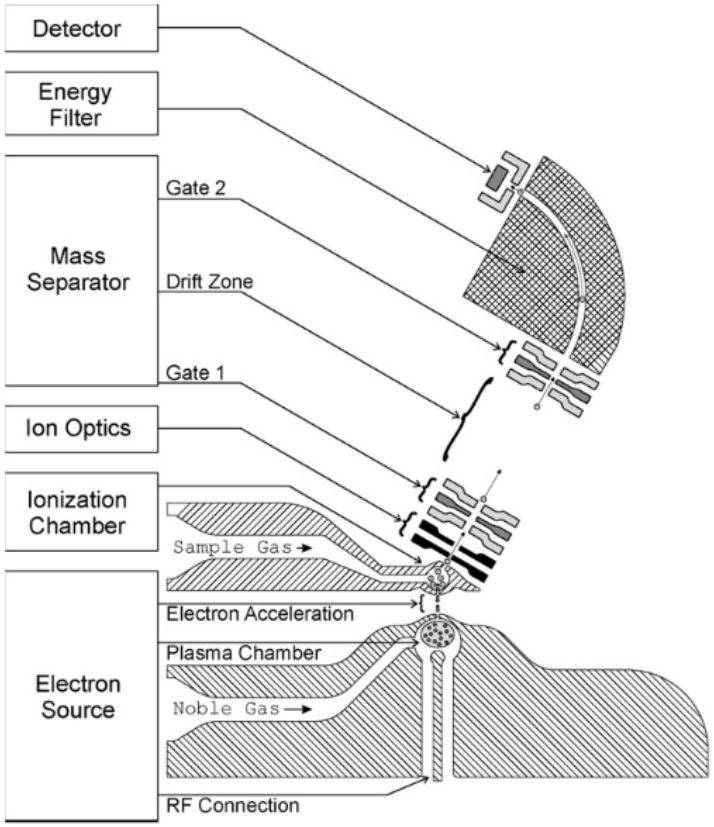

Figure 2.8: Schematic overview of the micro mass spectrometer (MMS) [127].

mass-separating section, then through a 90° cylindrical CPA energy-determining section with a K-factor of 7.5. The gate chops the beam so one ion can be sampled at a time. The detector used in this version of the device is a Faraday cup (see section 1.5.1) but in a later version an MCP has been used [106].

The structures for the ion optics are made using DRIE which allows for a good aspect ratio, as can be seen in the scanning electron microscope (SEM) image in figure 2.9. All the components are integrated on one chip and all of the critical parts are formed using

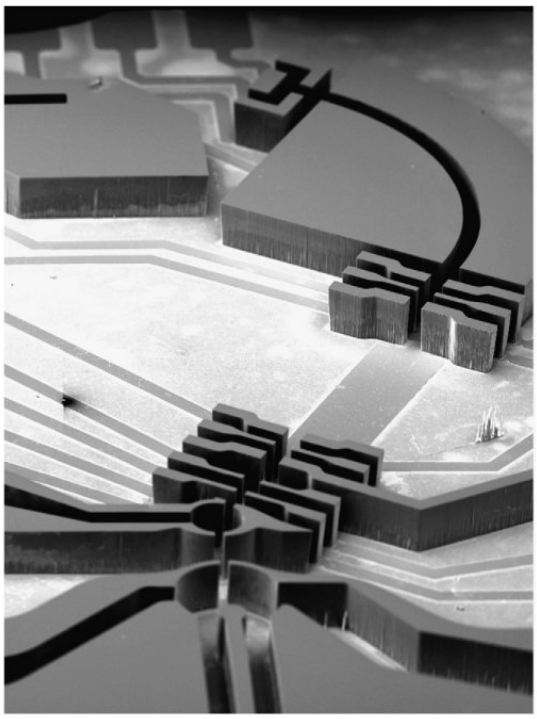

Figure 2.9: SEM image of MMS [127].

one mask. These components are formed in 0.3 mm thick highly conductive silicon and are sandwiched between two 0.5 mm thick pieces of borosilicate glass. Vias are formed using nickel conductors with gold contacts where they join with the silicon.

The truly tiny scale of this device can be seen in figure 2.10, though a final portable mass spectrometer instrument based on this chip is predicted to be about the size of a mobile phone [57].

2.3.3 Flat plasma spectrometers

These instruments are not as small as the MMS above, but nevertheless use MEMS components and are based on a patented design of planar electrostatic analyser channels in stacked flat wafer layers [35]. They were developed by various US institutes and have flown on the US Air Force Academy's microsatellite engineering (FalconSat) programme for senior cadets [24]. Three such devices have been discussed in public literature and are designed to make energy spectrum measurements for three different plasma populations;

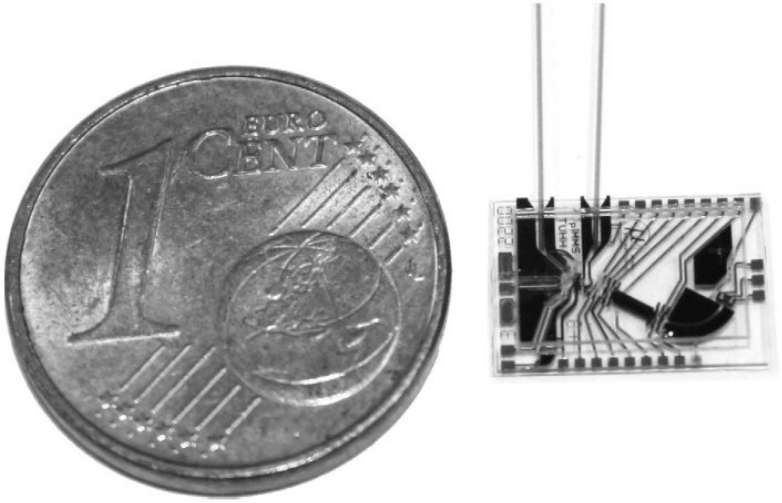

Figure 2.10: Scale of MMS [127].

- MESA (Miniaturized ElectroStatic Analyser) for 0.05 eV to 13 eV electrons [78].
- FlaPS (FLAt Plasma Spectrometer) for 0.1 eV to 16 eV ions [129].
- WISPER (Wafer Integrated SPectrometER) for ions up to 2 keV [128].

The WISPER design was later reused as Canary, a space weather monitor made for the International Space Station [39].

Like the Bessel box instrument, these designs use large numbers of repeated single analyser cells to create an instrument. These cells are simpler than the Bessel box design however, using the parallel plate charged particle optic design shown schematically in figure 2.11.

The principle of these instruments will be discussed using FlaPS as an example. The wafer layers of the FlaPS instrument are shown in figure 2.12. The uppermost (blue) layer is a collimator, selecting the incoming particles by direction. This consists of a silicon top plate, with anisotropically wet etched apertures (figure 2.13), bonded to a block of copper beryllium into which channels had been cut using wire EDM.

This collimator allows only particles within a 1.5° range of angles about the angle of orientation of the channel to successfully pass through it.

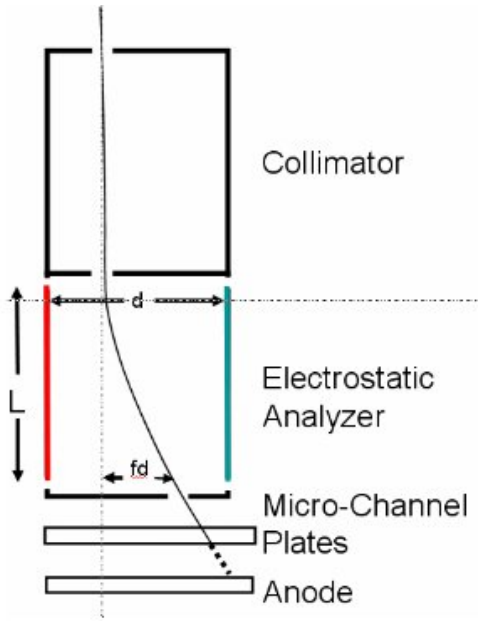

Figure 2.11: Schematic overview of a single pixel in the WISPER instrument (Canary, FlaPS and MESA are similar) [128]

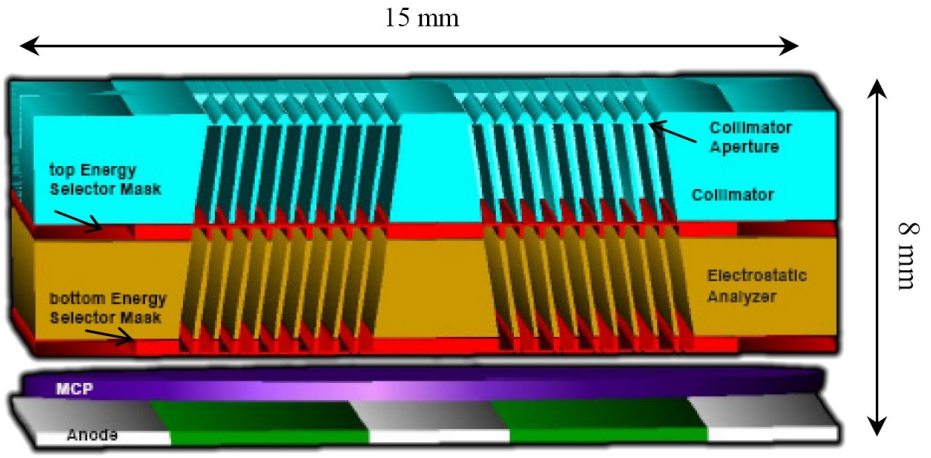

Figure 2.12: Cross section of FlaPS sensor head array (±8° pixel elements shown) [130]

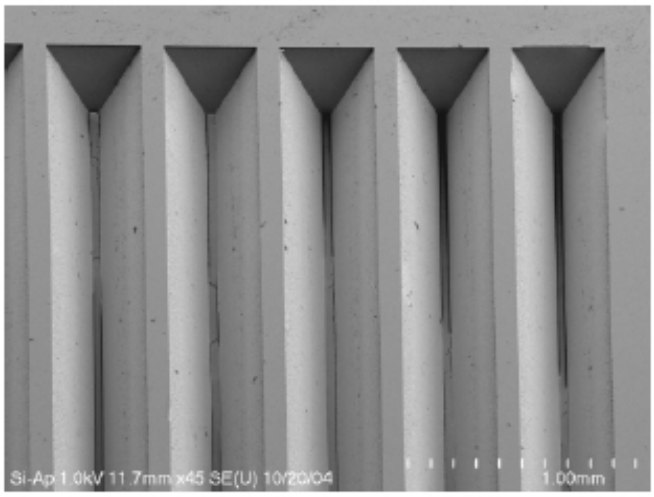

Figure 2.13: SEM image of FlaPS collimator aperture [130].

The next section, into which the direction-selected particles now pass, is the planar ESA section, in which the particles are filtered by energy/charge ratio. Here the channels have a constant electric field applied across them, which causes the trajectory of the particles to be deflected. Figure 2.14 shows the ESA channels which are made as two inter-digitated copper beryllium sections, cut using wire EDM, with a channel width, d, of 0.4 mm.

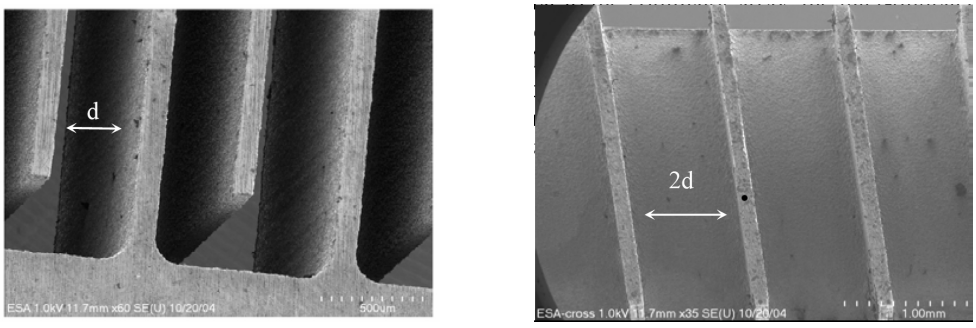

(a) Top view of inter-digitated electrodes.

(b) Cross section of angled electrodes.

Figure 2.14: SEM images of ESA [130].

As has already been shown schematically in figure 2.11, the entrance and exit masks (shown in red in figure 2.12) block most of each of the ends of the ESA channels, so that only particles experiencing a certain deflection (thus only particles with a certain energy/charge ratio) successfully make it to the MCP detector at the bottom where

they are detected.

The energy analyser masks are made from silicon-on-insulator (SOI) wafers and are shown in figure 2.15.

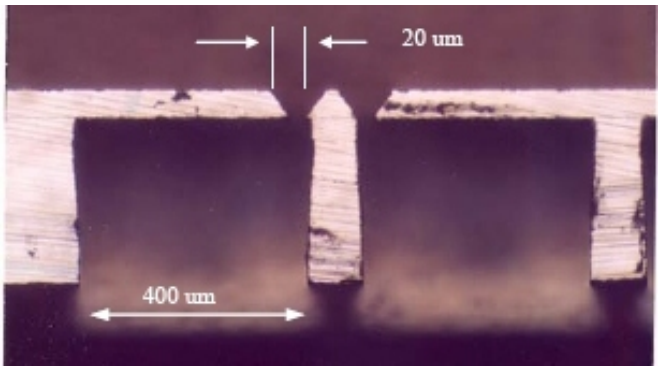

Figure 2.15: Cross section of FlaPS energy selector mask element [130].

These contain a one micron thick buried oxide layer which electrically isolates the ESA region from the rest of the instrument. Figure 2.16 shows the fully assembled FlaPS instrument, with a close up of the aperture area showing the five analyser cells for the five different look directions.

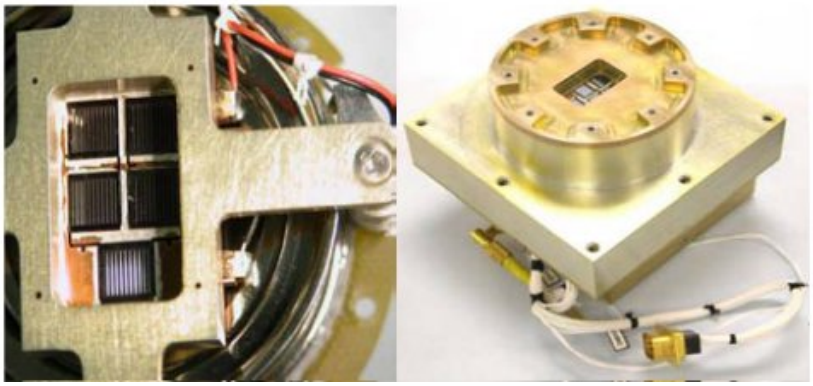

Figure 2.16: FlaPS flight instrument for FalconSat 3, showing a close up of the five pixel heads, apertures with different, highly directional fields of view. [130].

WISPERS is a development of FlaPS. It has seven pixels which are larger and, as well as having different look directions, have different K-factors by varying the channel electrode separation. The ESA wafer, shown in 2.17, is wire EDM cut as one piece from titanium. Titanium is used for a good match of thermal expansion coefficients with the

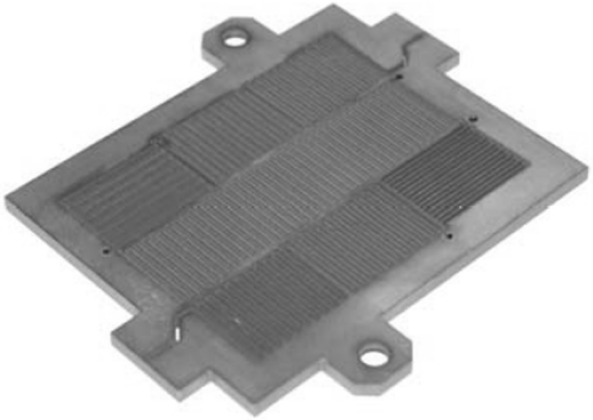

Figure 2.17: WISPERS ESA section prior to assembly. It is EDM cut from one piece of titanium [39].

silicon collimators. To maintain good mechanical alignment the square tabs at either end of the wafer keep the electrodes fixed together at the desired separation. When the wafer is assembled into the instrument these tabs are cut off to provide electrical isolation between the electrodes.

MESA predates FlaPS and uses stacked photolithographically-etched stainless steel plates with Teflon insulating layers, achieving an equally miniaturised, robust, prototype device without any silicon or typical MEMS processes [36].

2.3.4 Discussion

The instrument parameters and other details for MESA, FlaPS and WISPERS are compared in table 2.2. Shown alongside them are estimates for a hypothetical instrument [70, 71] which is based around the work in this thesis, specifically based on the 360° CATS concept that will be described in section 3.2.

Referring back to table 1.2, the instruments discussed in the previous chapter, the following observations can be made of the FalconSAT instruments. Although the reductions in the charged particle optics are significant, the reduction in the resource requirements of the complete package is a more modest evolution. This is because the electronics, detectors and packaging have not been considerably reduced in size. The instrument parameters are also more modest (apart from the resolving powers which are comparable). These can be excused partially since the FalconSats are, in part,

Table 2.2: Comparing parameters of the FalconSAT plasma analysers (blank where data not available)

Name	MESA	FlaPS	WISPERS [and Canary]	This project (projected) [70, 71]
Mission	FalconSat 2 & 3	FalconSat 3	FalconSat 5 [and ISS]	Generic space weather/Jupiter
Launch year	2006 (failed) & 2007	2007	2010 [and 2011]	2014+
Package mass	-	0.5 kg	0.66 kg	0.2 kg
Power req.	-	750 mW	1000 mW	400-500 mW
Particles detected	0.05 eV to 13 eV electrons	0.1 eV to 16 eV ions	0 keV to 1.35 keV ions	electrons & ions, few eV to 20 KeV
Energy resolution	25% (normal) 0.37% (full FOV)	$< 5\%$	5-10%	$\sim$22%
K-factor(s)	1.35	~ 11	3, 10, 30	$\sim$8
Geometric factor	-	5x10^{-}5 cm^2 sr ($\times$5 pixels)	-	$\sim$1x10^{-}4 cm^2 sr total
Field of view	60° by 80°	16°	15° by 15°	$\sim$17° by 360°
Angular resolution	-	1°	-	$\sim$17° by $\sim$7°
Pixels	2 (separate sensors)	5 (directions)	7 (directions and K-factors)	Not applicable

new technology demonstrators rather than the first choice for science, and since the FalconSat program is also, in part, a student training exercise—although not without scientific goals [53, 78]).

Nevertheless, the small geometric factors and lower energy ranges are potentially both real performance issues and 360° fields of view are important for some applications. An instrument derived from the concepts that will be presented in this thesis, along with separate developments in electronics, would go some way to ameliorate these issues. Since the fabrication techniques and detectors would be very similar to those used in the FalconSat mission it can be assumed that the cost of producing the instrument would also be similar.

2.4 Summary

This chapter has examined the main motivations for highly miniaturised analysers of which the most relevant applications to this thesis are low resource platform (e.g. CubeSat) based instruments and miniaturised science-grade instruments for constellation missions. I have described how the instrument parameters might scale, showing that the geometric factor is likely to be the greatest concern, and I have discussed ways to mitigate this.

MEMS fabrication techniques were then summarised, showing that LIGA and bulk micromachining are the methods which would allow for the high aspect ratios required. Finally some existing MEMS and MEMS-based electrostatic analysers were discussed, some of which have already flown in space. These represent the targets for which new analysers from this project should aim to surpass.

From here the thesis now looks to my own work, starting with the development of a prototype highly-miniaturised analyser head.

Chapter 3

Developing a Highly Miniaturised Design

The main starting point for the project was to decide on a design concept to pursue. This requires a consideration of the performance limitations of a miniaturised instrument and the constraints imposed by the MEMS fabrication processes. Since this work is investigating new small scale techniques, it was decided that a rapidly produced prototype was preferable to a rigorously designed and simulated instrument. This chapter describes how the CATS concept was arrived at and how a demonstration prototype analyser head was designed and constructed.

3.1 Design considerations

The top hat analyser design is powerful and well understood, so a MEMS based device might be highly desirable. It may be possible with surface micromachining techniques to produce the concentric hemispheres required, though this is unlikely, and new techniques would probably need to be developed before such a device is an option. Instead the current generation of top hat analysers provide a benchmark against which a MEMS instrument can be judged.

The planar geometry MEMS plasma analysers discussed in section 2.3.3 present an alternative and micromachinable approach and a design that could be improved upon

(e.g. mass analysis, better instrument parameters). Its simple layout allows for easy manipulation of instrument parameters (e.g. by changing channel width) and expansion by adding extra 'pixels'. Its construction is also relatively straightforward and one could imagine pixels being constructed in a surface micromachining manner, once techniques are sufficiently advanced.

Unlike a top hat design however, these planar designs do not have a focussing geometry. Where in a top hat all particles entering the aperture from one direction are brought together (focussed) onto the same spot on the detector, each channel in the FlaPS style design is a mini aperture that will accept particles from one direction only. To get a wide field of view FlaPS uses multiple pixels and to get a suitable geometric factor FlaPS has many channels in each pixel. Pixels can be optimised for different energies so the duty cycle time can be reduced as multiple energies are recorded simultaneously. Additional channels can be added to each pixel so more particles can be detected, improving the counting statistics and thus the accuracy of the instrument. While this sort of brute force approach is achievable with MEMS, a more elegant solution might be preferable and ultimately more powerful.

It is hoped that a MEMS instrument could at least match the overall performance of a top hat analyser and possibly even exceed it, but with considerably reduced mass, volume and power consumption. Meeting this demanding specification requires either a new focussing geometry to be found, or gains to be made in other areas. One possible area could be measuring simultaneously multiple parameters, for example:

- Multiple energies at the same time to get a spectrum of energies in a plasma with a reduced duty cycle time.
- Multiple particles, i.e. measuring ions and electrons at the same time.
- Multiple angles, to cover the whole sky at the same time.
- Repeated, identical apertures (like in a FlaPS pixel).

Although the FlaPS style design is very effective, it is not without its limitations and is not the only MEMS solution. A few alternative design approaches were considered, including:

3.1.1 Planar

One option could be based on a spectrograph design, like that of the Mars96 FONEMA instrument [63] (described in section 1.4.2). A previous study at MSSL [17] has looked into the design of a small spectrometer cell that could be made as a MEMS instrument (figure 3.1), perhaps in a similar, multi-cell, manner to FlaPS.

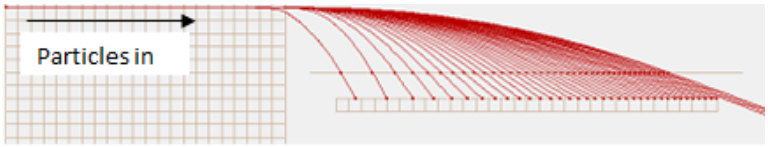

Figure 3.1: SIMION simulations of a simple charged particle spectrograph. [17]

Its simulated response was fairly non-uniform however and it did not present a very satisfying option.

3.1.2 Mushroom geometry

My main starting point however was investigating a funnel type geometry (shown in figure 3.2), with an aperture around the top in the manner of Top Hat analyser, and where a detector (not shown in figure) would be at the bottom of the funnel. This design was termed 'mushroom geometry' because the inner electrode is shaped a little like a mushroom.

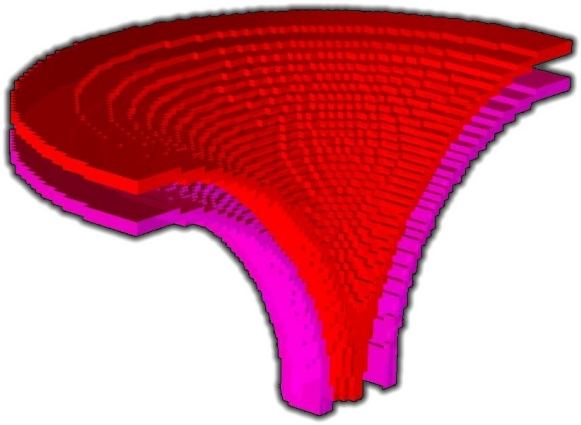

Figure 3.2: Mushroom Geometry (cutaway view)

This shape could probably be made on MEMS scales, perhaps even using conventional technologies and metals. Not having a fly-through geometry would make an electron detector based on this design more vulnerable to secondary electron contamination effects. Baffles to absorb such secondaries could be built into the inner mushroom section to mitigate this a little. Although it can accept incoming particles from 360° in one plane, simulations in SIMION show that there is little focussing, so it is not clear from the particle landing position on the detector as to what was its initial direction. A CEM would therefore be an ideal detector, but being blind to particle direction would make this design of limited use except in thermal plasmas.

Since this design was investigated, a similar concept has been independently investigated by another group. Their AMICCE (Advanced Mass and Ionic Charge Composition Experiment) instrument (figure 3.3) has a variable radius of curvature so that different energies of ion are focussed to different points around the circumference of the detector [32].

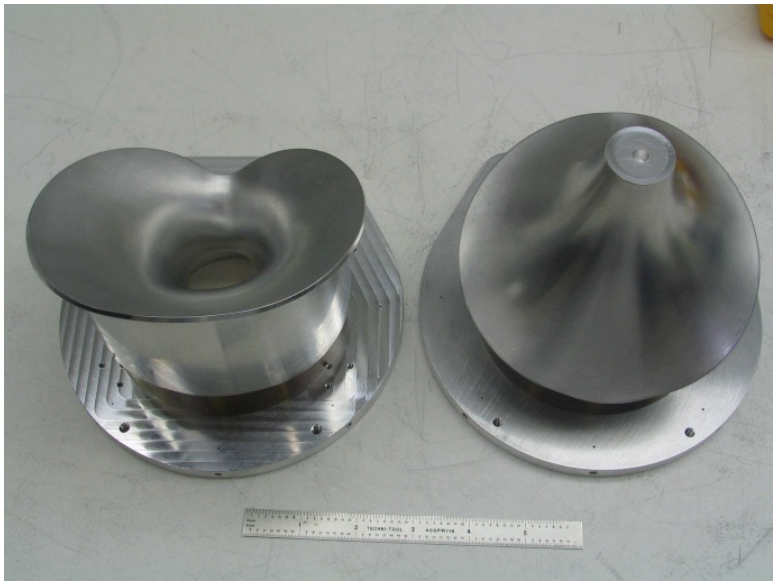

Figure 3.3: Prototype of AMICCE analyser head prior to assembly [32].

3.1.3 Concentric cylindrical geometry

The mushroom geometry led onto the consideration of a concentric cylindrical geometry, creating multiple channels. Being a 2D shape it is ideally suited to being made in MEMS

and cylindrical analysers have already been demonstrated by the MMS, discussed in section 2.3.2. Being in essence a slice of the mushroom geometry above, it is not a focussing geometry, however like FlaPS it could be made of many smaller apertures, each looking at their own small section of sky. This led onto the concept that came to be termed CATS and is explained in the following section.

3.2 Cylindrical And Tiny Spectrometer - CATS

A simple schematic cartoon of the CATS concept can be seen in figure 3.4.

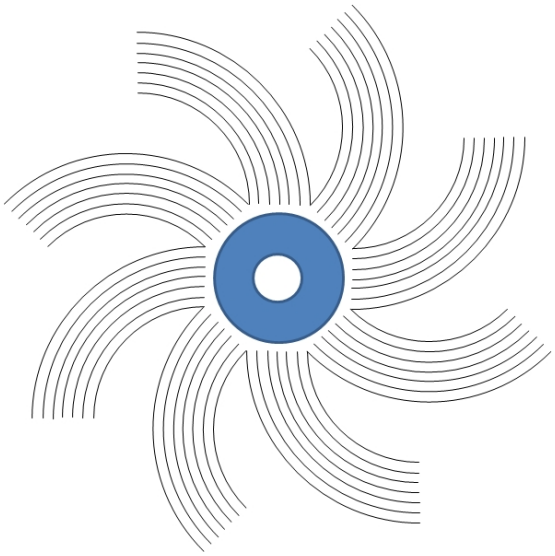

Figure 3.4: CATS schematic, showing ring MCP in blue in the centre and the arms, made up of channels, radiating out from it.

This shows how the instrument is made up of multiple curved arms and that each of these arms have multiple channels of concentric cylindrical analysers. The arms are each covering a different range of input angles (fields of view) so that all angles along the plane of this page can be covered. To allow for this circular 360° FOV arrangement, the truncation angle of each arm must be $\leq 90°$. This is at the expense of losing some particle focussing associated with a 127° truncation angle—like MIPA in section 1.7.3. With small-scale structures like these however, having a detector that covers a large area of the exit aperture area – and not just a focal point in the centre – is simple to implement and although there is a slight worsening of energy and angular resolutions

there is a consequential improvement in geometric factor.

The walls between each channel are alternately at positive electric potential and grounded, creating an electric field across all channels, which at any instant will be of the same magnitude throughout the instrument if the channel spacings are all the same.

Although the channel spacings and electric fields are the same in all channels, the radius of curvature of the channels within an arm are different. This has the effect that the channels within the arms will allow only charged particles with a certain energy-to-charge ratio[1] to pass through to their other end. Each channel within an arm is selecting a different range of particle energies. The peak energy of each channel can be approximated by equating the electric and centripetal forces of a charged particle travelling on circular orbit in the centre of the channel and thus arriving at equation 3.1.

$$K = \frac{E_{selected}}{V_{applied}} = \frac{R_0}{2 \times \Delta R} \tag{3.1}$$

Here K is the K-factor, $E_{selected}$ is the peak energy of the successfully transmitted particles (of unit charge), $V_{applied}$ is the potential difference between the channel walls, R_0 is the mean radius of curvature of the channel and ΔR is the channel width (which is assumed to be small compared to R_0). A more mathematically rigorous definition is given by:

$$K = \frac{E_{selected}}{V_{applied}} = \frac{1}{2 \ln \frac{R_{outer}}{R_{inner}}} \tag{3.2}$$

(from [68, 91, 133])

Where R_{outer} is the radius of the outer (larger) channel wall and R_{inner} is the radius of the inner channel wall. For the uses discussed in this thesis the difference between the results of equation 3.1 and equation 3.2 are negligible.

The energy resolution of a cylindrical analyser can be approximated as

$$\frac{\Delta E}{E} = \frac{\Delta R_{exit}}{R_0} \tag{3.3}$$

[1]Henceforth it will be assumed that only electrons or protons will be analysed and thus 'energy' will be synonymous with 'energy-to-charge ratio'.

(from [57])

where ΔR_{exit} is the width of the exit aperture, so for CATS:

$$\frac{\Delta E}{E} = \frac{2}{K} \tag{3.4}$$

The channels with larger radii will be selecting particles with higher energy to charge ratios and at improved (lower) energy resolution. The energy focussing can clearly be seen in figure 3.5, which shows electron ray traces from the initial SIMION simulations.

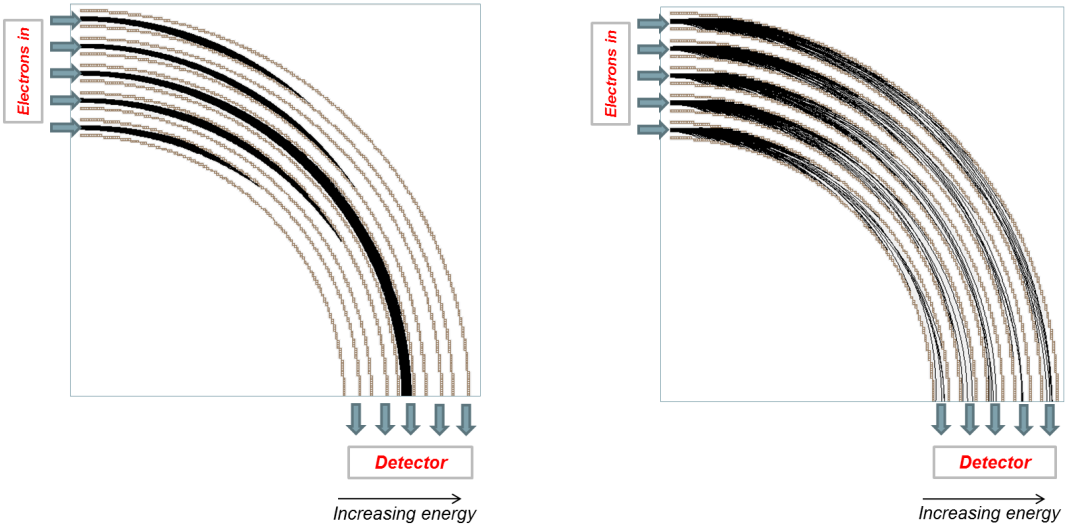

(a) Trajectories of electrons of a single energy (optimised for the central channel) with randomised positions and angles

(b) Trajectories of electrons with randomised energies positions and angles

Figure 3.5: Multi-energetic and mono-energetic electron beams fired through a development simulation of the CATS analyser.

These initial simulations will not be discussed in any detail, as they are vastly superseded in future chapters. Full details of the simulation process are given in chapter 4.

3.2.1 Simultaneously sampling electrons and ions

Since the channel walls are alternately at positive potentials and grounded and the larger radii (outer) wall of a smaller channel is the smaller radii (inner) wall of the adjacent larger channel, the E fields in adjacent channels are oppositely directed. Since

the channels in an arm all curve in the same way, the effect of the oppositely directed E fields in adjacent channels is that adjacent channels transmit alternately positive and negative particles, as illustrated in figure 3.6. CATS is therefore simultaneously an electron and an ion analyser.

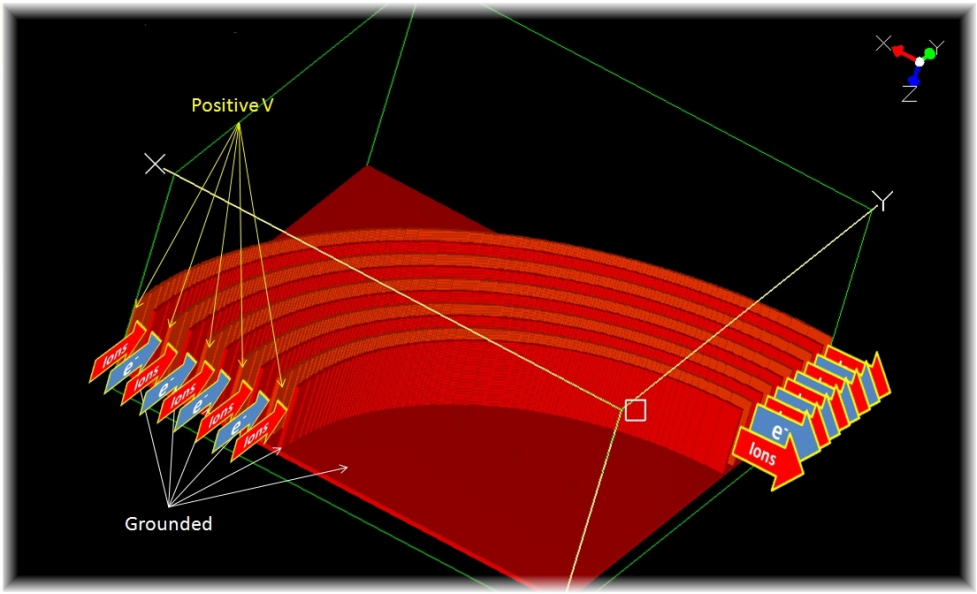

Figure 3.6: 3D view of one arm of CATS instrument, taken directly from the initial SIMION simulation model. Arrows indicate how adjacent channels transmit alternately positively and negatively charged particles.

Detecting the exiting electrons and ions is a challenge. One option would be to have a small CEM at the end of each channel so each channel in each arm could be independently read. Another option might be that shown in figure 3.7: two position sensitive MCPs offset from the plane of the arms, one at negative potential to detect ions, the other at positive potential to detect electrons. Alternatively an SSD or a custom MCP like that designed for AMPS (discussed in section 1.7.2 and shown in figure 1.19) could be used.

3.3 Designing a CATS prototype

The dimensions for CATS can be adjusted to achieve the required parameters for a given mission, e.g. appropriate K-factors for the energies to be sampled and the voltages available according to equation 3.1 and different geometric factors for the electron and

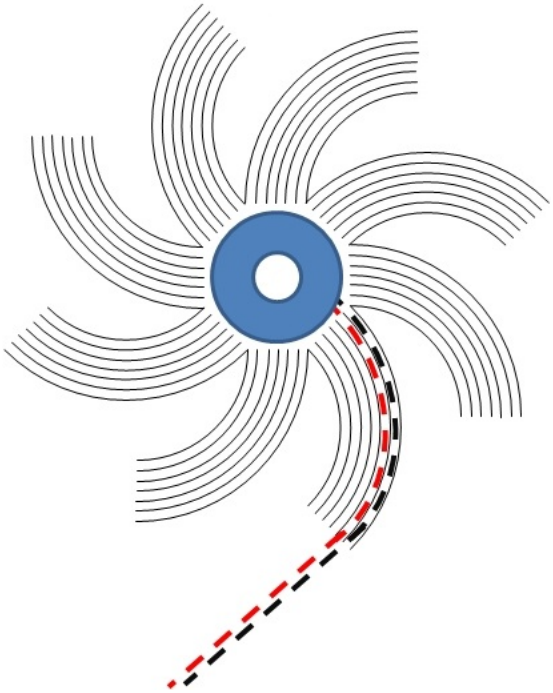

(a) Top view

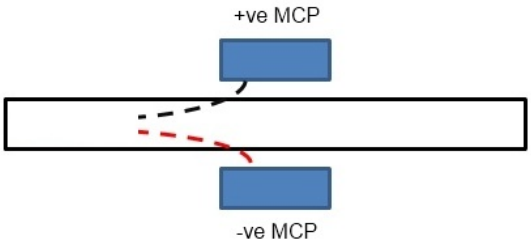

(b) Side view

Figure 3.7: Cartoon of offset ring MCPs configuration for the simultaneous detecting of ions and electrons. Black dashed line is track of an electron, red dashed line is the track of an ion.

ion channels according to their expected differing densities [46] .

A practical factor to consider is arcing between the electrodes. This is complex to predict but a very conservative empirical approximation is that in vacuum 1 µm of gap should be allowed per volt potential difference between them. Substituting this into equation 3.1 gives an approximate upper limit to the energy range of a cylindrical channel:

$$E_{max}(\text{eV}) = \frac{R_0(\mu\text{m})}{2} \tag{3.5}$$

A typical scale, selected as a starting point however was to be a few cm across with channels being 0.3 mm wide and 1.8 mm deep. It does happen however that with those dimensions and the number of arms pictured, the entire sky would not be covered. If full 360° angular coverage were a requirement, either the dimensions could be changed or three of these instruments could be stacked on top of each other and twisted slightly with respect to each other. For full angular coverage in the perpendicular dimension, deflector plates could be used, like those commonly implemented on top hat instruments e.g. IES (shown previously in figure 1.17). The highest guaranteed energy detectable, as given by equation 3.5 is 5 keV, corresponding to the largest radius channel with 300 V applied.

Another important consideration is how the sides of the cylindrical CATS channels are terminated as thus far, for simplicity, the channels have been modelled as either being sections of infinitely long cylinders, or as cylinders with insulating sides. Terminating electrode plates on the sides of cylindrical deflectors are known as Matsuda plates and by splitting them into many sections and applying different voltages to them it is possible to create approximations to toroidal fields in the cylindrical analyser and thus allow focussing in two directions [134]. For the purposes of a prototype MEMS device a simple design was necessary. The two favoured designs came to be known as I and C channels and are shown in figure 3.8.

The C channels became so-called because as viewed end-on from one end the channels resemble a row of letter Cs (as depicted in figure 3.8a); I channels (figure 3.8b) are the inverse arrangement—the configuration in figure 3.8c can thus be said to consist of alternately I and C-channels.

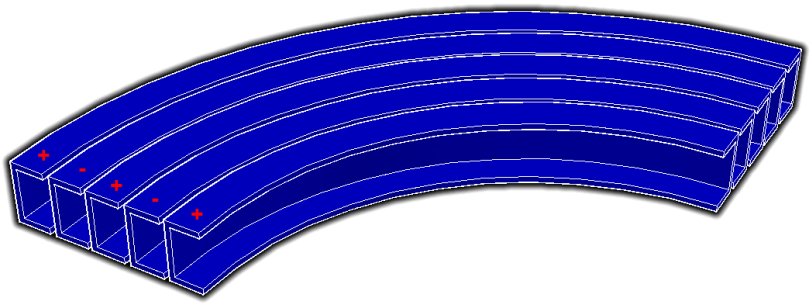

(a) C channels, alternately negative and positive. Innermost electrode wall not shown.

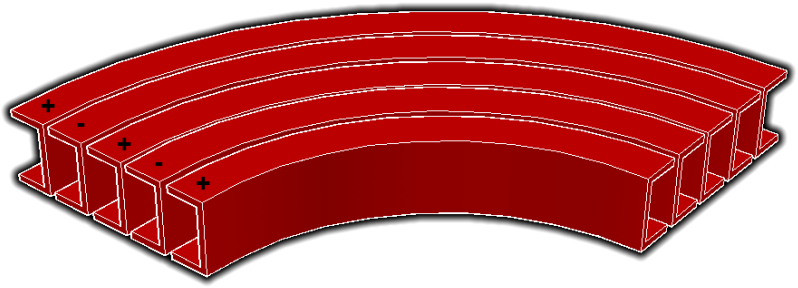

(b) Inverse C channels (I channels), alternately negative and positive. Outermost electrode wall not shown.

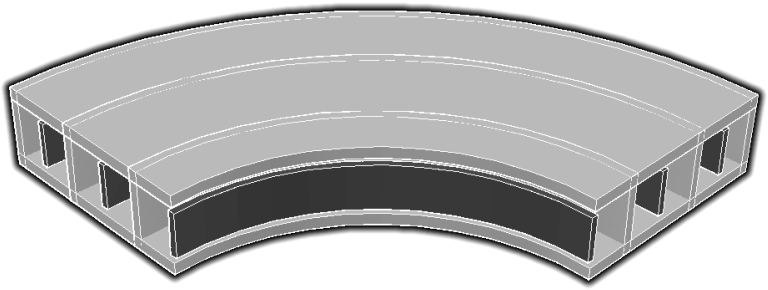

(c) Alternate I and C channels, black electodes and white electrodes have opposite polarities.

Figure 3.8: I and C channel configurations.

The two kinds of channels exhibit different properties. I-channels have side-walls which attract the charged particles under study, preventing some of them reaching the detector. This lowers the geometric factor but narrows (improves) the energy and angular resolutions, the opposite happens in the C-channels, where the side-walls act to focus the charged particles under study. This effect can be seen in figure 3.9 which shows results from the initial simulations.

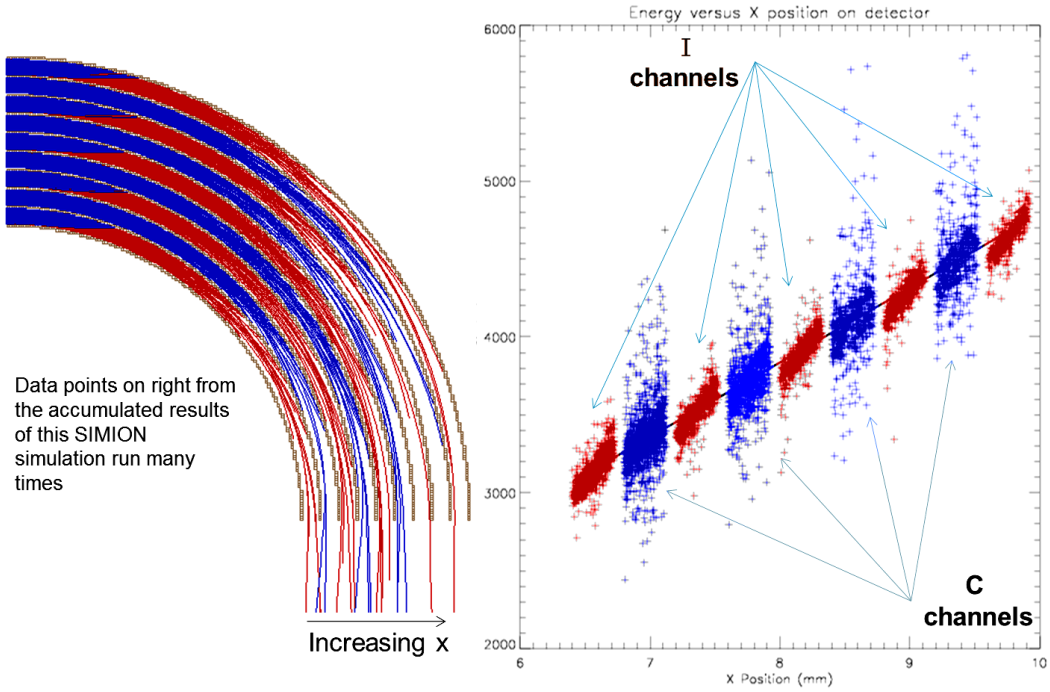

Figure 3.9: Randomised charged particles flown into simulation of I configuration analyser to demonstrate different energy selecting properties of I and C-channels.

The red and blue ray traces correspond to electrons and +1e charged ions. Since electrostatic analysers select only by energy/charge ratio they are completely independent of the mass of the particle.

The red and blue colour scheme will continue to be used where possible throughout the thesis, red for I-channels, blue for C-channels (think red-eye; red-i, sea-blue; c-blue).

3.4 Manufacture

A MEMS foundry was approached with the CATS concept and design options were looked into. LIGA was seen as a promising option and C-configuration designs including that in figure 3.10 were discussed.

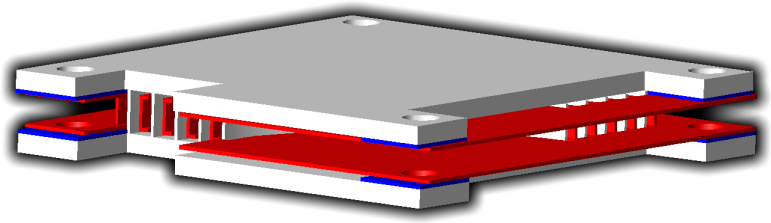

Figure 3.10: A possible design for a LIGA fabricated prototype of CATS

We could not get a satisfactory and cost effective aspect ratio however and so for the initial prototype a double sized model made using EDM and conventional methods was investigated. The design arrived at for this was one like figure 3.8c so it allows both I-channels and C-channels to be studied and characterised. When the design was presented to the manufacturer however he realised he could make it at the original size i.e. not doubled. The final design is shown in figure 3.11.

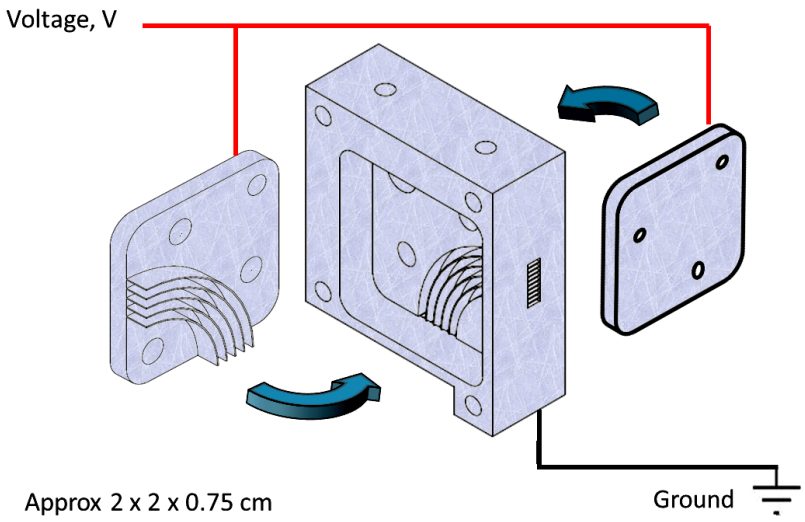

Figure 3.11: The three electrode components that make up CATS. Additional grounded panels (not shown) attach to either side so no high voltages are exposed.

It features five C-channels (numbered 1,3,5,7,9) and five I-channels (numbered 2,4,6,8,10) with an electrode to electrode gap of 0.3 mm and a depth of 1.8 mm. The aspect ratio is thus 6:1, which initial simulations had indicated to be satisfactory.

The exception to this is channel 10. Due to a mistake in the design this was specified to have an electrode to electrode gap that was 80 µm wider than the other channels (its depth and aperture dimensions were unchanged). This gives channel 10 a lower K-factor than might otherwise be expected.

The CATS entrance and exit apertures (which are identical) are each 0.3mm by 1.3mm in open area and 1mm in depth. Being a contiguous section of the central electrode, they are all electrically grounded allowing them to act as a Faraday cage, preventing the electric field within from disturbing plasma outside the analyser. The aperture dimensions are shown in figure 3.12, featuring the numbering scheme that has just been described. The channel dimensions are also shown here including their central radii of curvature, R. This channel numbering scheme will be used throughout this

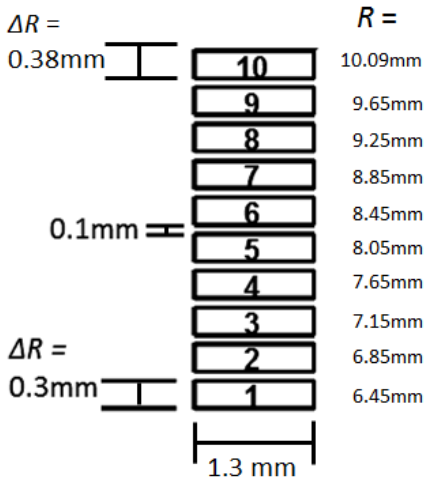

Figure 3.12: CATS aperture dimension, showing the electrode to electrode gap, ΔR, and central radius of curvature of the channels, R.

thesis. A contrived mnemonic I have found helpful is thinking of 'i' channels as 'ee' channels (as 'i' would be pronounced 'ee' in many other languages), so 'ee' channels have eeven numbers (2,4,6,8,10).

The CATS prototype was manufactured in aluminium and can be seen prior to assembly

in 3.13.

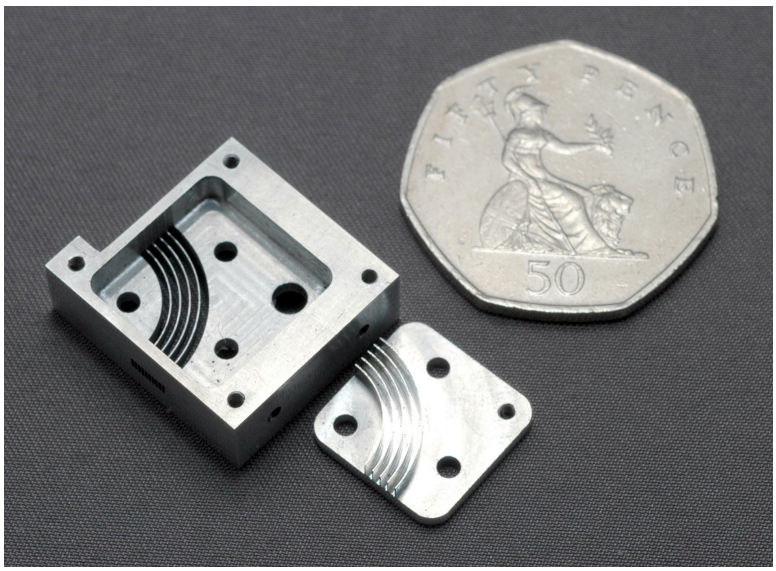

Figure 3.13: The prototype CATS analyser head shown alongside a fifty pence coin.

3.5 Assembly

To assemble CATS, insulating washers are placed around the three holes closest to the channels. The 'fins' are then lowered into position and cylindrical insulating dowels are inserted into the three holes. Screws are then put through the centre of the dowels and screwed into the far-side terminating (Matsuda) plate. Thus are the electrodes held in place and their alignment fixed.

From this point on the CATS prototype analyser will be described simply as CATS and any reference to the full CATS instrument concept (as was outlined in section 3.2) will be explicitly explained as such.

3.6 Summary

I have set forth in this chapter the outline of the Cylindrical And Tiny Spectrometer concept and the prototype model that has been made.

This prototype is not a MEMS instrument, but it is highly miniaturised and it does represent a design that, with some modifications, should be manufacturable as a MEMS

product. From here the discussion moves to the assessment of the charged particle optics and instrument performance of this design through extensive and meticulous computer simulations. Such is the subject of the next chapter.

Chapter 4

Simulating the Design

To predict the performance of an electrostatic analyser design, it can be simulated using charged particle ray-tracing software. This helps to determine the instrument parameters of the geometry and investigate how adjusting the geometry changes these parameters. This chapter discusses the SIMION charged particle optics software and how it has been used to produce highly detailed simulations of the CATS design.

4.1 Simulation setup

Historically, simulations of the electrostatic optics of plasma analyser instruments have been carried out using both bespoke, user-developed code, as well as using commercially available software. As commercial software becomes increasingly powerful and cost-effective, so it is being used increasingly in the plasma instrumentation community. Packages such as Lorentz[1] and CPO[2] offer sophisticated solutions, but SIMION[3], being simple and relatively cheap, is the most commonly used in this field and is the package that I have been using.

SIMION is software primarily used to calculate electric fields and the trajectories of charged particles in those fields when given a configuration of electrodes with voltages and particle initial conditions. I have been using version 8.0, which is produced by the

[1] http://www.integratedsoft.com/Products/Lorentz

[2] http://simion.com/cpo/

[3] http://simion.com/

Idaho National Engineering and Environmental Laboratory.

To use SIMION, first the geometry of the electrodes and the voltages applied to them must be defined to produce a .PA (potential array) file. Next the fields due to these electrode arrangements must be determined, a process termed 'refining'. The PAs are then placed in workbenches where virtual particles can be flown through them. Parameters of the individual particles within the instrument (e.g. their positions and velocities at certain points within the workbench) can be output from SIMION for further analysis to allow the bulk properties of the instrument to be investigated and understood. These steps are explained in greater detail in the following sections.

SIMION can also be used to simulate magnetic fields, but that feature has not been used in this work.

4.1.1 Define geometry

SIMION PAs are 3D volumes that are divided into grids of equal-sized tiny cubes. Each cube can be set to be either an electrode or empty space and thus the cubes form the resolution elements out of which large and complex electrode structures can be formed.

Simple electrode shapes can be drawn and studied within the software itself. More complicated structures of electrode (i.e. entire plasma spectrometer instruments) can be coded separately in a .GEM file. This latter method allows complex structures to be described vectorially as combinations of intersecting shapes (e.g. cylinders and cubes). The electrode designs can then be loaded into the SIMION workbench allowing the design to be visualised and manipulated.

The size of the grid unit, i.e. the length of one of the cubic resolution elements is clearly very important, since any dimension in the model can only be accurate to the nearest integer number of grid units (gu), and curved surfaces need to be modelled as steps of cubes. The software limit of SIMION 8.0 is approximately 200 million array points per PA. If there are planes of symmetry in the instrument design, these can be described in the .GEM file and can allow for massive savings in computer resource and simulation times.

Two planes of symmetry can be used with the CATS PA. These are shown in figure 4.1,

which shows slices of the CATS PA in two orientations to reveal the channels and the apertures. The coordinate and angle definitions that will be used throughout this thesis

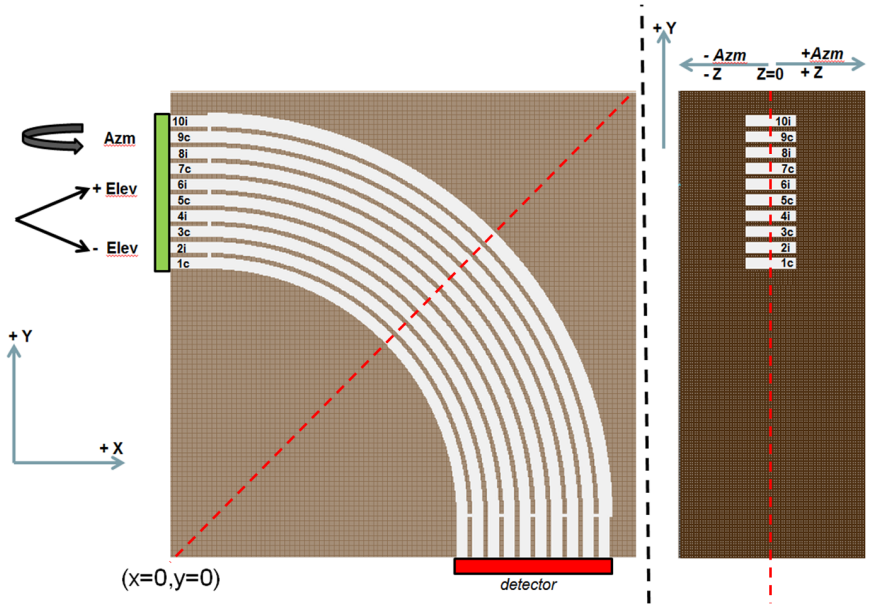

Figure 4.1: Azimuth and elevation directions with respect to CATS input apertures. Red dashed lines indicate the lines of symmetry used to optimise the simulations.

are also shown here, as are the CATS channel numbers. Channel numbers are from 1 to 10 with 1 as the channel with the smallest radius of curvature and 10 with the longest, as shown previously in figure 3.12.

4.1.2 Determine electric fields

Once the PA has been defined, voltages can be applied to the electrode points and the corresponding electric fields can be calculated. This process is called refining and is the process of solving the Laplace equation for the electrode geometry under consideration. The Laplace equation is as follows:

$$\nabla^2 V = \nabla \cdot \nabla^2 V = \nabla \cdot E = 0 \tag{4.1}$$

Where V is the electric potential and E is the electric field. This can approximately be understood as the number of field lines that go in (to a grid unit) is equal to the

number of field lines that go out (from a grid unit). It does not account for space charge effects, changes to the fields induced by the presence of many charged particles, but the conditions inside space plasma analysers are such that this simplification is appropriate.

The equation is solved numerically using a finite difference technique. The potential at a non-electrode point in the PA is set to the average of the six points immediately surrounding it (+ and - one grid unit in each dimension). This process is repeated several times until a stable solution is arrived at. Since this is a very laborious and time consuming process, many tricks are employed to speed it up. These include point-skipping, whereby in the initial iterations points are skipped (e.g. only every 10th point is considered) so that the broad overall shape of the field can be quickly obtained. SIMION also uses over-relaxation, a process whereby changes between some of the initial iterations are over-compensated (e.g. if a change between iterations raised a point potential by 1 V, the over relaxation might raise it by 2 V). This reduces the total number of iterations required.

4.1.3 Fly particles

The particle trajectories are integrated using 4th order Runge-Kutta method numerical approximations. The time step between velocity alterations varies, usually to allow one alteration per grid unit, but near field boundaries this can be increased to allow for improved accuracy. SIMION's behaviour here is determined by the TQ (trajectory quality) setting, which can be set up to a maximum of 500. For settings above zero and up to 100, TQ is adjusting the sensitivity of the field boundary detection for increased accuracy at points where there is a an abrupt change in the field. Above a TQ of 100, the relative step size all along the trajectory is also reduced. TQs of zero and below disable the field boundary detection optimisations and instead alter only the relative step size.

SIMION provides many features for flying different particles with varying initial conditions into the simulated instrument. The most flexibility is provided however by writing 'user programs' in Lua code to describe exactly the parameters of the particles desired. One method is to fire particles in discrete steps of energy, position and angle.

While this is well understood, and replicates the method used in the laboratory for instrument calibration, it is not typical of real space plasma environments and does not take full advantage of the computing power available with modern computers. For this study I have used newer features that allow randomised clouds of particles, within very flexible and controllable energy, position and angle parameters. This allows the entrance aperture of the simulated instrument to be illuminated with a whole swarm of particles, uniformly randomised within the ranges of parameters the instrument has a possibility of detecting.

For ease of implementation, the particles in my simulation are spawned only in the rectangular 2D area of the CATS entrance apertures, whereas it is more physical that the particles be created in an infinite 3D volume. This is therefore accounted for in post-processing, where a small number of particles are randomly removed with a probability of removal that increases the further they deviate from the normal to the aperture with a 1-cos(α) dependence, where α is the angle the velocity makes to the normal. With the narrow angular acceptances CATS has however, this effect is essentially negligible.

4.1.4 Analyse results

SIMION is able to export detailed data, in the form of ASCII text files, on the positions and other parameters of the particles flown within the simulation, at several points during the flight, if required. SIMION has no facility to process the output data it creates however, so these text files need to be handled by routines in an external application.

Building on the earlier work of others, I have created a tool-kit of modular programs within IDL to sieve and manipulate this data. Further modules analyse the data, save graphs of the results, and run new simulations (with modified parameters if required). The key focus of this software development was to leverage recent developments in software features and hardware capabilities for greatly more detailed data and visualisations and highly automated simulations.

The tool-kit allows particles to be fired over all channel apertures, automatically optimised to the transmission parameters of that channel. For a very precise simulation this can be run over days or weeks to produce very detailed data. The data files are

periodically filtered and analysed, and multiple detailed graphs of each channel, and summarised results of the entire CATS assembly are thus produced.

The data sieving routine creates an array of the initial parameters (positions, energies etc.) of the particles that are transmitted to the detector. This can then be binned by energy to find the energy distribution of the successfully transmitted particles. A Gaussian distribution can be fitted to this histogram and either the peak of the Gaussian or the peak of the histogram can be used to define the peak energy, and thus the K-factor. The full width at half maximum (and therefore the energy resolution) can be found either from the Gaussian or histogram results.

The energy acceptance can be found from the maximum and minimum energies in the successfully transmitted particle array. The azimuth and elevation angle parameters can be found in a similar manner by binning by polar and elevation angles respectively.

The energy-dependant geometric factor is determined using the equation described in 1.2, which for the rectangular CATS apertures and in elevation, azimuth coordinates becomes:

$$G = \left(\frac{N_{detected}}{N_{in}}\right)(\Delta y \Delta z)\left(4\arcsin\left(\sin\frac{\Delta\theta}{2}\sin\frac{\Delta\phi}{2}\right)\right)\left(\frac{\Delta E}{E_{peak}}\right) \tag{4.2}$$

Here $N_{detected}$ is the number of particles that reach the detector, N_{in} are the total number of particles fired (which must be large to minimise statistical uncertainty). Δy and Δz are the range of perpendicular dimensions over which they are fired (i.e. the height and width of the input aperture or the area in which the electrons are being spawned). $\Delta\theta$ and $\Delta\phi$ are the range of angles of the input (being greater than or equal to the angular acceptance of the instrument) and the trigonometric expression in which they appear describes the solid angle that the two orthogonal angles create. $\Delta E/E_{peak}$ is the energy resolution.

To visualise the subtleties of the instrument response, the histograms mentioned above are correlated in pairs as 2D histograms (matrices of histograms that produce 3D graphs) and are plotted as shaded IDL contour plots to produce colourful graphics from here on referred to as spectrograms. The parameters being compared are on the

x and y axes and the corresponding number of counts are indicated by a linear colour scale.

4.2 Precision and accuracy of simulations

The precision of the instrument parameters obtained from simulation data depends on the reduction of random error, and thus on the number of particles flown in the Monte Carlo simulation. Consequently simulations were run on loop, each loop appending data to the accrued results, increasing the resolution of the histograms (whose bin size scales automatically with counts) and thus adding detail to the spectrograms. While the instrument parameters could be extracted with good precision after a few hours, high quality spectrograms took much longer to produce. Although target numbers of particles could be set, the simulations could also be stopped or interupted at any point without any significant loss of data. Typically a 'set and forget' method was adopted whereby batches of simulations were set running on remote machines for periods of days or weeks, and often left until a new simulation was required or until they were terminated by hardware or software failure. The spectrogram results from some of the longest running simulations contain considerable levels of detail.

The accuracy of the instrument parameters obtained depends on the understanding of systematic errors present in the simulation. These are in order of process:

- The resolution and accuracy of the model of the electrodes.
- The accuracy to which the fields have been calculated for the models.
- The accuracy of the calculation of the electron trajectories.
- The accuracy of the extraction of the instrument parameters.

The first three are somewhat interrelated. The final one is perhaps of most significance and will be discussed first.

4.2.1 Parameter extraction

As mentioned in section 4.1.4, the energy and angular resolutions have been extracted using a Gaussian fit method and a direct reading from the histogram method. The histogram method however was generally less accurate as it is subject to statistical fluctuations in the histogram, so in most circumstances the Gaussian method was used. This method however assumes that the shape of the histogram is Gaussian, which is not always the case. The best Gaussian-fitting results were found by fitting the curve to the top two thirds below the maximum, as these fits produced the lowest chi-squared results (the tails of the distribution being the most irregular sections) and therefore produced the most consistent instrument parameters. IDL's GAUSSFIT routine was used, with three fitting terms which allowed for the uncertainty on the peak and on the FWHM to be easily extracted. Since these are the uncertainties in the fit of the Gaussian curve to the histogram, it follows that if the true histogram shape is not Gaussian, sizeable errors will remain regardless of how many additional particles are flown.

Equally, if the simulation has systematic flaws but the output distribution measured is Gaussian, then small error values will be returned.

4.2.2 Simulation resolution

Accuracy of electrodes

For the geometry files, the resolution of 25 µm per grid unit was initially chosen as it factorised exactly for all the CATS dimensions, with the exception of the accidentally oversized channel 10, which had to be simulated with a 3 µm smaller radius than the design.

Although this allows for a perfect mathematical description in the .GEM file, when this was converted to the block structure of the Potential Array, the curved surfaces become approximated to jagged steps. While the Laplace equation solving is effective for smoothing out jagged steps into smooth field lines, issues can arise when particles get close to edges as they can collide with the step like structure.

As more powerful computers became available to me and as I discovered new tricks

with SIMION I was able to double and then quadruple the resolution of the original potential arrays first producing a 12.5 µm per grid unit model and then a 6.25 µm per grid unit model.

Accuracy of refine

The SIMION refine settings (controlling the accuracy of the Laplace equation solving) were varied from the default up to the maximum sensitivity but were not found to have a noticeable influence on the results. Regardless of this, where time allowed for it, the highest refine settings were used.

Accuracy of electron trajectories

An automated system was produced to run simulations on loop, raising the trajectory quality each time. Initially tests were performed on the 25 µm per grid unit PA on the full range of TQs. It was soon clear however that the highest TQ simulations ran unacceptably slowly and that changing TQ values only produced a meaningful effect at lower TQ values. With a more refined version of the tool-kit, tests were then performed only with TQ values from 0-25 and on all three different resolution models. The results for Channel 10 can be seen in figure 4.2.

These graphs show the K and geometric factors, and energy and angular resolutions as a function of TQ, with the results for the three different resolutions over-plotted with different line-styles. As the TQ is increased (from left to right on the x axes) there seems to be no convergence in the resolution results while the K and geometric factors have some clear variation at low TQ. As the resolution increases however (dotted line to dashed line to solid line), the variation of these parameters at lower TQ is greatly reduced. The TQ tests were also performed on other channels and the results were found to be similar each time.

With the highest resolution model, variations at low TQ are barely noticeable, and it is only the variation introduced by the curve fitting that is of any real significance (although this is negligible compared with the accuracy to which laboratory-based measurements can be made). For tests where precise instrument parameters were important however, a TQ greater than 5 was used.

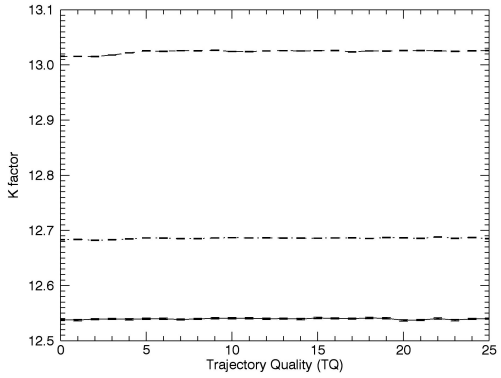

(a) (Absolute) K-factor variation with TQ

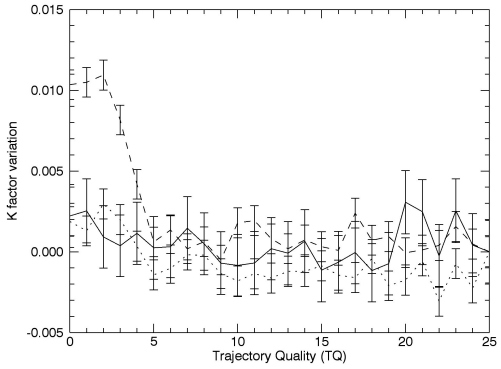

(b) K-factor difference (K-factor - K-factor at 25 TQ) variation with TQ

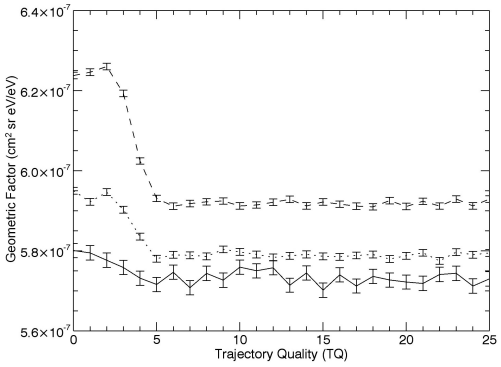

(c) Geometric factor variation with TQ

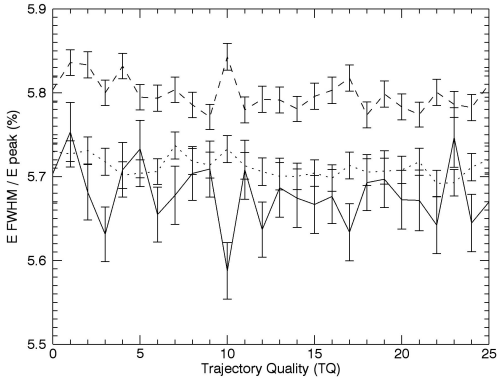

(d) Energy resolution variation with TQ

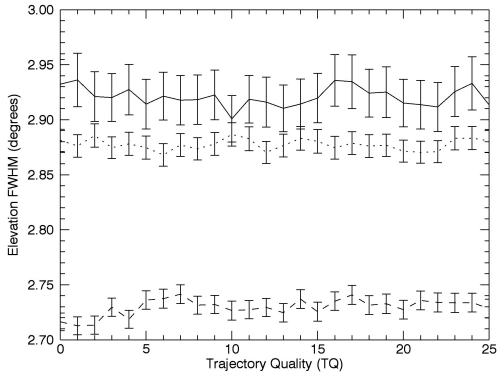

(e) Elevation FWHM variation with TQ

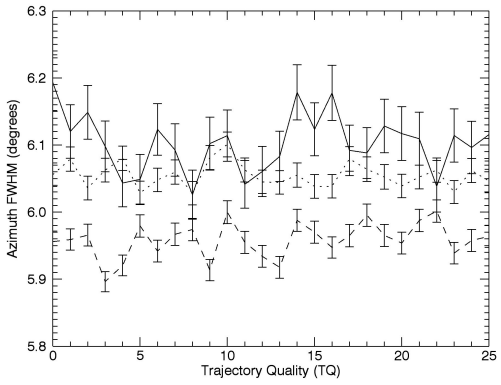

(f) Azimuth FWHM variation with TQ

Figure 4.2: Channel 10 Instrument parameter variation with TQ, using Gaussian fit data and 25 µm/grid unit model (dashed lines), 12.5 µm/grid unit model (dotted lines), 6.25 µm/grid unit model (solid lines).

As well as the TQ variation, the effect of the changing resolution is very noticeable in figure 4.2 as a systematic offset between the parameters extracted from the different resolution models. This is explored further in figure 4.3, which uses a different dataset and shows the comparison between the instrument parameter results for all ten channels and for the three different resolution models . The blue stripes are for the C-channels (1,3,5,7,9) and the red stripes for the I-channels (2,4,6,8,10). From left to right across each stripe (a to c) are the data points for the low, medium and high resolution models respectively.

Ideally many more resolutions would be tested, but the limits of the SIMION 8.0 PA size have been reached so higher resolution models have not been possible. The trend, in the majority of cases, is that the differences between the parameters extracted from the 25 µm model and the parameters extracted from the 12.5 µm model are larger than the differences between the parameters extracted from the 12.5 µm and the parameters extracted from the 6.25 µm model (which often have overlapping error bars), which would appear to indicate that the convergence is close.

A greater understanding of the origin of these differences can be sought by comparing the spectrogram outputs from the simulations. Figure 4.4 and figure 4.5 show some of these. Figure 4.4 shows spectrograms of the energy - entry elevation relationship of detected particles for an I-channel (left hand column) and a C-channel (right hand column), respectively channel 8 and channel 9. The top row shows results from the 25 µm model, the middle row shows results from the 12.5 µm model and the bottom row shows results from the 6.25 µm model. The differences between the I and C channels will be addressed later, the purpose of this figure is to illustrate the effect of changing the SIMION GEM file resolution. For the I-channel results it is immediately clear that in the lower resolution simulation there is an additional tail of lower energy particles at central elevations that is reduced as the resolution is increased. To a lesser extent a similar tail can be seen in the C-channel results. These tails were not expected and the fact that figure 4.4e has a short stubby tail suggests that an even higher resolution model would ideally be used.

Figure 4.5 shows for the same channels and resolutions, the entry azimuth and y position relationship. Looking at the left hand column it can be seen that in the I-channels

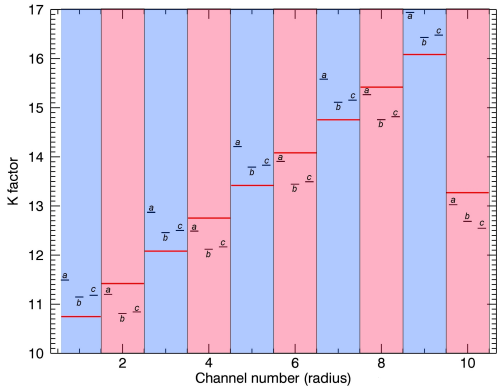

(a) K-factor variation with channel number and geometry resolution, theoretical K-factors shown as red bars

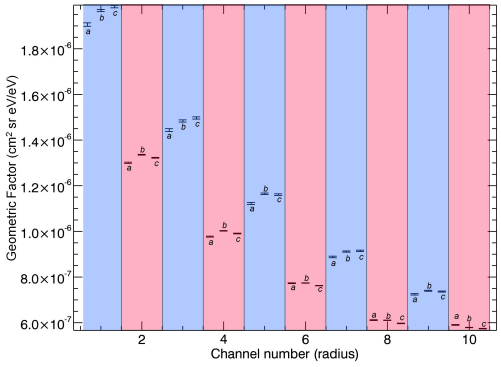

(b) Geometric factor variation with channel number and geometry resolution

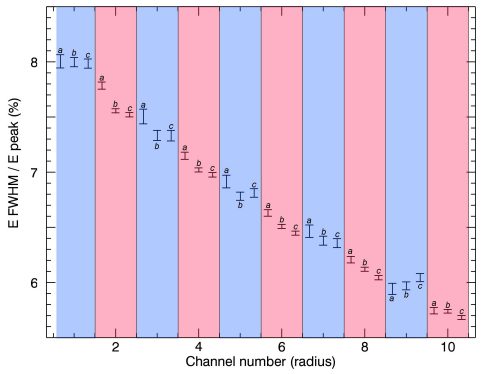

(c) Energy resolution variation with channel number and geometry resolution

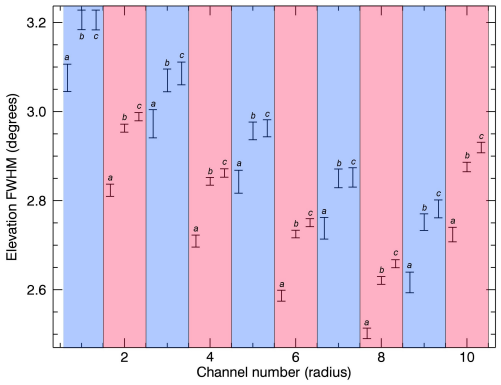

(d) Elevation FWHM variation with channel number and geometry resolution

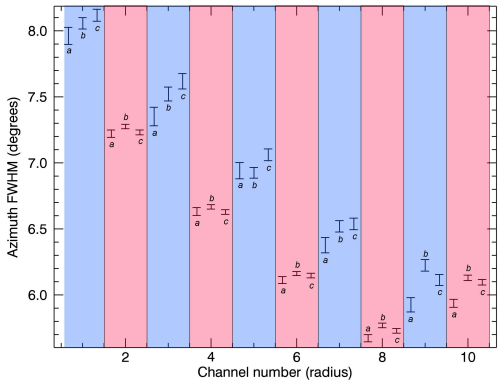

(e) Azimuth FWHM variation with channel number and geometry resolution

Figure 4.3: Instrument parameter variations with geometry resolution. Blue stripes are C-channels, red stripes are I-channels. Data points in each stripe are from left to right, a: 25 µm/grid unit model at 8 TQ, b: 12.5 µm/grid unit model at 10 TQ, c: 6.25 µm/grid unit model at 10 TQ

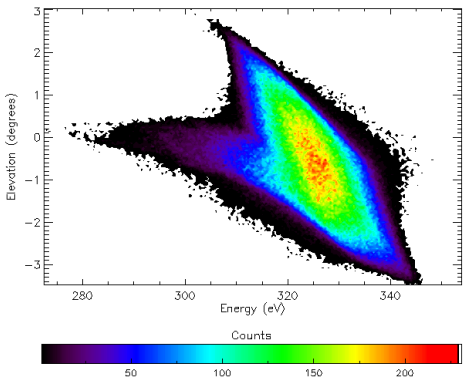

(a) Channel 8, 25 µm/grid unit model.

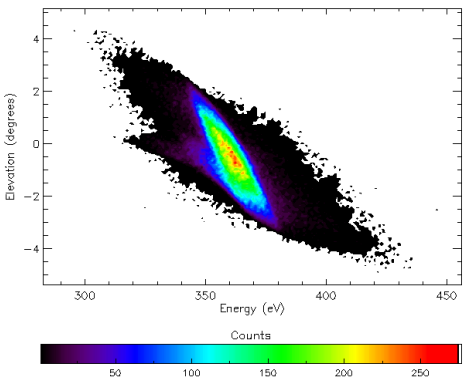

(b) Channel 9, 25 µm/grid unit model.

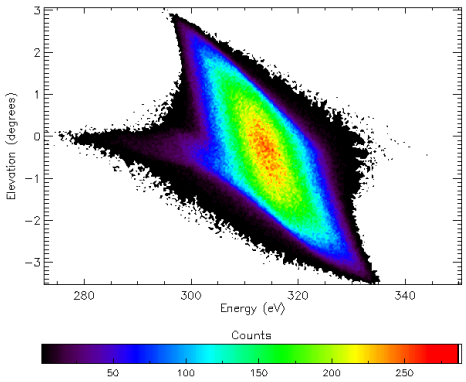

(c) Channel 8, 12.5 µm/grid unit model.

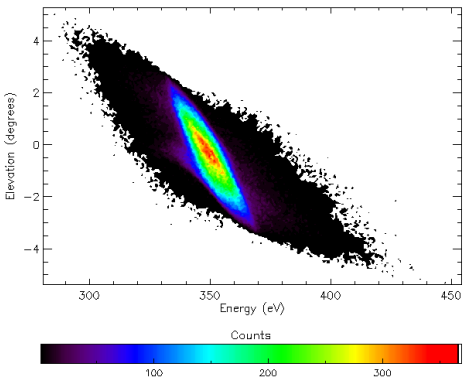

(d) Channel 9, 12.5 µm/grid unit model.

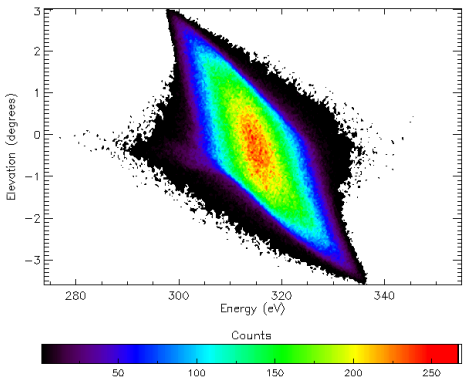

(e) Channel 8, 6.25 µm/grid unit model.

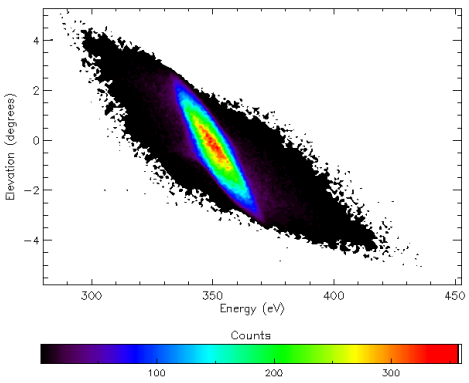

(f) Channel 9, 6.25 µm/grid unit model.

Figure 4.4: Elevation - energy plots for channels 8 (I-channel) and 9 (C-channel) for the three resolution models. Discrepancies introduced by lower resolution models are clearly visible in the I-channel. [N.b. Counts are not normalised between frames.]

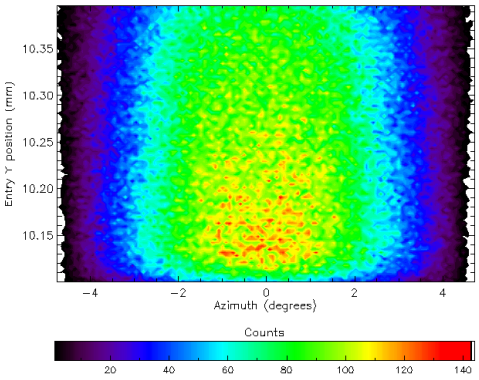

(a) Channel 8, 25 µm/grid unit model.

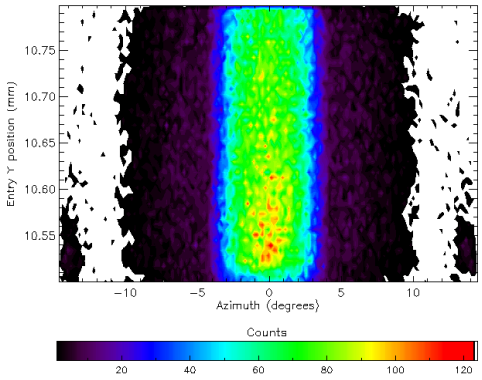

(b) Channel 9, 25 µm/grid unit model.

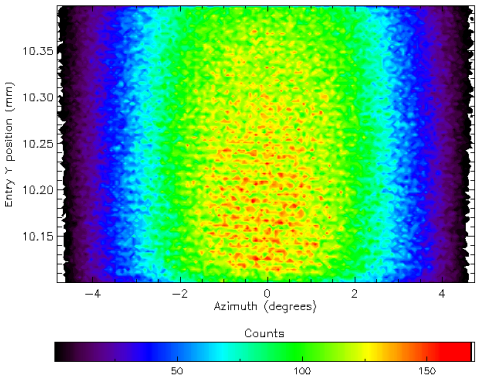

(c) Channel 8, 12.5 µm/grid unit model.

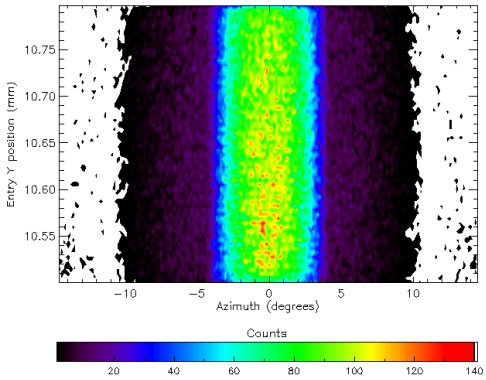

(d) Channel 9, 12.5 µm/grid unit model.

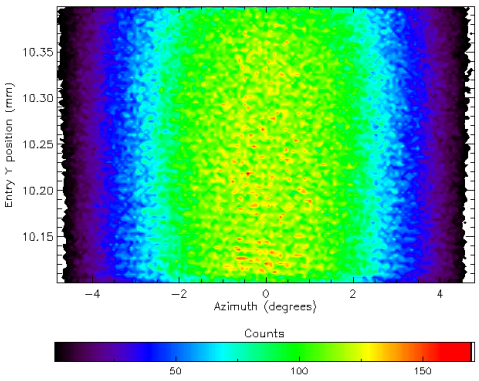

(e) Channel 8, 6.25 µm/grid unit model.

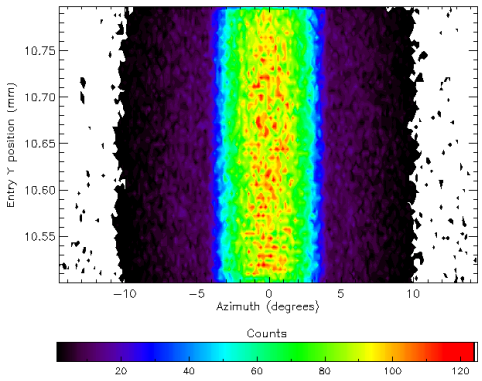

(f) Channel 9, 6.25 µm/grid unit model.

Figure 4.5: Y entry - azimuth entry angle plots for channels 8 (I-channel) and 9 (C-channel) for the three resolution models. Discrepancies introduced by lower resolution models are clearly visible in the C-channel. [N.b. Counts are not normalised between frames.]

at lower resolutions there is a greater concentration of particles at lower y positions for the central azimuths, whereas as the resolution is increased the distribution becomes more uniform with y. Additional spectrograms (not shown) confirm that these greater concentrations correlate with the increased low energy tail seen in figure 4.4 and correspond to particles entering normal to the aperture just above and parallel to the smaller radius curved wall. The same effect is also seen in the C-channels in the right hand column, but additionally here there is a discrepancy at wide azimuths and low y values, an effect which is greatly reduced at higher resolutions. It can be determined from other spectrograms that these extreme azimuths are not part of the low energy tail, instead they have mid-range energies.

These artefacts that have just been described will contribute to the energy and angular resolution variations seen earlier in figure 4.3. The changing K-factor however arises from the much more significant displacement of the energy response that occurs between resolution changes. This can be seen in the displacement of the spectrograms along their z-axes in figure 4.4. This suggests that the especially jagged edges in the lower resolution models are not just creating field distortions near the 'curving' channel walls, but throughout the entire channel.

For the main CATS simulations therefore, the 6.25 µm model has been used, where possible.

4.2.3 Verification

To verify that my simulation method and analysis routines were working correctly, I used them to simulate a known instrument, the PEACE LEEA instrument on Cluster. For this I used a SIMION .GEM file of LEEA that had been developed previously by Glyn Collinson for the discrete step analysis method in earlier versions of SIMION. For my test, rather than firing randomly over the entire cylindrical aperture of LEEA, which is not possible in the randomising code I have written, the cylindrical symmetry of the instrument was utilised. Firing over a single line (along the length axis of the aperture cylinder) was therefore all that was required, along with some scaling modifications to the IDL analysis code to compensate for this.

The results of my random simulation correspond well with Glyn's discrete simulation

results taken from the same geometry file, and also with previous studies of the LEEA instrument, or are otherwise within laboratory measureable accuracies (e.g. 0.5° angular resolution), see table 4.1.

Table 4.1: Comparing LEEA simulations

	Johnstone et al (1993)	Taylor (2005)	Discrete Simulation	My Simulation
K-factor	6.2	6.90	6.18	6.09
Angular Res.	2.79°	2.31°	2.81°	2.18°
GF ($cm^2sr \cdot eV/eV$)	1.92×10^{-3}	1.55×10^{-3}	1.71×10^{-3}	1.61×10^{-3}

4.3 CATS Simulations

While some of the CATS simulation results have already been shown in the context of their optimisation and development, now the final simulations results are presented and discussed.

4.3.1 CATS channel instrument parameters

CATS was simulated using the highest resolution (6.25 µm/grid unit) at 10 TQ and the simulation was allowed to run for several weeks. Summary graphs for the instrument parameters for each of the ten channels are shown in figure 4.6. The error bars, where large enough to be visible, show the error associated with extracting the parameters using the Gaussian fit routine.

It can be seen how in every figure, the I (even) and C (odd) channels stand apart, their different geometries systematically offsetting their parameters. It can also be seen how the extra 80 µm on the channel 10 outer radius adds a much greater variation to many of its parameters. Let us consider each graph in figure 4.6 in turn.

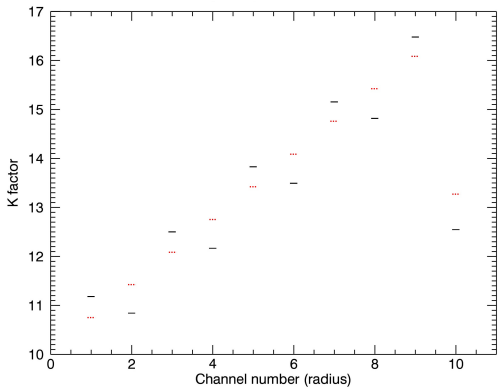

(a) K-factor variation with channel number, theoretical approximations in red.

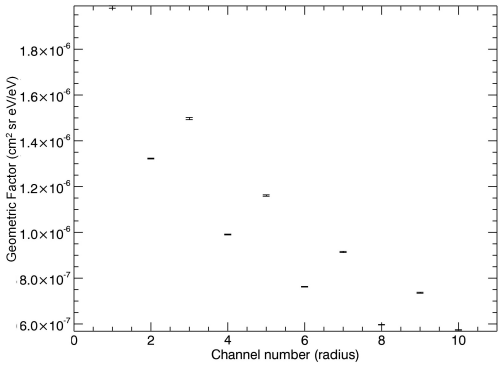

(b) Geometric factor variation with channel number and geometry resolution.

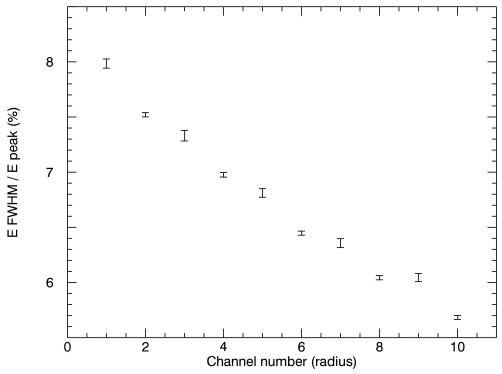

(c) Energy resolution variation with channel number.

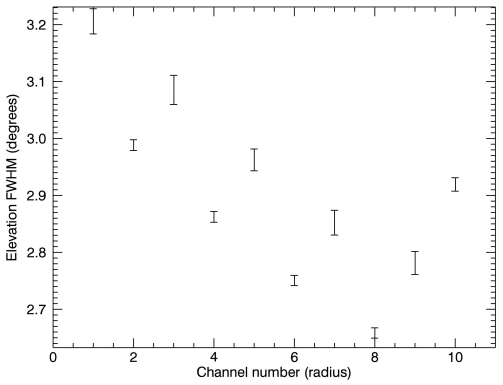

(d) Elevation FWHM variation with channel number.

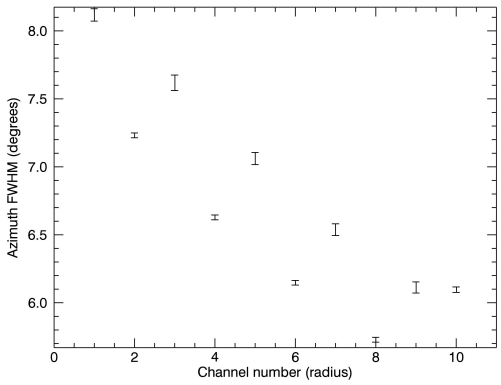

(e) Azimuth FWHM variation with channel number.

Figure 4.6: Instrument parameters for all CATS channels as extracted from the 6.25 µm/grid unit model simulated at 10 TQ for a period of several weeks

K-factors

Figure 4.6a shows the K-factors for the different channels in black, and the theoretical approximations (from equation 3.1) in red. It can be seen that the C-channel K-factors are consistently lower than the approximation, and that the I-channel K-factors are consistently higher by a slightly larger amount.

This effect is so great that each C-channel has a higher K-factor than its larger radiused I-channel neighbour. The exception to that is channel 10, where the wider gap reduces the K-factor, as would be expected from equation 3.1.

That adjacent channels have similar K-factors does not detract from CATS' utility as a plasma analyser, since adjacent channels are sampling electrons and positive ions alternately.

Geometric factors

Figure 4.6b shows the geometric factors for the different channels. Unlike the K-factor this decreases with increasing radius (as the path length of the channel increases while the gap between them and the size of the apertures remain constant). Again the C-channels have a larger value than corresponding I-channels. This can be attributed to the focussing effect of the side-walls, repelling all the particles inwards. The I-channels have the opposite effect, causing particles away from the centre to diverge and not be detected.

The larger channel 10 has been affected less, because although the channel gap is larger than that of the other channels, the apertures are same size.

Energy resolutions

The channel energy resolutions, shown in figure 4.6c, show least variation between I and C-channels of the results shown here. As the channels become longer, and the gap between them remains the same, so the bandpass of energies transmitted becomes smaller, and the energy resolution improves (decreases). The C-channels have only a fractionally worse (larger) energy resolution than the I-channels, and have a larger error bar as their energy response is further from an ideal Gaussian.

Angular resolutions

The channels' angular resolutions, shown in figures 4.6d and 4.6e, follow a similar pattern to the geometric factors. The exception to this is channel 10 where the larger gap allows for an increase in the size of the azimuthal bandpass and a significant increase in the elevation bandpass. Again the larger error bars are present on the C-channels due to their response deviating from an ideal Gaussian.

Discussion

Table 4.2 shows a summary of the performance parameters for each channel extracted from the simulation (quoted to a number of significant figures indicative of the uncertainty in the simulation result). The total geometric factor of all channels together is 1.05×10^{-5} cm^{2}sr ev/ev. This is an order of magnitude or two below the geometric factors of the analysers shown in table 1.2. That is not an entirely fair comparison however since they are fully fledged flight instruments. A fairer comparison would be to a FlaPS pixel, but even those have a geometric factor 5 times larger than CATS. It should be remembered though that there are missions which require low geometric factors (to prevent signal pile-up in dense plasmas) and that by trading off other parameters the CATS design can be adjusted for larger geometric factors.

The peak energies of channels 1 and 2, are similar as are 3 and 4, 5 and 6, etc., consistent with the K-factors seen previously in figure 4.6a. The energy resolution allows for suitable overlap between channels, which will be seen more clearly later in figure 4.7 and is competitive with the instruments in table 1.2 and 2.2.

The CATS angular resolution is larger (worse) compared with FlaPS, but this is not necessarily a strong requirement of all science missions and could be improved with collimation, if required, (e.g. at the expense of geometric factor).

4.3.2 Multidimensional spectrogram analysis

To investigate the subtleties of the instrument response the simulations were run until detailed spectrograms were produced. For completeness, these are reproduced in the following pages with the significant dimensions/ degrees of freedom cross-correlated

Table 4.2: CATS instrument parameters as extracted from 6.25 µm grid unit SIMION model with 21.25 V applied to electrodes.

Channel	1	2	3	4	5	6	7	8	9	10
Particles fired (1000)	81962	76462	86656	76195	82791	76789	85765	77407	85162	78282
Particles detected	381378	1776810	228336	1503530	323186	1426850	257828	1143840	267931	1124930
Geometric factor $\times 10^6$ (cm^2 sr eV/eV)	1.99	1.32	1.50	9.91	1.16	7.62	9.15	5.97	7.37	5.72
Peak energy (eV)	238	230	266	259	294	287	322	315	350	267
Maximum energy (eV)	323.9	262.2	389.6	292.4	390.7	325.5	435.2	355.2	454.6	302.8
Minimum energy (eV)	180.4	189.1	191.8	227.8	231.1	252.6	253.2	273.8	280.0	218.9
Energy resolution (%)	7.90	7.53	7.32	6.93	6.83	6.44	6.38	6.04	6.03	5.69
K-factor	11.18	10.84	12.50	12.17	13.83	13.49	15.16	14.82	16.48	12.55
Peak elevation (°)	-0.52	-0.44	-0.47	-0.39	-0.42	-0.36	-0.39	-0.34	-0.36	0.15
Maximum elevation (°)	6.79	3.84	6.51	3.59	5.89	3.28	5.84	3.04	5.34	3.76
Minimum elevation (°)	-6.98	-4.63	-6.35	-4.21	-6.24	-3.87	-5.66	-3.60	-5.79	-3.51
Elevation resolution (°)	3.2	2.99	3.1	2.86	3.0	2.75	2.9	2.65	2.8	2.92
Peak azimuth (°)	-0.10	-0.04	-0.10	-0.04	-0.08	-0.04	-0.08	-0.03	-0.07	-0.03
Maximum azimuth (°)	17.26	6.13	16.29	5.61	15.73	5.17	14.99	4.81	14.53	4.98
Minimum azimuth (°)	-16.58	-6.12	-16.19	-5.58	-15.64	-5.17	-14.99	-4.81	-14.56	-4.97
Azimuth resolution (°)	8.17	7.23	7.43	6.66	7.01	6.16	6.59	5.73	6.16	6.08

and compared. For cases where parameters from multiple channels do not overlap, datasets have been combined to allow direct channel-to-channel comparisons. In such cases I have normalised the number density of input particles to ensure that the colour-bar scale remains meaningful within an individual spectrogram. Each page of figures focusses on a different dimension (energy, angles, entrance and exit aperture spatial dimensions). Where these pages have columns, the left hand column shows channel 8 (or multiple I-channels) and the right hand column shows channel 9 (or all C-channels). The x-axis scales down each column are approximately consistent but sometimes vary column to column. The graphs at the top of each page show the 2D distribution of the parameter under discussion and, where there are two columns, allows the x-axis scales of the two to be easily compared; the main data being plotted as a shaded shape, with the curve from the counterpart graph in the neighbouring column over-plotted as a thin line. The y-axis scales are not always comparable between columns and the colour-bar scales are normalised and redrawn for each graph individually because the input particle densities are not always comparable.

Figure 4.7 shows spectrograms of the CATS energy response as a function of the various different dimensions. Channel 10 has been omitted from this set of figures as its energy bandpass overlaps with channel 4. Figures 4.7a and 4.7b show the K-factor difference between the two sets of channels by the x-axis offset between the over-plotted lines. A closer examination of the width of each of the peaks reveals the slight energy resolution difference channel to channel and between the two sets of channels.

Sub-figures (c) to (f) show the narrowing angular bandpass channel to channel. Sub-figures (g) and (h) show the relation between higher energies and larger radii (y values) as predictable by equation 3.1. Also clearly separated in the C-channels plot are the long, non-Gaussian tails that give the larger energy resolution values and larger error bars.

Figure 4.8 shows the elevation response of channels 8 and 9 as a function of the various different dimensions. It can be seen in the sub-figures (a) and (b) that the peak elevation is slightly negative, i.e. pointed slightly toward the inner radius. Sub-figure (d) shows how the I-channels' extreme energy tails are correlated with the extreme elevation tails, the highest energies having the most negative elevations corresponding

Figure 4.7: Plots comparing I-channel and C-channel energy distributions.

(a) I-ch. (2-8)–shaded red, C-ch.-blue line.

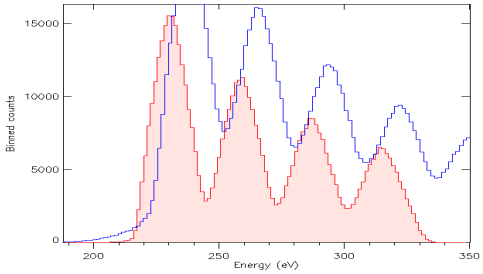

(b) C-ch.-shaded blue, I-ch. (2-8)–red line.

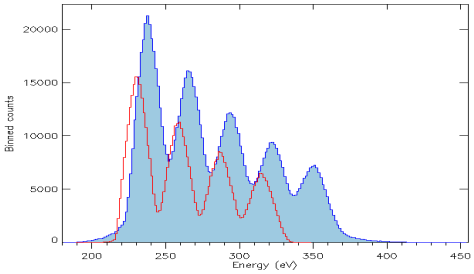

(c) I-channels (2-8), elevation - energy.

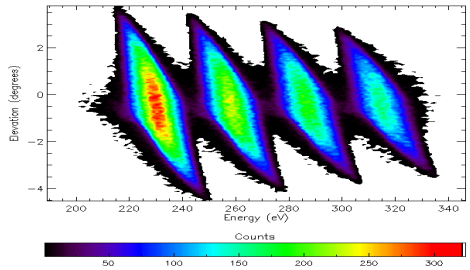

(d) C-channels, elevation - energy.

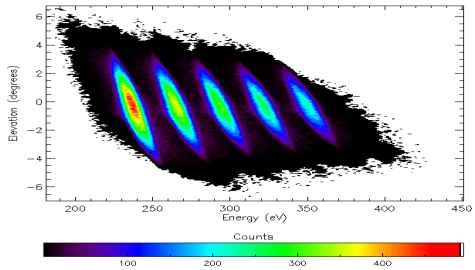

(e) I-channels (2-8), azimuth - energy.

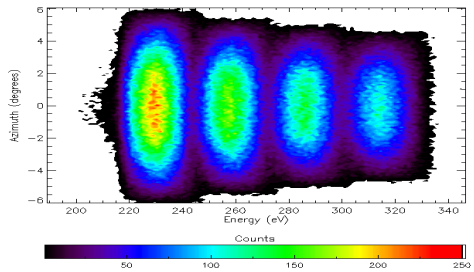

(f) C-channels, azimuth - energy.

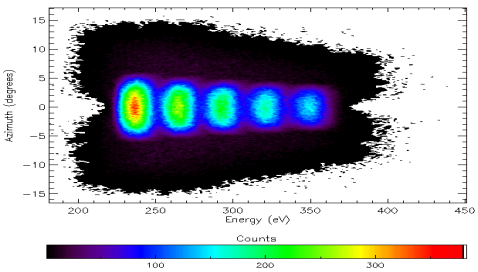

(g) I-channels (2-8), entry y - energy.

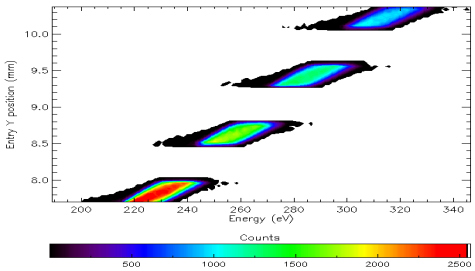

(h) C-channels, entry y - energy.

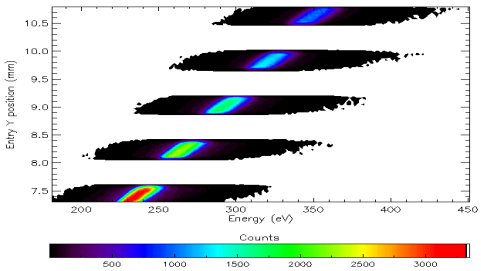

(i) I-channels (2-8), entry z - energy.

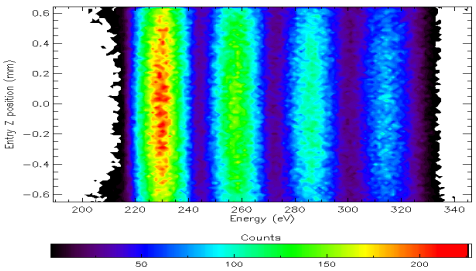

(j) C-channels, entry z - energy.

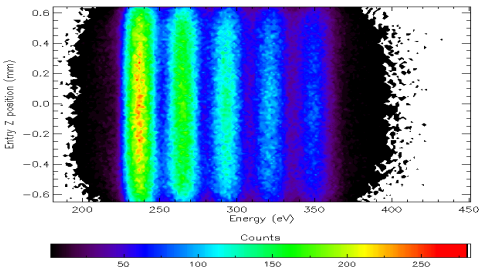

Figure 4.8: Plots comparing channel 8 (I) and channel 9 (C) elevation distributions.

(a) Ch. 8–shaded red, ch. 9–blue line.

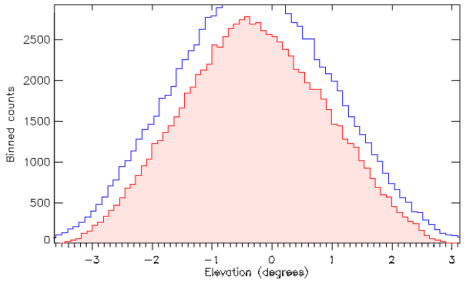

(b) Ch. 9–shaded blue, ch. 8–red line.

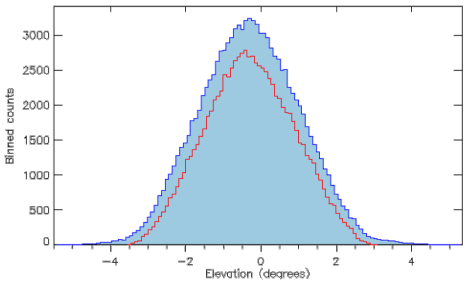

(c) Channel 8, energy - elevation.

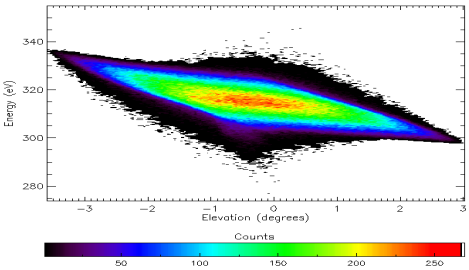

(d) Channel 9, energy - elevation.

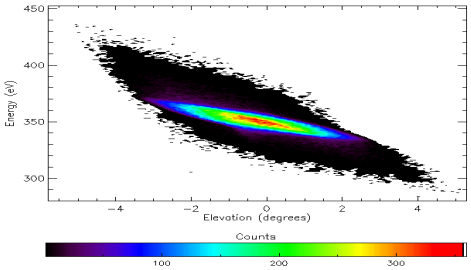

(e) Channel 8, azimuth - elevation.

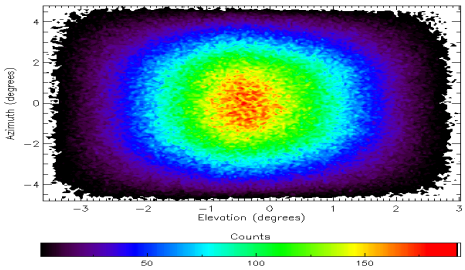

(f) Channel 9, azimuth - elevation.

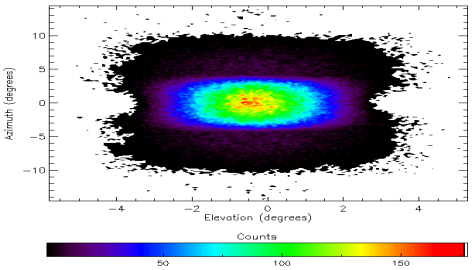

(g) Channel 8, entry y - elevation.

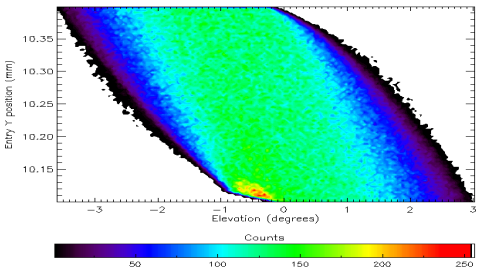

(h) Channel 9, entry y - elevation.

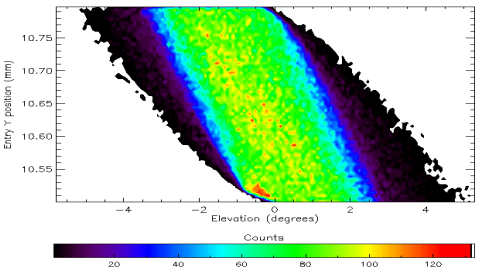

(i) Channel 8, entry z - elevation.

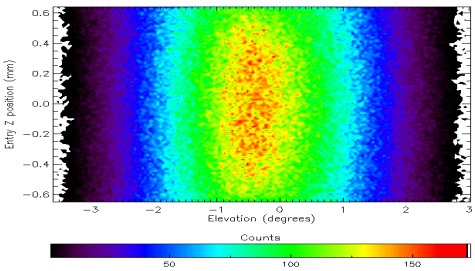

(j) Channel 9, entry z - elevation.

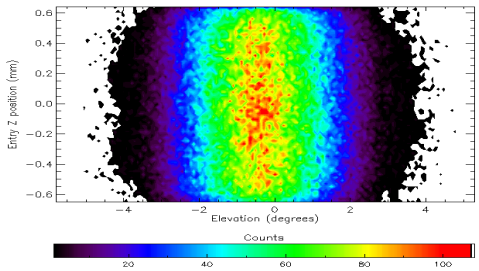

to the least amount of electrostatic deflection and the lowest energies the exact opposite. Sub-figure (c) shows that the lowest energy particles transmitted through the C-channels are through the stubby tail at central elevations, although this could be an artefact associated with an insufficiently high grid resolution (as discussed previously in section 4.2.2). Sub-figures (g) and (h) reveal a 'hot spot' just above the inner radius and at the peak elevation, although later figures will show that this is perhaps over-emphasised by this contouring and colour-bar scaling.

The next page of graphs, figure 4.9, shows the azimuth response of channels 8 and 9 as a function of the now familiar set of dimensions. In the C-channel 2D histogram (figure 4.9b) it can be seen that there are significant wings to the distribution, more-so than there has been in the elevation and energy distributions. This is attributable to the repulsive nature of the C-channel walls that work to contain some of the more extreme azimuths. These more complex trajectories with extreme azimuths form the two large clouds either side of the central feature in the C-channel spectrograms in the right hand column. The very sparse scatterings of particles in the I-channel data at azimuths with magnitudes greater than 10, and the very lowest energies in the C-channel spectrogram figure 4.9c are also potential artefacts from insufficient grid density as discussed earlier.

Figure 4.10, being plots of the spectrograms of the y (radial) axis at the CATS entrance aperture, is the first in this sequence of figures to show I and C-channels plotted together and the first to show all ten channels. This makes it, in effect, a more detailed version of figure 4.6 and highlights quite clearly the differences between the I and the C-channels. Figure 4.10a is analogous to figure 4.6b, showing the relative geometric factors between the channels. The following three figures (4.10b, 4.10c and 4.10d) show how the C-channel responses are, in general, the same as that of the I-channels, but with a more intense central region and with extended tails. Figure 4.10b can be compared with figures 4.6a and 4.6c, with this spectrogram version clearly showing both the energy offset and the differing bandpasses. Since figure 4.10b shows the energy bandpass is similar between different I-channels and between different C-channels, the improving resolutions channel to channel in figure 4.6c are thus attributable solely to increasing peak energy (K-factor). It can also be seen here that the extra electrode spacing gap in channel 10 gives it a slightly greater sensitivity to lower energy particles when compared with the other I-channels.

Figure 4.9: Plots comparing channel 8 (I) and channel 9 (C) azimuth distributions.

(a) Ch. 8–shaded red, ch. 9–blue line.

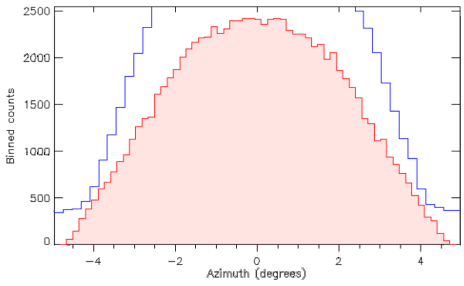

(b) Ch. 9–shaded blue, ch. 9–red line.

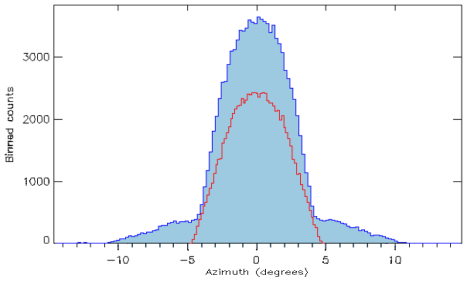

(c) Channel 8, energy - azimuth.

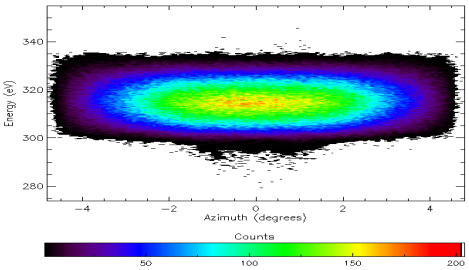

(d) Channel 9, energy - azimuth.

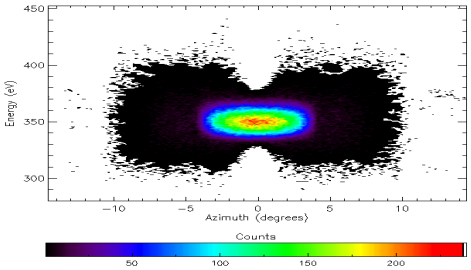

(e) Channel 8, elevation - azimuth.

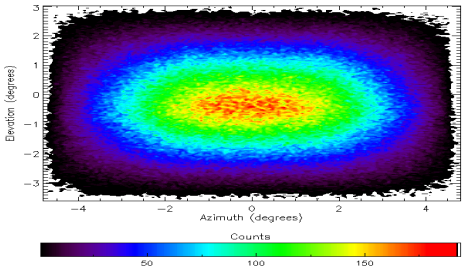

(f) Channel 9, elevation - azimuth.

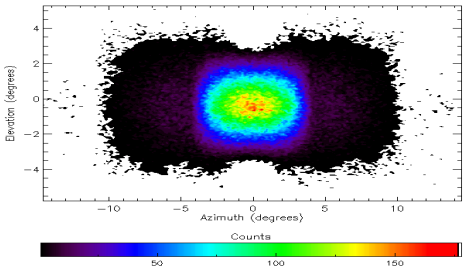

(g) Channel 8, entry y - azimuth.

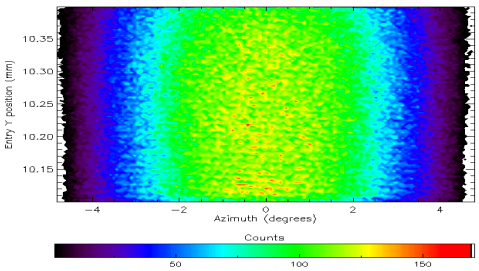

(h) Channel 9, entry y - azimuth.

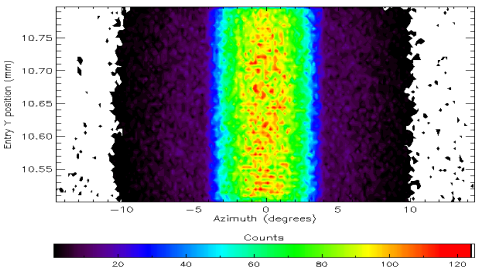

(i) Channel 8, entry z - azimuth.

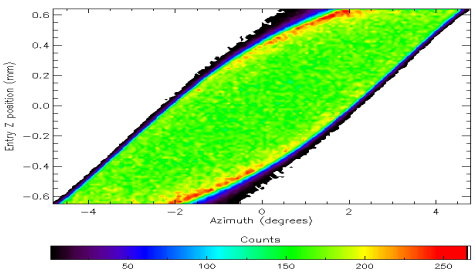

(j) Channel 9, entry z - azimuth.

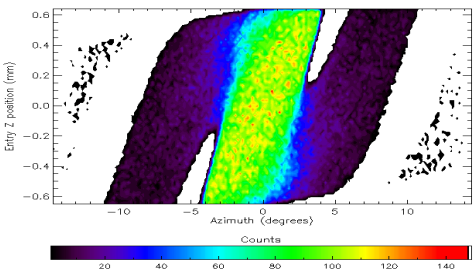

Figure 4.10: Spectrogram plots comparing entry y position distributions.

(a) All channels, entry y distribution histogram.

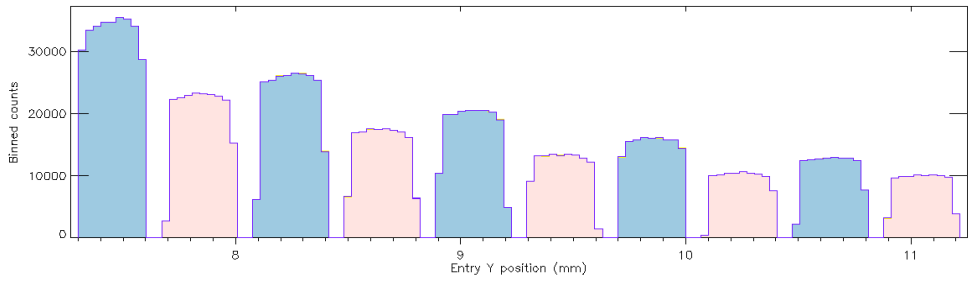

(b) All channels, energy - entry y.

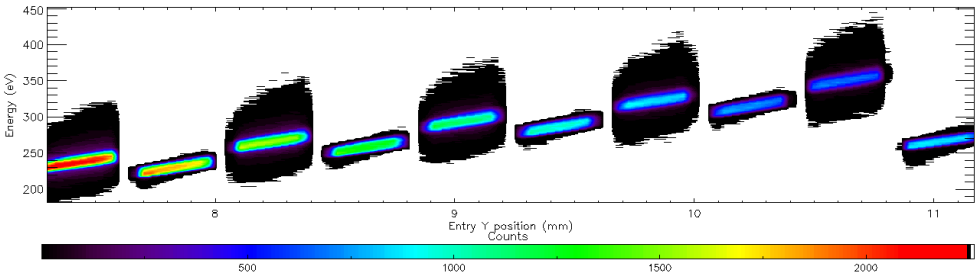

(c) All channels, elevation - entry y.

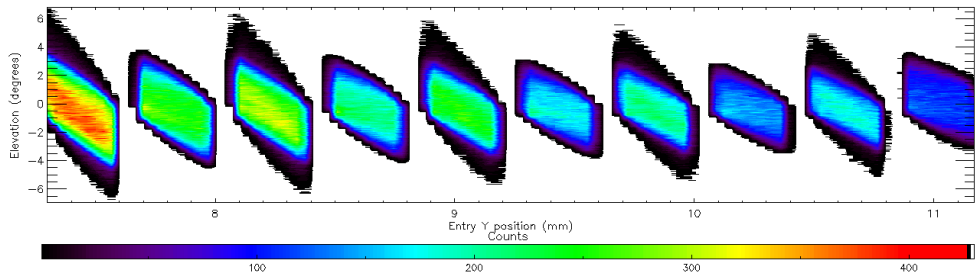

(d) All channels, azimuth - entry y.

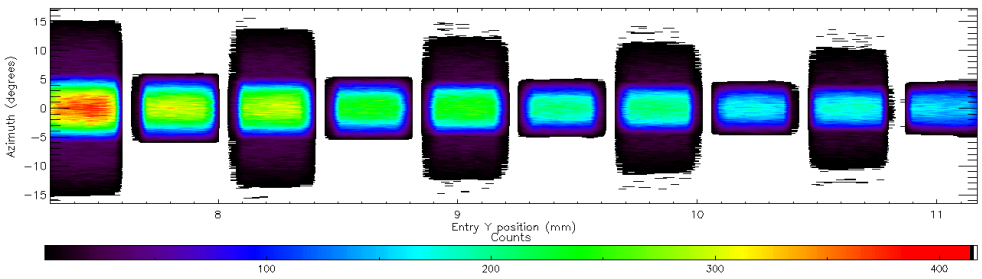

(e) All channels, entry z - entry y.

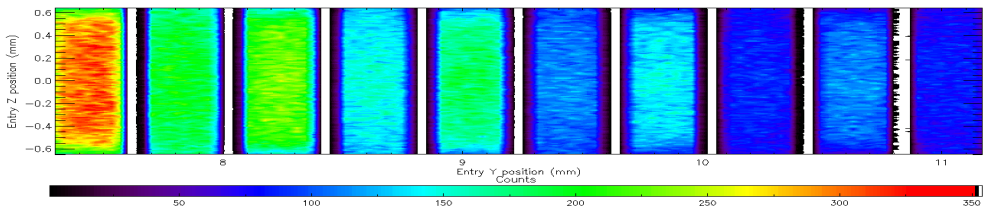

Figure 4.10c shows the elevation response for all channels and thus incorporates those already seen in figures 4.8g and 4.8h. With this histogram binning however, the hotspot features appears less pronounced. It can also be seen here how the elevation response for channel 10 is increased in accordance with its wider electrode spacing. Figure 4.10e, at the bottom, is analogous to the 2D area of the input apertures, showing that particles are accepted fairly uniformly across them with the geometric factor scalings that have already been discussed. This is consistent with theoretical studies which found that all areas of the exit apertures contribute approximately uniformly to the geometric factor [68].

The next set of graphs, figure 4.11, show histograms for the spatial dimension of the entrance aperture perpendicular to that shown in figure 4.10. Figure 4.11c shows that the particles in the extremes of the energy range in the I-channels enter only at the edges of the channels, closest to the side-walls, whereas sub-figure (d) shows that in the C-channels the opposite is true. The very lowest energy electrons in sub-figure (c) correspond to the suspected artefact tail and so can likely be disregarded.

The remaining spectrograms introduce, for the first time here, data from the CATS exit apertures. These allow the focussing properties of the analyser to be more closely investigated. Figure 4.12 shows spectrograms using the radial (x) dimension at the exit apertures and thus is very closely related with the radial (y) dimension at the input apertures shown previously in figure 4.10. On direct comparison the main difference that stands out is in figures (c), which reveal that some of the extreme elevations that could only be accepted from positions next to the outer and inner radii have become spread out along that dimension. If this were a full 127° analyser its focussing properties would ensure that figure 4.10c and figure 4.12c were the same [61].

Figure 4.13 shows the perpendicular spatial dimension of the exit apertures. These spectrograms are thus highly correlated with those in figure 4.11, and together these two sets of spectrograms provide insight into the azimuthal focussing behaviour of the analyser. Comparing first figures 4.13g and 4.11g it can be seen how the general outline of one is flipped with respect to the other. Since in the channel there is little contribution to the E field in this plane, so particles are largely undeflected in azimuth and consequently those with wider azimuth angles will track from one side of the

Figure 4.11: Plots comparing ch. 8 (I) and ch. 9 (C) entry z position distributions.

(a) Ch. 8–shaded red, ch. 9–blue line.

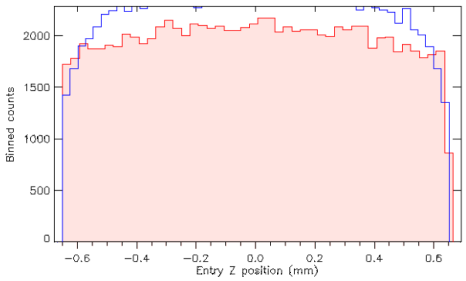

(b) Ch. 9–shaded blue, ch. 9–red line.

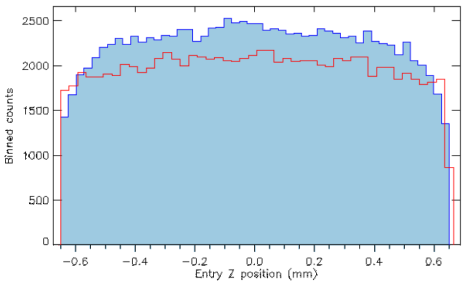

(c) Channel 8, energy - entry z.

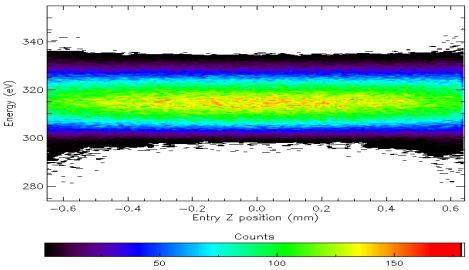

(d) Channel 9, energy - entry z.

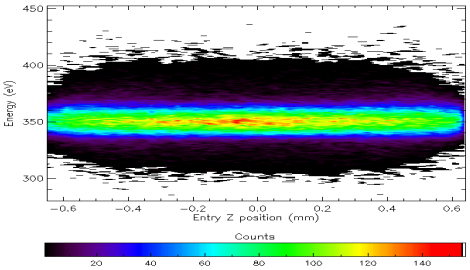

(e) Channel 8, elevation - entry z.

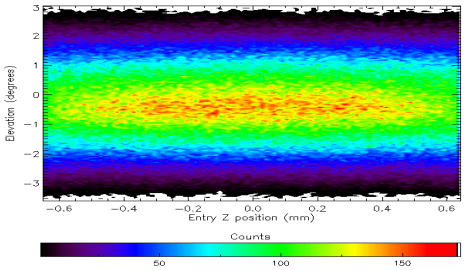

(f) Channel 9, elevation - entry z.

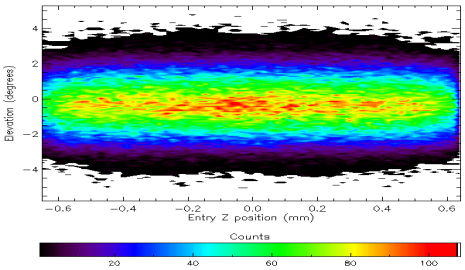

(g) Channel 8, azimuth - entry z.

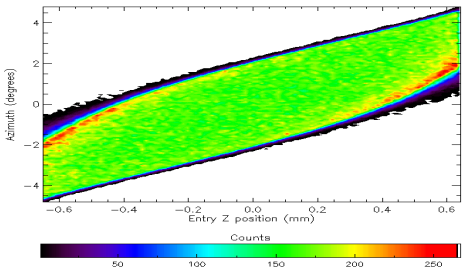

(h) Channel 9, azimuth - entry z.

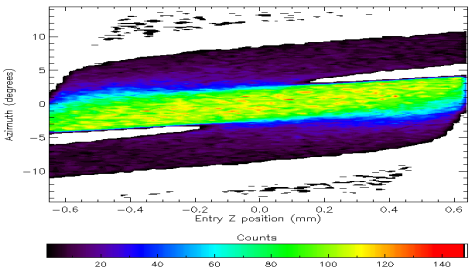

(i) Channel 8, entry y - entry z.

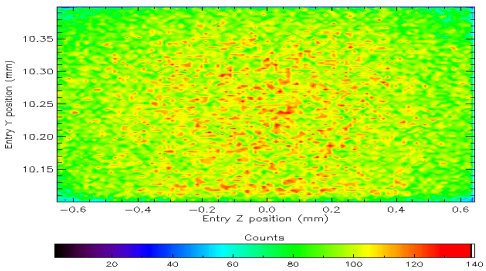

(j) Channel 9, entry y - entry z.

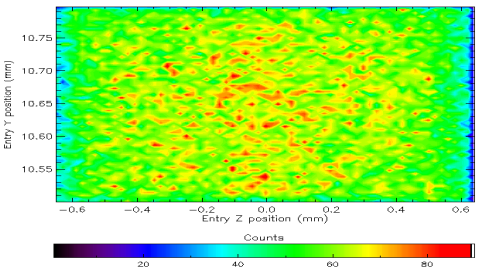

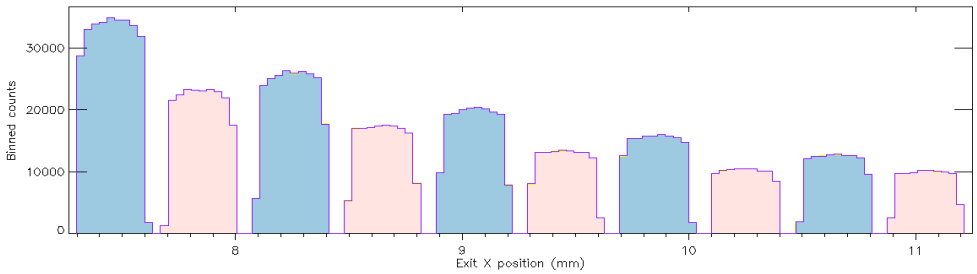

(a) All channels, exit x distribution histogram.

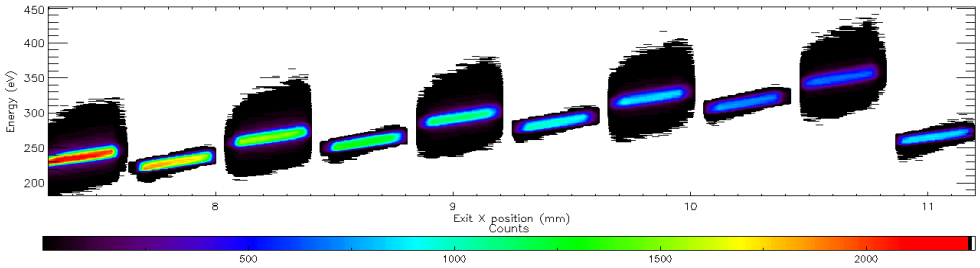

(b) All channels, energy - exit x.

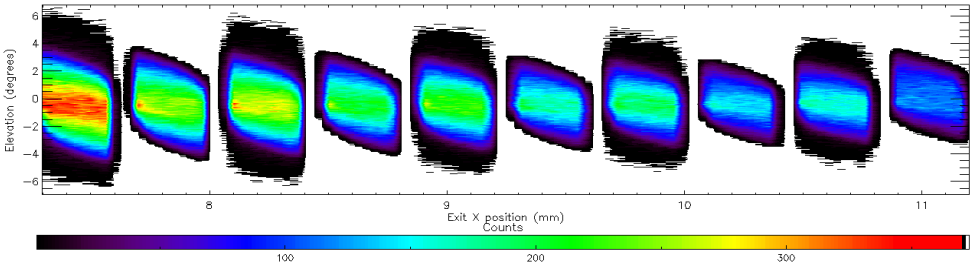

(c) All channels, elevation - exit x.

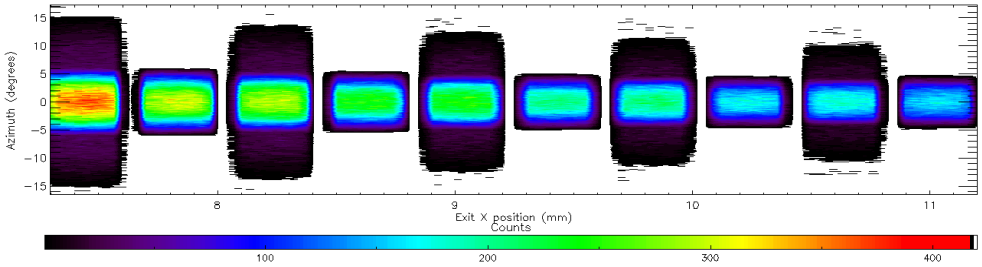

(d) All channels, azimuth - exit x.

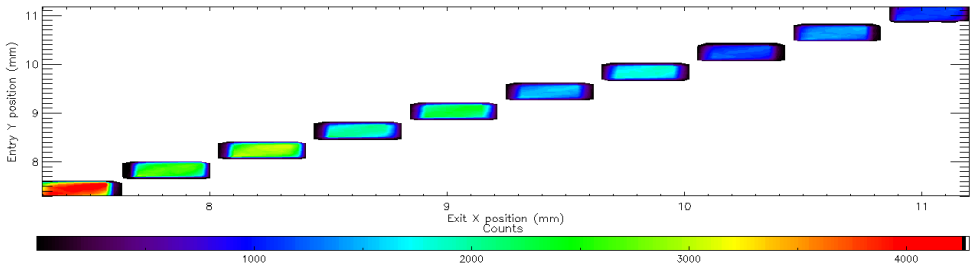

(e) All channels, entry y - exit x.

Figure 4.12: Spectrogram plots comparing exit x position distributions.

Figure 4.13: Plots comparing I-ch. (8) and C-ch. (9) exit z position distributions.

(a) Channel 8, exit z histogram.

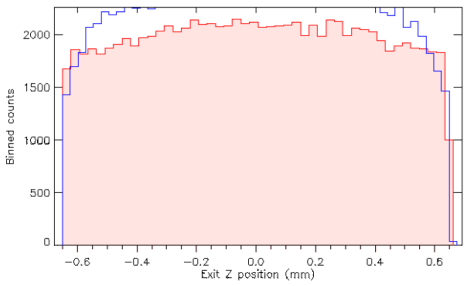

(b) Channel 9, exit z histogram.

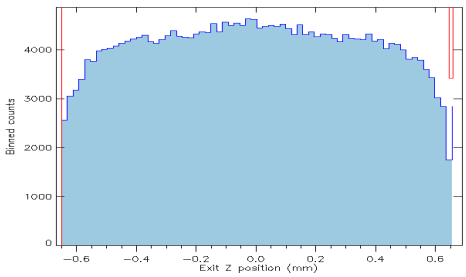

(c) Channel 8, energy - exit z.

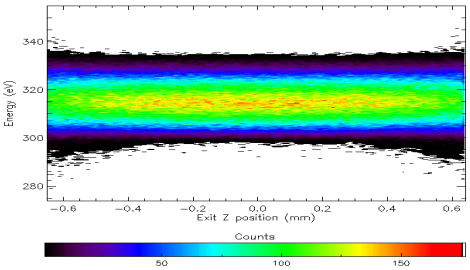

(d) Channel 9, energy - exit z.

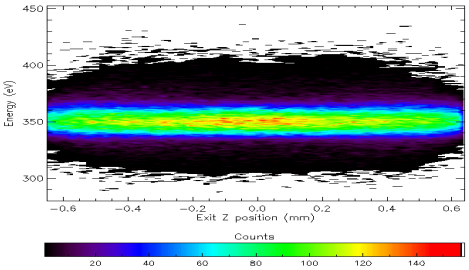

(e) Channel 8, elevation - exit z.

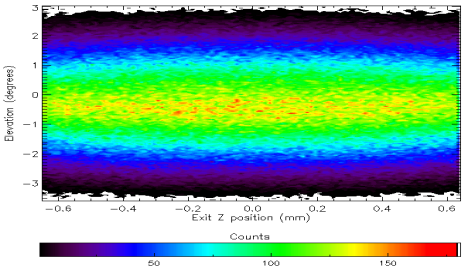

(f) Channel 9, elevation - exit z.

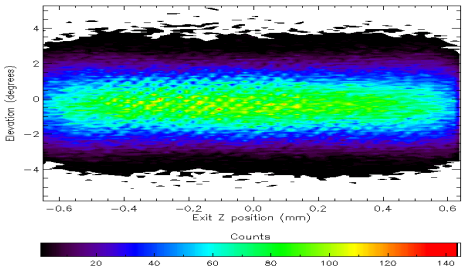

(g) Channel 8, azimuth - exit z.

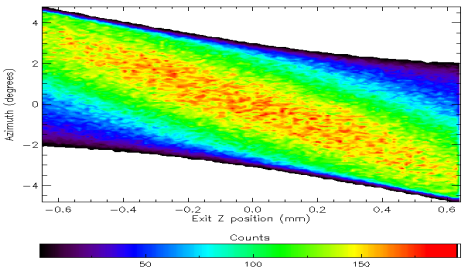

(h) Channel 9, azimuth - exit z.

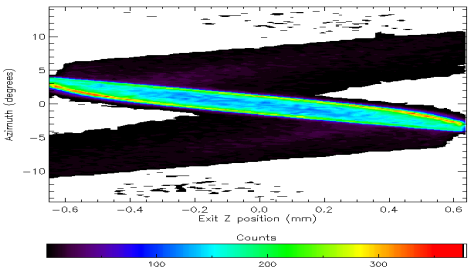

(i) Channel 8, entry z - exit z.

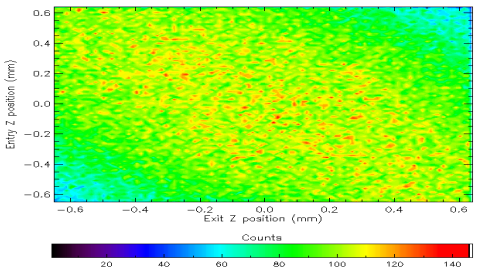

(j) Channel 9, entry z - exit z.

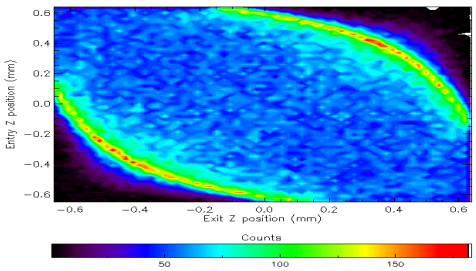

entrance aperture to the opposing side of the exit aperture. In the C-channel 9, things are a little different, as can be seen by comparing figures 4.13h and 4.11h. The central section from -5° to 5° azimuth is flipped in a similar way as we have just seen with channel 8, but the extreme azimuth wings appear not to have flipped. In fact they have flipped twice, as these wings correspond to particles that have been mirrored by the repellent C-channel walls. The most extreme azimuths $> |10|^\circ$ however have been mirrored three times within the C-channel so their azimuth spectrogram also appears to be reversed.

Figure 4.14 shows the intensity footprint of the particles as they would fall on a detector placed immediately at the exit apertures in (a) and at approximately 3 mm from the apertures in (b). The latter shows that at 3 mm the outer edges of the channels are overlapping. This is investigated further in figure 4.15, which shows that adjacent channels begin to overlap at CATS-detector separations between 1 and 2 mm

Since adjacent channels are alternately electrons and ions however, and most detectors would not detect both simultaneously, this channel overlap is unlikely to cause real-world problems.

4.3.3 Conclusions

Considering the I and C-channels separately, the simulation results have shown what would be reasonably be expected:

- K-factors vary according to the radius and channel gap in keeping with the approximation in equation 3.1
- Where channel path lengths increase and the apertures stay the same size, the geometric factors decrease.
- Geometric factors are small compared with the instruments discussed in the opening chapters.
- Energy and angular resolutions are comparable with existing instruments.
- Where the gap widens in channel 10, so the elevation acceptance increases.
- Positive elevations are associated with higher energies and negative with lower.

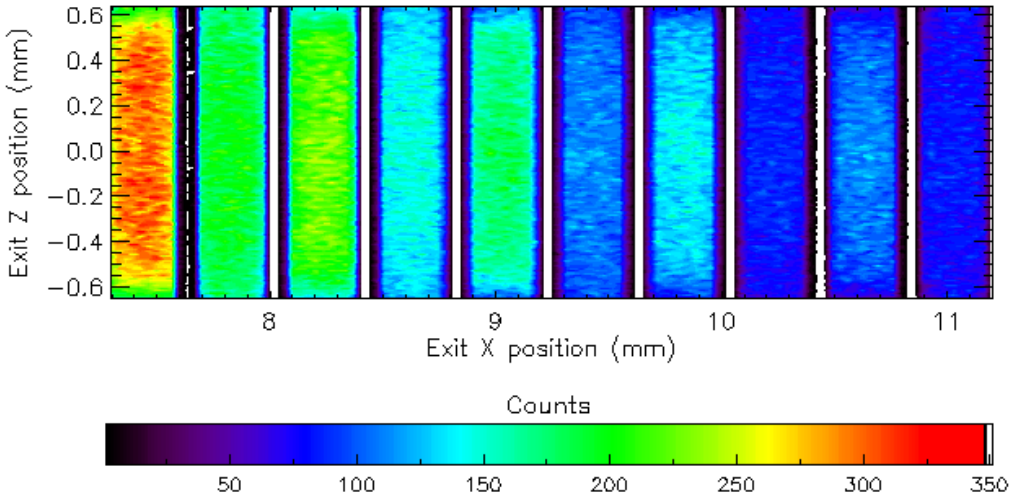

(a) Particle footprint at CATS exit aperture (to scale)

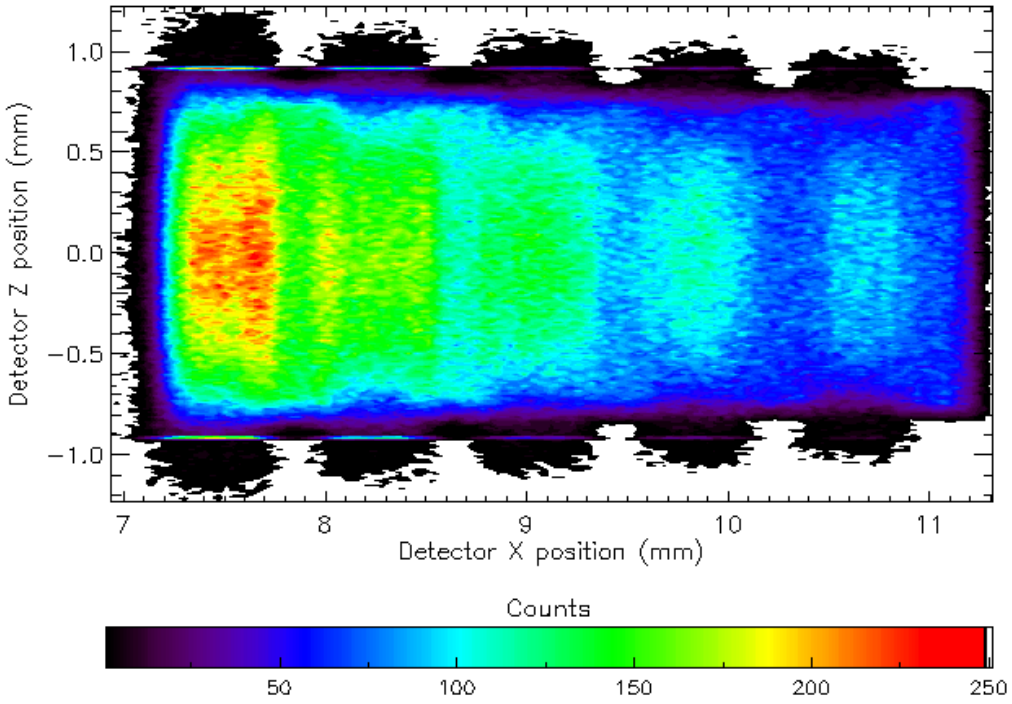

(b) Particle footprint 3mm from aperture (to scale).

Figure 4.14: Particle footprints at CATS exit apertures for all 10 channels

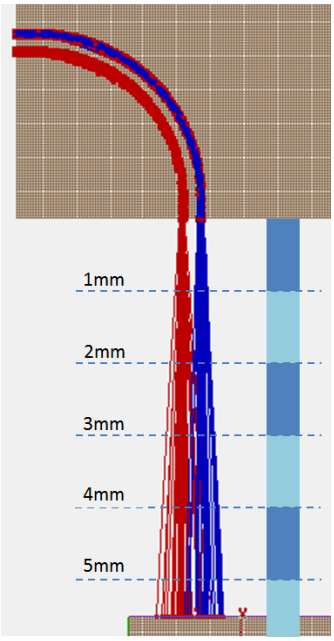

Figure 4.15: Divergence of trajectories from adjacent channels as they exit the analyser.

- Larger radius positions within a channel are associated with higher energies (again in correspondence with equation 3.1)

Unlike a top hat, CATS has been shown to have only partial beam focussing properties, but the discrete channels mean this is not requirement.

Of most interest from the results discussed in the previous section, is the difference between the I and C-channels. In general it can be said that I-channels are more precise and uniform, whereas C-channels transmit greater numbers of particles. The C-channels also have marginally higher K-factors. I-channels should be chosen where a regular and precise response is more important than a high throughput, and C-channels in the reverse scenario.

The I-channels' precision is achieved by the rejection of the more extreme angles, and thus also the rejection of the more extreme energies, due to their attractive side-walls. The C-channels greater acceptance is not solely due to their longer and broader distribution tails, the repellent side-walls also increase the particles at the peak.

This therefore allows for a third way. If collimators are applied to the C-channels the extreme angles can be cut out and the high central peaks maintained. Figure 4.8d has shown that collimating in elevation will result in a slight reduction in energy range.

Figure 4.9d has shown that a collimation in azimuth can offer a significant reduction in energy range, but only if the collimation is severe and only the central azimuths are admitted. This would also have the consequential effect of narrowing the elevation response so it became similar to that of the I-channels' as determined from figure 4.8f (and figure 4.8e).

CATS was not designed to meet specific requirements for parameters. The intention was to experiment with a miniature geometry that could be adjusted and optimised to meet a specific requirement. To this end I created a system to automatically and rapidly model, simulate and optimise CATS-like analysers to address specific requirements.

4.4 Creating highly automated simulations

The automated system consists of extensions to the IDL tool-kit described in section 4.1.4. These extensions allow for programmatic control of the geometry file of a single CATS channel. This includes changing truncation angle, curvature radius, depth, height, and side-wall characteristics. An automated trial and improvement routine was then applied to the input electron parameters to optimise the simulation, which was then run on loop as has been described in previous sections. The process, and a proposed extension to it is summarised in figure 4.16.

The simple idea was not trivial to implement, involving many coordinate transformations and optimisation algorithms to allow it to fit within the rest of the IDL analysis tool-kit.

In its current implementation however, the system only allowed for relatively large-sized grid units (low resolutions). Consequently it was used only for quick tests and for rough parameter estimates when brainstorming designs for the TechDemoSat CHAPS instrument. It has proven the method though and higher resolutions could be implemented with some recoding.

Some of the CATS-related tests investigated how the variation of the truncation angle and Matsuda plate configuration affected the instrument parameters. The results can be seen in figure 4.17. The x-axis shows the differing Matsuda plates. At 0% they are I-channels and as x increases, the outer radius channel starts to grow a lip that starts

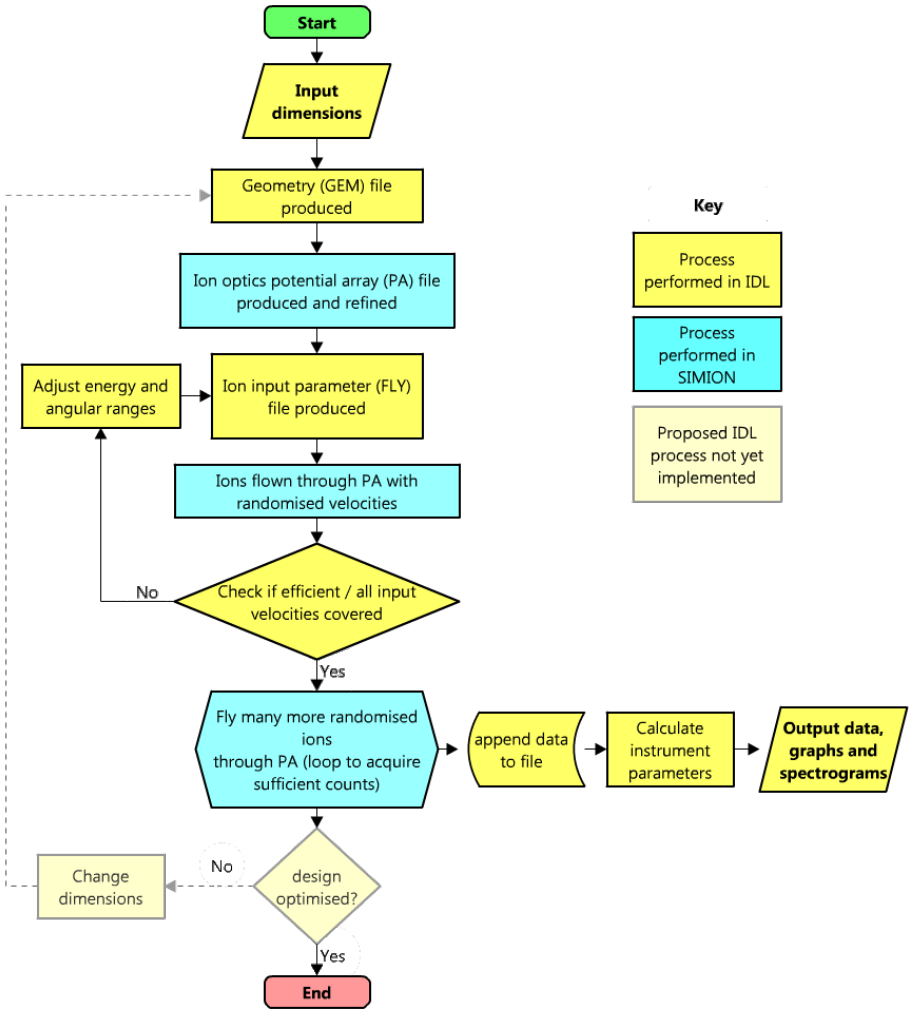

Figure 4.16: Flow chart of highly automated simulation system [14]

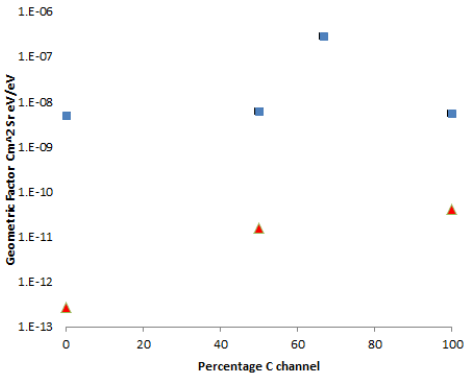

(a) Geometric factor variation from I-channel to C-channel.

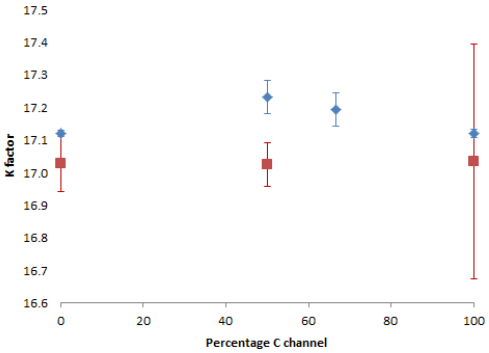

(b) K-factor variation from I-channel to C-channel.

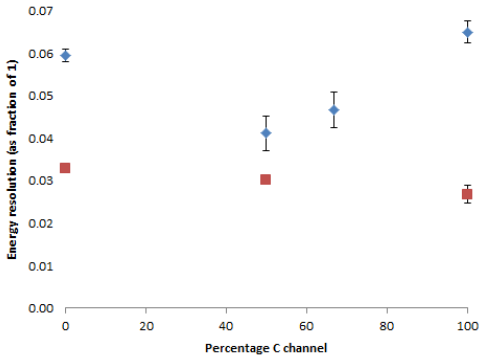

(c) Energy resolution variation from I-channel to C-channel.

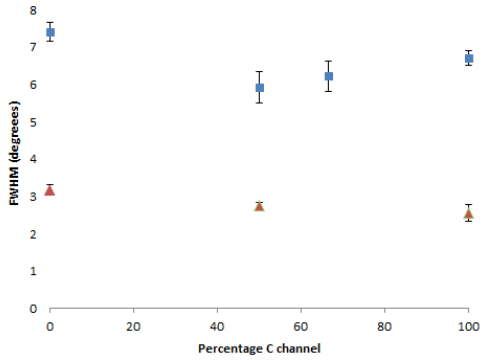

(d) Azimuth FWHM variation from I-channel to C-channel.

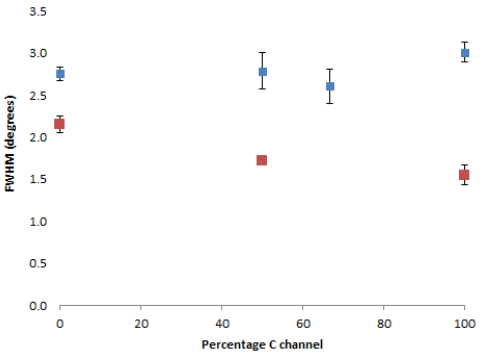

(e) Elevation FWHM variation from I-channel to C-channel.

Figure 4.17: AutoGEM results for I-channels, C-channels and hybrid 50:50 channels. Blue results are for 90° truncation angle, red results are for 180° truncation angle. Dimensions are similar to channel 10 and resolution is 25 µm/grid unit.

to displace the Matsuda plate so that by 100% a C-channel is created (figure 4.18). The

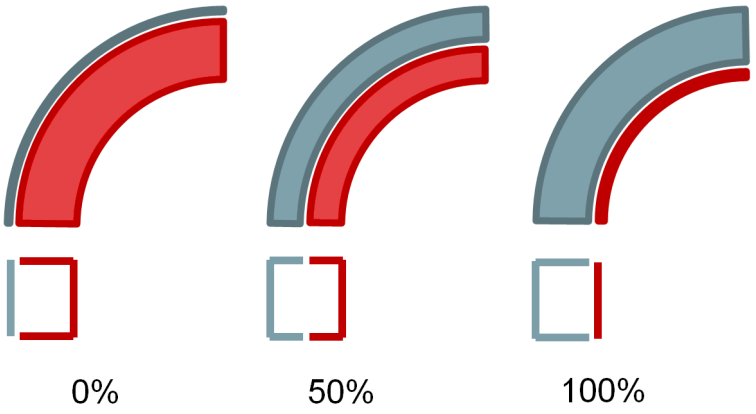

Figure 4.18: Percentage C channel; channels seen from above and end-on.

red and blue dots refer respectively to 180° and 90° truncation angles. The analysis routines used for this data were sub-optimal compared with the simulations discussed in previous sections, creating large errors in places. With these limitations in mind, the main message that this figure conveys is that the C and I-channel effects are smaller than the effects of a 90° degree addition to the truncation angle.

4.5 Summary

The SIMION charged particle optics software and my IDL tool-kit for it have been introduced and have been shown to be accurate. CATS has been simulated with a reasonable geometry resolution and with a very large number of particles in a Monte-Carlo type simulation. This provides a comprehensive set of baseline results against which the experimental work can be compared. It also produced highly detailed spectrograms providing insight into the focussing properties of the analyser and to the differing natures of the I and C-channels: I-channels being more precise and uniform in their acceptance responses, and C-channels having higher throughput (greater sensitivity). Collimation options were discussed that would allow a compromise between the two to be reached and an automated simulation system was discussed for further refining the design.

Simulation results based on the design drawings are only ever an ideal-world result.

Experimental results are essential to tune them to reality and such will be the topic of the next two chapters. With a theoretical understanding of CATS established, the thesis now looks to the laboratory work involved in testing the prototype. The starting point for this is the development of appropriate detectors, the subject of the next chapter.

Chapter 5

Detector Development

This thesis so far has discussed the design and theoretical performance of the CATS analyser head. This chapter describes the detectors which convert the particles exiting the analyser into electrical signals that can be processed further. Charged particle detectors have been briefly introduced in section 1.5. In this chapter the CEM and CCD detectors that have been used with the CATS analyser head are discussed in more detail along with the MSSL electron instrument calibration facility where they have been used.

The CCD work described herein has also been published in the Journal of Instrumentation [13].

5.1 The MSSL electron instrument calibration facility

To calibrate and test electron analysers, MSSL have a purpose built calibration facility [67, 85]. It is based on the setup discussed by Marshall et al [89] and consists of a vacuum chamber with an electron flood gun at one end and a platform with two motorised axes of rotation at the other and is depicted schematically in figure 5.1.

The (mercury vapour) UV lamp shines 254 nm wavelength photons onto a photo-cathode. The photo-cathode is a quartz disc that is coated with a thin layer of gold/chromium that has a work function closely matched to the wavelength of the UV photons from the lamp. Accordingly when the lamp is shone on the coated disc,

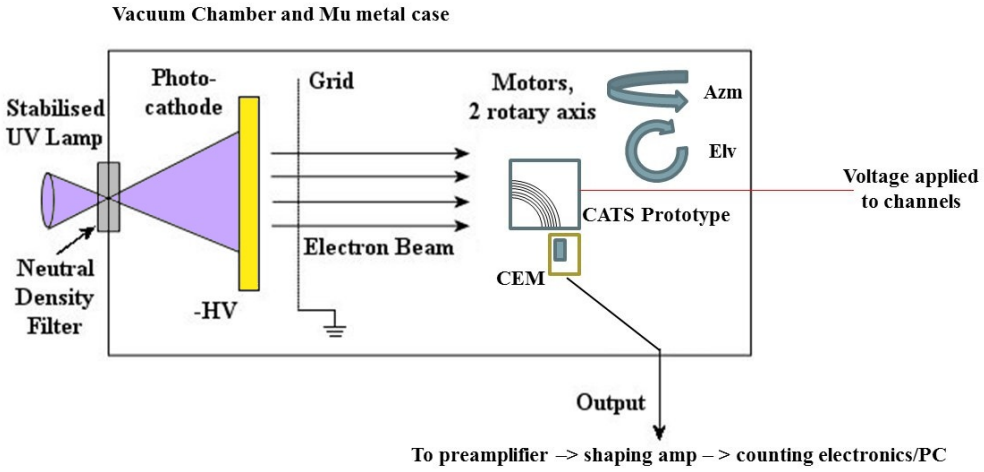

Figure 5.1: Schematic of lab chamber setup (as viewed from bottom looking upwards).

photoelectrons with negligible kinetic energies are produced. A negative high voltage is applied to the metallic layer on the disc so that the photoelectrons are accelerated towards a high-transmission, electrically-grounded grid mounted in front of and parallel to the photo-cathode. Electrons that pass through the grid then drift towards the instrument under test as a monoenergetic flood beam, orthogonal to the photo-cathode and to the grid. The energy of the electron beam can be varied by changing the voltage on the photo-cathode and the intensity can be changed with neutral density filters. The instrument that is being tested is mounted at the centre of the beam on rotary stages with axes of rotation passing through this central point. Rotating the stage allows the beam to enter the instrument from different angles to allow a full angular calibration. While for studying the energy response of the detector, the voltage on the photo-cathode can be varied to vary the energy of the electrons, for studying the energy response of the CATS analyser head, it is preferable to use a fixed energy electron beam and to instead vary the voltage on the analyser electrodes. In this latter way the beam profile and detector response are constant.

5.2 CEM setup

The first detector to be used with CATS was a Dr Sjuts KBL408 CEM, which was mounted in a specially designed aluminium box, shown in figure 5.2.

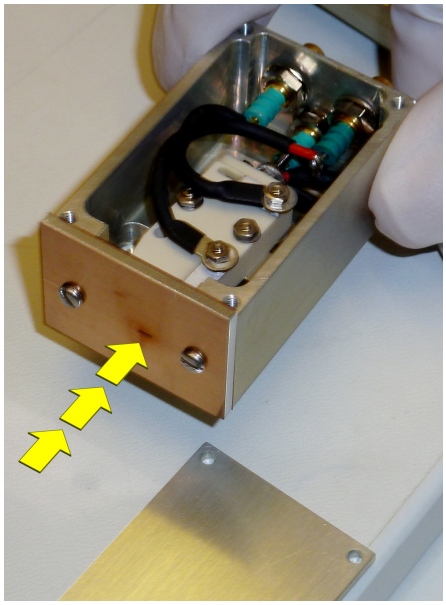

Figure 5.2: CEM mounted in an electrically grounded box with laser cut aperture/collimator. Yellow arrows represent where an electron beam would be incident on the aperture.

The box conceals the high voltage electrodes and a mask with only a small hole restricts the CEM input aperture to that of a single CATS channel, as illustrated in figure 5.3.

Initially just a single thin laser-cut mask was used to reduce the aperture size. When it was determined that particles from extreme and unwanted angles were also entering, a second mask was added with a thicker aluminium spacer between to create angular collimation. It will be seen later that this was only partially effective.

The CEM box was attached to a specially designed translation stage shown in figure 5.4. The micrometer adjuster allows the CEM to be translated back and forth so it can be positioned in front of different CATS apertures. CATS was mounted to the baseplate of the translation stage, in front of the CEM, and the whole assembly was mounted on the motorised rotary stages in the vacuum chamber of the calibration facility.

To operate, the CEM requires a high potential difference across it, with the more negative of the two terminals at the entrance aperture. As the potential difference across a CEM is increased from zero, the CEM's output charge pulse for each incident particle increases. Once this gain become high however, the large cloud of electrons produced at the output has sufficient space charge density to retard electrons further up

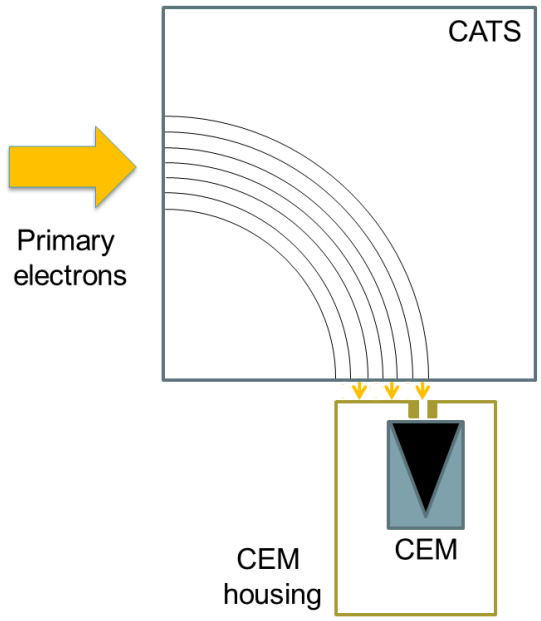

Figure 5.3: Schematic representing how the CEM housing was designed to isolate the CEM to individual CATS channels

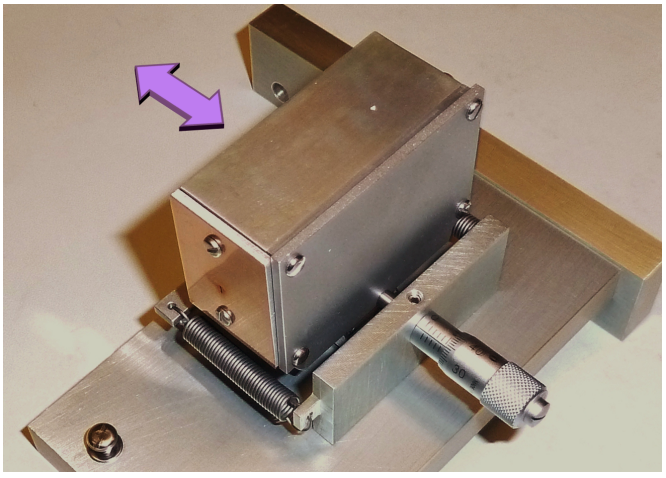

Figure 5.4: CEM on translation stage, purple arrow marks direction of translation.

the CEM. This retarding effect reduces the number of secondary electrons released by the CEM and thus a dynamic equilibrium is reached and above a certain (saturation) voltage the charge pulse size (gain) does not increase [79]. To prevent gain droop at high count rates [133] the potential across the CEM was typically set to ∼1600 V, ∼50 V above the knee of the counting rate plateau (see figure 5.5).

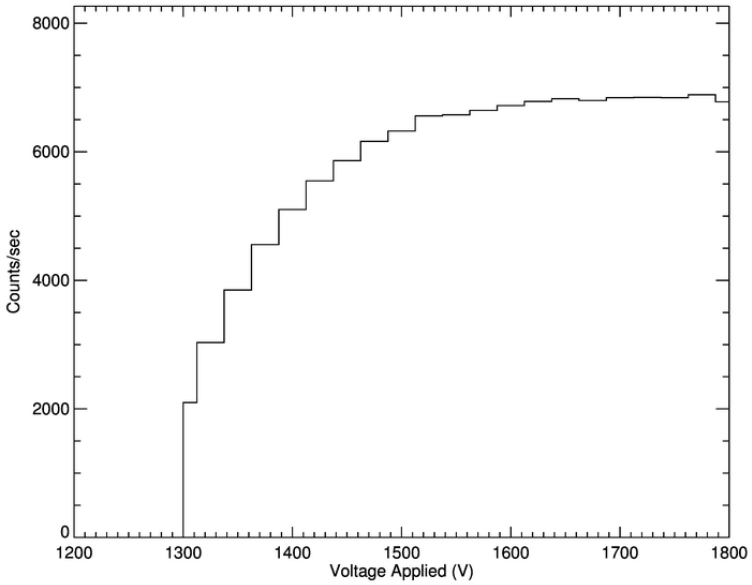

Figure 5.5: Number of particles detected at the CEM as a function of the voltage applied across its terminals with a constant beam. 1600 V was selected for operational voltage.

The potential of the CEM entrance can be used to accelerate, retard or repel incoming charged particles, as mentioned in section 1.5.2. This was held at 125 V to provide an accelerating potential for the lower beam energies (e.g. 30 eV) and kept at that voltage for the higher energy tests to keep the CEM gain constant. This does mean that secondary electrons are also attracted into the CEM, but these are only considerable in number in the highest energy (keV) electron beams. The front potential was achieved by connecting the front CEM terminal to ground through a Zener diode with a breakdown voltage of 125 V in reverse bias (figure 5.6).

At the back end, the anode was biassed to be the most positive of the three CEM terminals; this bias was applied through an Ortec 142 pre-amplifier which was located outside the vacuum chamber. The preamp capacitively decoupled the high bias voltage

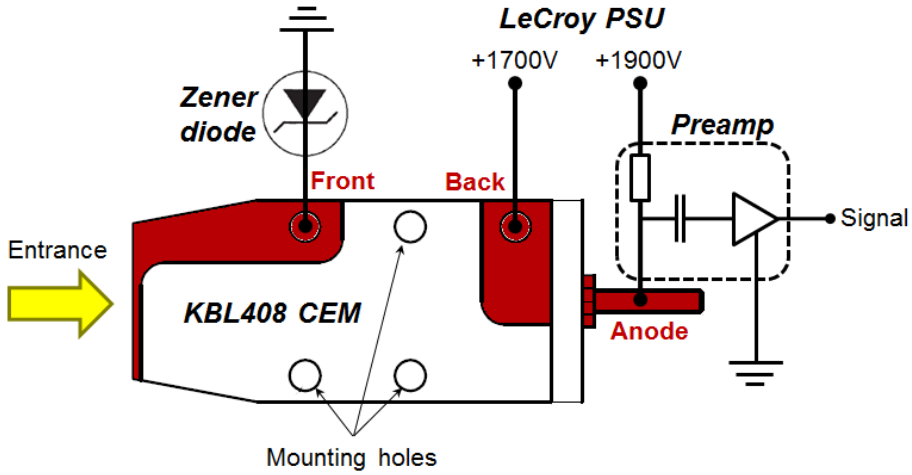

Figure 5.6: CEM electrical setup (typical), electrodes marked in red.

from the signal charge pulses, which were amplified as long tailed voltage pulses. This voltage pulse was sent to an Ortec 572 shaping amplifier where it was further amplified and shaped into a shorter more uniform pulse. The shaped pulse was sent to an Ortec 406A single channel analyser (SCA) which acted as a threshold discriminator, removing the lowest amplitude pulses which were known to be noise. The SCA output was connected both to a counter (for diagnostic and monitoring purposes) and to a data-logging PC running MS DOS.

The results obtained from using CATS+CEM have been very valuable in the insight they gave to the performance of CATS and will be discussed in chapter 6. The setup was subject to fundamental flaws and constraints however, including;

- The CEM position could not be adjusted without venting the chamber and then pumping down again. This required several hours, involvement from facilities staff, and could change the CEM response and beam intensity.
- It could not always be known with great precision which of the CATS channels the CEM was positioned in front of, or if it was positioned between two channels. Since the K-factors measured did not match the simulation results[1] they could not necessarily be identified by this method either.
- The aperture/collimator was not entirely effective in screening out secondary

[1]Which will be described in section 6.2 in the next chapter.

electrons from other channels.

Figure 5.7 shows CEM spectrograms (beam entry elevation against voltage applied to CATS analyser fin electrodes) taken with, and without, the collimation and improved foil covering. Although the CEM positions are slightly different, it can be seen that the background counts are greatly decreased and that only the directly neighbouring channels are visible. The background reduction is attributable to the improved foil covering, which prevented electrons entering the gap between CATS and the CEM box at low elevation angles. The neighbouring channel reduction is attributable to the collimator which denied CEM access to electrons approaching from wide angles.

At higher beam energies and over longer acquisitions however, all channels were still visible, even with collimation (figure 5.8). This did though allow all the C-channel K-factors to be approximated.

To resolve some of the issues listed above, and to learn more about CATS, a position-sensitive detector was required. The first detector I tried to set up for this purpose was an MCP.

5.3 Position sensing with an MCP

MCPs have been previously introduced in section 1.5.3. To take position-sensitive measurements with them, a position-sensitive anode system is required.

5.3.1 Discrete anodes

Top hat instruments typically achieve this with a discrete anode arrangement. For this, the area under the MCP is divided into separate anodes each of which is electrically isolated from each other and each of which has its own chain of amplification electronics. The requirement for these multiple chains of electronics usually restricts the number of discrete anodes. To enhance the accuracy of the position sensitivity, fine zone anodes can be added. These form comb structures with the other (coarse) anodes so that the charge is split between them. Providing particles are not arriving simultaneously at the detector, the amplification chains for the fine zones can be shared. This is demonstrated

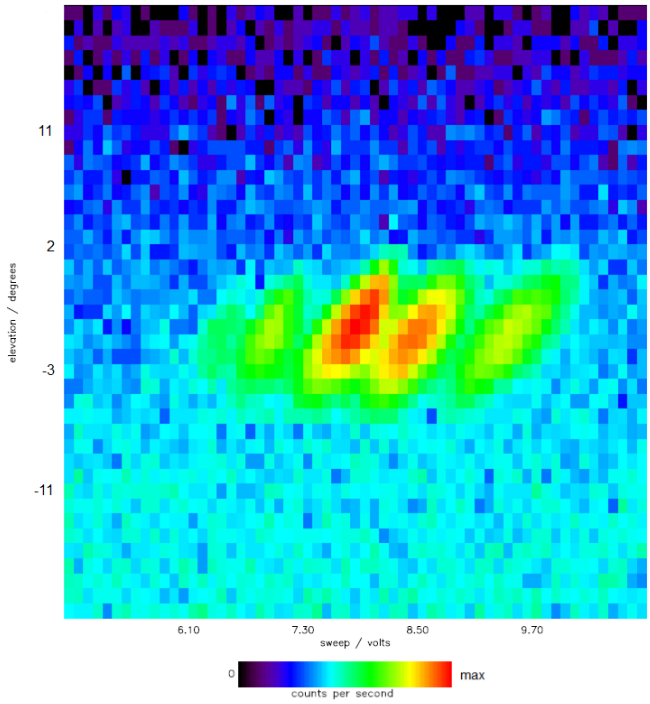

(a) Before collimation and improved foil covering fitted, CEM approximately centred on 5, channels 1,3,5,7,9 visible.

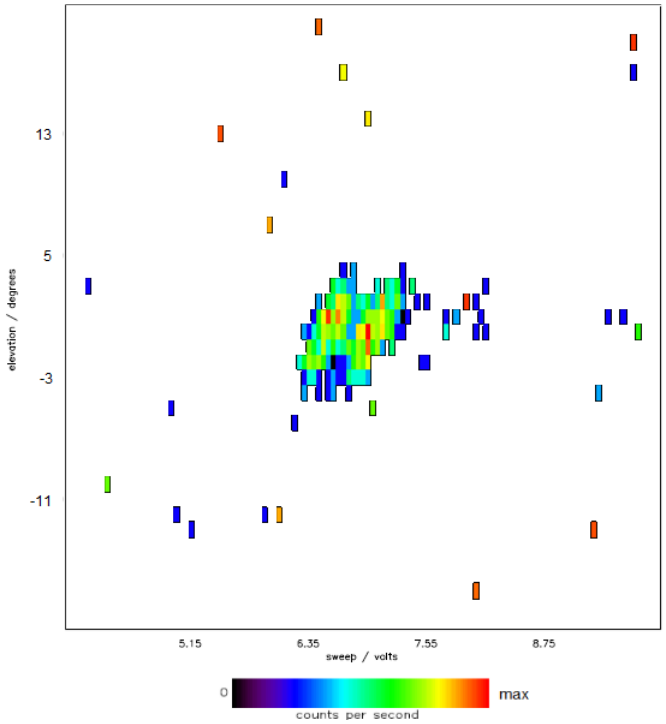

(b) After collimation and improved foil covering fitted, CEM centred on channel 8, channels 7 and 9 visible.

Figure 5.7: 100 eV electron beam, elevation - CATS electrode voltage scans before and after CEM collimator fitted.

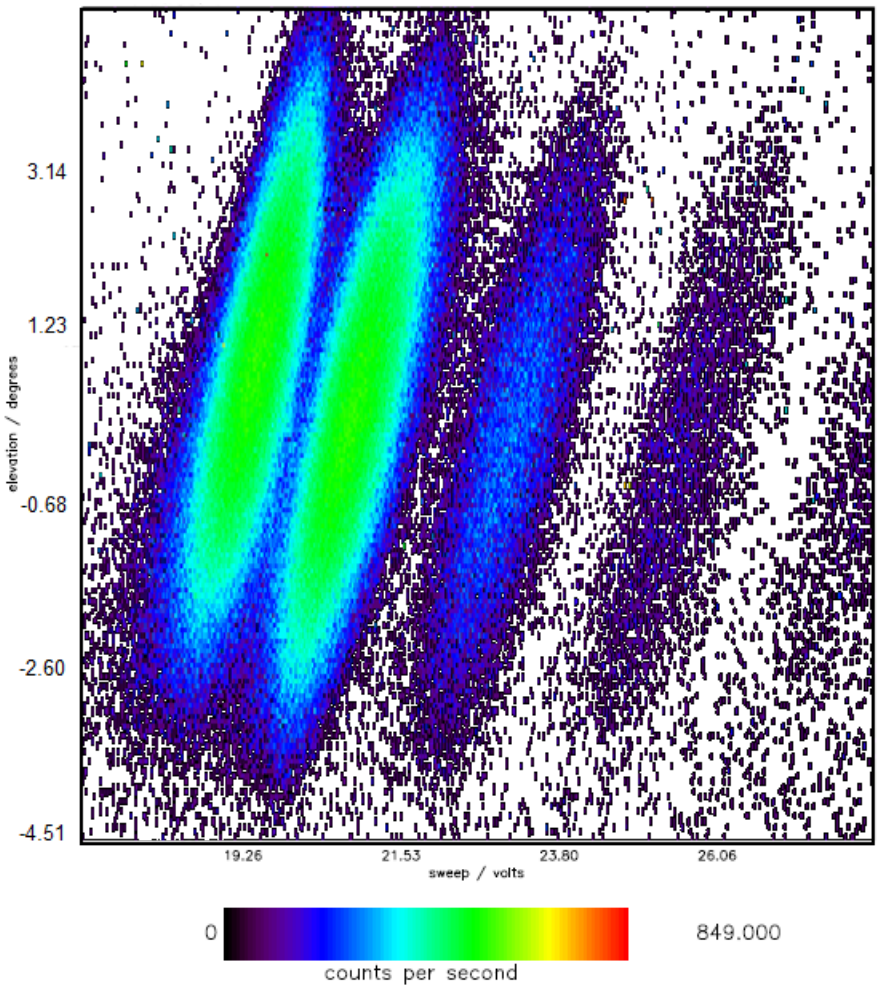

Figure 5.8: 300 eV electron beam, high resolution elevation - CATS electrode voltage scan, zoomed in relative to figure 5.7. CEM centred on channel 8, channels 1,3,5,7,9 visible.

in figure 5.9 which shows the coarse and fine zone MCP anode structure used for the PEACE instruments on Cluster [67].

A custom made discrete anode arrangement would be ideal for a CATS-based flight instrument, especially if implemented with the dual particle detecting format shown in 1.19.

For this experimental prototyping however, an imaging anode system is more attractive as it allows the details within the channel, the electron footprint, to be studied.

5.3.2 Imaging anodes

Several options exist for MCP imaging anodes. Resistive anodes allow the position of an incident charge pulse to be triangulated by comparing the pulses measured at different points across it (figure 5.10) [80].

Delay line anodes consist of a mesh of wires. Time differences in charge pulse arrival times at different ends of the wires are used to determine the position of the charge cloud causing it. Such anodes were used on the UVCS and SUMER instruments on the SOHO satellite [115].

Wedge and strip anodes [90] are designed so that the proportion of charge that falls on the wedge (W) anode varies across one dimension of the detector and the proportion of charge that lands on the strip (S) anode varies across the other dimension of the detector (see figure 5.11). The gap between the wedge and strip anodes is filled with the Z anode that picks up the rest of the charge cloud. This is required so the total charge of the cloud can be known. By measuring the proportion of charge detected on each anode the 2D position of the charge cloud from the detector can be determined from the equations below.

$$x = \frac{S}{S+Z} \tag{5.1}$$

$$y = \frac{W}{W+Z} \tag{5.2}$$

Such anodes have been used on instruments such as FONEMA [63] and it was one of the detectors developed for FONEMA that was available for use with CATS.

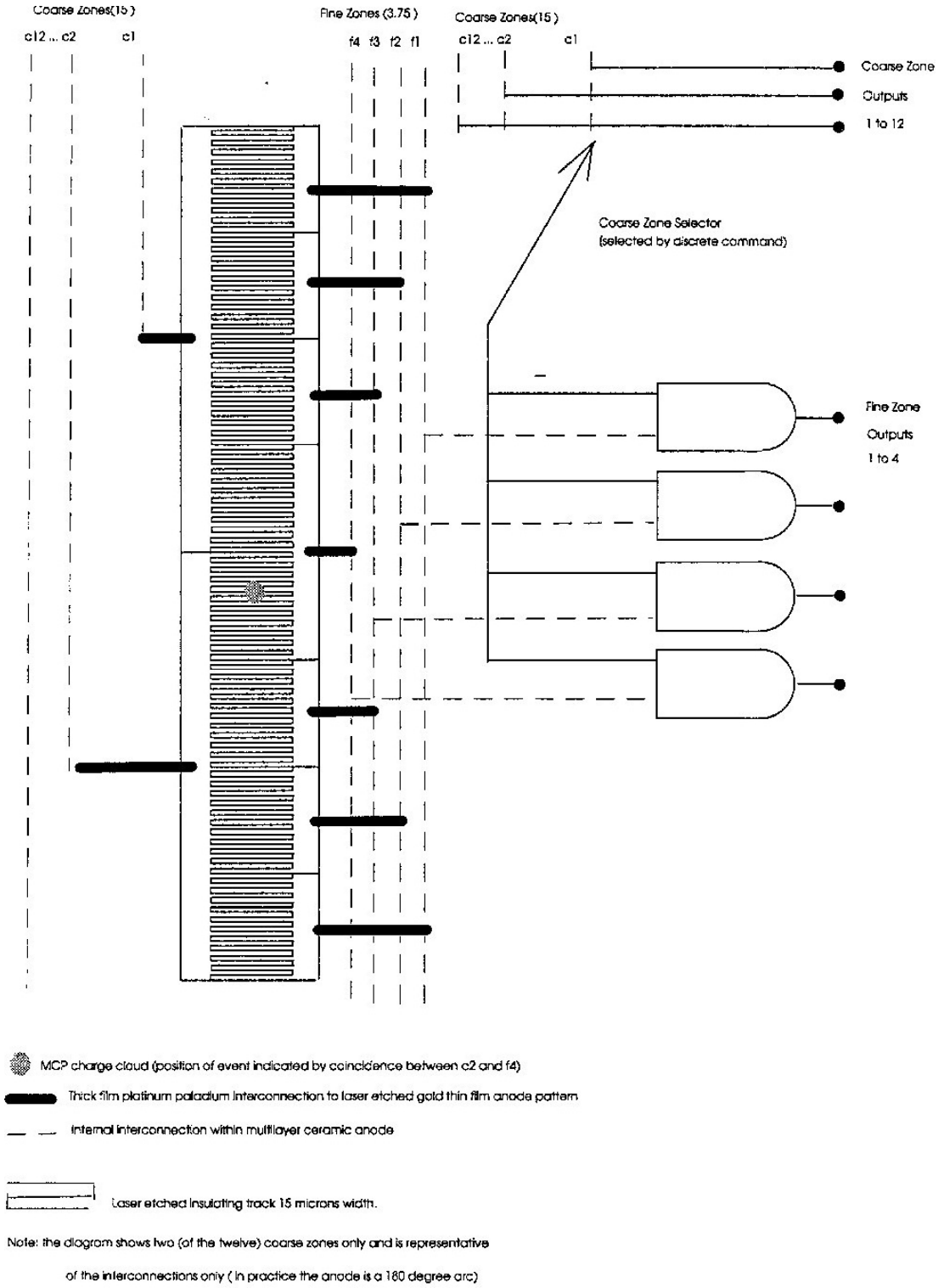

Figure 5.9: Discrete MCP anode arrangement for Cluster PEACE instruments, showing coarse and fine zone anodes and interconnections for amplifier sharing [67].

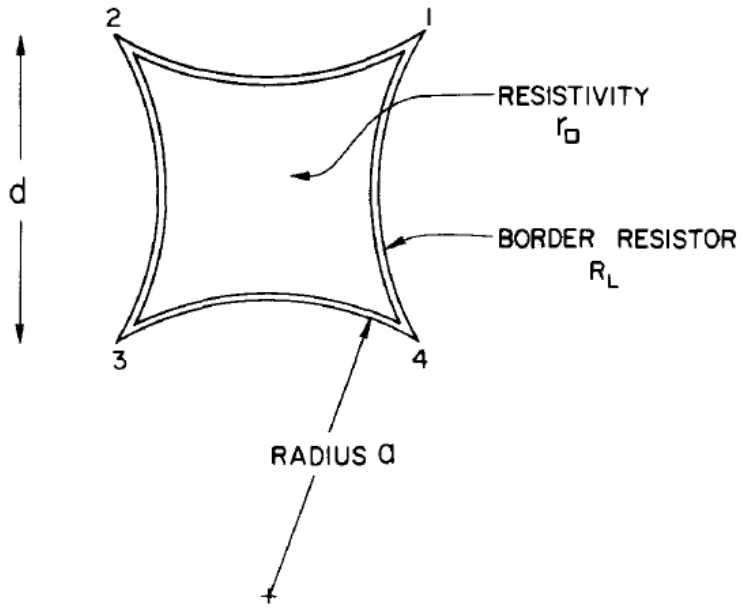

Figure 5.10: A distortion free resistive anode, consisting of 4 arcs of radius a. The charge cloud position is calculated from the ratios of the charge pulses measured at 1,2,3 and 4 [80].

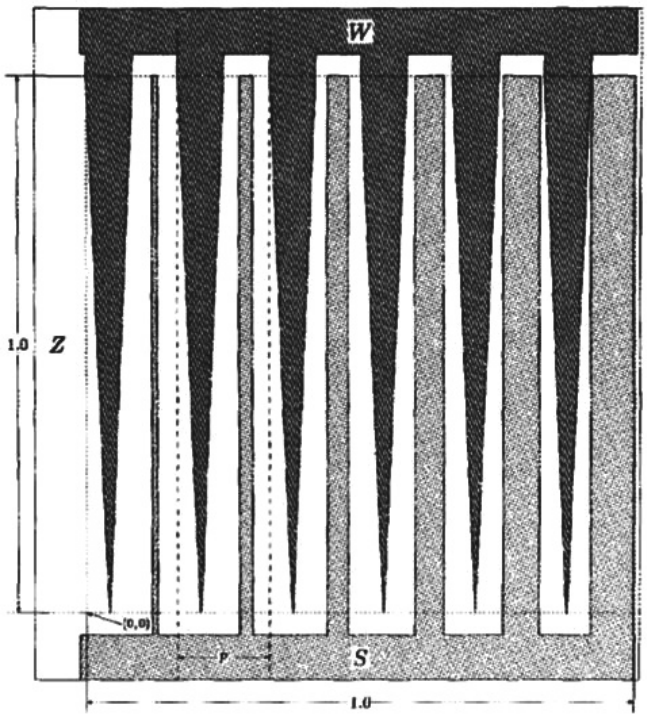

Figure 5.11: Wedge and strip detector anode [117] .

5.3.3 Experimental setup

The FONEMA detectors had been previously re-purposed as Tsunami, a radiation detecting experiment, which I dismantled to reveal the MCP in figure 5.12.

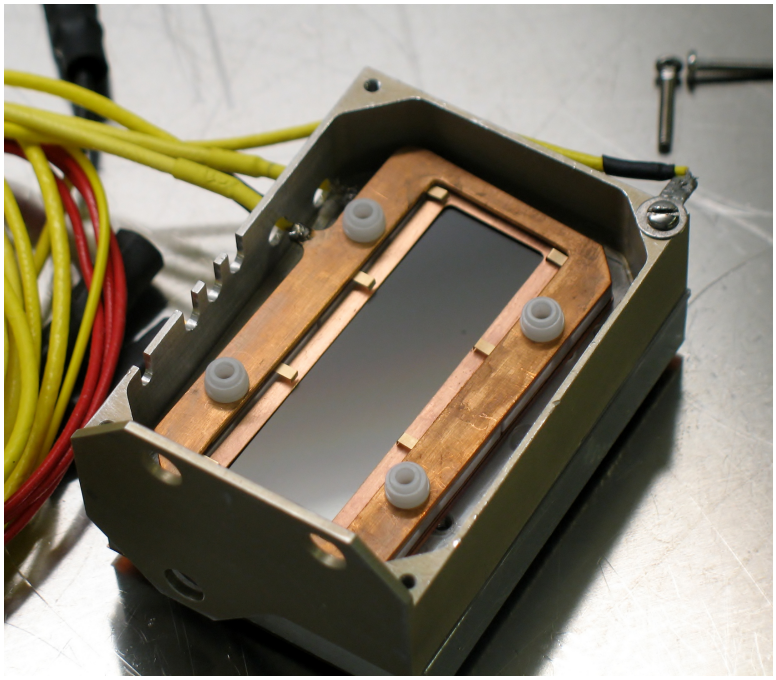

Figure 5.12: FONEMA MCP in Tsunami detector mount.

The wedge and strip anode mounted behind the MCP is shown in figure 5.13

The anode outputs (black wires in figure 5.13) were connected to Ortec pre-amplifiers, amplifiers and shapers like in the CEM setup discussed previously, however instead of passing to a single channel analyser they were connected to digitisers in a National Instruments PXI computer crate. A LabVIEW script was run on the crate to extract the pulse heights of the digitised pulses and to triangulate the position according to the formula.

Unfortunately this setup could not be made to work, it was thought that the anodes had become too tarnished over time, and would take a lot of work to be remade.

In the absence of another suitable anode or MCP setup, a new experiment was proposed.

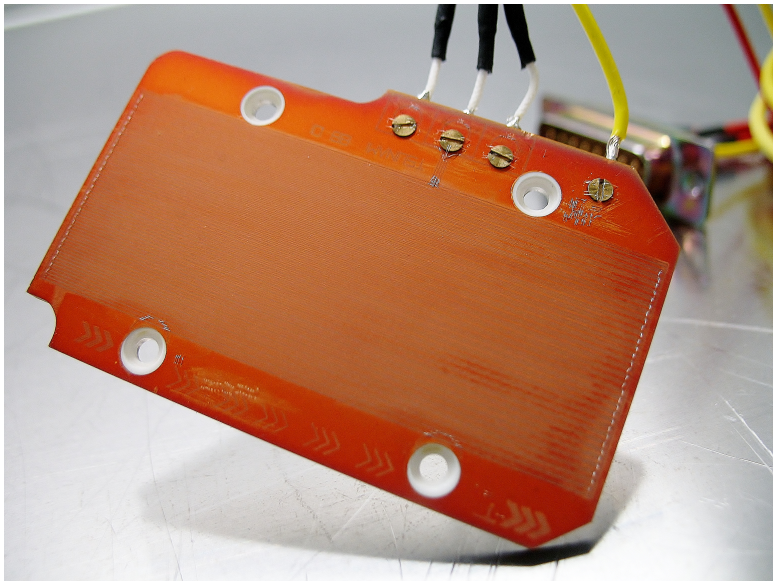

Figure 5.13: MCP wedge and strip anode from spare FONEMA detector

5.4 Direct detection of electrons with a CCD

As mentioned in section 1.5.4, while CCDs are more conventionally used to detect photons, their electron-detecting capabilities have been well documented [30, 120]. When an ionising particle is incident on the CCD detector, it penetrates into the silicon and deposits energy in the form of electron-hole pairs (transferring an average energy of 3.64 eV per pair [42]) until it has lost all of its energy. The electrons in these electron-hole pairs I refer to from here as 'generated electrons'. The generated electrons created are collected in the potential wells of the gate electrodes on the CCD front surface. It has been found that a standard front-side illuminated CCD makes a very poor electron detector, since firstly the gate structure interferes with the penetration of the electrons into the silicon and secondly irreversible damage is caused at the Si-SiO_2 interface [22]. Virtual phase CCDs alleviate some of these problems, for although they are front illuminated, they have electrodes that cover only half of each pixel, leaving the other half exposed. These CCDs have been shown to be effective detectors of electrons, although for incident energies under 10 keV, they cannot compete with the detection efficiencies of back illuminated devices [120].

Back illuminated CCDs are those that have been removed from the substrate that they were built on and have had their undersides thinned. By this means the detection

surface (the underside) is free of obscuring electrodes. At this exposed back surface a silicon-dioxide layer naturally grows and where this layer interfaces with the bulk silicon, positively charged defects are formed. The effect of these positive charges is to create a potential well for electrons at the CCD back surface. Any electrons produced in the vicinity of this region are attracted towards the back-side rather than to the electrodes on the front-side and thus are not counted. This makes detecting low energy particles particularly problematic since their penetration depths into the CCD are very short. To mitigate this effect various treatments for the back surface have been devised [64]. The method that has been implemented on the CCD used with CATS is ion-implantation and laser annealing. In this method ions (e.g. boron) are forced into the back surface of the CCD where they create a field that reduces the depth of the backside well and raises the conduction band energy above that in the drift region. This raising of the conduction band causes a slope in the potential, which works to sweep secondary electrons created beyond the well towards the front of the CCD. The ion-implanting process causes damage to the silicon lattice which, if left unrepaired, would result in high dark currents and low quantum efficiency. This is corrected by the laser annealing step mentioned above, which is able to reform the lattice.

An alternative CCD treatment, delta-doping, reduces the depth of the back surface potential well even further, allowing an order of magnitude lower particle energies to be detected [51, 97]. In this process molecular beam epitaxy (MBE) is used to add a very thin (1.5 nm) layer of silicon onto the back surface of the CCD with an even thinner but very dense layer of boron dopant embedded within it, just a few atomic layers from the back surface [59]. The doping profile is then similar to a mathematical delta function and so the process is thus named. Delta-doped CCDs are also the most suitable detectors for low energy ions (whose mass causes their penetration depths to be much shorter than electrons with the same energy). They have been found to be sensitive to incident protons down to a minimum detectable energy of about 1 keV compared to approximately 10 keV for an ion implanted device and approximately 100 keV for untreated devices [84]. A delta-doped CCD would be an ideal detector for CATS, but it was not something I had available to me.

5.4.1 e2V CCD64

The CCD used in this a back illuminated e2V CCD64 'x-ray' CCD sensor (figure 5.14), a spare special-order CCD from the SXI instrument for the GOES programme [114, 122], which was used together with the engineering model readout electronics from the INTEGRAL-OMC instrument.

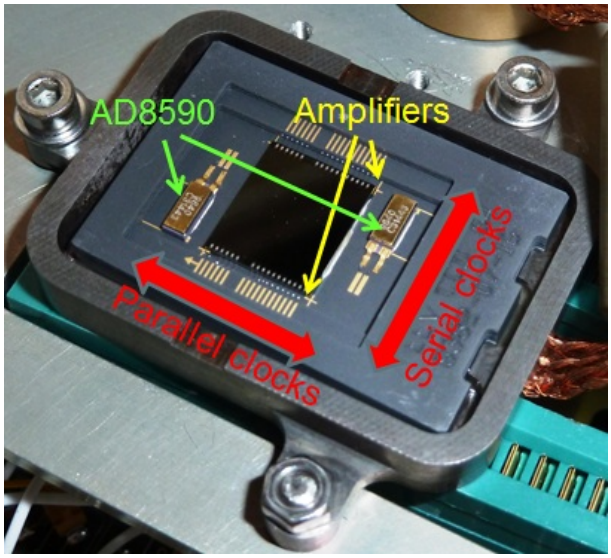

Figure 5.14: e2v CCD64 with cover plate removed, showing clock orientations and AD8590 temperature sensors.

The CCD is a full frame device with 512x580 16 µm pixels, a single serial output register with two amplifiers and two built-in AD8590 temperature sensors. It is housed in a rugged tungsten-copper and ceramic package.

5.4.2 Ionisation damage

The initial verification of the electron detecting capabilities of the CCD were obtained using a nickel radioactive beta source. This emits electrons with a distribution of energies peaking in intensity at 14 keV and extending in energy to 67 keV (as shown in figure 5.15).

A laser cut copper mask (with the design shown in figure 5.16a) was placed in front of the CCD and the beta source was placed in front of the mask. A fuzzy image of the mask confirmed that electrons were being detected.

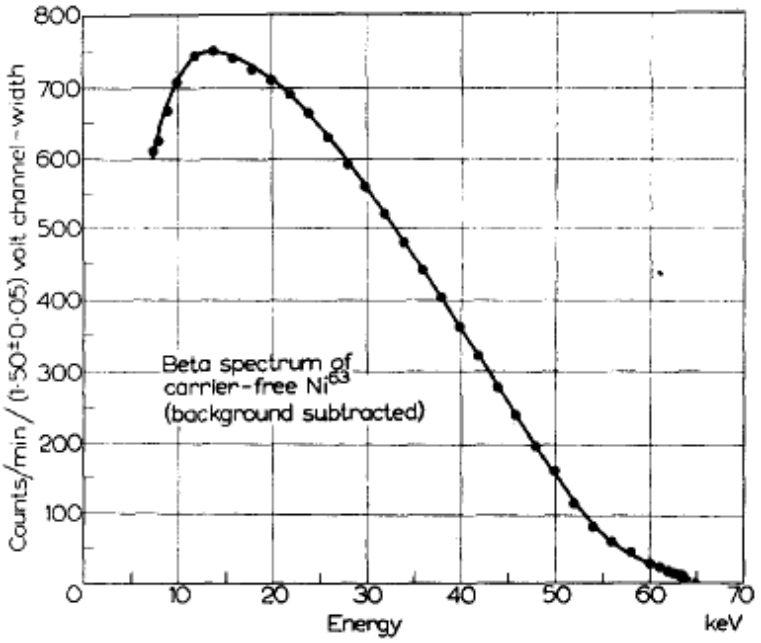

Figure 5.15: Beta particle energy spectrum of Nickel mounted on saturation backscattering thickness of platinum as determined in [104].

(a) The design used for the mask.

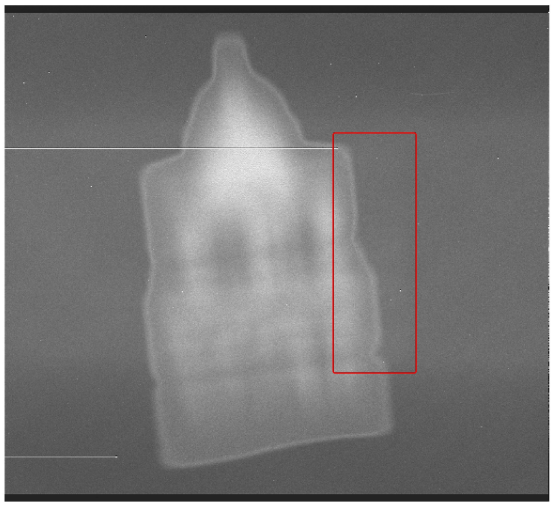

(b) The ionisation damage 'watermark' now present in every CCD frame. The red rectangle marks the area directly below the CATS exit apertures.

Figure 5.16: Initial tests of the CCD with a laser cut mask and a nickel radioactive source caused permanent ionisation damage.

Inconveniently however, when the nickel source was removed some six to twelve days later and the CCD was tested again, without the mask, there was still a fuzzy image it in the centre of the frame with an intensity proportional to the integration time (figure 5.16b).

This feature appears to be permanent and has remained as a watermark on all raw images recorded since. The prolonged exposure to the energetic electrons from the nickel source seems to have caused ionisation damage and corresponding areas of increased dark current. This has increased the noise and halved the length of the integration times achievable before pixels become saturated with counts.

Subsequent tests used only electrons with energies of 2.5 keV and below. These appear not to have caused any additional ionisation damage, although this has not been investigated in detail.

5.4.3 Experimental setup

Figure 5.17 shows CATS mounted above the CCD that is itself mounted in ZIF (zero insertion force) sockets set in an aluminium plate above the 'focal-plane' electronics. Between CATS and the CCD is a small aluminium plate that entirely covers the CCD except for a small hole around the CATS exit apertures.

Although the CCD dark current levels allowed for exposures of several seconds at room temperature, when the CCD was under vacuum it quickly heated up, increasing the dark current noise. To remove this heat a simple open-circuit liquid nitrogen cooling system was set up. This consisted of a large tank of liquid nitrogen outside the chamber that output through a metal pipe that passed through the inside of the chamber (as can be seen in figure 5.18). This pipe was thermally connected to the CCD through a flexible thermal braid (which can be seen in both figures 5.17 and 5.18). The coolant flow rate could only be regulated crudely and manually, so the CCD temperature tended to vary by a few degrees or fractions of a degree throughout the tests, and would stop entirely after a few hours.

It was also highly inefficient, at best cooling to just a little below room temperature (as recorded by temperature sensors built into the CCD package). Additionally the CCD setup was dogged by synchronisation gremlins between the PC software and controller

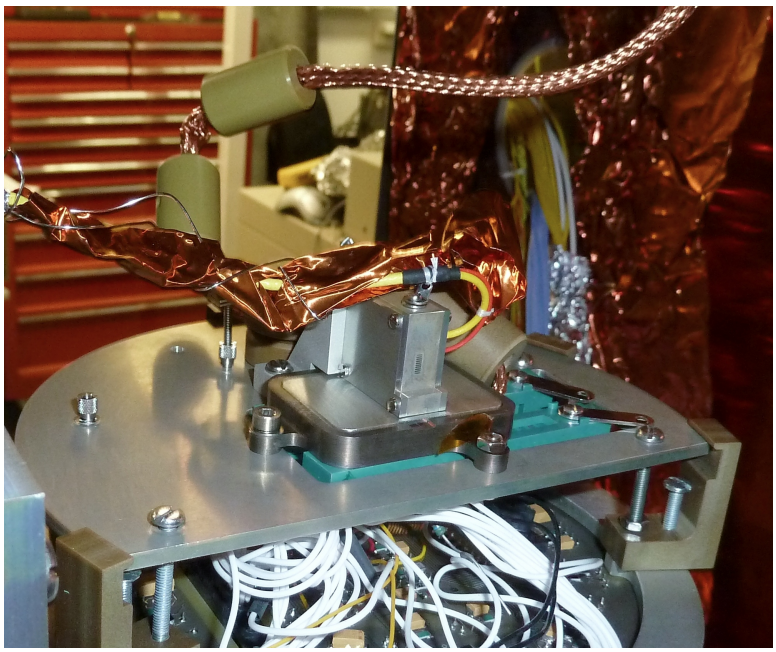

Figure 5.17: CATS mounted above the CCD on a thermally isolated plate above the focal plane electronics. An aluminium plate shields the unused areas of the CCD and a thermal braid is attached to its underside to provide cooling.

card and the CCD electronics as well as some poor connections in the focal plane electronics. This would frequently cause lines in the image data to slip or fail to read out.

Two custom readout methods were developed however, that were partially successful in extracting instrument response data. These are a current mode and a pulse mode and are explained below.

5.4.4 Current mode acquisitions (long integration)

A simple and effective method for the CATS calibration and aperture imaging was to take images with as long an acquisition time as possible before pixel saturation occurred (several seconds). Figure 5.19 shows a composite of a few hundred, processed, current-mode images showing electrons detected through some of the CATS channels during a voltage scan test performed at a few different angles. The area shown here is a smaller area within the red rectangle in figure 5.16b. The five bright rectangles are the electron footprints from the CATS C-channels, which are 0.3 mm wide and 0.4 mm

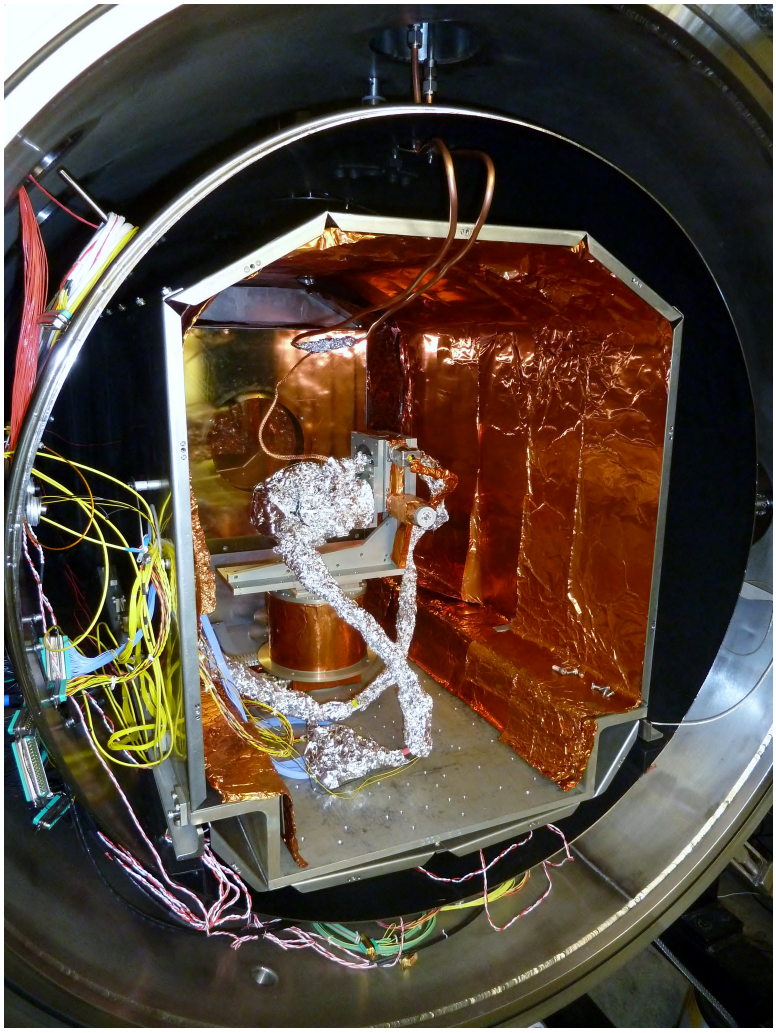

Figure 5.18: CCD setup in chamber, showing LN2 piping (at top) for cooling and foil wrappings to prevent insulating surfaces becoming charged.

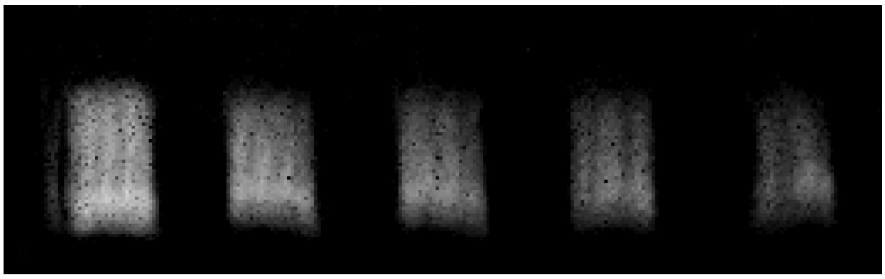

Figure 5.19: A composite image of the exit apertures of the CATS C-channels using the long integration, current-mode method

apart. Since the CCD pixels are 16 µm squares, each CATS aperture is about 20 pixels across. The electrons detected here all have the same energy; the varying brightness between channels seen here is due to the different geometric factors for each channel (discussed in section 4.3.1). The banding seen within each of the aperture footprints is an effect of combining together images taken at several discrete voltage and angular steps.

The equivalent compilation of pre-processed, full-sized, raw image frames from which figure 5.19 is obtained is in fact that shown previously in figure 5.16b. To reveal the electron signal, the image was processed thus: First a simple de-spiking algorithm (despike gen from the SolarSoft package[2]) was run on each raw image frame, removing hot pixels and electronics induced features. A similarly de-spiked background frame was then subtracted from each image frame to reveal just the electrons and any residual noise. The background frame is an exposure of the same integration time as the image frame, except with the analyser voltage reduced such that there were no electrons transmitted to the detector. As well as the thermal noise (mask shaped and otherwise) the background frame also included the large amount of stray UV light from the electron gun that was being reflected through the analyser head to the detector. In this acquisition mode a background frame would be taken as the first frame in a CATS voltage scan sequence each time the analyser was moved to a new angular position. It was found however that by the end of the voltage scan, there had usually been a noticeable change in the dark counts (i.e. temperature) and the background frame would no longer be representative of the true background counts in the image. To account for this the unused part of the CCD background image frame (i.e. everything outside of the aperture area) was scaled so its mean was the same as the corresponding area in the image frame. This temperature scaling factor means that a fraction of the reflected UV light (which is essentially independent of the detector and its temperature) is present in the final image. The impact of this effect appears to be negligible compared with other variations however.

[2]http://www.lmsal.com/solarsoft/

5.4.5 Pulse mode acquisition (short integration)

While the long integration method effectively measures a current of electrons, the second method aims to detect individual particles by using the shortest integration times the CCD electronics would stably allow, about 40 ms. In this mode several hundreds of frames were taken consecutively and no specific background frames were recorded. In most frames there were a few (perhaps two or three) pixels that were clearly above the local noise profile and located almost exclusively in the aperture area. To extract only these events, the frames were de-spiked (to remove much larger electronics-induced spikes) then summed and averaged. This averaged frame was then subtracted from each of the individual frames, again scaling for temperature variations in a similar way to that previously mentioned. With only a few electrons in each frame these would appear as small peaks above the residual noise after the subtraction.

Figure 5.20 shows a histogram of pixels values, from many thousands of these averaged-frame subtracted, pulse-mode frames. Pixel values from pixels in an area of the frame exposed to 2.5 keV electrons are shown plotted as a red curve. Pixel values in an identically sized area of the frame with no electrons bombarding, are plotted as a blue curve. The blue curve counts are therefore solely attributable to noise sources. Shot noise added by the electronics (read noise) is approximately 4 ADU (analogue digital units) and effects associated with the averaging and scaling process used to generate the background frame will have some effect. The largest contribution however, is from the shot noise on the dark current.

It can be seen that from above about 12 ADU there is a clear electron signal present in the red curve, but that any pixel cannot unambiguously be considered to be an electron unless it is greater than about 25 ADU. In the pulse-mode data therefore, after the processing described above, any pixels below a threshold of 1.5 standard deviations of the pixel values of the non aperture areas (which corresponds to the point where the red and blue curves diverge) were zeroed[3]. With increased cooling the dark current shot noise could be decreased, so the blue noise curve would be narrowed and the electron signal could be better resolved.

[3]I only realised later that this varying threshold has the unfortunate consequence that the detecting sensitivity varies between readings.

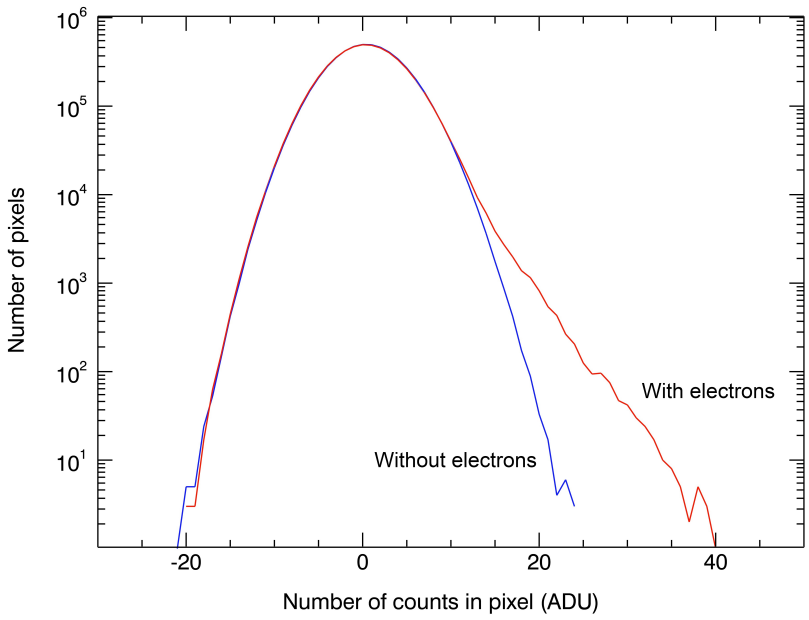

Figure 5.20: Histogram, with logarithmic y axis, of pixel values from many consecutive frames of, 'background' subtracted, short integration (pulse-mode) images. The blue line is for pixels under an inactive aperture and thus shows typical noise. The red line is the curve for pixels under an aperture transmitting 2.5 keV electrons.

Figure 5.21 shows an image from data acquired in this mode.It shows 2.5 keV electrons from a single CATS channel and consists of $\sim$ 1000 40 ms frames.

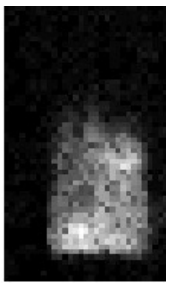

Figure 5.21: A pulse-mode image of 2.5 keV electrons from a single CATS channel, consisting of $\sim$1000 40 ms frames taken at a single voltage and a single angular position.

Unlike figure 5.19, this data has been acquired at a single CATS voltage and angular position. Some noise counts in dark shades of grey may just be discernible in the background corresponding to the signal/noise overlap region previously discussed. This pulse-mode, single particle method is of relevance to real space missions, where high sampling rates are required to resolve the time variation of particle fluxes and for spinning spacecraft to resolve the direction the particles have come from. The lack of a requirement of a background frame allows the instrument to be continuously detecting particles without gaps in the data.

The gain of the readout electronics is 1 ADU per 24 generated electrons. Correspondingly the long integration, (current mode) acquisition method was able to detect the lowest energy electrons since generated electrons from multiple incident electrons could accumulate in a single pixel up to a readable level (24 electrons). To study the response of the CCD to the energy of incident electrons, the energy of the electron beam was varied and the voltage on the CATS analyser adjusted accordingly so the profile of the beam on the detector remained constant.

Figure 5.22 shows the variation with energy of the total ADU counts over the pixels in the aperture area for background subtracted, current mode images, summed over many image frames. It can be seen that the lowest energy electrons detectable are about 500 eV and that at higher energies the signal generated by the electrons increases non-linearly. This will be discussed in the following subsection. The length of the integration times for the lowest energy tests were limited by the time it took for pixels to become

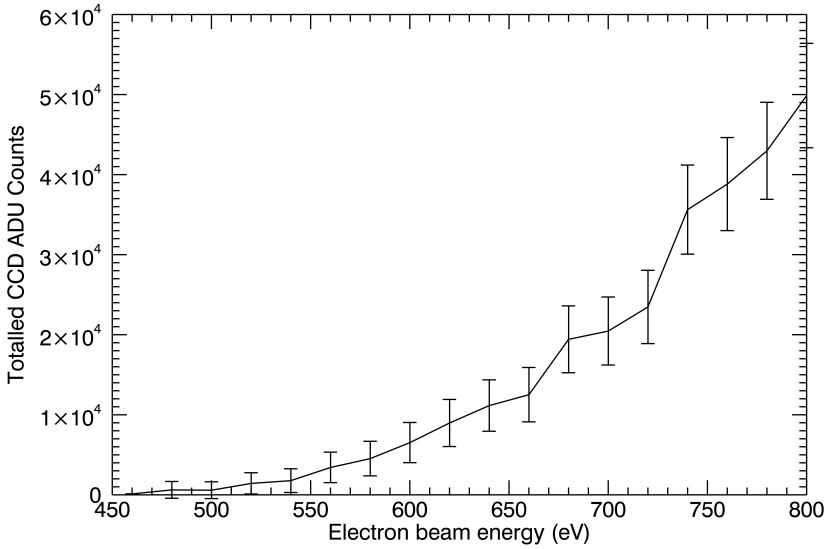

Figure 5.22: Total ADU counts in the aperture area, over several images, for different incident electron beam energies, using the current mode method.

saturated by dark current counts. It is possible that with longer integration times lower energies of incident electrons could be detected with this method. This would require better cooling however or a CCD with less ionisation damage.

Using the short integration time, pulse-mode method, the lowest electron energies detectable were about 800 eV. Figure 5.23 shows how the incident electron energy affects the typical signal in a pixel of a fully processed image taken using this method. This figure has been obtained in the same way as figure 5.20, but with the 1.5 standard deviation threshold applied (as discussed earlier in this section). It can be seen that higher energy incident electrons typically have higher pixel values, corresponding to more secondary electrons deposited and collected. As the beam energy is reduced, the electron signal disappears into the noise.

5.4.6 Modelling the CCD

The more kinetic energy an electron has, the deeper it is likely to penetrate into the CCD silicon before generating electron-hole pairs. To simulate the electron deposition within the CCD, a Mulassis [82] simulation was set up. Mulassis is GEANT4 based

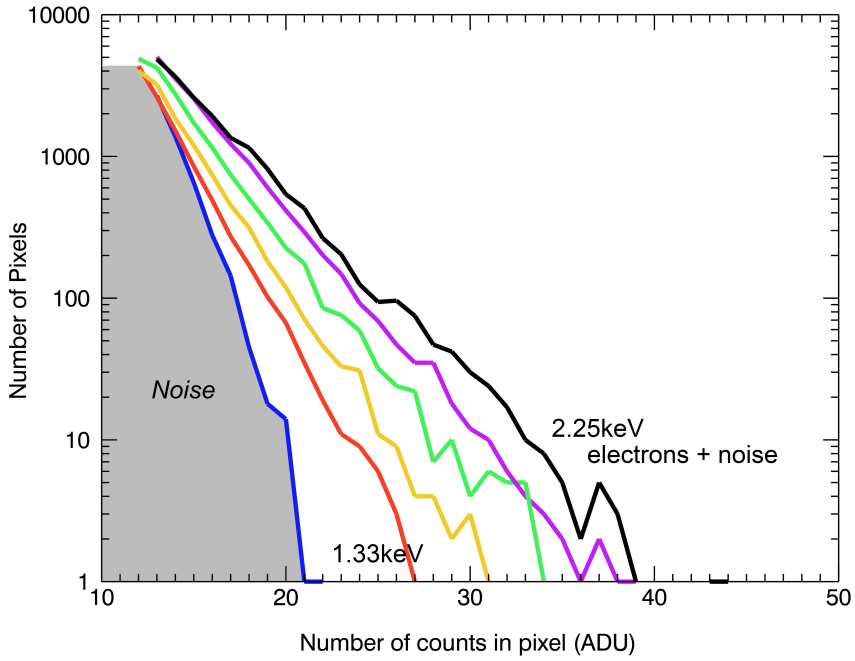

Figure 5.23: Histogram of pixels, from corrected pulse mode images, with the threshold cut-off applied, for electron beams of different energies. From left to right the curves correspond to; blue-no beam (i.e. noise), then electron beam energies of; red-1.33 keV, yellow-1.48 keV, green-1.64 keV, purple-1.82 keV, black-2.25 keV.

code produced by QinetiQ and freely available through the SPENVIS website[4]. The model simulated the CCD as a stack of slices of varying depth, the initial slices being silicon dioxide, corresponding to the silicon dead layer (assumed to be 5 nm thick), the remaining being silicon, up to a total thickness of 16 µm. A monoenergetic flood electron beam directed normal to the front surface was then simulated and in each slice the total ionising dose (TID, assumed to be equivalent to the deposited energy of generated electrons) was calculated and recorded.

Since the Mulassis setup had a limit of 20 slices the slice thickness had to be varied depending on the energy (and thus penetration depth) of the electron beam used. Particles were flown until the the random error[5] became negligible. Figure 5.24 shows how the charge deposited by the penetrating electron varies with the energy of the electron and the depth of penetration. It can be seen here how the charge is deposited deeper in the CCD at higher energies. Only at 500 eV (the dark blue curve) does the peak of the charge deposition occur beyond the dead layer. This is the lowest energy that I was able to measure electrons experimentally. By 800 eV (the minimum energy at which individual electrons were experimentally detectable, using the pulse mode method) there is a much larger amount of charge being deposited beyond the dead layer (light blue curve) and significantly increased counts in the current-mode method (as seen previously in figure 5.22).

The efficiency of the CCD pixel electrodes in collecting the generated electrons in the CCD silicon varies throughout its thickness and is termed the Charge Collection Efficiency (CCE). In the bulk of the CCD silicon, the generated electrons are all collected by the electrodes (CCE=1). At the farthest distances from the front electrodes (i.e. near the back surface) the CCE is significantly reduced.

A number of semi-empirical models exist for theoretically approximating the CCE. Stearns and Weidwald [120] use the following equation:

$$\eta(x) = 1 - (1 - \eta_0)e^{-x/L} \tag{5.3}$$

Where η is the CCE, x is the depth into the CCD away from the back surface, η_0 is the

[4]http://www.spenvis.oma.be/

[5]Intrinsic to the Monte-Carlo nature of the simulation engine.

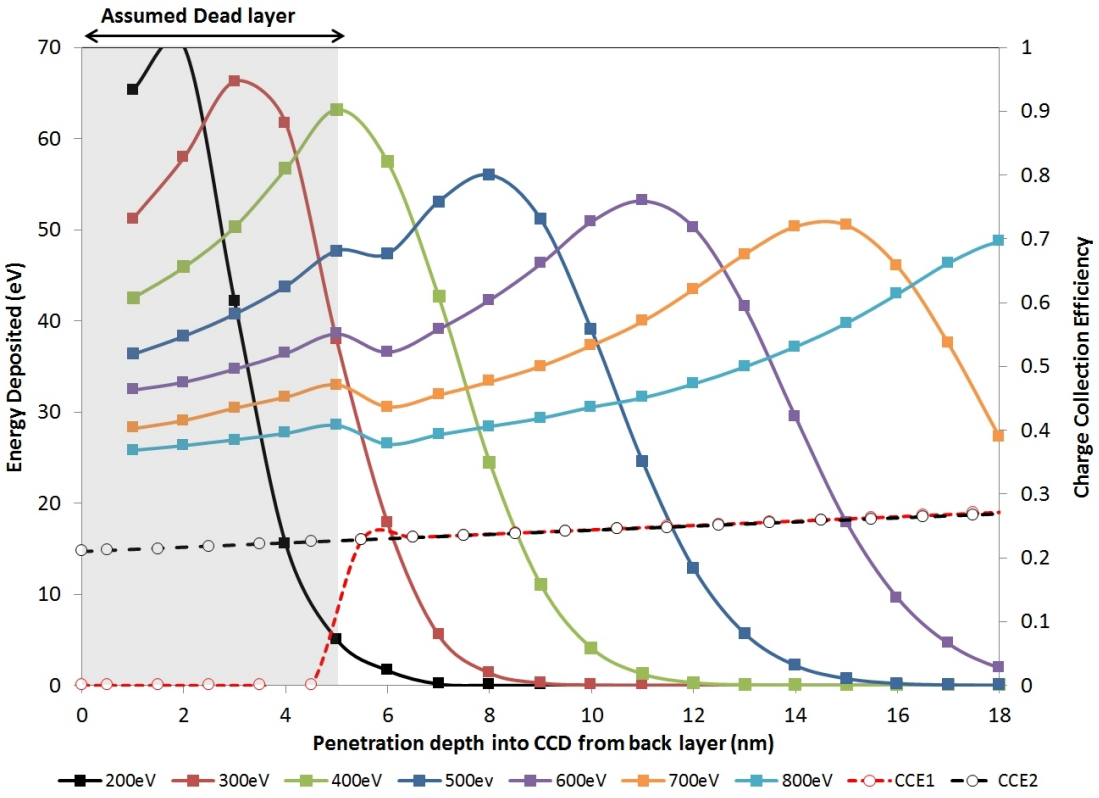

Figure 5.24: Mulassis simulated energy deposition of low energy electrons near the back surface of the CCD (assuming properties of Tektronix CCD in [121]). Also overlaid are the charge collection efficiencies, CCE1 and CCE2, calculated using two different methods.

CCE at the back-surface and L characterises the depth of the region of reduced CCE (for the CCD64 this was taken to be the ion implant depth). This was developed in the context of regular back illuminated CCDs. It uses an exponential function and assumes that even a small amount of charge will be detected from the dead layer. I refer to this method as CCE1. Stern et al [121] use a more sophisticated approach developed in the context of ion-implanted back illuminated CCDs like the one I have used. It allows for only a very small amount of charge to be collected from within the dead layer. This method I refer to as CCE2 and in its simplified form is given by:

$$\eta(x) = \begin{cases} \eta_0 + (1 - \eta_0) \times -x/L, & x < L \\ 1, & x > L. \end{cases} \tag{5.4}$$

While the necessary parameters for the CCD were largely unknown, such as the dead layer thickness, the ion implant depth and the initial charge collection efficiency (CCE), I used numbers from [121] where a similar ion implanted CCD (a specially processed TekTronix TK512CB) is studied, so that at least a qualitative understanding could be gained.

These theoretical charge collection efficiencies are over-plotted with the second y axis scale in figure 5.24. To investigate the signal that would be produced in the CCD, I calculated the charge collected at steps within the silicon by combining the charge deposited and the CCE. The corresponding ADU signal per electron as a function of energy is plotted in figure 5.25.

It can be seen here that the two CCEs produce very similar results. Initially there is a non-linear region at low energies corresponding to where the charge collection efficiency is increasing. Once the electrons have enough energy to deposit their charge in the main bulk of the silicon where the CCE is unity, the eV to ADU relationship becomes linear. The electron beam energies used in the experimental tests (shown enlarged in the inset box) can be seen to correspond to ADU of 4-9. ADU values of this order are consistent with the electron distributions in figure 5.23. The enlargement also emphasises the anomalies and irregularities in the curve. These occur when the thickness of the simulated Mulassis layers are changed (which is required as the higher energy electrons penetrate deeper into the silicon). Although (for reasons that will be

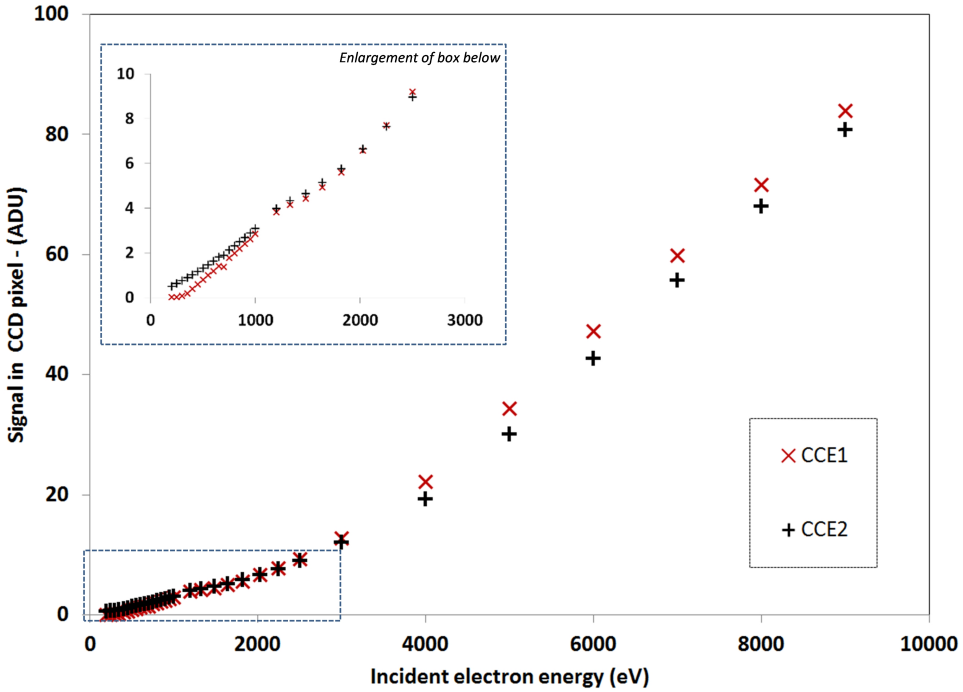

Figure 5.25: Simulated ADU counts per electron, for electrons of different energies, using data from figure 5.24. The inset enlargement shows the region that has been investigated experimentally. Irregularities occur when the thickness of the simulated Mulassis layers are changed as the higher energy electrons penetrate deeper into the silicon. CCE1 and CCE2 are two different methods for calculating the CCD charge collection efficiency.

explained in the next chapter) the electron beam was only used up to 2.5 keV, figure 5.25 indicates that at incident electron energies of 4 keV upwards a very strong signal (and thus good SNR) would be expected from the CCD.

5.5 Summary

A CEM and a CCD were successfully adapted for use as electron detectors with CATS.

The CEM setup allowed for sensitive, reliable and predictable performance with no limit to the length of time of experimental tests. It allowed for high resolution profiling of the angular responses. Its disadvantages arise due to its field of view and position insensitivity. It sampled neither a single CATS channel in isolation nor all the channels uniformly and to move its position required venting the chamber to manually adjust it, which was time-consuming and could result in a change in sensitivity relative to previous runs.

The e2v CCD64 ion-implanted device is a novel and suitable detector for use with low energy electron analyser instruments. I found it to be sensitive to electron energies of 500 eV upwards and, at the energies tested (up to 2.5 keV), resistant to significant ionisation damage (at least for occasional use). At higher energies (up to 67 keV) ionisation damage was permanent. Theoretical models suggest it would perform well for electron energies above 4 keV, although these were not tested.

The CCD allowed for position sensitive measurements so that the energy response of separate CATS channels could be easily discriminated and individual channel footprints inspected. The CCD's disadvantages were its SNR and reliability issues which were severe. The noise arose from ionisation damage and variable, inefficient cooling. The low signal arose from the 2.5 keV upper limit on electron energies from the photocathode. The reliability issues were mostly associated with synchronisation problems between the software, the PC and the electronics.

Chapter 6

CATS Testing

The previous chapter has explained how the CEM and CCD setups were arranged. This chapter describes how they were used to obtain the CATS energy and angular response results and how these results relate to the simulated CATS results in chapter 4.

The technical issues mentioned in the previous chapter limited the comprehensiveness of the data garnered. The focus of this chapter is consequently more on understanding how the CATS simulations relate to the as-built analyser head, rather than attempting an exhaustive instrument calibration.

6.1 Setup

The MSSL electron instrument calibration chamber is a well established facility, having been used for the calibration of the Cluster PEACE instruments [67], the Cassini CAPS ELS instrument [85] and many others. It has already been introduced in section 5.1 in the context of the detector development work. This section builds on that description to explain how the setup was used to characterise the CATS analyser.

Figure 6.1 shows the experiment assembly of the CEM detector on its micrometer mount (shown previously in figure 5.4) integrated into the calibration chamber (shown schematically previously in figure 5.2). The electron beam and axes of rotation of the rotary stages are orthogonal to each other and the CATS entrance aperture is located at approximately the central point of all three. The polarities of the elevation and

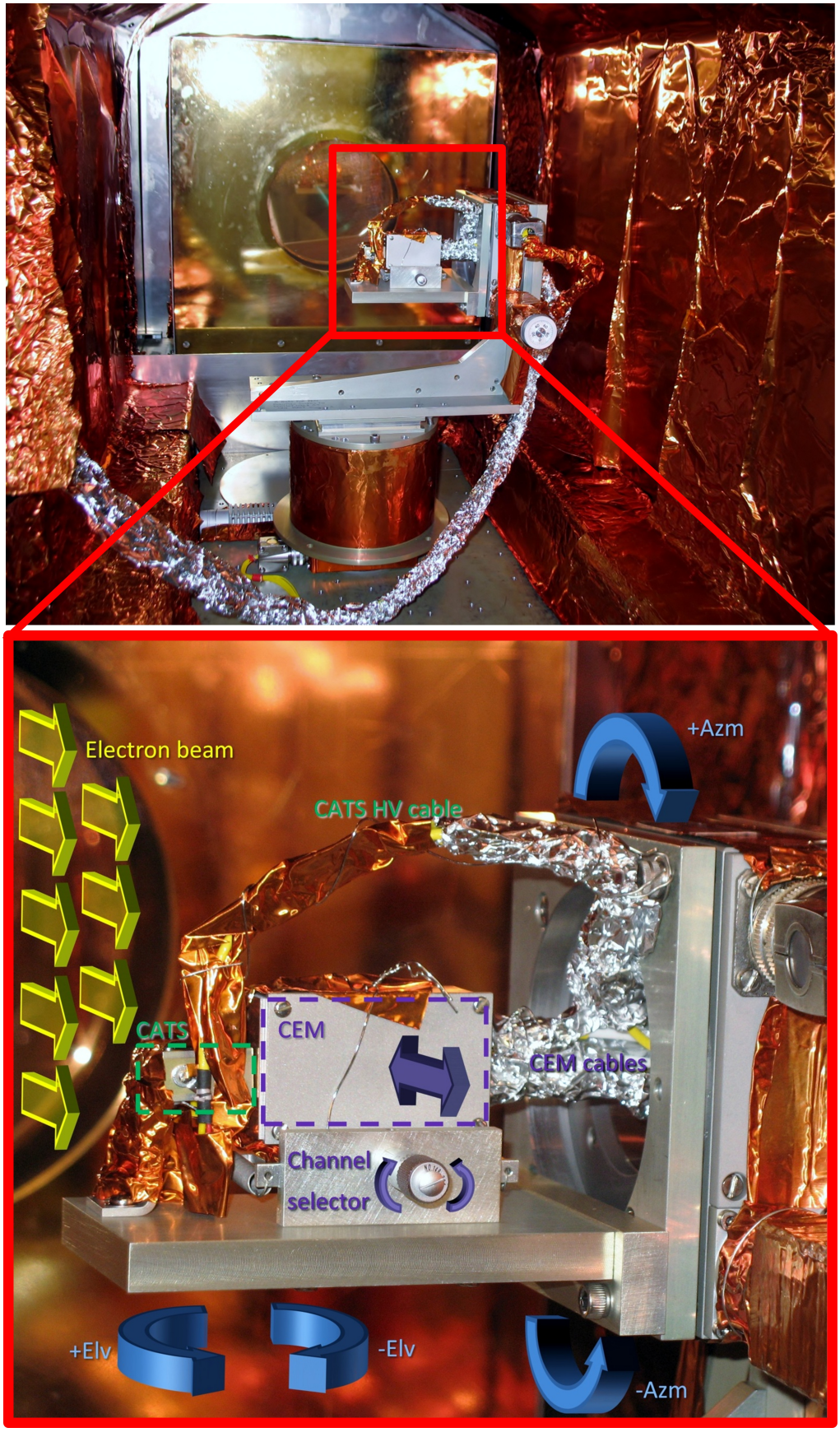

Figure 6.1: CATS+CEM mounted in electron calibration chamber

azimuth angles are defined in this thesis such that they correspond with the simulation coordinate system shown previously in figure 4.1.[1] The CCD setup was similar except that everything was rotated 90° clockwise around the direction axis looking down the electron beam so that CATS was mounted on top of the CCD (as shown previously in figure 5.17) and the azimuth and elevation axes were effectively switched.

The rotary stages are Newport Micro-Controle UR100 rotation stages with position feedback and have a relative angular accuracy of 0.01° or better. Offsets in the beam, CATS mounting and stage mounts can all lead to a slight systematic angular offset in precision.

The units which supplied voltages to the CEM and the photocathode were specialist high voltage supplies capable of providing stable high potentials (kV) to electrodes that had negligible current flowing from them. As discussed in section 5.2, the CEM requires ∼1600 V to operate in saturation mode, and since this potential is used to attract electrons it should be positive in polarity. Conversely, to repel electrons off itself, and thus form the electron beam, the photocathode requires that the voltage supplied to it is negative. CATS also requires voltages in the range from tens to hundreds of volts. The CATS electrodes are the fin sections (shown previously in figure 3.11). To transmit electrons through the C-channels a negative voltage is required. To transmit electrons through the I-channels a positive voltage is required.

The manufacturer quoted ripples in the supplies were small (e.g. 200 mV), but they were known to be slightly imprecise i.e. an offset can be observed when measuring their output with a voltmeter and comparing it to the set value.

The lowest voltage supply used was a Thurlby QL355TP. This could supply voltages up to 70 V with high precision (±0.03%) and was used with CATS for the lower energy beam tests.

Higher voltages, up to 2.5 kV, were supplied by a multichannel Lecroy model 1454 high voltage mainframe which was used to supply the CEM, the CATS voltages for the higher beam energy tests and the photocathode for lower beam energy tests. This unit was less precise than the Thurlby; voltages could have an offset of ±8 V to that set, as measured by its own internal voltmeters. For this reason it was preferred to use

[1] Although the conventions of the chamber and thus the actual control code were defined differently.

this supply only towards the top of its range where the voltage offset made a smaller difference (as a percentage of the total voltage applied).

The highest voltages (up to 30 kV, with ±2% / 20 V accuracy) were provided by a Brandenburg N10 which was used only with the photo-cathode. At the start of the CCD based tests however, the Brandenburg supply became inoperable due to a critical hardware failure, so the highest energy beams became unobtainable.

Consequently most of the CATS+CCD tests used the LeCroy unit to supply the photocathode. To obtain the best available SNR the highest available voltage (2.5 kV) was used. This unfortunately meant that the CATS electrodes required voltages that were higher than those that the Thurlby could provide, but within the lowest voltages and thus the lowest accuracy regime of the LeCroy supply. To improve the accuracy a resistive divider box was used. This box contained a sequence of high voltage rated resistors wired in series. Depending at which point in the resistor chain the voltage from the LeCroy was added, the output voltage could be divided by 2,3,4 etc. In this way higher voltages could be produced with low percentage errors which could then be scaled down to the smaller voltage required, the error scaling down by the same amount.

The beam profile was not investigated, but previous calibrations have shown that at higher beam energies the profile is altered as the grid bends under the increased electrostatic forces. This effect is largely mitigated by the small size of the CATS aperture, its placement at the centre of the beam, and that throughout any individual calibration test performed the beam was kept constant.

The voltage supplies and stepper motors described above all interface with a datalogging and control PC. This PC runs PACIDERM (Plasma Automated Chamber Integrated Data Extraction Routine Miscellany), a DOS-based set of custom-made programs written in C++ by Dave Walton in the early nineties. PACIDERM was used to automate and synchronise these systems as well as to record CEM data through a counter card connected to the CEM SCA. The CCD required additional hardware and Windows based software, so it was controlled by a separate computer which was connected to the PACIDERM computer by an RS-232 serial interface. This serial connection was only able to act as a dumb trigger back and forth, so the experimental setup had to

be programmed into both computers separately so the data and logs could be brought together later once the tests had been completed. I was continually developing and debugging this system which, combined with the technical issues mentioned in chapter 5, meant that test runs were continually being stopped, started and restarted. Consequently CCD data files on the CCD PC very regularly became out of sync with the motor and voltage logs on the PACIDERM PC, and required tests to be redone and extensive corrections in post-processing.

6.2 Energy response

In section 3.3 the rule of thumb for safe voltages (equation 3.5) gives a value of 100 V for the CATS electrode design, since the fins to aperture distance is 100 µm. By carefully monitoring the current levels for the first signs of arcing (together with cautiously set current trips) the voltage supplied to CATS was gradually increased above this. The highest voltage attempted through this approach was 500 V, which was found to be perfectly stable and maintainable. This gave a maximum detectable electron energy of ∼8 keV.

As has been mentioned previously, the energy response tests were obtained using a fixed energy beam and varying the voltage applied to CATS. The tests were usually repeated at several elevation and azimuth positions, which would be summed together at each voltage.

The most important aspect of the energy response to understand is the K-factor of each channel. A summary of the peak K-factors for each channel and their comparison to the simulation data are shown in figure 6.2.

While the laboratory and simulation numbers clearly do not match up, there is a definite offset; the C-channels are always under the simulation result by a small amount, the I-channels are always over by a larger amount.

This offset first became apparent once the CEM data had been processed and it made me suspect that there might be a misalignment making the I-channels narrower than expected and the C-channels wider than expected. Although various calculations (using equation 3.1) and exploratory simulations backed this hypothesis the nature of the

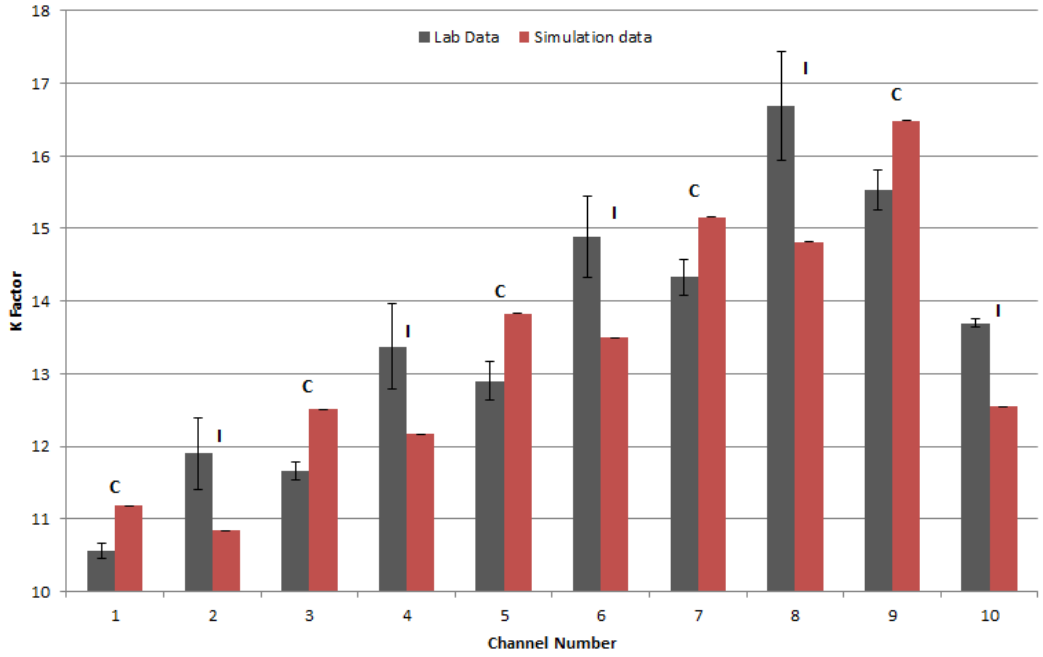

Figure 6.2: Simulated (red) and measured (grey) peak K-factors for each CATS channel, results extracted from a combination of CEM and CCD tests.

CATS design and manufacture did not seem to allow for this and the offset was considered to perhaps be attributable to another technical issue with the CEM setup. The CCD setup measured the K-factors to be the same as the CEM had however, only with greater accuracy and greater certainty.

Figure 6.3 shows all the C-channels, taken with the CCD in current mode at zero az/el position. It can be seen there that if the CCD K-factor data is increased by 6%, it then matches much better with the lab results. It shows the energy resolution and the relative geometric factors to be behaving approximately as expected in the x-axis and y-axis respectively.

Unfortunately there are no equivalent complete data sets for the I-channels as all the tests had issues, but the I-channel K-factors could still be extracted from other CCD tests with high confidence.

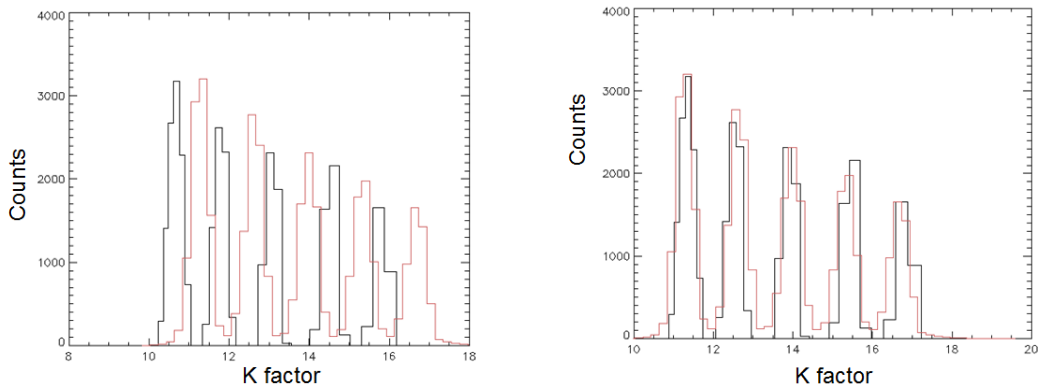

(a) Results normalised to peak counts.

(b) With ×1.06 multiplier applied to CCD data x-axis.

Figure 6.3: C-channel K-factor response, red line is simulation data, black line is CCD acquired data (in current mode). The two have been approximately normalised by peak height

6.3 Angular response

The best angular response data were obtained with the CEM, though the CCD data were in general agreement with it.

The CEM issues have been described previously in section 5.2. In all these tests the CEM collimator has been used, except where it is specifically mentioned otherwise.

CEM measurements were only made in a few positions but the stray secondary electrons from channels outside the intended field of view allowed a wider range of channels to be studied. Figure 6.4 shows how primary and secondary electron beam results compare. It should be noted that because the x-axis is the CATS electrode voltage and not the electron energy, these appear reversed in x compared with figures 4.7a and 4.7b i.e. in descending order of channel compared with ascending order.

For the left frames in figure 6.4a the CEM was apparently[2] positioned over channel 7. Secondary electron results from other channels can be seen, but attenuated in counts and in range compared with figure 4.7d. The right frame shows the same channels, but

[2]The micrometer adjuster scale had no absolute reference points on CATS so the CEM position had to be inferred from the K-factors observed.

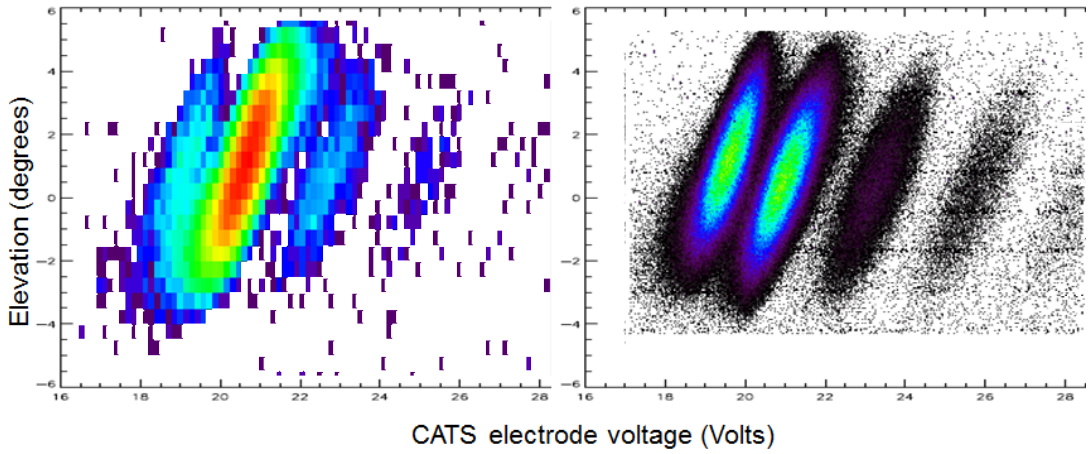

(a) C-channels, 9,7,5,3,1. Left frame CEM centred on channel 7, right frame CEM centred on channel 8 (and at much higher resolution, i.e. more voltage and elevation steps.)

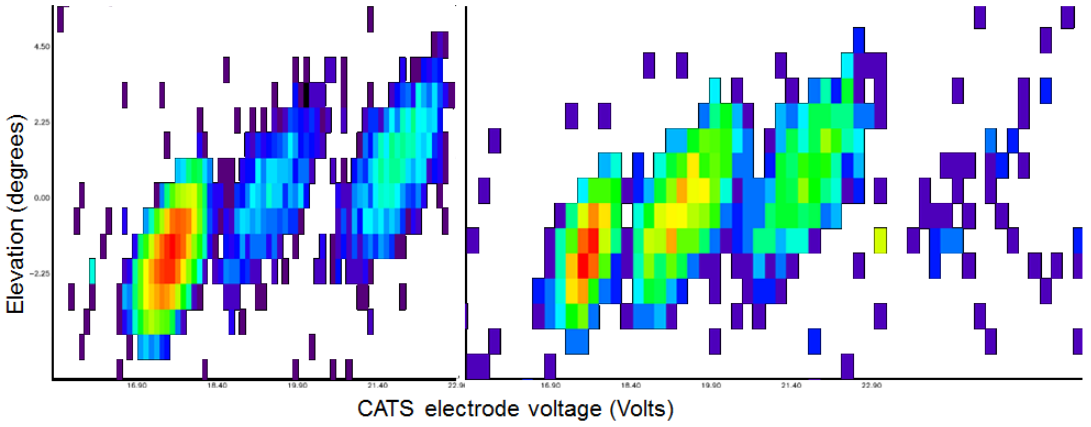

(b) I-channels 8, 6, 10 & 4 (combined). Left frame CEM centred on channel 8, right frame CEM centred on channel 7.

Figure 6.4: Elevation-CATS voltage spectrograms for 300 eV electron beam, each normalised to the standard colour scale. Left frame shows primary electron result (with neighbouring channel secondary results), right frame shows (corresponding) secondary results only. As explained in the text CATS channels here appear in descending order with x.

with the CEM apparently positioned between channels 7 and 9 (i.e. over channel 8). Since the channel 8 response is very similar left to right it was assumed that secondary results from immediately neighbouring channels can be used as a good approximation for primary detection results. Figure 6.4a shows a similar result for I-channels.

Both primary and secondary electrons from neighbouring channels have been used to produce angular response curves in the sections below, the captions will denote which, and the inferred position of the CEM aperture.

6.3.1 Azimuth

Figure 6.5 shows graphs of the CATS+CEM response as a function of azimuth, summed over several voltages and elevation angles and with varying additive and multiplicative noise floors removed from each.

Equivalent energies and elevations from the highest resolution simulation data were extracted allowing the equivalent azimuth response histogram to be underplotted in red columns.

In all cases there appears to be a $-1°$ offset. This is not necessarily induced by the CATS electron optics but is quite likely to be intrinsic to the setup, especially since the CCD setup showed a different constant offset in azimuth. Errors and uncertainties in mounting positions and beam profiles can easily create an absolute offset of a degree or two.

The resolutions appear to be approximately comparable, the wings in the C-channels and their absence in the I-channels being the case in both the laboratory and simulation data. The slightly wider than simulated response in figure 6.5a could be attributable to the lack of collimation. A careful examination of the experimental azimuth response in figure 6.5d shows a slight bump around $+9°$ azimuth. This is especially noticeable in figure 6.6, which shows an elevation-azimuth spectrogram of channel 7 from a different dataset, which contained a greater number of azimuth data points. Closer examination of the data shows this to be a genuine feature of the analyser (rather than noise), presumably an azimuthal reflecting effect. Few data were taken at wide azimuths however so it is not clear why it is so pronounced and anti-symmetric in this example.

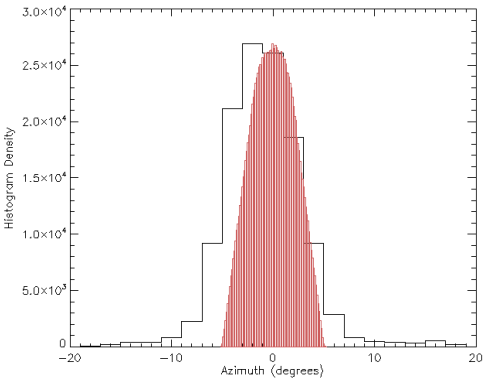

(a) Channel 6 azimuth response (primaries from 30 eV beam, CEM centred on channel 6 and without CEM collimator).

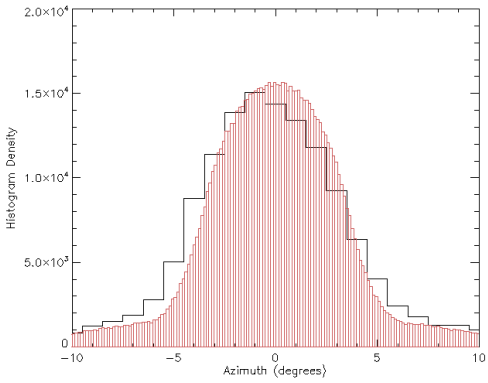

(b) Channels 5 and 3 combined azimuth response (secondaries from 100 eV beam, CEM centred on channel 6 and without CEM collimator).

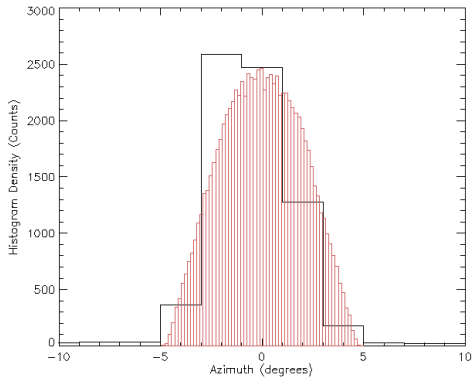

(c) Channel 8 azimuth response (primaries from 300 eV beam, CEM centred on channel 8).

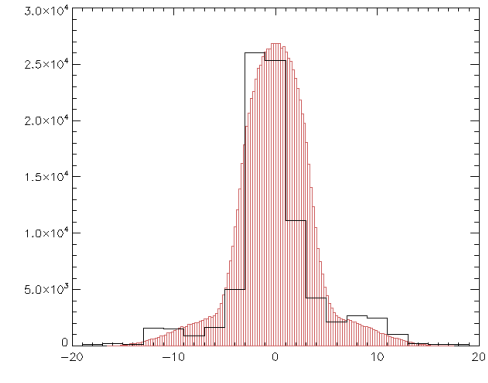

(d) Channel 9 and 7 combined azimuth response (secondaries from 300 eV beam, CEM centred on channel 8).

Figure 6.5: Azimuth responses normalised by peak height. Black lines - CEM data summed over available CATS voltages and elevation angles. Red columns - corresponding simulation data.

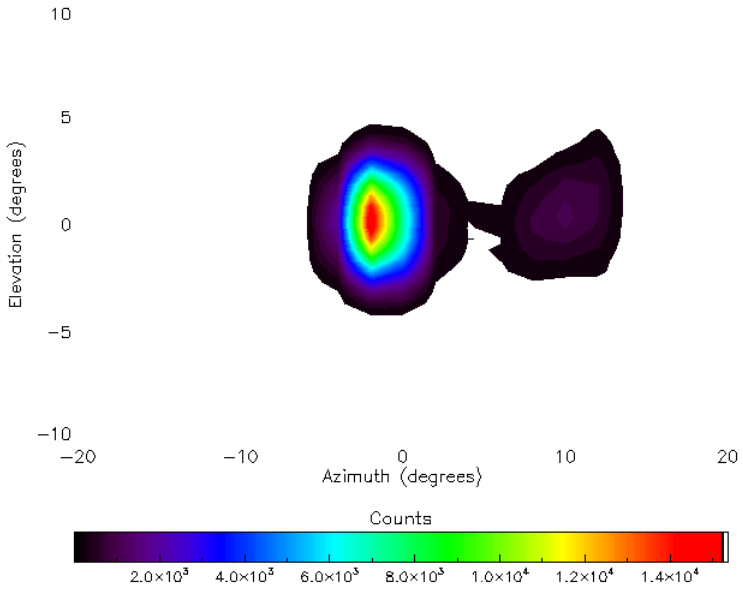

Figure 6.6: Azimuth-elevation scan (voltages summed) for primary 300 eV electrons through channel 7 (CEM centred on channel 7) showing signs of reflected electrons on one side only (large isolated events that were clearly noise have been removed).

6.3.2 Elevation

Figure 6.7, shows graphs of the CATS+CEM response as a function of elevation, summed over the available voltages and azimuth angles (in many tests only the zero azimuth position was used), again with additive and multiplicative noise floors removed when required. It can be seen that there is a sizeable discrepancy between the peak elevation expected from simulations and the actual peak elevation measured by the CEM. If this were consistent across all channels – like the offset seen in the azimuth results – it would be unsurprising. It can be seen however, that the offsets vary considerably between the two channel types; I-channels have peaks shifted to slightly more positive elevations whereas the C-channels have peaks shifted to greatly more negative elevations. While the absolute peak elevation positions are still subject to uncertainty, their relative positions are most certainly separated.

The elevation resolution has not been thoroughly understood. It can be seen in figure 6.7 that it is often larger (worse) than simulated and it will later be shown to vary with beam energy.

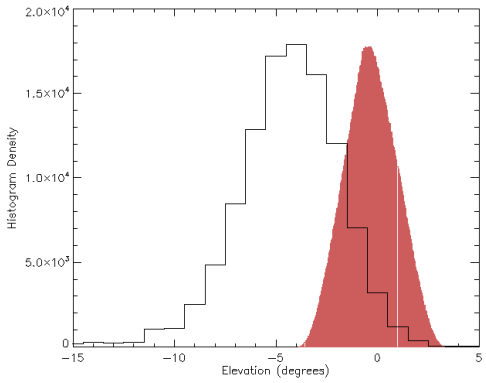

(a) Channel 6 elevation response, primary 30 eV electrons, CEM centred on channel 6 without collimator.

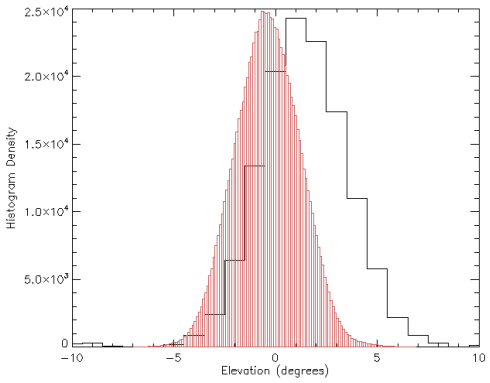

(b) Channels 3 and 5 combined elevation response, secondaries from 100 eV electrons, CEM centred on channel 6 and without CEM collimator.

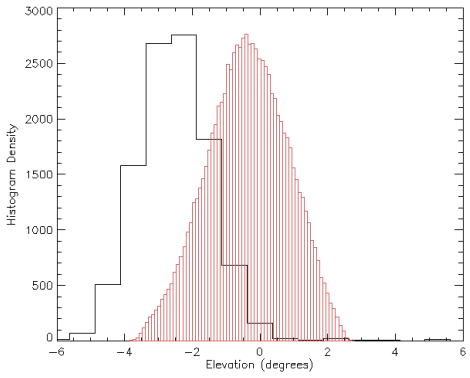

(c) Channel 8 elevation response, primary 300 eV electrons, beam centred on channel 8.

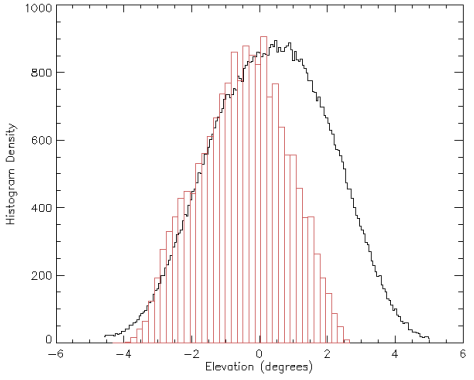

(d) Channel 9 elevation response, secondaries from 300 eV electrons, beam centred on channel 8.

Figure 6.7: Elevation responses normalised by peak height. Black lines - CEM data summed over available CATS voltages and azimuth angles. Red columns - simulation data (filtered by azimuth and energy to match the lab data).

6.4 Resolving the discrepancies

These unexpected results for both the CATS energy and elevation responses proved vexatious for a long period of time and great effort was exerted to try and understand them.The most decisive insight however, was obtained after all the chamber based tests had been done, and necessarily so.

6.4.1 Visual inspection

With the CCD results offering no further explanation as to the origin of the disagreement with the simulations, the misalignment hypothesis was returned to. The most unambiguous way to measure this was to do so visually, but this was a non-trivial proposition. To be able to view the position of the fins relative to the grounded electrodes required removing the finless Matsuda plate electrode (pictured on the right in figure 3.11), but to do so meant that the alignment of the fins would be lost. Although the CEM and CCD testing had long been finished (other projects had displaced them from the calibration facility), CATS' capability as an electron analyser could not be compromised. This was because it had already been reserved as the central component of PoleCATS (of which more in the next chapter).

The solution arrived at was to glue the fins into position with large blobs of Stycast glue on the edges furthest from the CATS channels (figure 6.8a). The glue is vacuum compatible and insulating and, being located where it is, does not interfere with the electrodes nor expose itself to electrons. With the fins fixed in place, the Matsuda plate electrode was removed and the alignment of the channels revealed (figure 6.8b)—the discrepancies in channel widths were immediately and glaringly apparent.

CATS was placed under an inspection microscope for closer assessment and measurement (figure 6.9). As well as the predicted channel-to-channel variation in widths, the individual channels were seen to vary in width along their length, in part at least because the fins were varying in thickness by up to $\pm$ 30 µm. Additionally large flecks of swarf could be seen. These might disrupt the shape of the electric field, and reduce the magnitude of the voltages that could be applied to CATS before arcing occurs.

Producing an accurate summary of the CATS channel measurements from the inspec-

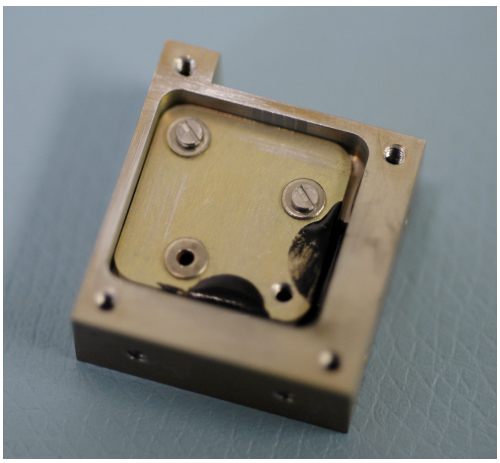

(a) Fins glued into position with Stycast glue.

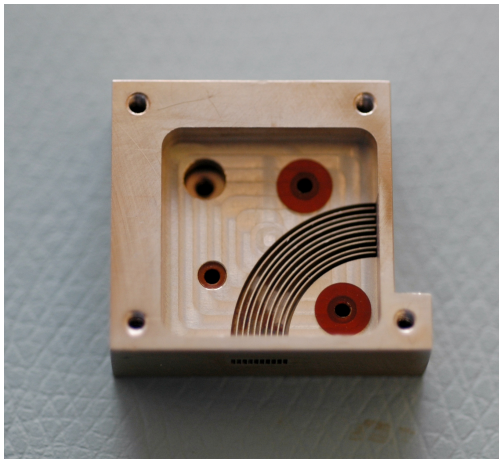

(b) Matsuda plate removed reveals fins.

Figure 6.8: Fixing CATS fins in position so electrode alignment can be assessed

tion microscope was proving tricky but a far simpler method was then discovered: CATS was placed on a standard office flatbed scanner and the image in figure 6.10 was obtained. Not only is it convenient to have the whole of CATS in one image (the camera port on the microscope has a very narrow field of view) but lens-based distortions are also greatly reduced.

From an optimised version of the scanner image, the channel widths were measured at five points along their length at 22.5° intervals, where the entrance aperture is at 0° and the exit aperture is at 90°. These measurements were used to approximately model their variation (figure 6.11). It can be seen from the figure how the I-channels (including channel 10) are typically slightly narrower than their design specifications and how the C-channels are wider than specification by a greater extent. The variation along the length of the channel can also be seen to be significant, in many places to the extent that the five data points alone are too low a resolution to accurately sample the overall shape of the variations.

To investigate a misalignment between the two electrodes, circles were fitted (by eye) to the curving channel walls (figure 6.12). From this it would appear that the two electrodes are not greatly misaligned with respect to each other, although it does suggest that the centre of curvature for the both electrodes is shifted slightly away from the exit apertures. The variations in the fin thicknesses can also be seen in places.

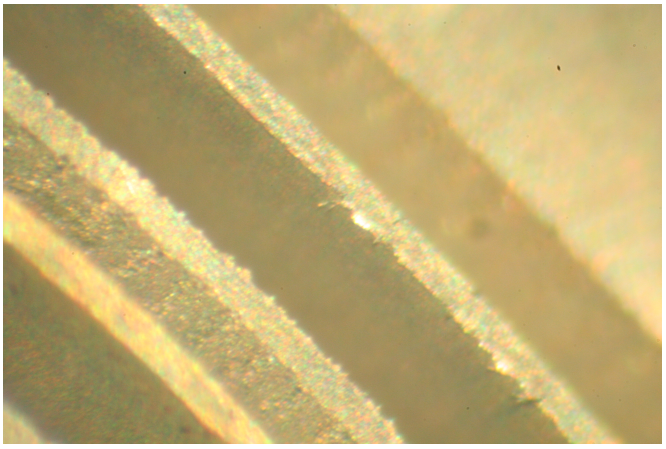

(a) The channel widths vary along the length of the channels and in places the variations are particularly egregious.

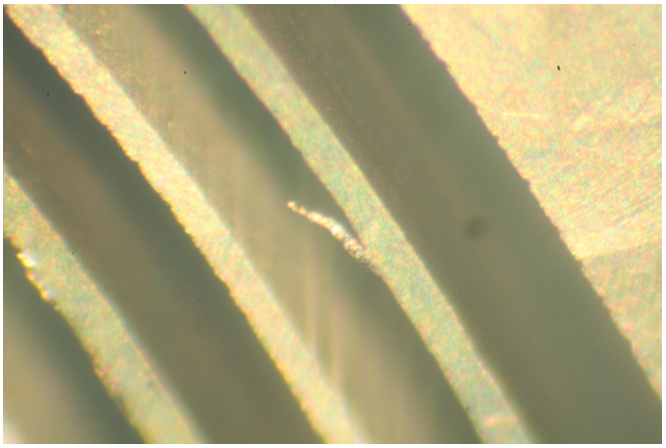

(b) Several large flecks of swarf were discovered.

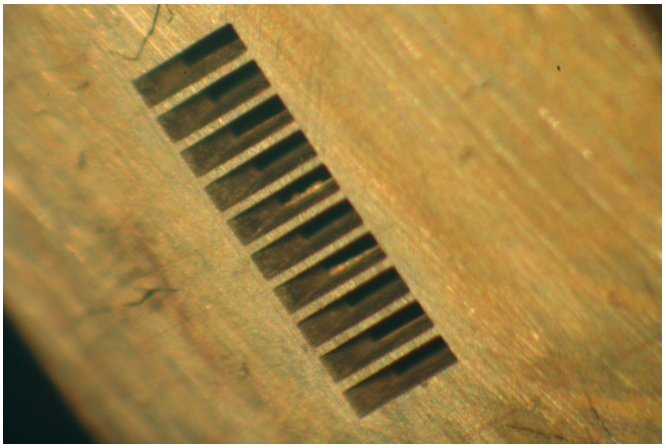

(c) The apertures appear to be free from obstructions.

Figure 6.9: Microscope views of CATS

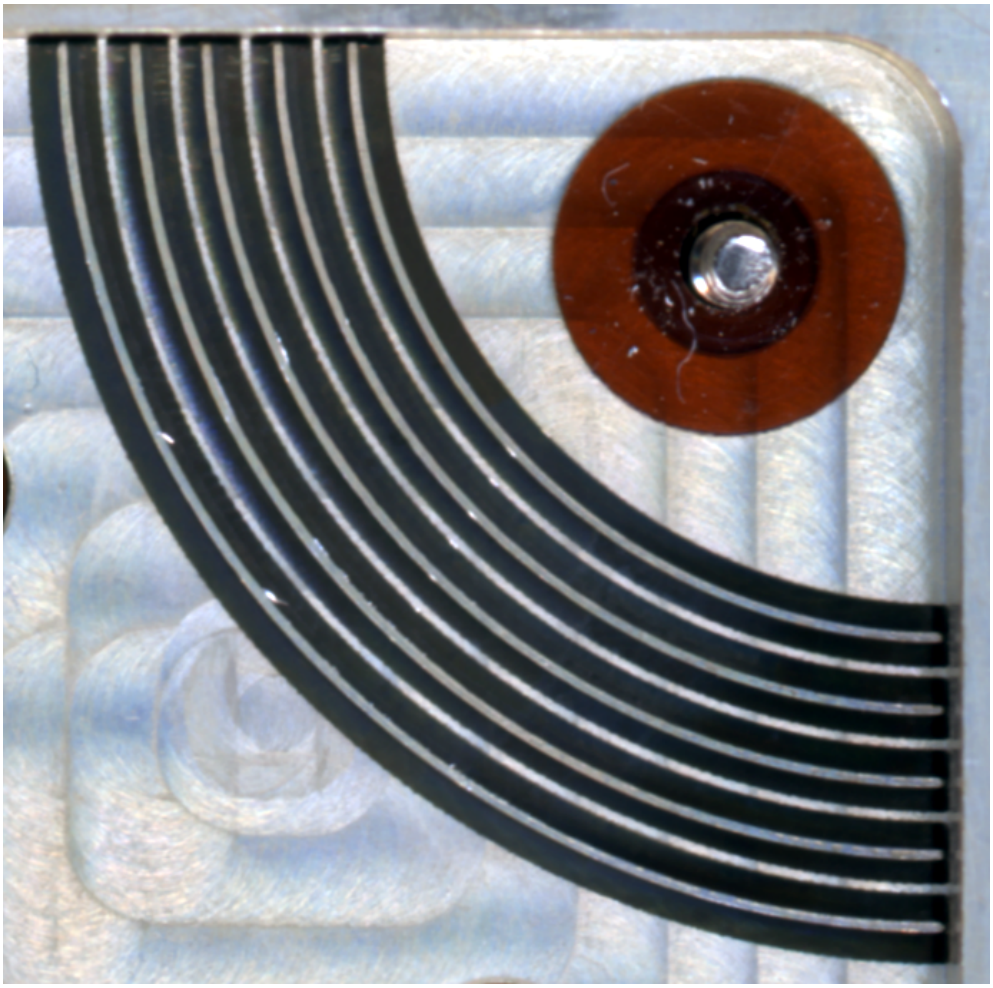

Figure 6.10: A flatbed scanner image of CATS channels (a CATSscan). Raw, unoptimised image – entrance apertures are at the top of the page, exit apertures on the right.

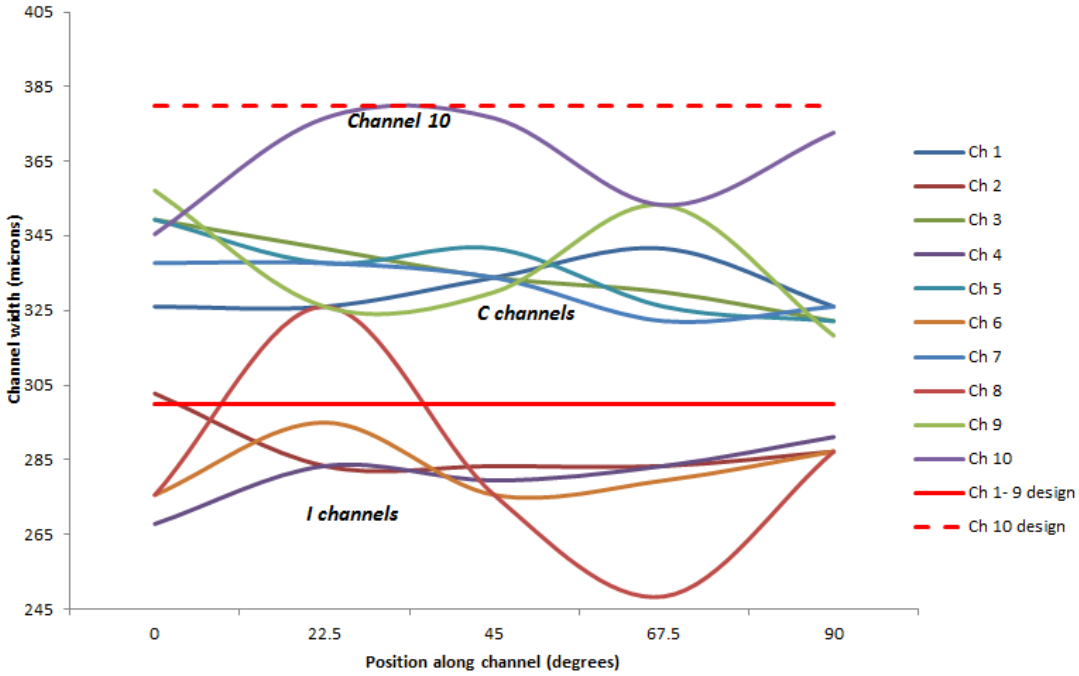

Figure 6.11: Approximate channel widths for each channel, as a function of angular position around CATS. Widths as extracted from figure 6.10 by measuring five points and fitting a smoothed line to them.

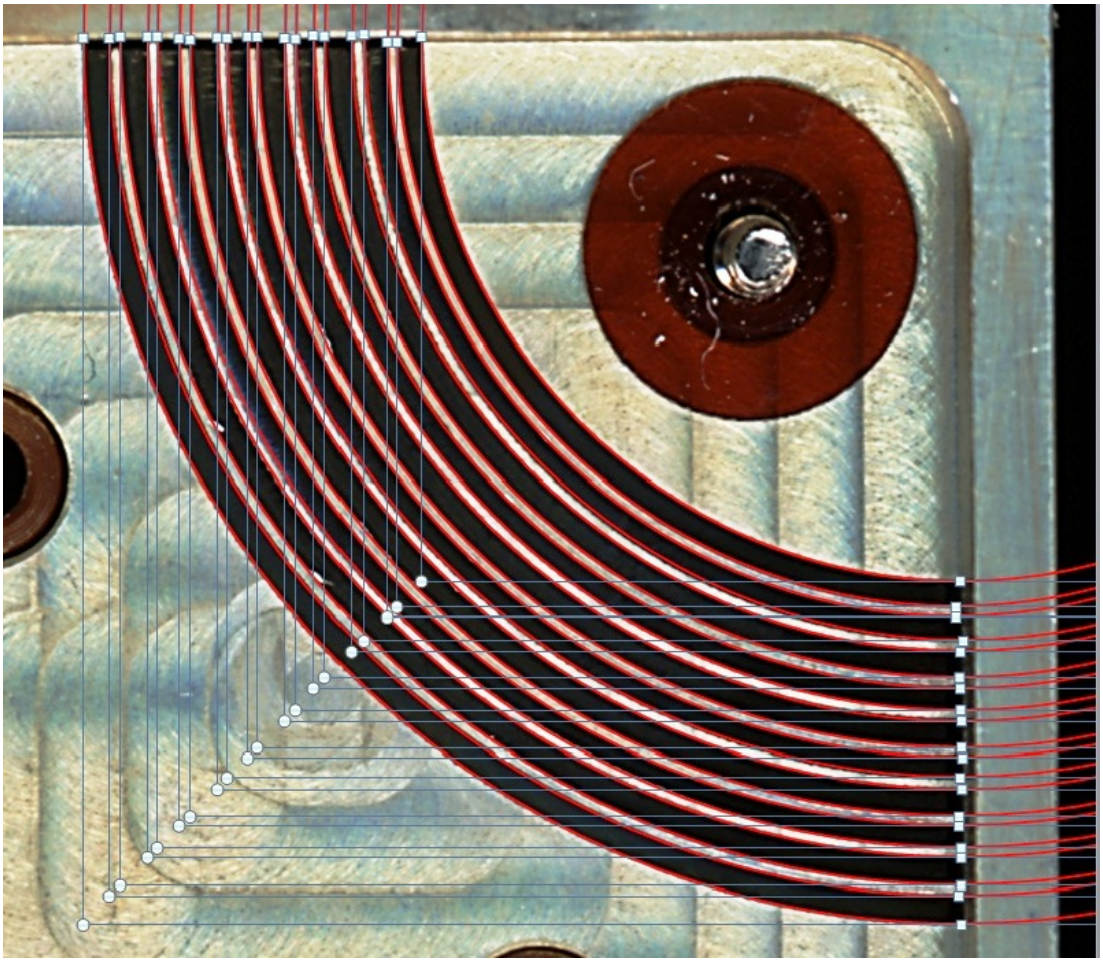

Figure 6.12: CATSscan from figure 6.10, optimised for contrast, brightness and noise, with red circles fitted (by eye) to the curving channel walls. White squares mark the corners and halfway points of squares encapsulating the circles.

6.4.2 Correlating K-factors

When the K-factors seen in figure 6.2 were measured and a misalignment was postulated, I estimated the extent of the channel width variation by adapting equation 3.1. Since the channel gap, ΔR, is small compared with R_0, the central radius, the K variation can be simply approximated as variation in ΔR only. Accordingly the actual CATS channel width can be inferred from the energy response measurements by:

$$\Delta R_{inf} = \Delta R_{sim} \times \frac{K_{lab}}{K_{sim}} \tag{6.1}$$

where ΔR_{inf} is the channel width that is being inferred from K_{lab}, the lab measured K-factor and ΔR_{sim} and K_{sim} are the simulated (design spec) channel width and simulation measured K-factor respectively. When compared with the channel widths measured from the CATSscan in section 6.4.1, for any given channel ΔR_{inf} was found to be in very good agreement with the narrowest of the channel width measurements for that channel (blue and brown bars in figure 6.13).

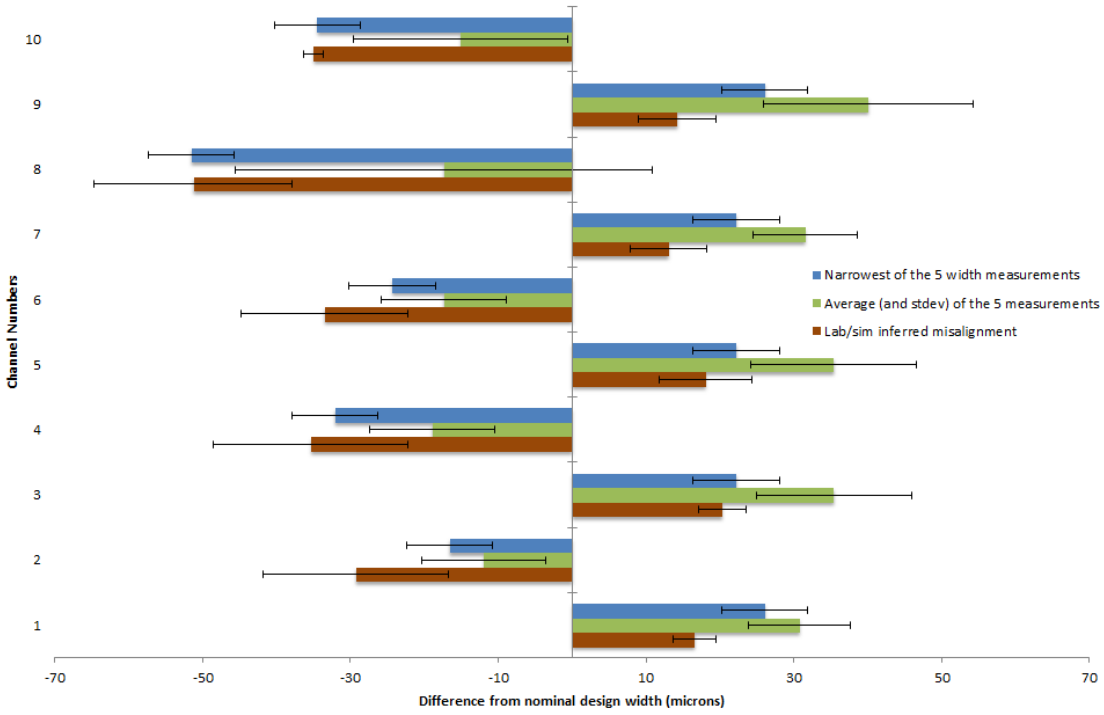

Figure 6.13: Comparing the difference from the nominal design channel width for the visually measured channel widths (both average results and minimum width results) and channel widths inferred from K-factor measured.

6.4.3 Correlating peak elevations

The discrepancies in the observed peak elevations have proved greatly more enigmatic however. The following analysis will show that the offsets as measured in section 6.4.1 are unlikely to account for the peak elevations observed experimentally.

This conclusion is based on speculative misalignment simulations that were made before the visual inspection was performed. These simulations modelled misalignments of the fins relative to the rest of CATS in the arrangements indicated in the cartoons in figure 6.14.

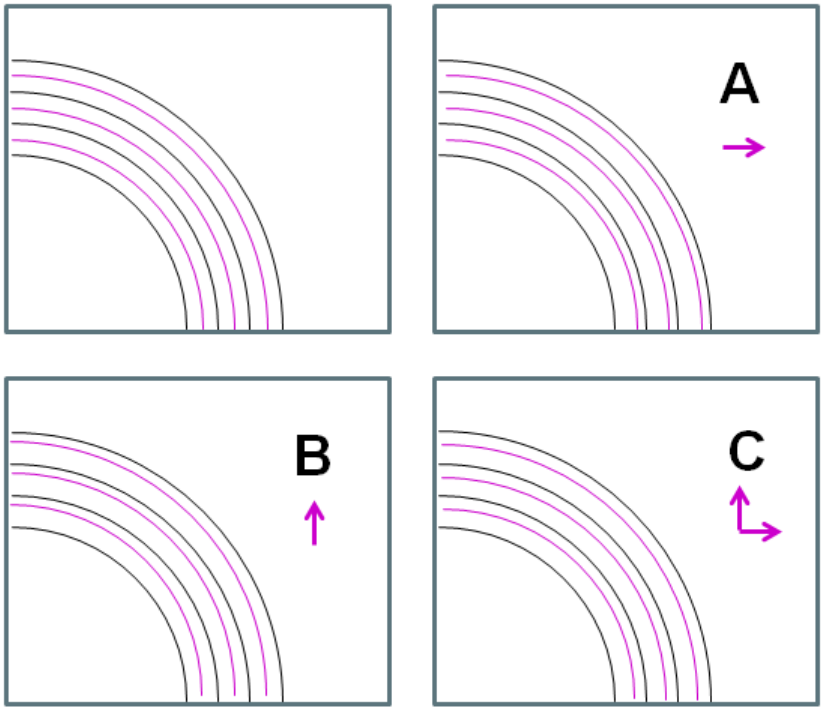

Figure 6.14: Cartoons of (exaggerated) modelled misalignments to CATS. Top left- no misalignment, A- fins shifted 12.5 µm away from entrance, B- fins shifted 12.5 µm away from exit, C- fins shifted 12.5 µm away from exit and 12.5 µm away from entrance

All the modification variations produce narrowed I-channels and widened C-channels in keeping with the K-factor variations previously discussed. In addition to the models in figure 6.14, there was an AA model which was identical to the A model but with a shift of 25 µm and similarly a BB model. The 25 µm shift equivalent of the C model was referred to as model D, but neither of these latter models were extensively used.

These simulations were performed on an earlier version of the SIMION setup to that used for the main results described in chapter 4. In comparison to the latest simulations this setup used fewer particles, the mid-resolution (12.5 µm) grid units and a geometry file that contained a few small errors in its dimensions (other than those purposefully introduced!). They also suffered from technical glitches that meant that the higher energy electrons were not flown in the simulations, which does impact the elevation response slightly.

The results from these rough simulations for the displacement of elevation peaks from nominal simulation predictions[3], for CATS CEM data and for misaligned simulations is shown in figure 6.15.

Although the simulations are rough, a definite pattern can be seen whereby the A type simulations show positively displaced peak elevations for the C-channels and negatively displaced peak elevations for the I-channels and B type simulations show the opposite. The D simulations show a slight positive displacement for both C and I-channels.

The CEM data (which has been extracted from figure 6.7 and similar data) matches closest to the AA model although in the case of the I-channels the displacement observed by the CEM is greatly more exaggerated.

Looking back to figure 6.14, the A type displacement can be seen to correspond to I and C-channels of equal and nominal widths at the entrance and as they progress towards the exit, the I-channels become narrower and the C-channels become wider.

Looking again at figure 6.11 however it can be seen that in general from 0° to 90° the C-channels become slightly narrower, whereas the I-channels become slightly wider. This would correlate qualitatively with B in figure 6.14. To make a more quantitative assessment I measured the channel widths from the AA and BB simulations at five points in the same manner as I had done earlier with the CATSscan. Figure 6.16 shows the results of this and how they compare with the actual CATS channel deformities. While there is no great similarity between the measured and simulated models, the BB is probably more alike to the measured curves than AA. This is in opposition to conclusion drawn from the trend observed in figure 6.15.

[3]For CEM data the peak elevations from the best simulations discussed in chapter 4 are used, for the A,B,AA,BB,D models a non-misaligned version of these lower quality geometry files is used.

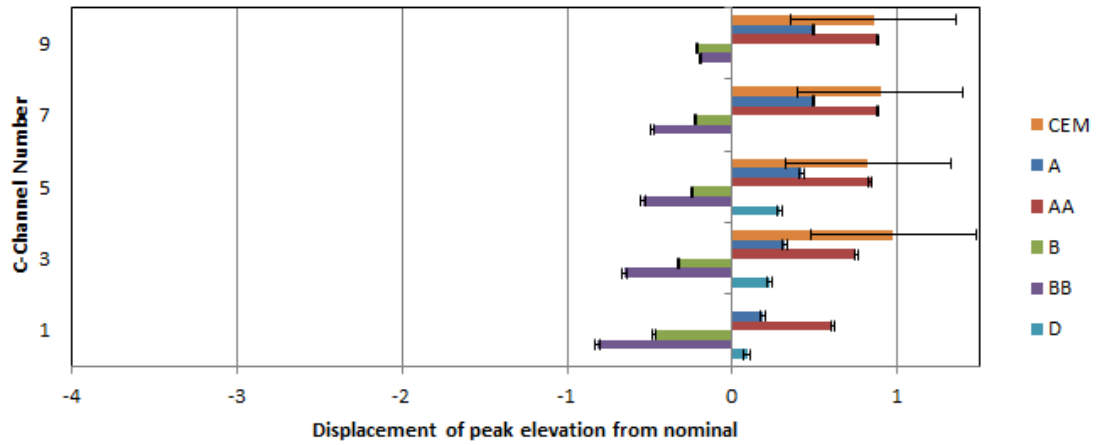

(a) C-channels.

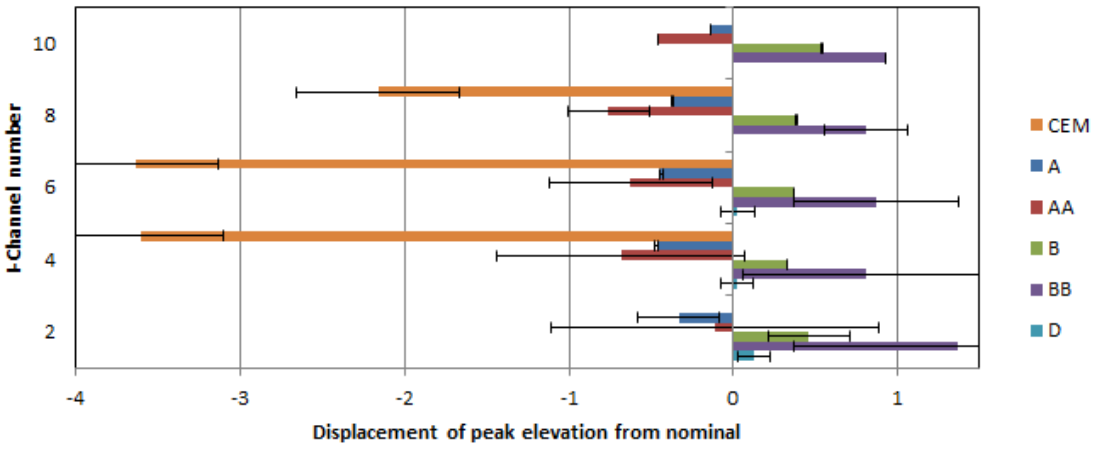

(b) I-channels.

Figure 6.15: Displacements of elevation peaks from nominal simulation predictions, for CATS CEM data and for misaligned simulations. CEM and D simulation data were not available for all channels and no C simulation data were available. Error bars approximate uncertainty introduced by technical issues and experimental offsets.

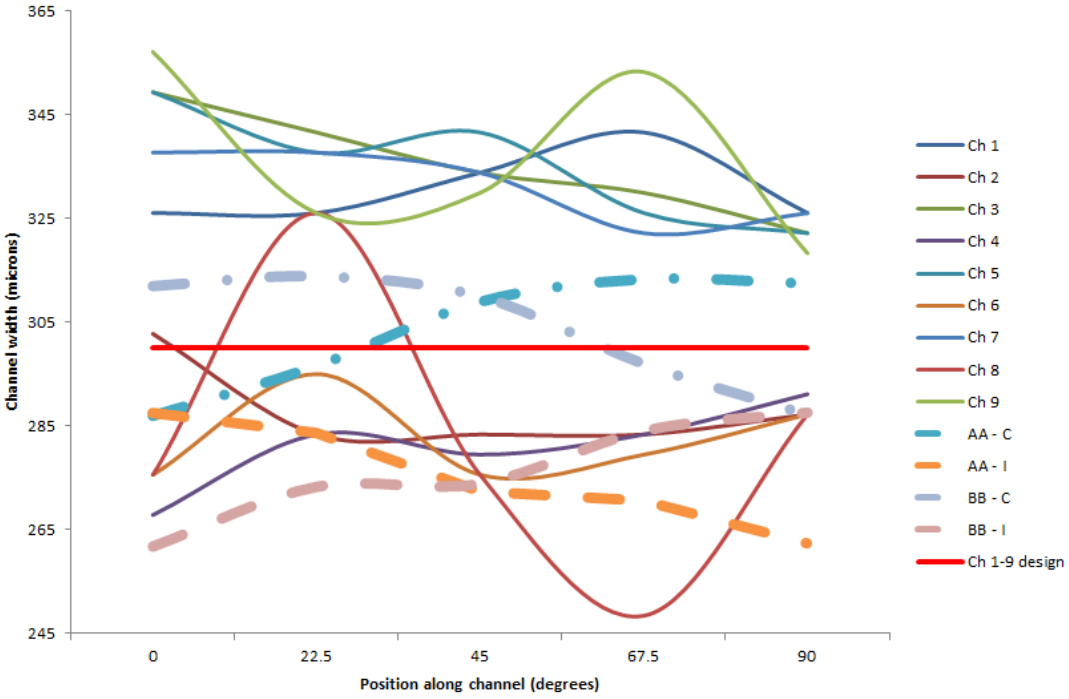

Figure 6.16: Channel width as a function of angular position around AA and BB misaligned fins simulations (dotted lines) shown alongside visually measured channel widths from figure 6.11 (solid lines).

When I first discovered this disagreement, I felt sure that it would be a mistake that could easily be reconciled. Both simulation and laboratory experiments had undergone many iterations of design, and their data had undergone many iterations of processing featuring several transforms in coordinate systems. A mix up between the positive and negative directions of the beam elevation, for example, would allow both results to be brought into agreement.

After rigorous checking and re-checking however I have been unable to find such a mix up. I can only conclude therefore that the peak elevation shift is attributable to a more subtle effect that I have thus far been unable to simulate or to measure.

6.5 Detector footprint

As well as allowing the signal from different CATS channels to be more easily separated, the CCD allowed the electron footprint across each channel to be studied.

Select examples of processed CCD frames from an I-channel voltage scan are shown in figure 6.17. It can be seen there how as the voltage supplied to CATS is increased, different channels transmit electrons and how their footprints have distinct and complex shapes. Such behaviour is of course a consequence of behaviour that has already been studied in the simulations. The simultaneous signals seen in channels 4 and 10 in frames B and C are a consequence of the overlapping K factors shown in figure 4.6a and ultimately caused by the extra-wide electrode spacing in channel 10. The asymmetry of an individual channel lengthways (i.e. up and down the page) is associated with a non-zero azimuth position—consider a slice through a single azimuth of figure 4.13g—and is indicative of the large offset induced by the CATS+CCD mounting in the peak azimuth mentioned in section 6.3.1. The variation (with voltage) in the channel 2 footprint between frames D and E is consistent with that expected from figure 4.12b and the slight feature at the bottom end of the footprint in frame E is consistent with the concentration of low energy particles at extreme z positions shown in figure 4.13c.

In CCD tests no electrons were observed exiting channel 8, although they were in the CEM tests. This will be discussed further in section 6.7.

Although the CCD data was patchy, some basic spectrograms summarising position

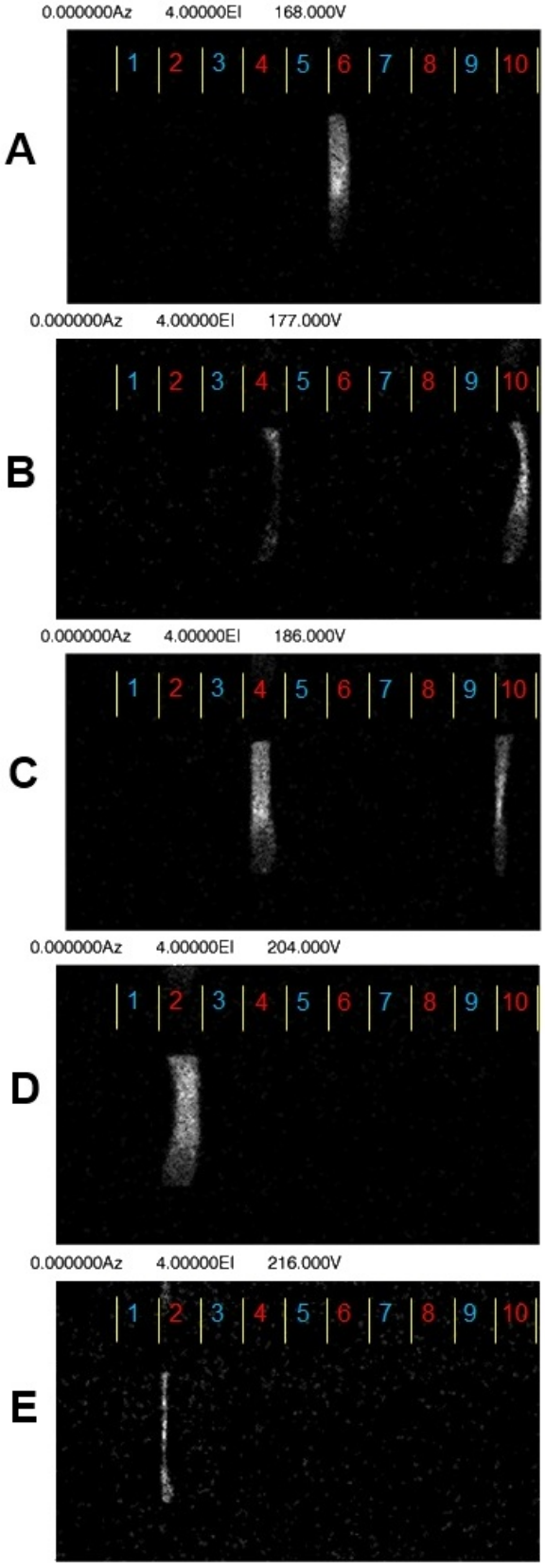

Figure 6.17: Select examples of processed CCD frames from an I-channel voltage scan under a 2.5 KeV beam.

information across the channel could be salvaged. Figure 6.18 shows the entrance Azimuth - exit Z variation across channel 5. The overall shape of the CCD results and

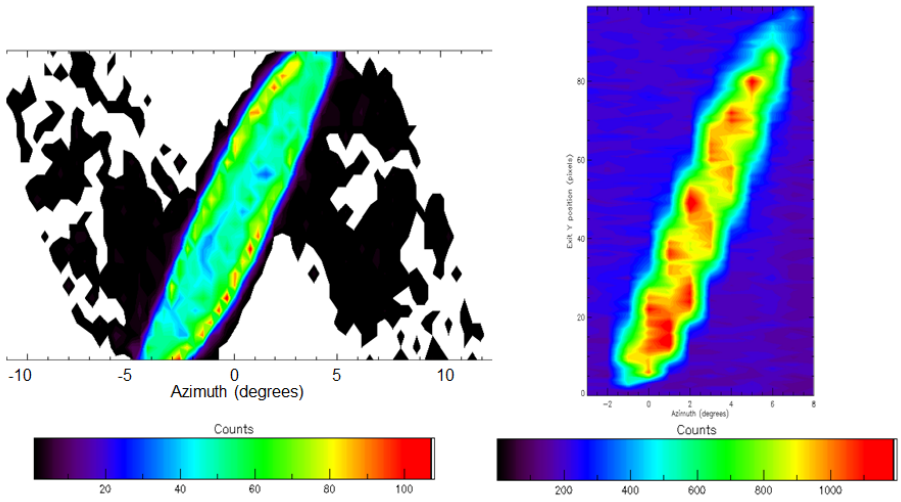

Figure 6.18: Azimuth - exit Z variation from simulation (left) and CCD (right). Axes are to scale with each other but absolute positioning may vary.

simulated results match and the size of the azimuthal offset can be seen. The CCD data is of low angular and energy resolution however so the more detailed features of the simulation cannot be compared. Figure 6.19 shows a similar situation for the entrance elevation - exit X variation across channel 5. The simulation records the particle positions immediately at the CATS exit aperture, whereas the CCD is spaced a few mm away. Figure 4.15 has shown that beams exiting the analyser diverge slightly, which explains why in both figure 6.18 and figure 6.19 the CCD result is spread longer in the spatial dimension than the simulation result.

6.6 Secondary electron contamination effects

Secondary electrons have been frequently mentioned, especially in respect to enabling CEM measurements for channels beyond the field of view, but for actual plasma instrument operation their presence is often unwelcome.

First discovered in 1902 by Austin and Starke [77], secondary electron emission refers to the low energy (tens eV) electrons released by a metal when it is exposed to higher

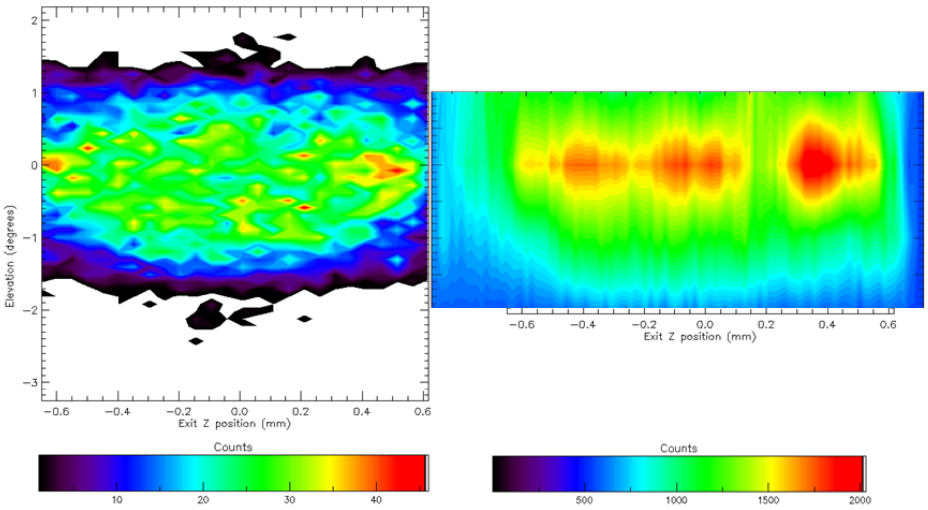

Figure 6.19: Channel 5, Elevation - exit X variation from simulation (left) and CCD (right). Axes are to scale with each other but absolute positioning may vary.

energy (hundreds+ eV) particles. Further studies [83] revealed three distinct processes that were producing these electrons, which can be seen in figure 6.20, a typical secondary electron spectrum from a metal.

The point S shows the peak of the 'true' secondary electrons. These are electrons from the metal's crystal lattice that have received sufficient energy to allow them to escape. The point R is at the energy of the primary beam and corresponds to primary electrons that have been elastically scattered through Coulomb interactions with the nucleus [107]. The section inbetween, from about 50 eV to point U, is attributable to rediffused primary electrons, those which have undergone inelastic collisions in the metal before reemerging.

High secondary electron emission rates were always expected in CATS because, unlike a top hat instrument, it does not have a fly-through geometry. Rather than passing out the other side of the instrument, high energy electrons that enter the aperture collide with the curved aluminium surface of the channels. In aluminium 85% of secondaries created are below 20 eV [20]. This is too low an energy to be detected by the CCD or the CEM. The CEM however, for most of the tests, was used with a +125 V accelerating potential at its front end. This improved its efficiency for lower energy particles, but also presented the possibility of secondary electrons contaminating the results.

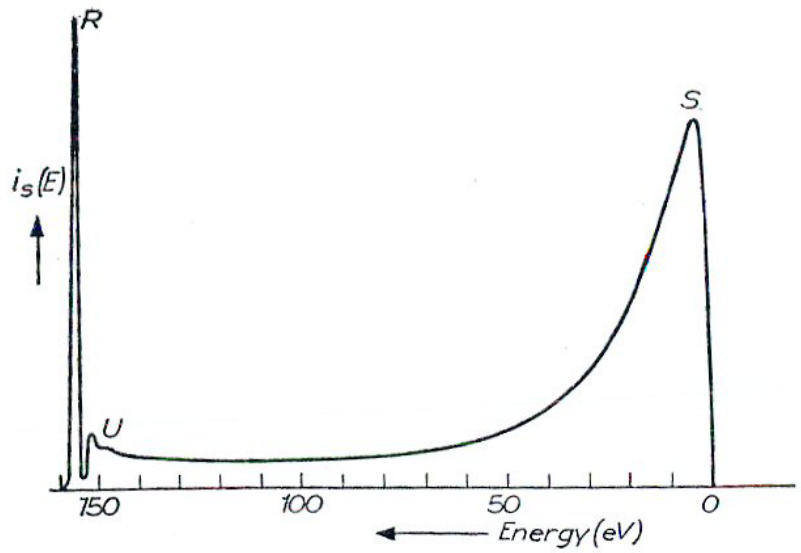

Figure 6.20: The general shape of the energy distribution of electons emitted by metal when exposed to a ~155 eV electron beam [54].

Figure 6.21 shows elevation-voltage spectrograms of channel 9 CEM data taken at different beam energies. While the scale and ranges vary between beam results, the

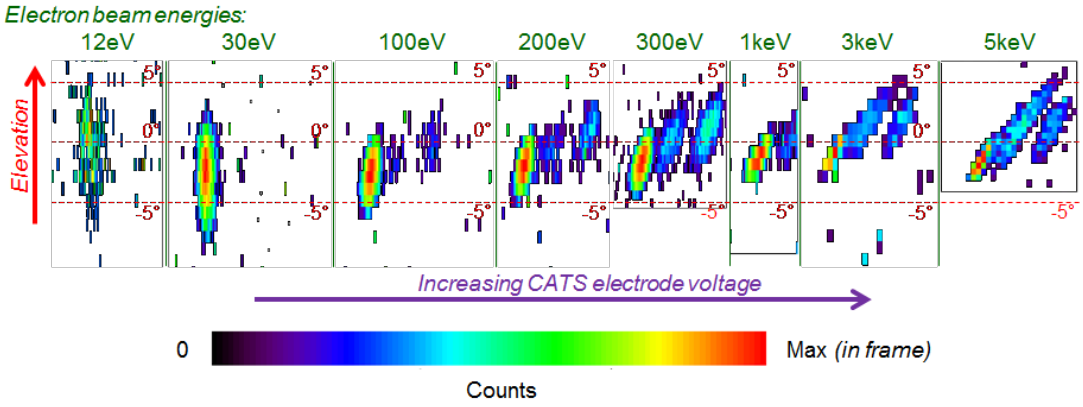

Figure 6.21: Elevation-CATS voltage spectrograms at central azimuth for different beam energies, with CEM positioned over channel 9. Secondary electrons from channels 7 and 5 can be seen at higher beam energies.

primary beam is clearly visible in red, green and yellow in the left of each frame. Since the frames are scaled to be approximately comparable, it can be seen that the shape of the response changes with beam energy. This is not a simulation predicted effect and is perhaps attributable to differing contributions of secondary electrons, as well as

perhaps to changes in the electron beam profile as the grid is deformed under higher beam voltages.

As the beam energy is increased, smears of blue can be seen to the right of the channel 9 primary beam, corresponding to the K-factors of channels 7 and 5. Since the CEM box aperture is aligned only to channel 9, these were thought to correspond to secondary electrons produced at the exit apertures of those channels. At keV beam energies the secondary electrons become diagonally extended in elevation and electrode voltage.

Figure 6.22 shows the 5 keV test again, first with the front of CEM set at the standard 125 V and then again with −21 V.

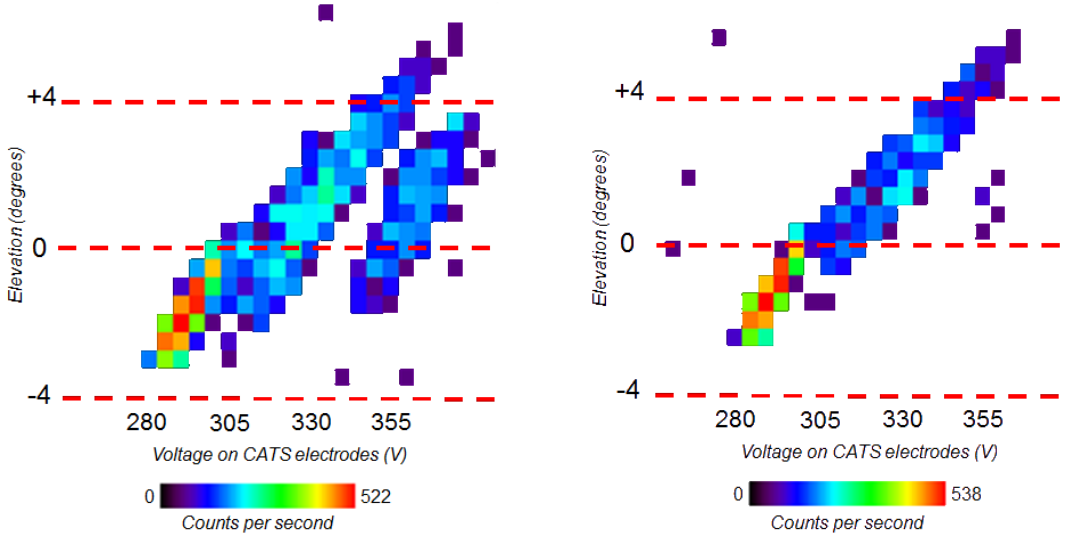

(a) Front of CEM at −125 V.

(b) Front of CEM at −21 V.

Figure 6.22: CEM results for CATS voltage-elevation tests showing secondary electrons produced when channel 9 is under a 5 keV electron beam.

With the negative voltage at the front of the CEM, secondary electrons are either deflected or retarded in energy to the point that the CEM is insensitive to them

With the secondary electrons removed, events at higher voltages are reduced, but a long smear remains extending into positive elevations, seemingly from channels 9 and 7. It is not entirely clear why this is happening but it must be an effect associated with rediffused or elastically scattered primary beam electrons.

6.7 Nickel source and light reflection tests

During the early vacuum chamber testing of CATS+CCD, the nickel source (used for the initial CCD testing in section 5.4.2) was placed in the CATS field of view.

While previously this source caused damage to the CCD, this time it was protected from the destructive higher energies since the only access to the detector was through CATS and thus the energies of electrons it received could be controlled.

It was these tests that initiated the development of the pulse-mode readout method. The pulse-mode method development was finished later however – during the electron beam testing phase – and although the intention was to perform further tests with the nickel source afterwards, ultimately time could not be found for it.

It has not been possible to extract a convincing spectrum from test data taken during this development process, since at this stage the image processing was done on-the-fly so the only data recorded per pixel per frame was a 1 for a supposed particle detection or a 0 for a supposed absence. Without the complete raw data frames the more advanced correction algorithms that were developed later could not be used here. Specifically the issues are:

- Since the thresholds were unknown so are the relative sensitivities between measurements.
- There appears to be a flatfield of noise across the frame that is not understood.
- The despiking routine was not implemented at this time.
- The detector sensitivity has not been measured above 2.5 keV and these results extend to 8 keV.
- The calibration of the relative geometric factors between channels has not been thoroughly studied.

Not all of these would need to be known as some could be inferred from the other. If time and facilities had been forthcoming, a test could be run that stepped the voltage so that each channel could consecutively be set to observe approximately the same energy

bandpass. If this were repeated at a few energies, and if all data were successfully recorded, many of the issues above could be resolved.

Some small insights can still be gained by looking at test data sets of individual voltages however, like those in figure 6.23.

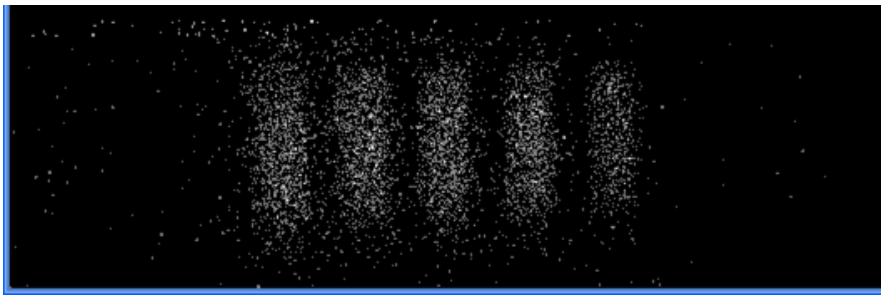

(a) C-channels in ascending numerical order.

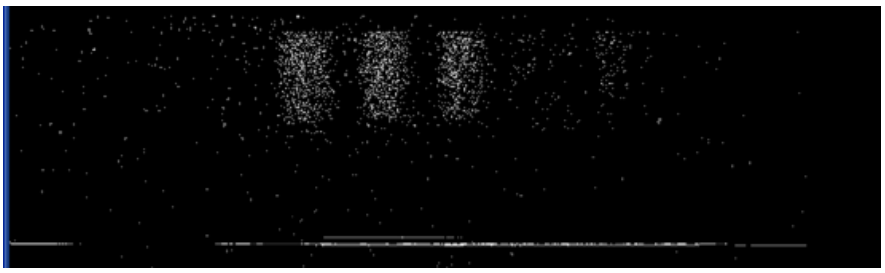

(b) I-channels in ascending numerical order. A readout electronics glitch has caused half of the frame to be cut and the noise at the bottom of the frame to appear. Channel 8 is seemingly blocked and channel 10 partially blocked.

Figure 6.23: Pulse mode CCD frames of electrons from nickel beta source as transmitted by CATS with 339 V applied (∼3.6 keV to 5.3 keV).

These correspond to a beta energy spectrum just below the starting energy of the curve in figure 5.15 which, if extrapolated back (as a straight line to zero), might be expected to show an increasing flux with increasing energy.

Figure 6.23a shows the reverse of this however, the higher energy channels appear to have a lower flux. This is expected though because the higher number channels have lower geometric factors (figure 4.6b) which decrease by a greater amount channel-to-channel than the (extrapolated) count rate increases. Also expected are the longer footprints at lower channel numbers, as seen previously in the simulations in figure 4.14b.

Figure 6.23b highlights some of the issues encountered in the CCD tests. It can be

seen how the frame has slipped so the channel footprints are no longer fully visible and how stripes of noise have appeared at the bottom of the image. The severe attenuation to channels 8 and 10 is clear here also. Although not intrinsic to the CCD, this effect appeared to be associated with the CCD setup as it was not observed with the CEM setup. Given that the problem persisted with the electron beam tests, the idea of a quirk in the Nickel energy spectrum could be disregarded. Additionally, as no appreciable current flowed between the CATS electrodes when 500 V was applied, any material forming a physical obstruction in a CATS channel would have to be insulating. Reflected light tests (figure 6.24) showed only a gradual channel by channel reduction corresponding qualitatively with the increasing channel length (and thus number of reflections required), suggesting such an obstruction would also have to be translucent.

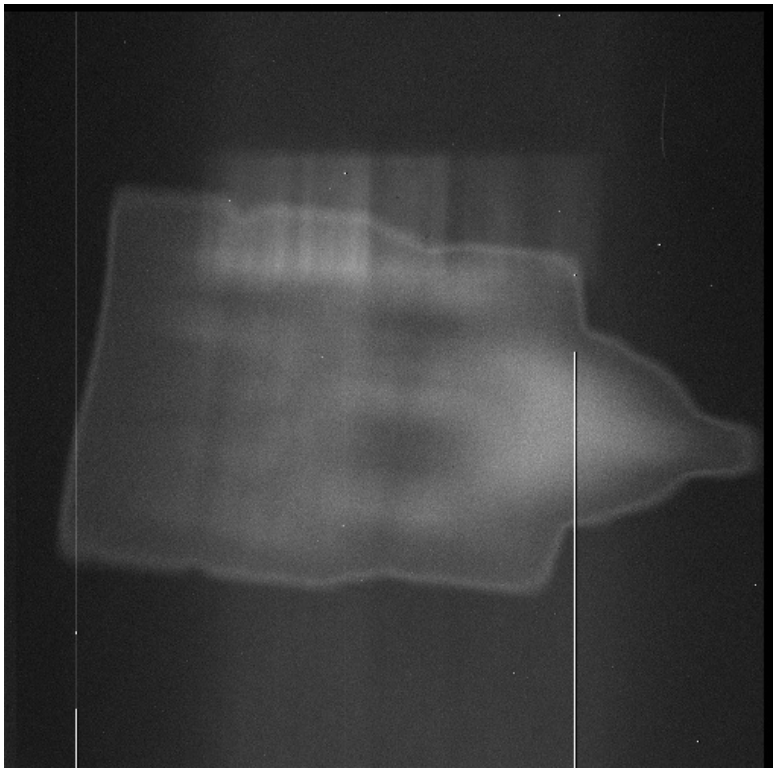

Figure 6.24: 1 second exposure from CCD+CATS setup with no electron beam and with the chamber door open exposing the setup to the room lighting. CATS channels are visible on the upper edge of the UCL logo.

No obvious cause was noted in the visual inspection (described previously in sec-

tion 6.4.1). The large flecks of swarf might possibly create electric fields which attenuate the passage of charged particles, but none were more obviously present in channel 8 or 10 than the others, the prominent example in figure 6.9b is in channel 9 (which showed no obvious attenuation). It is conceivable that the offending obstructions were dislodged as CATS+CCD was dismantled.

6.8 Tolerances

While CATS functions as an electron energy analyser, its response did not match the predictions because it was inaccurately made. The analyser can still be useful though, since careful calibration can reveal the true response.

The discussion of resolutions in SIMION in section 4.2.2 gives a clue to the tolerances required, relative to the average smoothness of the curves, to replicate the simulation results. It is shown there how a 12.5 µm difference in grid unit resolution can change the extracted angular resolutions by $\sim 0.2^\circ$ and the energy resolution by an equally small amount. Halving the difference in grid resolution approximately quarters the difference in response, so the error is minor. A 5 µm tolerance requirement in overall smoothness of parts would therefore allow for essentially perfect geometry comparisons between simulation and laboratory.

This is not to suggest that the simulation is entirely accurate, but that a design made to this accuracy would allow for a better assessment of the accuracy of the simulations as tolerances would not be a significant factor. Neither is this to suggest that such tight tolerances are required to meet typical instrument performance requirements. It is likely that they are not.

It has been shown however, in section 6.4.2, that the K-factor is very sensitive to the minimum channel gap along its length and this could be more problematic. If accurate K-factors are important, the electrodes should be aligned such that any deviations (due to the individual part tolerances or otherwise) do not create a minimum in electrode spacing more than a few µm below the nominal design.

6.9 Summary

Electron beam tests in the MSSL calibration chamber have revealed the CATS energy and elevation response peaks to be markedly different from those simulated in SIMION. The azimuth response was closer to the simulation results.

To investigate this unexpected behaviour the CATS fin electrodes were glued in place so the CATS channel dimensions and alignments could be scanned and measured. The channels were considerably different from their design specification and the unexpected K-factors were found to correspond closely to the narrowest point in the misshapen channels. The unexpected peak elevation response remains unaccounted for.

The detector footprint measurements behave largely as expected and brief CEM tests confirm the presence of secondary electrons and scattered primary electrons. The nickel source electrons were sampled with CATS+CCD but further testing is required before a spectrum can be produced

CATS channels 8 and 10 transmitted greatly attenuated particle fluxes throughout the CCD tests. Various reasons have been considered but none are conclusive.

This completes the description of the experimental work in this thesis; to put it into context, the next chapter will discuss applications of how CATS can be implemented as a flight instrument.

Chapter 7

Applications

This chapter discusses future applications of CATS and CATS-like analysers. This includes work conducted at Astrium Ltd, who part-sponsored my studentship and an introduction to PoleCATS, a student-led, educational flight project that will use CATS and the CCD.

7.1 A complete instrument

To create a space-bound instrument from the setup that has thus far been discussed requires that much of the laboratory-based hardware be recreated as smaller automated units that can interface with the required spacecraft. Figure 7.1 shows a block diagram of the components required for a typical instrument.

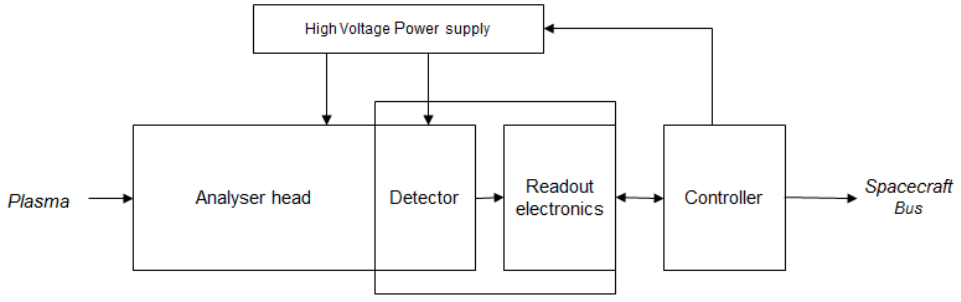

Figure 7.1: Block diagram of a typical plasma analyser.

The analyser head would be CATS and the detector would be CEMs or an MCP. A

CCD-based instrument would be slightly different and will be discussed in section 7.3. The HV power supply would be required to perform the role of the LeCroy HV unit and would need to operate from a low DC voltage supplied by the spacecraft. To sample wide energy ranges within a short duty cycle, it would need to be able to step between voltages quickly and smoothly. Any detector readout electronics required would need to be miniaturised and optimised for the selected detector, perhaps with ASICs (Application Specific Integrated Circuits). Finally, a controller would be needed to replace the functions of the controlling computers, and to greatly automate all the processes. As well as basic hardware control this could include part-processing and compressing the data. For more complex designs an FPGA (Field Programmable Gate Array) would be required; simpler designs could use a microcontroller.

7.2 Applications

Whilst previously section 2.1 discussed, in general terms, potential applications for highly miniaturised analysers, this section looks at more specific applications that have been considered for CATS.

7.2.1 Mission possibilities

While the concept of the CATS development is that it can be adapted to replace almost any existing analyser, some specific mission examples are outlined below.

Space weather

1 keV to 10 keV electron detectors have been recommended for some nanosatellite space weather monitoring beacons [56] and CATS and CATS-like analysers have been discussed as possible miniaturised particle sensors for future space weather missions [70]. A highly miniaturised magnetometer developed at Imperial College [98] would be particularly complementary and concepts have been discussed integrating a CATS-like analyser and the magnetometer together with an energetic particle sensor all on one PCB [72].

Magnetospheric research

Cross-scale and Magnetospheric Constellation have been mentioned in section 2.1.3 as potential multi-satellite magnetospheric research missions that were ultimately not selected for flight development. Eckersley et al have produced a basic, high-level study [33] showing a possible nanosatellite based, Cross-scale-like mission based on a plasma analyser developed from CATS, and other similarly miniaturised instruments. The assumed analyser for this study would, like CATS, be a combined electron and ion instrument, would offer mass power and volume savings of ∼90% compared to the proposed instruments for Cross-scale and would be available by 2020 at the latest. The study found that with 12 nanosats with just the electron/ion analyser, and the miniaturised magnetometer (and no other instruments), could achieve over 30% of the Cross-scale science objectives, with considerably reduced cost and complexity.

Jupiter

CATS and CATS-like analysers have also been discussed as ideal candidate instruments for the forthcoming JUICE (JUpiter ICy moons Explorer) mission to the Jupiter system [71]. A significant challenge of this mission is the harsh radiation environment that it would be operating in and the requirement for a 4π sr field of view. The low geometric factor of CATS-like instruments would be well suited to this environment however.

Demonstrating Highly Integrated Instruments

A highly integrated space weather package using CATS has already been discussed above. PRISM (Payloads with Resource-efficient Integration for Science Missions) is another integrated system. It is a collaborative project between Astrium, SciSys, Imperial College and MSSL, that centralises the processing electronics for an MSSL Extreme UV Imager (EUI) and an Imperial College magnetometer to save spacecraft resources and to offer operational advantages [34].

An option could be that the EUI be exchanged for a miniaturised plasma analyser, as its data rate is lower and, like the magnetometer, it is making in-situ measurements, which might make for a more natural partnership of instruments.

7.2.2 A CubeSat instrument

Section 2.1.1 has mentioned how CubeSats are a potential platform for miniaturised plasma analysers. During the CASE placement at Astrium, that formed part of my PhD, I considered how CATS-like analysers might be used with CubeSats [12].

It was assumed that the analyser and electronics could be assembled onto a single card (figure 7.2) and a provisional version of the UKUBE-1[1] payload interface document (PID) was examined for potential incompatibilities and issues [11].

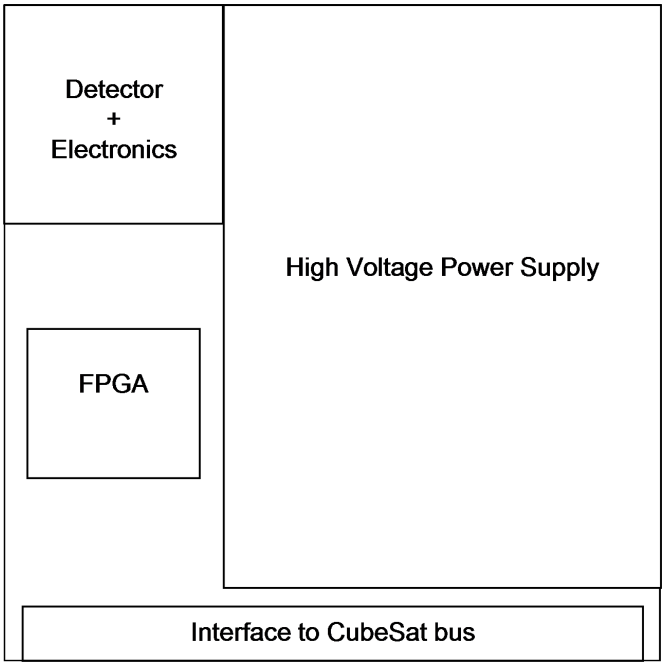

Figure 7.2: Possible 90×90 mm CubeSat board layout.

All the PID requirements were deemed achievable, but the most challenging were thought to be:

- Orbital average power available: 600 mW
- Mass: 0.4 kg
- Data: 300 kb/orbit

The power and data limitations would likely mean the analyser would be used only on short sections of the orbit, perhaps over the poles. While the mass limit is realistic,

[1] http://www.bis.gov.uk/ukspaceagency/missions/ukube-pilot-programme

any centre of mass restriction imposed on top of this could present issues (a specific UKUBE requirement for this was TBC on the PID used).

A unique advantage of a CubeSat-based plasma analyser, that became apparent during this study, is that (schedule permitting) the entire satellite can be fitted into the MSSL electron calibration facility, allowing the instrument to be calibrated from within the spacecraft. This would allow for spacecraft induced effects to be included as part of the calibration.

It is highly likely that if a CubeSat instrument were developed, or if funds became available to do so, then a flight opportunity would be easy to find—indeed offers to this effect have already been received.

Some of the mission concepts listed in the previous section could be implemented as a CubeSat mission and these and others are summarised in table 7.1. None of these missions stands out especially above the others, but they could be selected as opportunities dictate.

7.3 PoleCATS - a student sounding rocket experiment

This section discusses the destination of the actual CATS components that have been discussed in this thesis. Specifically the CATS analyser head and CCD detector combination, which are being recreated as PoleCATS[2], a selected mission for REXUS 14 (Rocket-borne EXperiments for University Students)[3]. This is a student payload opportunity on a low altitude sounding rocket to be launched from Esrange in Sweden in the first half of 2013. Since funding was initially very limited, and available development time equally so, the component options were also limited. The CCD (using the short integration acquisition mode) was the detector selected to be used with CATS, primarily because it was available and working, and because it does not require high voltages and high vacuums. Its novelty as an electron detector also made it a more interesting candidate for what would essentially be a technology demonstration mission. The trade-offs that were considered for the detector choice are shown in Table 7.2 and are discussed below.

[2]PoleCATS – The Polar test of CATS – www.rexuspolecats.com

[3]www.rexusbexus.net

Table 7.1: Possible CubeSat missions for CATS or a CATS-like analyser [12].

Configuration	Comments	Costs	Size	Science value	Advantages	Disadvantages
Single analyser head – CATS or similar – flown on a CubeSat.	Primarily technology demonstration.	Low.	1U.	Low.	Simplest option, all MSSL technology	Achieves little beyond tech. demonstration.
Space Weather Package: MSSL plasma analyser, ICL fluxgate magnetometer and Surrey energetic particle detector all on one CubeSat bus compatible PCB.	There has been little progress reported on this so far.	Medium.	1U	Medium.	Best value for resources if all instruments required. Generic solution intended to be suitable for all CubeSats.	Otherwise resource hungry. Not ideal configuration for science (i.e. mag not necessarily on boom, not full FOV for plasma analyser).
PRISM: Payloads with Resource-efficient Integration for Science Missions. Currently with an ICL magnetometer and an MSSL EUV imager.	Might be adaptable for use in CubeSats with suitably miniaturised instruments, i.e. plasma analyser and magnetometer.	Medium.	1-3U.	Medium	Breadboard setup exists already. Astrium have shown interest.	Not originally intended for CubeSats and plasma analysers.
Multiple plasma analysers: analyser heads pointing out all sides of the CubeSat for all-sky FOV at multiple energies and electrons and ions.	Useful for magnetospheric science.	High.	6U.	High: especially if you can get a magnetometer or two on it as well.	Comprehensive. Could be useful for X-scale type multi-point missions.	Complex: lots of calibration required Instrument may not be sufficiently refined at this stage to do 'useful science'.
Auroral study: Plasma analyser and UV imager.	Leicester university have interests here.	Medium.	1-3U.	Medium: Compare auroral oval plasma and photons.	Fairly simple instruments. Earth Images are good for outreach. Has good science purpose	Requires pointing at Earth. High bandwidth required for images.

Table 7.2: Trade-off table for a detector for the CATS plasma analyser on an instrument for a REXUS sounding rocket

	Faraday cups	**MCP**	**CEMs (current mode)**	**CEMs (pulse mode)**	**CCD**
Approx minimum detectable energy	1 eV.	1 eV.	1 eV.	1 eV.	1 keV (electrons only).
Simultaneous CATS channels usable.	10	5 (either electrons or ions).	2–4 (insufficient space to fit 1 per channel).	2–4 (insufficient space to fit 1 per channel).	5 electrons (CATS ion energies too low to be detectable).
Number of incident particles required for data point	6x10^6 per pA.	1	6 per pA.	1.	1.
Vacuum Required	No.	1×10^{-6} mbar.	$< 1 \times 10^{-5}$ mbar.	1×10^{-5} mbar.	No, although cooling could cause condensation.
Outgassing issues	No.	Yes, would need to be in vacuum from launch or a very large pore MCP (rare).	Fewer.	Fewer.	No.
Read out electronics	Femto/pico ammeter per channel.	Pre-amp + shaping amp + counter per channel.	Nano ammeter (floating at high voltage.	Pre-amp + shaping amp + counter per CEM.	Clock controllers etc.
Power supply	Low voltage.	∼2 kV to 3 kV, 30 µA.	∼1 kV.	∼2 kV to 3 kV, 30 µA.	32 V.

The Faraday cup, which would simply collect incident electrons on a collector plate electrode and measure their current directly, was ruled out as being insufficiently sensitive to the low fluxes of particles we expect to find. MCPs presented serious complications with respect to vacuum requirements. To prevent electrical arcing in an MCP, the tiny glass pores of which it is made must be free from air and moisture when it is in operation. To achieve this it needs to be under vacuum for a prolonged period of time to allow it to out-gas. For a satellite based instrument, which operates in the vacuum of space for long periods of time, this is easily accomplished. The REXUS rocket however will not be in atmosphere that is sufficiently thin with enough time for the MCP to out-gas and take measurements. To overcome this the MCP could be hermetically sealed and under vacuum prior to launch with a mechanism that releases a sealing door at the appropriate pressure/altitude, however this was deemed too complicated and risky for this instrument.

CEMS were the second choice of detector for the instrument. They have less strict vacuum requirements, are commonly used in low energy space plasma analysers and have already been used with CATS. They could be operated in 'pulse mode' where they would perform like an MCP (only position insensitive), or in a current mode where they would operate similarly to the Faraday cup option but with electron multiplication. Although they are available in many sizes and configurations it is unlikely that we would find an affordable and workable solution that would allow us to use more than a couple of the CATS analyser channels since the channel exit apertures are very closely spaced, and one CEM would be needed to cover each aperture. Like MCPs, CEMs require kilovolts applied to them during operation, which complicates the design of the power supply unit and is considered very unfavourably by the rocket operators. The lack of a high voltage requirement from the CCD was thus another of its attractive qualities.[4]

The disadvantages to using the CCD, apart from its highly experimental nature, are that it is not sensitive to the lower energy electrons that MCPs and CEMs are able to detect. It is also very sensitive to photons, which the CATS analyser is not optimally configured to reject, and to temperature, although this will be mitigated with Peltier

[4]Although high voltages are still required for the CATS analyser head, these are still several times lower that those demanded by MCPs and CEMs.

coolers. Also the data will require significant processing, but since the instrument will be recovered post-flight, all the raw data can be written to flash memory for processing on the ground. Since quality science data is not a high priority of the project, compared to education and technology demonstration, these disadvantages have been considered acceptable in view of the simplifications they enable and the novelty of the setup. The main challenges are thought to be stray light reflections through CATS, low populations of electrons and short mean free paths of the electrons at the altitudes visited.

7.3.1 Electrical overview

The PoleCATS electronics has been designed in detail by Alexander Edwards-Smith and is shown in overview in figure 7.3.

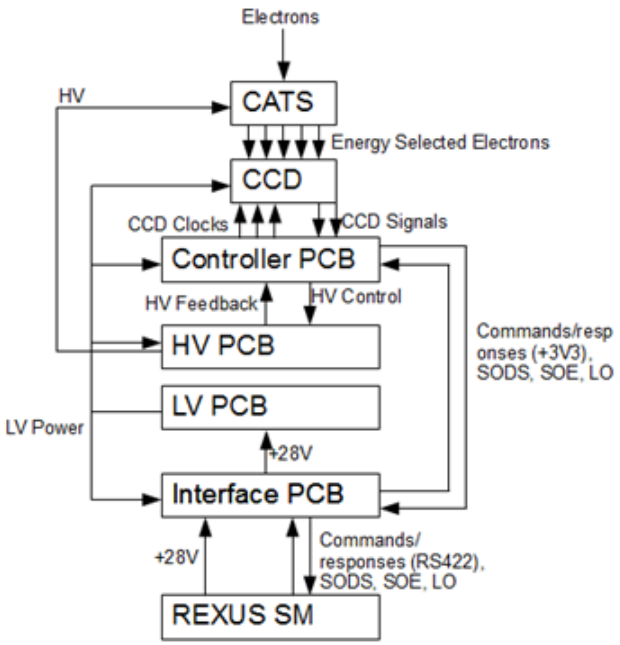

Figure 7.3: PoleCATS electronics block diagram, [81].

It is based around the PC/104 specification as it is a convenient format and aides the design being adapted for CubeSat use in potential future projects.

The controller PCB is responsible for overall control of the experiment. It provides CCD control and readout through a AD9920A CCD driver IC, storage with an SD

card and the main payload controller, a 16-bit PIC24EP512GU810.

The HV PCB converts input power from the unregulated REXUS 28 V power to voltages from 0 V to −500 V for the CATS electrode, allowing electrons with energies up to 8 keV to be sampled. It is controlled by an analogue voltage supplied from the payload controller.

The LV PCB supplies every other voltage PoleCATS requires and contains hatch actuator and Peltier cooler drive circuitry and connectors. The Interface PCB handles communications to the REXUS service module (SM) and has a backup storage SD card

The experiment is expected to have a peak power draw of 17.5 W of which 11 W is for the Peltier coolers and 2.6 W for the hatch actuator (in a stalled state) [81].

7.3.2 Mechanical overview

The PoleCATS mechanical components have been designed in detail by Anna Daurskikh and Matt Hills and are shown in overview in figure 7.4.

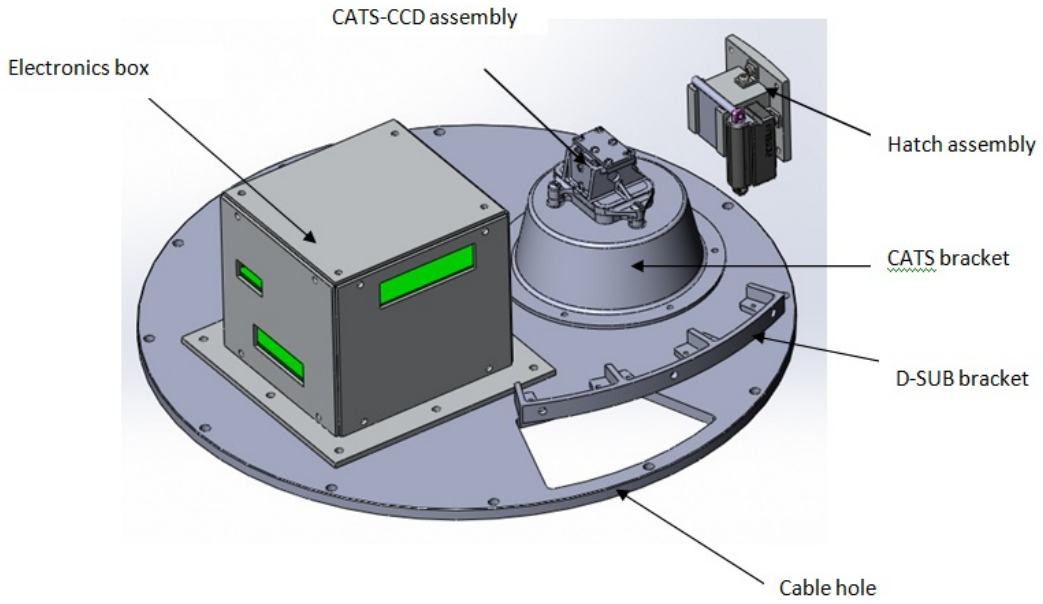

Figure 7.4: CAD image of PoleCATS experiment mounted on rocket payload bulkhead [81].

The experiment is projected to weigh ∼2 kg and consists of three main parts; the electronics box, the hatch assembly and the CATS+CCD assembly. The electronics box is approximately equivalent to a CubeSat chassis and contains the 4 PCBs discussed in the previous section.

While initially the intention was to simply have a small aperture in the rocket skin, the hatch assembly was recommended by the REXUS staff so that the payload could be protected from the hot gases that would stream in during lift off and re-entry. The shutter will be made of Perspex so that if it jams or if the actuator fails, then light will still be able to reach CATS. This will allow the stray light reflections to be measured so at least the background noise can be studied.

The CATS assembly contains CATS, the CCD, the Peltier coolers and heat-sinks and is shown in figure 7.5.

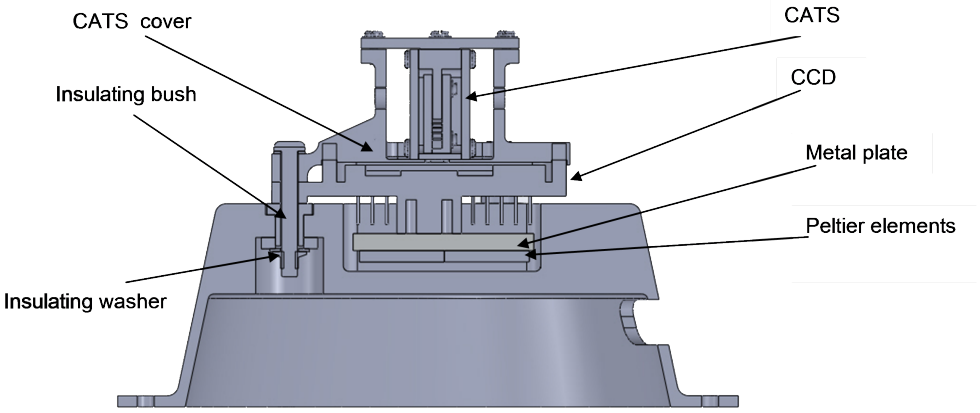

Figure 7.5: Cross-section of CATS assembly; CATS+CCD on the 'flowerpot' bracket [81].

CATS is mounted on the CCD through a new bracket that holds it securely in place over a undamaged portion of the CCD, with the rest of the sensor completely covered. This entire assembly is cooled to 10 °C or lower by two[5] Multicomp model MCHPE-071-10-08-E Peltier coolers, which are mounted inside the 'flowerpot'[6] bracket. CATS and the CCD are thermally isolated from the flowerpot which is used as the thermal reservoir for dumping heat from the CCD. The flowerpot is additionally thermally isolated from

[5]For redundancy.

[6]So-called because in the initial designs it closely resembled an upturned flowerpot.

the rocket bulkhead, as this is known to heat up considerably during flight [81].

7.4 Summary

The components required to convert the laboratory breadboard setup into a flight instrument – a miniaturised HV power supply, readout electronics and an experiment controller – have briefly been introduced. Different applications for CATS have been considered including magnetospheric research, Jupiter missions and demonstrations of highly integrated instrument technologies. A CubeSat compatible instrument has been discussed in a number of configurations, with mass, power and data rate identified as the key challenges. Finally, PoleCATS, an instrument that will fly CATS and the CCD on a sounding rocket has been discussed in more detail. The CCD is ideal for this mission since it does not have requirements for vacuum conditions or high voltages.

Chapter 8

Conclusions

To complete the thesis, this chapter brings together the conclusions from throughout the work and arranges them under the different themes of the research. Finally ideas and recommendations for extensions and follow-on projects are suggested.

8.1 Highly miniaturised analysers

This project has considered how space plasma analysers could be miniaturised, and how they might be made with MEMS. The following conclusions have been made:

- MEMS plasma instruments require simple geometries, e.g. planar or cylindrical.
- EDM can make analyser components on MEMS scales, but not necessarily with MEMS tolerances.
- To be closely comparable with simulations, the tolerance in deviations of the curved surfaces (in CATS-scale devices) should be 5 µm or less, and the tolerance in electrode alignment about half that.

8.2 CATS

CATS, a prototype for a highly miniaturised analyser, has been designed and tested. The following conclusions have been made:

- The CATS design has the instrument parameters given in table 4.2
- The EDM CATS prototype differs from the design due to variations in the fin widths up to ∼10 µm and variation in fin spacings up to ∼30 µm.
- Consequently the instrument parameters also vary, the C-channel K-factors being ∼ 6% below nominal, and the I-channel K-factors being ∼ 11% above nominal.

8.3 SIMION simulations

SIMION charged particle optics software has been used extensively for simulating CATS. Further conclusions specific to this, and arising from this, are listed below:

- SIMION trajectory qualities of TQ=10 or higher are required for fully optimised CATS simulations.
- 6.25 µm sized SIMION PA grid units are acceptable for CATS simulations, although a smaller size would be optimal.
- The attractive side-plates of the I-channels create a more uniform and precise response compared with the repulsive side-plates of the C-channels. The C-channels however allow for greater numbers of particles to be transmitted, i.e. have larger geometric factors.
- Collimation applied to the C-channels will allow for an approximation of the best instrument parameters of both I and C channels.

8.4 Electron detecting with a CCD64

A back-illuminated, ion-implanted CCD has been used for directly detecting low energy electrons with CATS. Conclusions specific to this are listed below:

- The e2v CCD64 is an effective detector of low energy electrons.
- With a pulse-mode readout method it can detect electrons of energies of at least 800 eV.

- With a current-mode readout method it can detect electrons of energies of at least 500 eV.
- Cooling is required for extended periods of operation in vacuum, to prevent excessive dark current.
- 67 keV electrons can cause permanent ionisation damage to the CCD.
- Since, unlike CEMs and MCPs, the CCD does not require a high vacuum it is a convenient detector for use on a low-altitude sounding rocket mission.

8.5 Future work

This section makes suggestions and recommendations for how this research could be extended and followed up.

8.5.1 Optical blacking for CATS

CATS currently has highly-reflective interior surfaces that can cause light to reach the detector and contaminate the electron readings. Typically treatments such as Ebanol-C blacking are applied to low energy electron analysers [2]. Ebanol-C produces an electrically-conductive, matte-black, fur-like surface of tiny filaments that trap photons. This was considered for PoleCATS, but since CATS has much narrower channels and electrode spacings than conventional instruments there was deemed a risk that, if coated with Ebanol-C, the fields would be adversely affected and electrical arcing may be a problem. Preliminary discussions with Acktar[1] suggest that they might be able to supply a much thinner surface coating that is black and electrically conductive [109]. This coating could be tried with CATS to see how effective it is.

8.5.2 CATS II

CATS is primarily a laboratory-based prototype. A successor would likely be made as a flight instrument and this should be optimised for instrument parameters appropriate to the plasma population of flight environment, or for a range of environments if the

[1] www.acktar.com

flight is unspecified. Such a successor should be developed in much closer co-operation with space plasma physicists, the end-users.

If this were to be made by EDM, more informed discussions could now be had with the manufacturer on tolerances, accuracies and designs. Any relevant new capabilities in EDM can be considered and design improvements implemented, e.g. ensuring the alignment of the fins can be measured visually prior to closing up the box (i.e. fitting the fin-less Matsuda plate).

MEMS plasma analysers should also be re-investigated with respect to new MEMS techniques available. It would be beneficial to think again, and more openly, on possible MEMS plasma analyser ideas. My approach before was to adapt the ideas seen in previous space instrumentation to a MEMS compatible design. There might be much insight to be gained however from looking at the problem from the other direction: seeing what MEMS charged particle optics exist, and how they can be adapted into a design compatible with analysing space plasmas.

There are many applications of charged particle optics in MEMS, from inkjet printer heads to the MMS instrument (discussed in section 2.3.2). Working collaboratively with experts from such fields might bring forth concepts for MEMS plasma analysers that might never have been considered previously.

8.5.3 Simulation extensions

An underlying limitation with much of the simulation work was SIMION's usage of RAM (random access memory). To fly virtual particles, the entire PA must be loaded into memory. To model curved details with precision, the grid unit size must be small, so the number of grid units required is large and so is the amount of memory required. The simulation computers were well specified (with 8 GB of RAM) but SIMION 8.0, using 32-bit addressing, is limited to only 2 GB of RAM per PA and so the limits this imposes on PA size and resolution were frequently encountered.

The recently released SIMION 8.1 however, uses 64-bit addressing which allows it to assign 190 GB of RAM to each array. It also has additional tricks for minimising the memory required for each array[2] and since it now supports parallel use of multiple

[2]Such as additional symmetry options and cuboid grid units.

processor cores[3] the relative time taken for a given simulation is reduced compared with version 8.0.

With a sufficiently high specification PC, this could revolutionise the way plasma analyser charged particle optics simulations are performed. SIMION has the ability to convert .STL (stereo lithography files) output from CAD software into PAs. While I attempted to use this for CATS the resolution was too low to be useful. With the RAM limit lifted however, much higher resolutions could be used. If it were found to be accurate and reliable, this technique would save the tedious need to create .GEM files. Additionally, the instrument scientist making the CAD files could interface with the design engineer with greater lucidity as they iterate the actual CAD design files back and forth. For further clarity and testing pre-manufacturing, the .STL files could be printed on a 3D printer. Conversely the manufactured pieces can be 3D laser scanned [15] and that model fed back into SIMION, although the current, world-class, UCL facility for this would not offer sufficient accuracy to usefully map the inaccuracies discovered in the CATS electrodes.

With the RAM limitation lifted, the highly automated simulations discussed in section 4.4 could be greatly enhanced, as they could be performed at greatly increased resolutions. The scope of the geometries available could also be increased.

Adding flexibility to automated solutions tends to decrease the computer resource usage efficiency, as it is no longer optimised around one scenario. With increased computing resources available however, efficiency is not so important.

There are additional ways that the simulations could be extended. Gershman and Zurbuchen have shown that, with some clever extensions, SIMION can be made to model stray UV light reflections in electrostatic analysers [49]. This method could be implemented, and quite possibly extended, to include secondary electron simulations. An additional, and perhaps more speculative, extension would be to build tolerance analysis into the automated geometry system, as I have done in a previous project [9]. Through working with manufacturers and engineers, the tolerances and their probabilities of occurrence could be quantified and used to automatically create many different analyser geometries with randomly introduced manufacturing errors. Each of these

[3] Additionally support for GPUs is likely to be made available soon as a free update.

analysers would go through the standard simulation process and their instrument parameters compared so the uncertainty of the parameters could be quantified prior to manufacture. Perhaps the most useful extension to add to any simulation package would be to work with space plasma physicists to simulate the instrument's use in space, sampling plasma distributions typical of the environment for which it is designed, and extracting the moments of that plasma distribution. A simulation setup of this character is described by Kessel et al in [74].

For very large, high resolution simulations, modern desktop computers would be insufficiently powerful and time would be needed on very high performance computers running MS Windows[4]. A cost efficient and effective way to do this could be through cloud computing services, such as Amazon Web Services, which are used for scientific applications in other fields [31, 69]. Such services provide a 'pay as you go', remote desktop connection over the internet, to a virtualised machine with a specification and operating system of your choice. I have already successfully set up and demonstrated SIMION on this service. One of the tantalising possibilities of this system is the ability to automatically produce additional virtualised machines on-the-fly. This would allow the automated simulations that are described above to initialise as many virtual computers as they need so that all the simulations can be performed simultaneously, in parallel. This would allow the entire operation to be performed extremely quickly for a similar cost as it would be if it were run serially on one virtual machine. The design optimisation routines shown in figure 4.16 would still need to be run serially however. Such large-scale projects would, of course, benefit from the input of more experienced and formally trained software engineers who could ensure it was set up in a way that was formalised, efficient and suitably documented.

Alternatively, a more mathematically inclined person might be consulted to research a more elegant, and less computationally elephantine, solution.

[4]No Linux version of SIMION exists and it runs slowly in Wine. Virtual Windows machines on a Linux system may work.

8.5.4 Extended CCD64 testing

The CCD64 was available with several different surface treatments applied to it—different 'flavours' as described in [114]. While their relative performances for x-ray detection have already been assessed (and found to be very similar) [114, 122], their effects on electron detection are unknown and their study would be of interest, perhaps a suitable project for a masters student.

An improved setup would be highly desirable, ideally with:

- A temperature-controlled Peltier cooler (like that used for PoleCATS), to enable long duration tests with stable sensitivity.[5]
- A wider range of beam energies available for the electron energy response testing.
- Reliable readout electronics – perhaps PoleCATS spares.

8.5.5 Alternative silicon-based detectors

For longer term developments, silicon-based devices are a very attractive choice for highly miniaturised plasma analysers. The principle advantages are that they do not require high voltages, and that they can easily detect electrons and ions simultaneously. Techniques like delta-doping [59] allow the silicon dead layer to be reduced to a few nm in thickness, allowing ions with energies as low as 700 eV [66] and electrons with energies as low as 50 eV [97] to be detected. Delta-doping has been applied to CCDs, EMCCDs [62] , SSDs [96] and CMOS [60] detectors which have variously been demonstrated to be effective detectors of low energies of molecular and atomic positive, negative and neutral particles [51, 66]. Additionally silicon photodiodes [44, 45, 108] and avalanche photodiodes [99, 100], with thin dead layers have all been demonstrated as effective detectors of low energy electrons and ions.

Looking further to the future, for MEMS plasma analysers, silicon detectors can be built into the structure of silicon-based devices. Like their conventional-scale counterparts these could be Faraday cups, secondary electron multipliers, or p-n junctions. Faraday cups are the simplest and have been demonstrated in the MMS (discussed in

[5] This was not done initially due to vacuum compatibility concerns.

section 2.3.2). MEMS secondary electron multipliers are discussed as a future feature of the MMS in [57], where they envisage electrodes arranged to form a voltage cascade, supplied by a metal thin film resistor. P-n junctions are the fundamental technique used in the silicon photodiodes, and similar, discussed above.

8.5.6 Improved CCD-based calibrations

The great advantage of the CEM setup, was that it could be left in unattended operation for days, allowing very highly detailed datasets to be garnered (like that displayed in figure 5.8). Although this level of detail is not a priority for instrument calibrations for space plasma physics purposes, it is of academic interest to me as it offers the capability of assessing the accuracy of the very high resolution simulations that I have been producing.

To produce an equivalent level of detail in the CCD-based calibrations requires many of the detector modifications discussed in section 8.5.4, i.e. higher energy particles, continuous cooling, reduced ionisation damage and reliable electronics.

Additionally the control and coordination could be improved by merging the separate CCD and Control PCs into one PC with updated hardware and software[6]. Multi-core processors can handle performing several complex tasks simultaneously, LabVIEW-based GUI control systems offer more intuitively extensible control and automation, and more recent operating systems offer fast and effective remote desktop connection controls for offsite operation.

Based, in part, on previous experiences automating hardware setups with LabVIEW [10], I would make the following recommendations for a LabVIEW control system;

- Use of TDM file format (or similar). This is hardbuilt into LabVIEW and has a hierarchical file structure that arranges data in highly organised and intuitive data sets, and allows for highly detailed file headers. Tools could be made to convert these TDM files into IDL and Matlab structures for more detailed later analysis.

[6] A practical difficulty here would be acquiring modern Windows and LabVIEW drivers for old hardware. The alternative, updating the specialised pieces of laboratory hardware, might be too costly to justify.

- Automatically fill file headers or prompt the user for an input where that is not practicable. The present system requires the user to remember to update fields in a text file.

- Provide feedback to the display. Not just the current state of the program but, where possible, basic on-the-fly data analysis and estimated time remaining. This saves time by allowing issues to be identified early in a test.

- Regularly save and checkpoint results, to prevent data-loss in the event of sudden failures.

- While all key parameters should be logged in the TDM file header, inexpensive webcams can also be pointed at key areas, such as cable patch panels and display screens (of devices independent of the PC). These can take regular, time-stamped images of negligible file-size, allowing experimental conditions to be verified at a later date. Camera screenshots can be displayed at the start of a test run so the user can verify that their views are unobstructed and in focus.

A control setup not dissimilar to that which I describe here has been set up for the LEPIC (Low Energy Plasma and Ion Calibration) system, currently being used to calibrate the EAS instrument [27, 88].

8.5.7 Alternative charged particle sources

A radioactive source offers an ideal test for CATS. If time had been found for further testing with the nickel source, it would have enabled a very interesting test of the CCD response and of the issues involved with using CATS to make real measurements. Such an experiment could produce interesting data on the rarely-studied, lower energy end of the nickel source energy spectrum. Tritium, which has previously been used as an analyser calibration source [67], emits electrons up to an energy of 18.6 keV and would be better suited to the CATS energy range, were such a source to be available.

An area entirely open to investigation is the assessment of the CATS and the CCD response to ions.

8.6 Closing remarks

We, the space plasma community, have not yet arrived at a fully integrated MEMS plasma analyser; but CATS marks a milestone along the road. This chapter has discussed some of the steps that could be taken for the continuing journey.

With the continuing progress of MEMS technology, plasma science and space technologies, I believe that these instruments would be capable of opening up new applications and new science at an unprecedented range of magnetospheric scales, and could be commonplace within ten years.

Acknowledgements

This PhD was funded by a CASE Studentship between STFC and Astrium Ltd, with additional personal funding support from the Worshipful Company of Scientific Instrument Makers. All of these parties deserve additional thanks for their extremely generous additional sponsorship that has made PoleCATS happen.

Specifically, I wish to thank:

- Dhiren Kataria, whose vision conceived this project and whose imagination, support and patience kept it going.
- Alan Smith, who made it all possible.
- Steven Eckersley, who showed me the other side of the fence.
- Dave Walton, who remained unharassed by my harassments.
- The design office, who were able to convert my mumblings into designs.
- The mechanical workshop, who were able to convert the designs into components.
- Arrow Lee, for advice, proof-reading and incredible efforts leading PoleCATS.
- Glyn Collinson and Andy Walsh, for advice and wisdom.
- Carl Singer Saunders, for his expertly timed jab to the ribs.
- Gareth Haslam, Adam Kaplan, Amy Scott and Izabela Spaleniak, who are unlikely to realise how much they have inspired me.
- Any friends willing to forgive me for ignoring them during the extended times I was entirely absorbed in this PhD.

Bibliography

[1] J. Allen, J. Wolfe, and G. Schweitzer. A new electron spectrometer design. *International Journal of Mass Spectrometry and Ion Physics*, 8(1):81–83, 1972.

[2] C. Alsop, S. Scott, and L. Free. UV Rejection Design and Performance of the PEACE Electrostatic Analyzers. In R. F. Pfaff, J. E. Borovsky, and D. T. Young, editors, *Measurement Techniques in Space Plasmas – Particles*, page 269, 1998.

[3] V. Angelopoulos. Magnetospheric constellation: Past, present, and future. *Geophysical monograph*, 109:247–262, 1999.

[4] V. Angelopoulos. The THEMIS Mission. *Space Science Reviews*, 141(1-4):5–34, Apr. 2008.

[5] S. Barabash, A. Fedorov, R. Lundin, and J.-A. Sauvaud. Martian atmospheric erosion rates. *Science (New York, N.Y.)*, 315(5811):501–3, Jan. 2007.

[6] S. Barabash, R. Lundin, H. Andersson, K. Brinkfeldt, A. Grigoriev, H. Gunell, M. Holmström, M. Yamauchi, K. Asamura, P. Bochsler, P. Wurz, R. Cerulli-Irelli, A. Mura, A. Milillo, M. Maggi, S. Orsini, A. J. Coates, D. R. Linder, D. O. Kataria, C. C. Curtis, K. C. Hsieh, B. R. Sandel, R. a. Frahm, J. R. Sharber, J. D. Winningham, M. Grande, E. Kallio, H. Koskinen, P. Riihelä, W. Schmidt, T. Säles, J. U. Kozyra, N. Krupp, J. Woch, S. Livi, J. G. Luhmann, S. McKenna-Lawlor, E. C. Roelof, D. J. Williams, J.-A. Sauvaud, A. Fedorov, and J.-J. Thocaven. The Analyzer of Space Plasmas and Energetic Atoms (ASPERA-3) for the Mars Express Mission. *Space Science Reviews*, 126(1-4):113–164, Jan. 2007.

[7] S. Barabash, J. Sauvaud, and H. Gunell. The Analyzer of Space Plasmas and

Energetic Atoms (ASPERA-4) for the Venus Express Mission. *Planetary and Space*, pages 1–50, 2007.

[8] W. Baumjohann and R. A. Treumann. *Basic Space Plasma Physics*. Imperial College Press, 1997.

[9] R. Bedington. Fibre optic delay lines for wavefront correction in adaptive optics systems. Master's thesis, University of Durham, 2007.

[10] R. Bedington. Automating a fourier transform spectrometer for use at the large millimeter telescope site. Technical report, INAOE, 2010.

[11] R. Bedington. Developing a proposal for plasma analyser/space weather package as a flight demonstration payload for ukube-1. Technical report, Astrium Limited, 2010.

[12] R. Bedington. Miniaturised plasma analysers for cubesats. Technical report, Astrium Limited, 2010.

[13] R. Bedington, D. Kataria, and D. Walton. Using a CCD for the direct detection of electrons in a low energy space plasma spectrometer. *Journal of Instrumentation*, 7(01):C01079–C01079, Jan. 2012.

[14] R. Bedington, D. O. Kataria, A. Smith, and S. Eckersley. Development of a highly miniaturised low resource plasma analyser suitable for small satellite applications. In *Proceedings of the Symposium on Small Satellite Systems and Services (4S)*, volume 18, page 6, Funchal, 2010. ESA.

[15] J. Beraldin, F. Blais, and P. Boulanger. Real world modelling through high resolution digital 3D imaging of objects and structures. *ISPRS Journal of ...*, pages 230–250, 2000.

[16] R. L. Boggess and L. H. Brace. Langmuir probe measurements in the ionosphere. *JGR*, 64(10):1627–1630, 1959.

[17] A. Brantus. Miniaturised plasma analysers. Master's thesis, UCL - MSSL, 2009.

[18] H. Bridge, C. Dilworth, B. Rossi, F. Scherb, and E. Lyon. An instrument for the investigation of interplanetary plasma. *Journal of Geophysical Research*, 65(10):3053–3055, 1960.

[19] K. L. Brown. Faraday-Cup Monitors for High-Energy Electron Beams. *Review of Scientific Instruments*, 27(9):696, 1956.

[20] H. Bruining and H. Bruining. *Physics and applications of secondary electron emission*, volume 391. Pergamon Press, 1954.

[21] J. L. Burch, R. Goldstein, T. E. Cravens, W. C. Gibson, R. N. Lundin, C. J. Pollock, J. D. Winningham, and D. T. Young. RPC-IES: The Ion and Electron Sensor of the Rosetta Plasma Consortium. *Space Science Reviews*, 128(1-4):697–712, Dec. 2006.

[22] J. C. Cheng, G. R. Tripp, and L. W. Coleman. Intensified CCD readout system for ultrafast streak cameras. *Journal of Applied Physics*, 49(11):5421, 1978.

[23] F. Chollet and H. Liu. A (not so) short introduction to micro electro mechanical systems. `http://memscyclopedia.org/introMEMS.html`, May 2008. This is an electronic document published under Creative Commons Attribution-NonCommercial 2.5 License (`http://creativecommons.org/licenses/by-nc/2.5/legalcode`).

[24] C. Cinar and C. Lokcu. The undergraduate satellite design, fabrication, launch and operations program at the United States Air Force Academy. In *Recent Advances in Space Technologies, 2005. RAST 2005. Proceedings of 2nd International Conference on*, pages 829–833. IEEE, 2005.

[25] A. J. Coates. The Solar System in the next millennium. *Philosophical Transactions of the Royal Society A: Mathematical, Physical and Engineering Sciences*, 357(1763):3299–3317, Dec. 1999.

[26] A. J. Coates, F. J. Crary, G. R. Lewis, D. T. Young, J. H. Waite, and E. C. Sittler. Discovery of heavy negative ions in Titan's ionosphere. *Geophysical Research Letters*, 34(22):6–11, Nov. 2007.

[27] G. Collinson. *The computer simulated design of an improved plasma analyser towards an electron spectrometer for Solar Orbiter*. PhD thesis, University College London, 2010.

[28] G. A. Collinson, J. C. Dorelli, L. A. Avanov, G. R. Lewis, T. E. Moore, C. Pollock, D. O. Kataria, R. Bedington, C. S. Arridge, D. J. Chornay, U. Gliese, A. Mariano, A. C. Barrie, C. Tucker, C. J. Owen, A. P. Walsh, M. D. Shappirio, and M. L. Adrian. The geometric factor of electrostatic plasma analyzers: a case study from the Fast Plasma Investigation for the Magnetospheric Multiscale mission. *The Review of scientific instruments*, 83(3):033303, Mar. 2012.

[29] S. Curtis. Remanent magnetism at Mars. *Geophysical research letters*, 15(8):737–739, 1988.

[30] T. Daud, J. R. Janesick, K. Evans, and T. Elliott. Charge-coupled-device response to electron beam energies of less than 1 keV up to 20 keV. *Optical Engineering*, 26(Aug):686–691, 1987.

[31] E. Deelman and G. Singh. The cost of doing science on the cloud: the montage example. In *International Conference for High Performance Computing, Networking, Storage and Analysis, 2008. SC 2008.*, volume 1, pages 1–12, 2008.

[32] M. Desai, F. Allegrini, R. Livi, and S. Livi. The Entrance System for An Advanced Mass and Ionic Charge Composition Experiment (AMICCE) for Heliospheric Missions. *galprop.stanford.edu*, pages 1–4, 2009.

[33] S. Eckersley, R. Wall, S. J. Schwartz, M. Pudney, and R. Bedington. A nanosatellite multi-scale mission concept, enabled by highly miniaturised plasma physics payloads. *Proceedings of the Symposium on Small Satellite Systems and Services (4S)*, P(5):7, 2010.

[34] O. Emam, T. FitzGeorge, A. Whittaker, A. Wishart, S. Fowell, M. Prochazka, R. Bentley, R. Cole, P. Brown, C. Carr, E. Cupido, and T. Oddy. Payloads with Resource-Efficient Integration for Science Missions (PRISM). In *ESA Special Publication*, volume 669 of *ESA Special Publication*, may 2009.

[35] C. Enloe. Laminated electrostatic analyzer, 28 2004. US Patent 6,797,951.

[36] C. L. Enloe, L. H. Krause, R. K. Haaland, T. T. Patterson, C. E. Richardson, C. C. Lazidis, and R. G. Whiting. Miniaturized electrostatic analyzer manufactured using photolithographic etching. *Review of Scientific Instruments*, 74(3):1192, 2003.

[37] C. Escoubet, M. Fehringer, M. Goldstein, and Others. Introduction The Cluster mission. *Annales Geophysicae*, 19(10/12):1197–1200, 2001.

[38] D. S. Evans. Low Energy Charged-Particle Detection Using the Continuous-Channel Electron Multiplier. *Review of Scientific Instruments*, 36(3):375, 1965.

[39] H. S. Feldmesser, M. a. G. Darrin, R. Osiander, L. J. Paxton, a. Q. Rogers, J. a. Marks, M. G. McHarg, R. L. Balthazor, L. H. Krause, and J. G. FitzGerald. Canary: ion spectroscopy for ionospheric sensing. In *Proceedings of SPIE*, volume 7691, page 76910K, 2010.

[40] J. Fennell, H. Spence, T. Moore, and J. Galloway. Magnetospheric Constellation Missions. In *Cluster-II Workshop Multiscale/Multipoint Plasma Measurements*, volume 449, page 235, 2000.

[41] R. Feynman. There's plenty of room at the bottom [data storage]. *Microelectromechanical Systems, Journal of*, 1(1):60–66, 1992.

[42] J. Fiebiger. Pair-Production Energies in Silicon and Germanium Bombarded with Low-Energy Electrons. *Journal of Applied Physics*, 43(7):3202, 1972.

[43] C. Freidhoff, R. Young, S. Sriram, T. Braggins, T. O'Keefe, J. Adam, H. Nathanson, R. Syms, T. Tate, M. Ahmad, and Others. Chemical sensing using nonoptical microelectromechanical systems. *Journal of Vacuum Science & Technology A: Vacuum, Surfaces, and Films*, 17:2300, 1999.

[44] H. Funsten. Response of 100% internal quantum efficiency silicon photodiodes to 200 eV-40 keV electrons. *IEEE Transactions on Nuclear Science*, 44(6):2561–2565, 1997.

[45] H. Funsten, S. Ritzau, R. Harper, and R. Korde. Response of 100% internal carrier collection efficiency silicon photodiodes to low-energy ions. *IEEE Transactions on Nuclear Science*, 48(6):1785–1789, 2001.

[46] H. O. Funsten and D. J. McComas. Limited resource plasma analyzers : Miniaturization concepts. In *Geophysical monograph*, volume 102, pages 157–167. American Geophysical Union, 1998.

[47] H. O. Funsten, S. M. Ritzau, R. W. Harper, and R. Korde. Fundamental limits to detection of low-energy ions using silicon solid-state detectors. *Applied Physics Letters*, 84(18):3552, 2004.

[48] M. Geear, R. Syms, S. Wright, and a.S. Holmes. Monolithic MEMS quadrupole mass spectrometers by deep silicon etching. *Journal of Microelectromechanical Systems*, 14(5):1156–1166, Oct. 2005.

[49] D. J. Gershman and T. H. Zurbuchen. Modeling extreme ultraviolet suppression of electrostatic analyzers. *The Review of scientific instruments*, 81(4):045111, May 2010.

[50] G. Gloeckler, J. Geiss, H. Balsiger, P. Bedini, J. Cain, J. Fisher, L. Fisk, A. Galvin, F. Gliem, and D. Hamilton. The solar wind ion composition spectrometer. *Astronomy and Astrophysics Supplement Series*, 92:267–289, 1992.

[51] R. Goldstein, S. Nikzad, M. Davis, R. Frahm, D. Slater, and T. Jones. Results of measurements of the response of a delta-doped CCD to neutral and charged particle beams. *Advances in Space Research*, 47(11):1931–1936, June 2011.

[52] G. Gustafsson, R. Boström, B. Holback, G. Holmgren, A. Lundgren, K. Stasiewicz, L. Åhlén, F. Mozer, D. Pankow, P. Harvey, et al. The electric field and wave experiment for the cluster mission. *Space Science Reviews*, 79(1):137–156, 1997.

[53] L. Habashkrause, R. Balthazor, M. Mcharg, and B. Reinisch. Development of a campaign to study equatorial ionospheric phenomena over Guam. *Advances in Space Research*, 42(4):791–796, Aug. 2008.

[54] O. Hachenberg and W. Brauer. Secondary electron emission from solids. *Advances in Electronics and Electron Physics*, 11:413–499, 1959.

[55] S. Hahn, R. Elphic, T. Murphy, M. Hodgson, R. Byrd, J. Longmire, D. Lawrence, B. Barraclough, K. Fuller, T. Prettyman, and Others. A validation payload for

space and atmospheric nuclear event detection. *Nuclear Science, IEEE Transactions on*, 50(4):1175–1181, 2003.

[56] M. Hapgood, S. Eckersley, R. Lundin, M. Kluge, U. Prechtel, E. Daly, and A. Glover. Nanosatellite beacons for space weather monitoring - esa 6th round table on mnt, October 2007.

[57] J. Hauschild, E. Wapelhorst, and J. Muller. Mass spectra measured by a fully integrated MEMS mass spectrometer. *International Journal of Mass Spectrometry*, 264(1):53–60, June 2007.

[58] H. Heidt, J. Puig-Suari, A. Moore, S. Nakasuka, and R. Twiggs. CubeSat: A new generation of picosatellite for education and industry low-cost space experimentation. In *Proceedings of the Thirteenth Annual AIAA/USU Small Satellite Conference, Logan, UT*, 2000.

[59] M. Hoenk, P. Grunthaner, F. Grunthaner, R. Terhune, M. Fattahi, and H. Tseng. Growth of a delta-doped silicon layer by molecular beam epitaxy on a charge-coupled device for reflection-limited ultraviolet quantum efficiency. *Applied physics letters*, 61(9):1084–1086, 1992.

[60] M. E. Hoenk, T. J. Jones, M. R. Dickie, F. Greer, T. J. Cunningham, E. R. Blazejewski, and S. Nikzad. Delta-doped back-illuminated CMOS imaging arrays: progress and prospects. *Proceedings of SPIE*, 7419(1):15, Aug. 2009.

[61] A. Hughes and V. Rojansky. On the analysis of electronic velocities by electrostatic means. *Physical Review*, 34(2):284, 1929.

[62] B. Jacquot and M. Hoenk. Direct Detection of 100-5000 eV Electrons With Delta-Doped Silicon CMOS and Electron-Multiplying CCD Imagers. *IEEE Transactions on Electron Devices*, 59(7):1988–1992, 2012.

[63] A. James, A. Johnstone, D. Walton, O. Vaisberg, and A. Fedorov. A fast omnidirectional ion detector for the study of space plasmas. *Geophysical monograph*, 102:281–285, 1998.

[64] J. Janesick. *Scientific charge-coupled devices*, volume 83. Society of Photo Optical, 2001.

[65] S. Janson, H. Helvajian, S. Amimoto, G. Smit, D. Mayer, and S. Feuerstein. Microtechnology for space systems. In *Aerospace Conference, 1998. Proceedings., IEEE*, volume 1, pages 409–418. IEEE, 1998.

[66] A. D. Jewell, T. J. Jones, M. P. Sinha, and S. Nikzad. Simultaneous direct detection of sub keV molecular and atomic ions with a delta-doped charge-coupled device at the focal plane of a miniature mass spectrometer. *Applied Physics Letters*, 88(4):043501, Jan. 2006.

[67] A. Johnstone, C. Alsop, S. Burge, P. Carter, A. Coates, A. Coker, A. Fazakerley, M. Grande, R. Gowen, C. Gurgiolo, and Others. PEACE: A plasma electron and current experiment. *Space Science Reviews*, 79(1):351–398, 1997.

[68] A. D. Johnstone. The Geometric Factor of a Cylindrical Plate Electrostatic Analyzer. *Review of Scientific Instruments*, 43(7):1030, 1972.

[69] G. Juve, E. Deelman, K. Vahi, G. Mehta, B. Berriman, B. P. Berman, and P. Maechling. Scientific workflow applications on Amazon EC2. *2009 5th IEEE International Conference on E-Science Workshops*, pages 59–66, Dec. 2009.

[70] D. Kataria, A. Aruliah, B. Bentley, A. Smith, and R. Bedington. Miniaturised particle sensors suitable for future space weather missions - the geomagnetic field: Preparing for the swarm multi-satellite mission, October 2009.

[71] D. Kataria, A. Coates, M. D.J., G. Jones, C. Arridge, A. Fazakerley, C. Owen, G. Branduardi-Raymont, R. Bedington, D. Young, F. Crary, M. Desai, S. Bolton, S. Selci, R. Leoni, A. Di Lellis, F. Bagenal, R. Johnson, S. Miller, N. Achilleos, S. Cowley, E. Bunce, and S. J. Miniaturised plasma analysis techniques for the jummp investigation - europa jupiter system mission instrument workshop, July 2009.

[72] D. Kataria, A. Smith, P. Brown, T. Horbury, T. Vladimirova, C. Underwood, C. Carr, M. Dougherty, A. Coates, and R. Bedington. Development of a cubesat-based highly integrated science payload package suitable for future planetary missions. In *European Planetary Science Congress 2009*, volume 1, page 562, 2009.

[73] W. Keith. Development of an ion/electron plasma spectrometer. *Master of Science Thesis, Rice University, Houston, Texas*, 1999.

[74] R. L. Kessel, a. D. Johnstone, a. J. Coates, and R. a. Gowen. Space plasma measurements with ion instruments. *Review of Scientific Instruments*, 60(12):3750, 1989.

[75] M. Kivelson and C. Russell. *Introduction to space physics*. Cambridge university press, 1995.

[76] G. Knoll. *Radiation detection and measurement*. Wiley, 2000.

[77] R. D. Knthodemstrahlem. Ueber die Reflexion der Kathodenstrahlen und eine damit verbundene neue Erscheinung secundärer Emission. *Annalen der Physik*, 1902.

[78] L. H. Krause, C. Enloe, R. Haaland, and P. Golando. Microsatellite missions to conduct midlatitude studies of equatorial ionospheric plasma bubbles. *Advances in Space Research*, 36(12):2474–2479, 2005.

[79] J. Ladislas Wiza. Microchannel plate detectors. *Nuclear Instruments and Methods*, 162(1-3):587–601, June 1979.

[80] M. Lampton and C. W. Carlson. Low-distortion resistive anodes for two-dimensional position-sensitive MCP systems. *The Review of scientific instruments*, 50(9):1093–7, Sept. 1979.

[81] A. Lee, R. Bedington, A. Edwards-Smith, M. Hills, T. Nordheim, A. Daurskikh, V. Roitch, N. Edge, R. Lee, and H. Dalgeish. Student experiment documentation: Polar test of the conceptual and tiny spectrometer v3.0. Technical report, Eurolaunch, A DLR and SSC cooperation, 2012.

[82] F. Lei, P. Truscott, C. Dyer, B. Quaghebeur, D. Heynderickx, P. Nieminen, H. Evans, and E. Daly. MULASSIS: a geant4-based multilayered shielding simulation tool. *IEEE Transactions on Nuclear Science*, 49(6):2788–2793, Dec. 2002.

[83] P. Lenard. *Quantitatives ber Kathodenstrahlen*. PhD thesis, Heideberg, 1918.

[84] S. T. Lepri, S. Nikzad, T. Jones, J. Blacksberg, and T. H. Zurbuchen. Response of a delta-doped charge-coupled device to low energy protons and nitrogen ions. *Review of Scientific Instruments*, 77(5):053301, 2006.

[85] G. Lewis, C. Arridge, D. Linder, L. Gilbert, D. Kataria, A. Coates, A. Persoon, G. Collinson, N. André, P. Schippers, J. Wahlund, M. Morooka, G. Jones, A. Rymer, D. Young, D. Mitchell, A. Lagg, and S. Livi. The calibration of the Cassini -Huygens CAPS Electron Spectrometer. *Planetary and Space Science*, 58(3):427–436, Feb. 2010.

[86] Z. Liu, C. Escoubet, and Z. Pu. The double star mission. *Annales Geophysicae*, 23(July 2001):2707–2712, 2005.

[87] R. L. D. M Elisabeth Pate-Cornell. Success factors and future challenges in the management of faster-better-cheaper projects: Lessons learned from NASA. *Engineering Management, IEEE*, 48(1):25–35, 2001.

[88] R. Marsden and D. Mueller. Solar orbiter definition study report. Technical report, European Space Agency, 2011.

[89] F. J. Marshall, D. A. Hardy, A. Huber, J. Pantazis, and J. McGarity. Calibration system for electron detectors in the energy range from 10 eV to 50 keV. *Review of Scientific Instruments*, 57:229–235, feb 1986.

[90] C. Martin. Wedge-and-strip anodes for centroid-finding position-sensitive photon and particle detectors. *Review of Scientific Instruments*, 52(7):1067, 1981.

[91] D. McCann, S. Barabash, H. Nilsson, and a. Bhardwaj. Miniature ion mass analyzer. *Planetary and Space Science*, 55(9):1190–1196, June 2007.

[92] D. J. McComas, J. E. Nordholt, J.-J. Berthelier, J.-M. Illiano, and D. Young. The Cassini Ion Mass Spectrometer. In *Geophysical monograph*, volume 102, pages 187–193. American Geophysical Union, 1998.

[93] S. Moseley, R. Arendt, and R. Boucarut. Microshutters arrays for the JWST near infrared spectrograph. *Proc. SPIE*, 2004.

[94] M. Neugebauer and C. Snyder. Mariner 2 observations of the solar wind 1. Average properties. *Journal of Geophysical Research*, 71(19):4469–4484, 1966.

[95] H. Niemann, S. Atreya, and G. Carignan. The Galileo probe mass spectrometer: Composition of Jupiter's atmosphere. *Science*, 1996.

[96] S. Nikzad, T. J. Cunningham, M. E. Hoenk, R. P. Ruiz, D. M. Soules, and S. E. Holland. Direct detection of 0.1-20 keV electrons with delta doped, fully depleted, high purity silicon p-i-n diode arrays. *Applied Physics Letters*, 89(18):182114, 2006.

[97] S. Nikzad, Q. Yu, A. L. Smith, T. J. Jones, T. a. Tombrello, and S. T. Elliott. Direct detection and imaging of low-energy electrons with delta-doped charge-coupled devices. *Applied Physics Letters*, 73(23):3417, 1998.

[98] H. O'Brien, P. Brown, T. Beek, C. Carr, E. Cupido, and T. Oddy. A radiation tolerant digital fluxgate magnetometer. *Measurement Science and Technology*, 18(11):3645–3650, Nov. 2007.

[99] K. Ogasawara, K. Asamura, T. Mukai, and Y. Saito. Avalanche photodiode for measurement of low-energy electrons. *Nuclear Instruments and Methods in Physics Research Section A: Accelerators, Spectrometers, Detectors and Associated Equipment*, 545(3):744–752, June 2005.

[100] K. Ogasawara, S. Livi, E. Grotheer, and D. McComas. Thin dead-layer avalanche photodiodes enable low-energy ion measurements. *Nuclear Instruments and Methods in Physics Research Section A: Accelerators, Spectrometers, Detectors and Associated Equipment*, 614(2):271–277, Mar. 2010.

[101] R. Osiander, M. Darrin, and J. Champion. *MEMS and Microstructures in aerospace applications*. Taylor & Francis, 2006.

[102] G. Paschmann, H. Loidl, and P. Obermayer. The plasma instrument for AMPTE IRM. *Geoscience and*, 23(3):262–266, 1985.

[103] A. Pedersen, F. Mozer, and G. Gustafsson. Electric field measurements in a tenuous plasma with spherical double probes. *Geophysical monograph - American Geophysical Union*, 103:1–12, 1998.

[104] I. Preiss and R. Fink. The beta spectrum of carrier-free Ni63. *Journal of Inorganic and Nuclear*, 4(January):233–236, 1957.

[105] F. Primdahl. The fluxgate magnetometer. *Journal of Physics E: Scientific Instruments*, 12:241, 1979.

[106] M. Reinhardt, G. Quiring, R. R. Wong, H. Wehrs, and J. Müller. Helium detection using a planar integrated micro-mass spectrometer. *International Journal of Mass Spectrometry*, 295(3):145–148, Aug. 2010.

[107] E. Rutherford. The scattering of α and ßparticles by matter and the structure of the atom. *Philosophical Magazine Series 6*, 21(125):669–688, 1911.

[108] A. Sakic, L. Nanver, T. Scholtes, C. Heerkens, G. van Veen, K. Kooijman, and P. Vogelsang. Silicon photodiodes for high-efficiency low-energy electron detection. In *Solid-State Device Research Conference (ESSDERC), 2010 Proceedings of the European*, pages 102–105, 2010.

[109] Y. Salomon, N. Sternberg, and I. Gouzman. Qualification of Acktar black coatings for space application. In *International Symposium on Materials in the Space Environment*, volume 11, pages 2–8, 2009.

[110] P. Schagen. Advances in image pick-up and display, vol. 1. *Academic Press, New York*, 197(4):1I, 1974.

[111] S. J. Schwartz, T. Horbury, C. Owen, W. Baumjohann, R. Nakamura, P. Canu, A. Roux, F. Sahraoui, P. Louarn, J.-A. Sauvaud, J.-L. Pinçon, A. Vaivads, M. F. Marcucci, A. Anastasiadis, M. Fujimoto, P. Escoubet, M. Taylor, S. Eckersley, E. Allouis, and M.-C. Perkinson. Cross-scale: multi-scale coupling in space plasmas. *Experimental Astronomy*, 23(3):1001–1015, Mar. 2008.

[112] A. Sharma and S. Curtis. Magnetospheric multiscale mission. *Nonequilibrium phenomena in plasmas*, pages 179–195, 2005.

[113] E. Shelley, A. Ghielmetti, H. Balsiger, R. Black, J. Bowles, R. Bowman, O. Bratschi, J. Burch, C. Carlson, A. Coker, and Others. The toroidal imaging mass-angle spectrograph (TIMAS) for the Polar mission. *Space Science Reviews*, 71(1):497–530, 1995.

[114] L. Shing, R. Stern, P. Catura, and M. Morrison. CCD development and characterization for the GOES N and O Solar X-ray Imager. *Proceedings of SPIE*, 3765(July):299–309, 1999.

[115] O. Siegmund, J. Stock, and D. Marsh. Delay-line detectors for the UVCS and SUMER instruments on the SOHO Satellite. *Proceedings of SPIE*, 2280:89–100, 1994.

[116] A. Smith. Final Report of the QB50 SSWG. Technical report, QB50 Sensor Selection Working Group, 2012.

[117] A. Smith, R. Kessel, J. S. Lapington, and D. M. Walton. Modulation effects in wedge and strip anodes. *Review of Scientific Instruments*, 60(11):3509, 1989.

[118] R. Snare. A history of vector magnetometry in space. *Geophysical monograph - American Geophysical Union*, 103:101–114, 1998.

[119] R. Stalder, S. Boumsellek, T. Van Zandt, T. Kenny, M. Hecht, and F. Grunthaner. Micromachined array of electrostatic energy analyzers for charged particles. *Journal of Vacuum Science & Technology A: Vacuum, Surfaces, and Films*, 12(4):2554–2558, 1994.

[120] D. G. Stearns and J. D. Wiedwald. Response of charge-coupled devices to direct electron bombardment. *Review of Scientific Instruments*, 60(6):1095, 1989.

[121] R. Stern, L. Shing, and M. Blouke. Quantum efficiency measurements and modeling of ion-implanted, laser-annealed charge-coupled devices: x-ray, extreme-ultraviolet, ultraviolet, and optical data. *Applied optics*, 33(13):2521–2533, 1994.

[122] R. A. Stern. Characterization of the flight CCD detectors for the GOES N and O solar x-ray imagers. *Proceedings of SPIE*, 5171:77–88, 2004.

[123] M. Swartwout. The Argus mission: Detecting thruster plumes for Space Situational Awareness. *Aerospace Conference, 2011*, 2011.

[124] I. Szücs, I. Szemerey, P. Kiraly, W. Sharp, N. Shutte, T. Cravens, T. Gombosi, K. Gringauz, A. Nagy, S. Sheronova, and Others. The HARP electron and ion

sensor on the phobos mission. *Nuclear Instruments and Methods in Physics Research Section A: Accelerators, Spectrometers, Detectors and Associated Equipment*, 290(1):228–236, 1990.

[125] A. G. Union, R. Pfaff, J. Borovsky, and D. Young. *Measurement techniques in space plasmas: fields*. Geophysical Monograph. American Geophysical Union, 1998.

[126] A. Vampola. Measuring energetic electrons-what works and what doesn't. *Geophysical monograph - American Geophysical Union*, 102:339–355, 1998.

[127] E. Wapelhorst, J. Hauschild, and J. Muller. Complex MEMS: a fully integrated TOF micro mass spectrometer. *Sensors and Actuators A: Physical*, 138(1):22–27, July 2007.

[128] D. M. Wesolek, M. A. G. Darrin, and R. Osiander. Wafer Scale Integration Enabling Space Science. *2008 IEEE Aerospace Conference*, pages 1–7, Mar. 2008.

[129] D. M. Wesolek, F. a. Hererro, R. Osiander, and M. A. G. Darrin. Design, fabrication, and performance of a micromachined plasma spectrometer. *Journal of Microlithography, Microfabrication, and Microsystems*, 4(4):041403, 2005.

[130] D. Wesoleka, a.G. Darrina, R. Osiandera, S. Lehtonena, R. Edwardsa, and F. Hererrob. Micro Processing a Path to Aggressive Instrument Miniaturization for Micro and Picosats. *2005 IEEE Aerospace Conference*, pages 1–8, 2005.

[131] B. Wilken, A. Korth, and S. Livi. RAPID: The imaging energetic particle spectrometer on Cluster. *Cluster: mission,*, pages 399–473, 1993.

[132] M. Wueest. Time-of-flight ion composition measurement technique for space plasmas. *Geophysical monograph - American Geophysical Union*, 102:141–156, 1998.

[133] M. Wüest, D. Evans, and R. von Steiger. *Calibration of Particle Instruments in Space Physics*. ESA Communications, 2007.

[134] M. Yavor. *Advances in Imaging and Electron Physics: Optics of Charged Particle AnalyzersVolume 157 of Advances in Imaging and Electron Physics*. Advances in Imaging & Electron Physics. Elsevier Science, 2009.

[135] D. T. Young. Space Plasma Particle Instrumentation and the New Paradigm: Faster Cheaper, Better. In R. F. Pfaff, J. E. Borovsky, & D. T. Young, editor, *Measurement Techniques in Space Plasmas – Particles*, page 1, 1998.